

UNIVERSITY OF CALIFORNIA SAN DIEGO

Process-Based Models of Optimal Complexity

A dissertation submitted in partial satisfaction of the
requirements for the degree of Doctor of Philosophy

in

Engineering Sciences (Mechanical Engineering)

by

Alvaro Ruiz-Martinez

Committee in charge:

Professor Daniel M. Tartakovsky, Chair
Professor Terrence J. Sejnowski, Co-Chair
Professor James R. Friend
Professor Marcos Intaglietta
Professor Bo Li

2018

Copyright

Alvaro Ruiz-Martinez, 2018

All rights reserved.

The Dissertation of Alvaro Ruiz-Martinez is approved and is acceptable in quality and form for publication on microfilm and electronically:

Co-Chair

Chair

University of California San Diego

2018

EPIGRAPH

It can scarcely be denied that the supreme goal of all theory is to make the irreducible basic elements as simple and as few as possible without having to surrender the adequate representation of a single datum of experience.

Albert Einstein

TABLE OF CONTENTS

Signature Page	iii
Epigraph	iv
Table of Contents	v
List of Figures	viii
List of Tables	xii
Acknowledgements	xv
Vita	xvi
Abstract of the Dissertation	xvii
Introduction	1
Chapter 1 Analytical Models of Heat Conduction in Fractured Rocks	3
1.1 Introduction	3
1.2 Problem Formulation	5
1.3 Analytical Solutions	7
1.3.1 General solution in Fourier-Laplace space	7
1.3.2 Explicit models of temperature in the fracture	8
1.3.3 Accuracy of analytical solutions	10
1.4 Comparison with existing models	11
1.4.1 No dispersion in semi-infinite fracture	11
1.4.2 Longitudinal dispersion in semi-infinite fracture	11
1.5 Results and Discussion	12
1.5.1 Effects of heat conduction in matrix	13
1.5.2 Performance of geothermal systems	14
1.6 Conclusions	15
1.7 Future Research	17
Chapter 2 Efficient Multiscale Models of Polymerization Applied to <i>in vitro</i> FtsZ Assembly	28
2.1 Introduction	28
2.2 Model of FtsZ Assembly	31
2.2.1 Model formulation	31
2.2.2 Model parametrization	38
2.3 Results and Discussion	42
2.3.1 Model predictions at high concentrations, $C_{\text{tot}} = 3.0 - 10.0 \mu\text{M}$	42
2.3.2 Physiological insights	43

2.3.3	Comparison with alternative models	44
2.4	Conclusions	46
Chapter 3	Efficient Multiscale Models of Polymerization Applied to <i>in vivo</i> FtsZ Ring Assembly in <i>Escherichia coli</i>	56
3.1	Introduction	56
3.2	Average Feature Model of Polymerization	57
3.2.1	Short-time kinetics	58
3.2.2	Long-time kinetics	59
3.2.3	Concentration of species sets	60
3.2.4	Model's calibration, validation, and computational cost	62
3.3	FtsZ-Ring Assembly in <i>E. coli</i>	63
3.3.1	Timing of FtsZ ring formation	63
3.3.2	FtsZ ring features	65
3.3.3	ZapA deficiency	66
3.4	Conclusions	67
Chapter 4	Stochastic self-tuning hybrid algorithm for reaction-diffusion systems	76
4.1	Introduction	76
4.2	Description of the model	77
4.2.1	Compartment size choice	79
4.2.2	Time-step choice	80
4.2.3	Modified Gillespie algorithm	81
4.3	Algorithm	83
4.4	Results and discussion	86
4.4.1	Performance analysis	86
4.4.2	Limit case scenarios	89
4.4.3	Effect of number of molecules	91
4.5	Conclusions	92
Chapter 5	Conclusions	104
Appendix A	Analytical Models of Heat Conduction in Fractured Rocks	107
A.1	Green's functions	107
A.1.1	Green's function for fracture BVP	107
A.1.2	Green's function for matrix BVP	108
A.2	Integral solutions of BVPs	108
A.3	Fourier-Laplace inversions	109
A.3.1	Inverse Laplace transform of \tilde{T}^f	110
A.3.2	Inverse Fourier transform of \hat{T}^f	111
A.3.3	Limits of applicability of analytical model (1.13)	112
Appendix B	Efficient Multiscale Models of Polymerization Applied to <i>in vitro</i> FtsZ As- sembly	114

B.1	Ordinary differential equations for concentrations	114
B.2	Conservation of mass and energy	116
B.3	Parameter identification from steady-state, low concentration data ($C_{\text{tot}} = 0.7 - 3.0 \mu\text{M}$)	117
B.4	Model validation	119
Appendix C Efficient Multiscale Models of Polymerization Applied to <i>in vivo</i> FtsZ Ring Assembly in <i>Escherichia coli</i>		
		129
C.1	ODEs for <i>in vitro</i> Systems	129
	C.1.1 Conservation of mass	131
	C.1.2 Conservation of energy	131
C.2	Model Parametrization	132
	C.2.1 Model calibration procedure	136
C.3	Model Validation	138
	C.3.1 Transient, low-concentration phenomena	138
	C.3.2 Steady-state, high-concentration phenomena	140
C.4	Comparison of Computational Costs	141
	C.4.1 Comparison of <i>in vivo</i> predictions	142
C.5	AFM-based Description of Z-ring Formation	144
	C.5.1 Physiological considerations	144
	C.5.2 ODEs for <i>in vivo</i> systems	148
	C.5.3 Model parametrization	150
	C.5.4 ZapA deficiency	152
C.6	<i>In vitro</i> bundling reactions and their rates	153
	C.6.1 Forward bundling rate	153
	C.6.2 Backward bundling rate	156
C.7	<i>In vivo</i> bundling reactions and their rates	159
Appendix D Stochastic self-tuning hybrid algorithm for reaction-diffusion systems		
		184
D.1	Effect of number of molecules	184
Bibliography		
		189

LIST OF FIGURES

Figure 1.1.	Single fracture embedded in an infinite matrix.	20
Figure 1.2.	Distributions of the relative temperature along the fracture for flow velocity $u = 1.4 \times 10^{-4}$ m/s and different values of the dimensionless parameters R and K , computed with the analytical and numerical solutions. The liquid is injected at $x = 0$ during (a) $t = 1$ month and (b) $t = 1$ year.	21
Figure 1.3.	Distributions of the relative temperature along the fracture for flow velocity $u = 1.4 \times 10^{-3}$ m/s and different values of the dimensionless parameters R and K , computed with the analytical and numerical solutions. The liquid is injected at $x = 0$ during (a) $t = 1$ month and (b) $t = 1$ year.	22
Figure 1.4.	Relative temperature in the fracture T_r^f , as a function of advection time $t_a^* = tu/x$, computed with the 1-D solution and the 2-D solution for $D_L^m = 9.16 \times 10^9$, 9.16×10^8 , and 9.16×10^7 m ² /s. Fracture aperture $2b$ is set to (a) 2×10^4 m, (b) 5×10^4 m, and (c) 10^3 m	23
Figure 1.5.	Isolines of the geothermal performance P_f in the space of advection (t_a^*) and diffusion (t_d^*) times, for (a) $R = 1$, (b) $R = 2$, and (c) $R = 5$	24
Figure 1.6.	Isolines of the geothermal performance P_f in the space of diffusion time t_d^* and the inverse fracture-matrix Péclet number R , for (a) $1 \leq R \leq 20$ and (b) $1 \leq R \leq 5$	25
Figure 1.7.	Distributions of the relative temperature in the porous matrix for fracture aperture $2b = 1 \times 10^{-3}$ m and distance from the center of the fracture $z = 5 \times 10^{-2}$ m computed with the analytical and numerical solutions for dimensionless parameter $R = 1, 10$ and 100	26
Figure 1.8.	Distributions of the relative temperature in the porous matrix for fracture aperture $2b = 1 \times 10^{-3}$ m and distance from the center of the fracture $z = 5$ m computed with the analytical and numerical solutions for dimensionless parameter $R = 1, 10$ and 100	27
Figure 2.1.	Basic polymer structures and reactions and their graphical representation.	52
Figure 2.2.	Shortening of a bundle of two filaments by hydrolysis (left) and its mathematical representation in our model (right).	53
Figure 2.3.	Temporal evolution of the average number of monomers connected longitudinally into filaments and bundles (left) and the average number of filaments per bundle (right), for $C_{tot} = 3.0, 5.0$, and 10.0 μM	54

Figure 2.4.	Length/width for the filaments and bundles at steady state, for a range of concentration C_{tot}	55
Figure 4.1.	Temporal evolution of the concentration of the species C in the region \mathcal{D}' for a case with dominant diffusion effects ($D_1 = 10^{-12} \text{ m}^2/\text{s}$, $k_{r1} = 3 \times 10^3 \text{ mM}^{-1}\text{s}^{-1}$). Solid line is the deterministic solution in both graphics	97
Figure 4.2.	Temporal evolution of the concentration of the species C in the region \mathcal{D}' for a case with similar diffusion and reaction effects ($D_2 = 10^{-13} \text{ m}^2/\text{s}$, $k_{r1} = 3 \times 10^3 \text{ mM}^{-1}\text{s}^{-1}$). Solid line is the deterministic solution in both graphics.	98
Figure 4.3.	Temporal evolution of the concentration of the species C in the region \mathcal{D}' for a case with dominant reaction effects ($D_2 = 10^{-13} \text{ m}^2/\text{s}$, $k_{r2} = 3 \times 10^4 \text{ mM}^{-1}\text{s}^{-1}$). Solid line is the deterministic solution in both graphics	99
Figure 4.4.	Top: Relative error for different regimes, from diffusion-controlled ($D = 10^{-14} \text{ m}^2/\text{s}$) to reaction-controlled ($D = 10^{-11} \text{ m}^2/\text{s}$). Bottom: Computational time for different regimes	100
Figure 4.5.	Temporal evolution of the concentration of the species C in the region \mathcal{D}' for a case with highly dominant reaction effects. Solid line is the deterministic solution in both graphics	101
Figure 4.6.	Temporal evolution of the concentration of the species A in the region \mathcal{D}' for a case with highly dominant diffusion effects. Solid line is the deterministic solution in both graphics	102
Figure 4.7.	Top: Relative peak concentration, N_r , for different initial number of molecules of A. Bottom: Computational time required to reach the steady state for different initial number of molecules of A	103
Figure B.1.	Convergence of the system at the maximum concentration $C_{\text{tot}} = 10 \text{ }\mu\text{M}$. Bundles with more than 10 filaments can be considered negligible.	125
Figure B.2.	Temporal evolution of FtsZ concentrations in the monomer, filament and bundle forms for total concentration $C_{\text{tot}} = 2.0 \text{ }\mu\text{M}$ and $10.0 \text{ }\mu\text{M}$. The sum of these three concentrations remains constant and equal to C_{tot} at all times t	126
Figure B.3.	Kinetics of the initial FtsZ-F268C assembly detected by the Fluorescence Resonance Energy Transfer experiment [CE5b], for three values of total concentration C_{tot}	127

Figure B.4.	Temporal evolution of the average number of monomers connected longitudinally into filaments and bundles (left) and the average number of filaments per bundle (right), for $C_{\text{tot}} = 1.0, 2.0,$ and $3.0 \mu\text{M}$	128
Figure C.1.	Graphical representation of basic polymer structures and reactions.	176
Figure C.2.	Kinetics of the initial FtsZ-F268C assembly observed in [CE5b], for three values of total concentration C_{tot} . The data points and compared with predictions of the models in [CE5b] (solid lines) and [RMBST16] (dashed lines), as well as with those of AFM (dotted lines)	177
Figure C.3.	Monomers per filament-to-Filaments per bundle ratio (or Monomers longitudinally connected per filament-to-Monomers laterally connected per bundle ratio) at steady state predicted by [RMBST16] (blue line) and AFM (red line), for a range of concentration C_{tot}	178
Figure C.4.	The number of ODEs (top row) comprising the model [RMBST16] (blue lines) and AFM (red lines) and computational cost (bottom row) as a function of the <i>in vitro</i> (left column) and <i>in vivo</i> (right column) total concentration C_{tot}	179
Figure C.5.	Top row: <i>Escherichia coli</i> cell before (left) and after (right) ring formation. Bottom row: Cross-section of the cell (left) and a magnified region near the cell membrane (right).	180
Figure C.6.	Alternative representations of a bead in a wide bundle of average width $\bar{f}_{\text{wb}} = 9$	181
Figure C.7.	Graphical representations of a bead in a two-dimensional wide bundle of $\bar{f}_{\text{wb,ZapA}} = 8$	182
Figure C.8.	Graphical representations of a bead in a three-dimensional structure made of cross-linked clusters of $\bar{f}_{\text{wb,ZapA}} = 36$	183
Figure D.1.	Temporal evolution of the concentration of the species C for $N_{A_0} = N_{B_0} = 60$ particles. Solid, dashed, and dash-dot lines are the deterministic solution, the solution obtained by Choi et al., model setting $\Delta x = \Delta y = \Delta z = L/4$, and the solution obtained by our model, respectively	185
Figure D.2.	Temporal evolution of the concentration of the species C for $N_{A_0} = N_{B_0} = 6 \times 10^2$ particles. Solid, dashed, and dash-dot lines are the deterministic solution, the solution obtained by Choi et al., model setting $\Delta x = \Delta y = \Delta z = L/8$, and the solution obtained by our model, respectively	186

Figure D.3. Temporal evolution of the concentration of the species C for $N_{A_0} = N_{B_0} = 6 \times 10^3$ particles. Solid, dashed, and dash-dot lines are the deterministic solution, the solution obtained by Choi et al., model setting $\Delta x = \Delta y = \Delta z = L/16$, and the solution obtained by our model, respectively 187

Figure D.4. Temporal evolution of the concentration of the species C for $N_{A_0} = N_{B_0} = 6 \times 10^4$ particles. Solid, dashed, and dash-dot lines are the deterministic solution, the solution obtained by Choi et al., model setting $\Delta x = \Delta y = \Delta z = L/32$, and the solution obtained by our model, respectively 188

LIST OF TABLES

Table 2.1.	Comparison of the kinetic <i>in vitro</i> models in terms of their complexity, applicability range, and ability to predict the observed features of FtsZ assembly. M1, M2, and M3 designate the models introduced in [LDWS08], respectively	49
Table 2.2.	Reaction rates and bond energies. [‡] The energy units are expressed in terms of the Boltzmann constant k_B and room temperature T. [†] Simple bundling model.	50
Table 2.3.	Steady-state monomer concentration, and average length and width, predicted with our model and observed in experiments [CE5b].	51
Table 3.1.	Comparison of the kinetic <i>in vitro</i> models in terms of their complexity, applicability range, and ability to predict the observed features of FtsZ assembly. M1, M2, and M3 designate the models introduced in [LDWS08], respectively; AFM denotes our Average Feature Model	69
Table 3.2.	Eighteen reactions comprizing our FtsZ kinetics model. The subscripts $z^-/f^-/b^-$ (and $z^+/f^+/b^+$) designate a monomer/filament/bundle lost (or gained) by a species.	70
Table 3.3.	Species, reaction and concentration of species sets. FW and BW designate forward and backward reactions, respectively.	71
Table 3.4.	Timing of FtsZ ring formation for a characteristic range of <i>in vivo</i> FtsZ concentrations, $C_{\text{tot},C;0} = 6 - 18 \mu\text{M}$	72
Table 3.5.	FtsZ ring features for a characteristic range of <i>in vivo</i> FtsZ concentrations, $C_{\text{tot},C;0} = 6 - 18 \mu\text{M}$, at steady state ($t \rightarrow \infty$).	73
Table 3.6.	Large FtsZ structures for a range of <i>in vivo</i> FtsZ concentrations, $C_{\text{tot},C;0} = 6 - 18 \mu\text{M}$	74
Table 3.7.	FtsZ species features for a characteristic range of <i>in vivo</i> FtsZ concentrations, $C_{\text{tot},C;0} = 6 - 18 \mu\text{M}$, in the absence of ZapA at steady state.	75
Table 4.1.	Values of the areas over the 3 seconds time-course of the deterministic solution and the values of the areas and the correspondent relative errors of Choi et al., model and ours based on average of 1000 iterations	93
Table 4.2.	Values of the relative errors of Choi et al., model and our model based on average of 100 iterations and computational times based on average of 10 iterations.	94

Table 4.3.	Values of relative peak concentration, N_r , and the relative time gap, ϕ_r , correspondent to Choi et al., model and our model for different initial concentrations of molecules, N_{A_0} and N_{B_0} , based on average of 1000 iterations.	95
Table 4.4.	Values of the computational time until steady-state is reached correspondent to Choi et al., model and our model for different initial concentrations of molecules, N_{A_0} and N_{B_0} , based on average of 10 iterations.	96
Table B.1.	Lower and upper bounds for the kinetic parameters used in the model calibration procedure.	121
Table B.2.	Lower and upper bounds for the concentrations (in μM , with $i = 2, \dots, 6$ and $j = 2, \dots, 10$), average length and average width, informed by the data in [CE5b].	122
Table B.3.	Initial guesses for the concentrations (in μM , with $i = 2, \dots, 6$ and $j = 2, \dots, 10$), average length and average width.	123
Table B.4.	Steady-state monomer concentration ($[Z^{\text{na}}]_{\text{ss}} + [Z]_{\text{ss}}$), and average length (\bar{L}_{tot}^m) and width (\bar{W}_{tot}^m), predicted with our model and observed in experiments [CE5b].	124
Table C.1.	Reaction rate constants and bond energies. The energy units are expressed in terms of the Boltzmann constant k_B and room temperature T	165
Table C.2.	Lower and upper bounds, and initial guesses, for the kinetic parameters used in the model calibration procedure.	166
Table C.3.	Lower and upper bounds for the concentrations (in μM , with $i = 2, 3$ and $j = 2, 3$), average length and average number of filaments per bundle, informed by the data in [CE5b].	167
Table C.4.	Initial guesses of the concentrations (in μM , with $i = 2, 3$), average length and average number of filaments per bundle.	168
Table C.5.	Steady-state average length (\bar{L}_{tot}^m), number of filaments per bundle (\bar{f}_{tot}) and monomer concentration ($[Z^{\text{na}}]_{\text{ss}} + [Z]_{\text{ss}}$), predicted by [RMBST16], [CE5b] and AFM, and observed in the low-concentration experiment [CE5b].	169
Table C.6.	Steady-state average length (\bar{L}_{tot}^m), number of filaments per bundle (\bar{f}_{tot}) and monomer concentration ($[Z^{\text{na}}]_{\text{ss}} + [Z]_{\text{ss}}$), predicted by [RMBST16], [CE5b] and AFM, and observed in the high-concentration experiment [CE5b].	170

Table C.7.	Comparison of timing predictions of FtsZ ring formation for a characteristic range of <i>in vivo</i> FtsZ concentrations, $C_{\text{tot},C;0} = 6 - 18 \mu\text{M}$. * denotes that the model [RMBST16] has been slightly modified by introducing <i>in vivo</i> factors.	171
Table C.8.	Comparison of FtsZ ring feature predictions for a characteristic range of <i>in vivo</i> FtsZ concentrations, $C_{\text{tot},C;0} = 6 - 18 \mu\text{M}$, at steady state ($t \rightarrow \infty$). * denotes that the model [RMBST16] has been slightly modified by introducing <i>in vivo</i> factors.	172
Table C.9.	MATLAB Benchmarking (times in seconds)	173
Table C.10.	Parameters of the <i>in vivo</i> model.	174
Table C.11.	Average number of filaments in a reactant R_i without and with ZapA proteins.	175

ACKNOWLEDGEMENTS

Chapter 1, in part, is a reprint of the material as it appears in Analytical models of heat conduction in fractured rocks 2014. Ruiz-Martínez, Á.; Roubinet, D.; and Tartakovsky, D.M., Journal of Geophysical Research, Solid Earth, 2014. The dissertation/thesis author was the primary investigator and author of this paper.

Chapter 1, last pages, are currently being prepared for submission for publication of the material. Ruiz-Martínez, Á. and Tartakovsky, D.M. The dissertation/thesis author was the primary investigator and author of this material.

Chapter 2, in full, is a reprint of the material as it appears in Efficient multiscale models of polymer assembly 2016. Ruiz-Martínez; Á., Bartol, T.M.; Sejnowski, T.J.; and Tartakovsky, D.M., Biophysical Journal, 2016. The dissertation/thesis author was the primary investigator and author of this paper.

Chapter 3, in full, is a reprint of the material as it appears in Efficient models of polymerization applied to FtsZ ring assembly in Escherichia coli 2018. Ruiz-Martínez; Á., Bartol, T.M.; Sejnowski, T.J.; and Tartakovsky, D.M., PNAS, 2018. The dissertation/thesis author was the primary investigator and author of this paper.

Chapter 4, in part is currently being prepared for submission for publication of the material. Ruiz-Martínez; Á., Bartol, T.M.; Sejnowski, T.J.; and Tartakovsky, D.M., The dissertation/thesis author was the primary investigator and author of this material.

VITA

- 2011 Bachelor of Science (Mechanical Engineering, two minors), Carlos III University of Madrid, Spain
- 2013-2018 Graduate Student Researcher, University of California San Diego and Salk Institute
- 2015 Master of Science, University of California San Diego
- 2017-2018 Teaching Assistant, University of California San Diego
- 2018 Ph. D. in Engineering Sciences (Mechanical Engineering), University of California San Diego

PUBLICATIONS

Ruiz-Martínez, Á., Roubinet, D., and Tartakovsky, D.M. Analytical models of heat conduction in fractured rocks, *J. Geophys. Res. Solid Earth*, 119, 83-98, 2014.

Ruiz-Martínez, Á., Bartol, T.M., Sejnowski, T.J., and Tartakovsky, D.M. Efficient multiscale models of polymer assembly, *Biophysical Journal*, 11(1):185-96, 2016.

Ruiz-Martínez, Á., Bartol, T.M., Sejnowski, T.J., and Tartakovsky, D.M. Efficient models of polymerization applied to FtsZ ring assembly in *Escherichia coli*, *PNAS*, 115 (19) 4933-4938, 2018.

Ruiz-Martínez, Á., Bartol, T.M., Sejnowski, T.J., and Tartakovsky, D.M. Stochastic self-tuning hybrid algorithm for reaction-diffusion systems, 2018. *To be submitted to The Journal of Chemical Physics*.

Ruiz-Martínez, Á. and Tartakovsky, D.M. Analytical models of heat conduction in fracture networks, 2019. *Under preparation*.

FIELDS OF STUDY

Major Field: Engineering Sciences (Mechanical Engineering)

Research in Computational Engineering and Computational Biology

Professors Daniel M. Tartakovsky and Terrence J. Sejnowski

ABSTRACT OF THE DISSERTATION

Process-Based Models of Optimal Complexity

by

Alvaro Ruiz-Martinez

Doctor of Philosophy in Engineering Sciences (Mechanical Engineering)

University of California San Diego, 2018

Professor Daniel M. Tartakovsky, Chair
Professor Terrence J. Sejnowski, Co-Chair

At their best, mathematical models of physical and biological systems strive to represent the nature faithfully while maximizing their simplicity and efficiency. Large numbers of variables involved in biophysical and geophysical processes make it necessary to develop predictive models with the minimum conceivable level of complexity. The combination of coupled phenomena, spatial and temporal scales, different regimes of behavior, and plethora of agents interacting simultaneously constitutes an unmanageable amalgamation of factors that unavoidably reduce both performance and tractability of mathematical models. Creating models with the optimal complexity requires finding the balance between the following characteristics: accuracy, compu-

tational cost, applicability to multiple scales and regimes, ability to represent realistic scenarios, and versatility. In this dissertation, we present analytical models of heat transfer in fractured porous media, *in vitro* and *in vivo* kinetics models of polymerization, and a hybrid algorithm for reaction-diffusion systems. These models provide more accurate representations of reality than their current counterparts, and they do so at the small fraction of the computational cost.

Introduction

This dissertation presents different models for complex problems based on previous works to show that, with feasible approaches, we can achieve remarkable improvements. Simplistic models can imply small errors and reasonable computational speeds in limited scenarios, but once they are developed to extend their range of applications or become part of bigger models, such shortcomings entail noticeable and unnecessary lacks of efficiency. In Chapter 1, we propose new analytical models for heat transfer in fractured porous media (*M1*); in Chapter 2, an *in vitro* kinetics model of polymerization is introduced (*M2*) to be later improved and extended to *in vivo* scenarios in Chapter 3 (*M3*); finally, in Chapter 4, we present a self-adjusted hybrid model for reaction-diffusion systems (*M4*).

In comparison to their counterparts, our models keep a better balance between all the following properties:

- *Accuracy and computational cost* - Without losing accuracy, *M1* proposes an analytical solution to a 2D diffusion problem that needed to be numerically solved in previous studies; *M2* presents an *in vitro* kinetics model of FtsZ protein polymerization that predicts faster and better than its predecessors by reducing the number of Ordinary Differential Equations (ODEs) from hundreds/thousands to seventeen; *M3* improves the latter by reducing the computational cost and making it independent on the total concentration, what makes it optimal for crowded *in vivo* scenarios; *M4* presents a more accurate hybrid model than its predecessor while keeping a reasonable computational cost by redefining both the step size and the time step depending on the particle spatial distributions.

- *Applicability to multiple scales and wide ranges of scenarios* - Solution presented in *M1* makes predictions for the entire spatial domain, for periods of time that cover from days to years, and for scenarios with dominant diffusion effects; *M2* works for short and long times as well as a wide range of concentrations; *M3* improves the latter by accurately predicting in crowded *in vivo* environments, where concentrations can be up to two orders of magnitude higher than in *in vitro* scenarios; *M4* self-adjusts dynamically both step size and time step to the appropriate scale and remains efficient in both reaction and diffusion-controlled regimes.
- *Realistic representation* - Model *M1* represents reality more faithfully than its analytical counterparts by introducing the effects of 2D diffusion and an infinite domain; polymer kinetics description in *M2* introduces the combination of bundling and GTP-hydrolysis that other models neglected; *M3* also includes the effects of membrane in real cells, the role of other proteins, and the influence of crowded environments in polymer diffusion; *M4* predicts location and time of particle interactions more realistically than its counterpart as well as fast concentration variations in time and space.
- *Versatility* - By applying the principle of superposition to our analytical solutions in model *M1*, we can potentially develop predictive models for heat transfer in fracture networks; *M2* and *M3* can be ideal as submodels of bigger kinetics models with more species and chemical reactions and as efficient compartmentalized and spatially distributed representations of *in vivo* polymerization processes; self-adjusted nature of model *M4* makes it much more versatile than models that need predefined step sizes, time steps, or parameters that determine the dominant regime in the system.

Summarizing, the desired simplicity for a model must be relative to the level of complexity that we attempt to represent. We modestly believe that the physical and chemical models presented in this dissertation got much closer to such optimal point than their predecessors.

Chapter 1

Analytical Models of Heat Conduction in Fractured Rocks

1.1 Introduction

Heat transfer in fractured rocks is a critical phenomenon that drives the performance of both enhanced geothermal systems (wherein heat transferred from hot dry rocks warms water circulating in fractures) [WRWT96, GLK12] and enhanced oil recovery (wherein oil viscosity is reduced by injecting hot water or steam, thus increasing rock temperature) [AHB01]. Heat conduction impacts the structural properties of ambient rocks by creating new or reopening existing microfractures [WBC⁺89, Lin02] and/or modifying rock alteration patterns [XP01]. Its negative effects are manifested in seismic activity induced by geothermal energy extraction [GFJ03, CS11] and in nuclear waste leakage due to heat generated by radioactive decay [XZ12, WTCW81].

Heat transfer in fractured subsurface environments takes place in at least two distinct phases: fluid-filled fractures and ambient solid matrix. Existing analytical and semianalytical models of heat conduction in fractured rocks consider single isolated fractures [Mey04] and networks of equally spaced horizontal [BT82] or vertical [YY09, GWO75] fractures. It is important to recognize that single-fracture representations are important not only in their own right, but also as conceptual representations of mobile/immobile regions in natural fractured systems [ZLM⁺07]. Such models are amenable to the same mathematical treatment as their

counterparts developed for mass transport in discrete fracture networks. Examples of the latter include analytical [TFS81], semianalytical [RdDT12, SF82] and numerical [RLdD10] models of solute transport due to advection and diffusion in fractures and pure diffusion in the host matrix. A key difference between heat and mass transfer in fractured environments is that heat readily diffuses through both solid and fluid phases, whereas solutes spread largely in the fluid phase. While potentially important (e.g., [BGRF06]), investigation of variable-density flow and heat transport lies outside the scope of the present study.

Analytical solutions, such as those mentioned above, provide significant physical insight into these transport phenomena and act as an invaluable component in field-scale screening and management (decision support) models. Yet they rely on a number of simplifying assumptions that might not be valid in a specific application. While these solutions routinely neglect longitudinal diffusion in the matrix, its impact on heat and mass transfer can be significant [MPCP07, RdDT12]. Likewise, longitudinal diffusion in the matrix (which is typically neglected in analytical models) is an important mechanism of heat transfer in a system of several fractures [CGD01, BK09, Kol95]. It can overestimate the thermal drawdown by up to 11% after 20 years of heat mining from HDRs in fractured crystalline rocks [Kol95].

In the present study we develop an analytical model of heat transfer in individual fractures, which accounts both for longitudinal and transverse diffusion in the matrix and for longitudinal and transverse dispersion and diffusion in the fracture. Section 1.2 provides a mathematical formulation of the problem. Section 1.3 contains its general solution in the Fourier-Laplace space. This solution is inverted analytically under conditions that are typical of most geothermal reservoirs (Section 1.3.2). We compare our analytical solutions with their existing counterparts in Section 1.4, and demonstrate their physical and practical implications in Section 1.5. Major conclusions from our study are summarized in Section 1.6.

1.2 Problem Formulation

Consider fluid flow and heat transfer in a fracture with aperture $2b$ and infinite length, that is embedded in a homogeneous rock matrix with porosity ϕ (Fig. 1.1). Following the standard practice in the field (e.g., [Kol95, CGD01, BK09, XZ12]), we assume the steady-state flow to be single phase, incompressible and laminar; the gravity effects and density variation with temperature to be negligible, and the fracture walls to be smooth and parallel to each other. Some of these assumptions can be relaxed, as discussed in the concluding remarks in Section 1.6. Since the problem is symmetric about the plane $z = 0$, we restrict our analysis to the upper half of the computational domain, so that the fracture is represented by $\Omega_f = \{(x, z) : -\infty < x < \infty, 0 \leq z \leq b\}$ and the matrix by $\Omega_m = \{(x, z) : -\infty < x < \infty, b \leq z < \infty\}$. Fluid temperature in the fracture, $T^f(x, z, t)$, satisfies an advection-dispersion equation

$$\frac{\partial T^f}{\partial t} + u \frac{\partial T^f}{\partial x} = D_L^f \frac{\partial^2 T^f}{\partial x^2} + D_T^f \frac{\partial^2 T^f}{\partial z^2} + f, \quad \mathbf{x} \in \Omega_f \quad (1.1)$$

where $\mathbf{x} = (x, z)^\top$ is the position vector; u is the fluid velocity; $f(\mathbf{x}, t)$ is a source term; and D_L^f and D_T^f are the longitudinal and transverse dispersion coefficients, respectively. For a fluid of density ρ_f and heat capacity c_f , these are given by $D_L^f = \lambda_L^f / \alpha_f + E_L^f / \alpha_f$ and $D_T^f = \lambda_T^f / \alpha_f + E_T^f / \alpha_f$, where $\alpha_f = \rho_f c_f$, λ_L^f and λ_T^f are the longitudinal and transverse thermal conductivity coefficients, and E_L^f and E_T^f the longitudinal and transverse thermal dispersion coefficients [YY09].

The ambient matrix Ω_m is assumed to be impervious to flow. The heat spreads throughout the matrix by conduction, so that temperature in the matrix, $T^m(\mathbf{x}, t)$, is governed by a diffusion equation

$$\frac{\partial T^m}{\partial t} = D_L^m \frac{\partial^2 T^m}{\partial x^2} + D_T^m \frac{\partial^2 T^m}{\partial z^2}, \quad \mathbf{x} \in \Omega_m, \quad (1.2)$$

where $D_L^m = \lambda_L^e / c_e$ and $D_T^m = \lambda_T^e / c_e$ are the longitudinal and transverse diffusion coefficients, c_e is the effective heat capacity of the matrix, and λ_L^e and λ_T^e the longitudinal and transverse thermal

conductivity coefficients in the matrix.

Let $T_i(x, z)$ denote the initial temperature in the system. Then equations (1.1) and (1.2) are subject to initial conditions

$$T^f(x, z, 0) = T_i(x, z), \quad T^m(x, z, 0) = T_i(x, z). \quad (1.3)$$

Equation (1.1) is subject to boundary conditions

$$T^f(\pm\infty, z, t) = T_i, \quad \frac{\partial T^f}{\partial z}(x, 0, t) = 0, \quad (1.4)$$

and equation (1.2) to boundary conditions

$$T^m(\pm\infty, z, t) = T_i, \quad T^m(x, \infty, t) = T_i. \quad (1.5)$$

At the fracture-matrix interface $z = b$, both the temperature and the heat flux are continuous, giving rise to two interfacial conditions

$$T^f = T^m, \quad \phi_m D_T^m \frac{\partial T^m}{\partial z} = D_T^f \frac{\partial T^f}{\partial z} \equiv r, \quad z = b, \quad (1.6)$$

where $\phi_m = \phi + (1 - \phi)\rho_s c_s / (\rho_f c_f)$; ρ_s and c_s are the density and heat capacity of the solid phase, respectively; and $r(x, t)$ is the (unknown) thermal flux between the fracture and matrix. Since the boundary value problems (BVPs) (1.1)–(1.6) are invariant under transformations $T = T^j - T_i$ ($j = f, m$), we set, without loss of generality, $T_i = 0$.

In what follows, we first develop general solutions of BVPs (1.1)–(1.6), which are applicable to a wide range of source functions $f(\mathbf{x}, t)$. Then we proceed by analyzing these solutions in detail for f representing a point injection of heat at $x = 0$. This setting is relevant to both natural and forced convection. For example, it represents fluid injection through a well that intersects a fracture at $x = 0$. If the temperature of the injected fluid is appreciably different from

the initial temperature T_i of the host fluid, then this setup can be used to characterize fractured rocks by collecting temperature logs at the well; [PGP07, PPCG10] used it to detect the presence of active fractures under natural groundwater flow conditions. Another example described by the model is an enhanced geothermal system, in which the fluid velocity u is induced by, e.g., groundwater extraction at point $x = x_i > 0$. If the fracture fluid is at the initial temperature T_i , the objective is to evaluate how the temperature of the fluid extracted at $x = x_i$ is modified by warmer/colder water injected at $x = 0$ under forced flow conditions.

1.3 Analytical Solutions

The fracture BVP consists of (1.1), (1.3), (1.4) and the second condition in (1.6). The matrix BVP is composed of (1.2), (1.3), (1.5) and the second condition in (1.6). Let $G^f(x, z; x', z'; t - t')$ and $G^m(x, z; x', z'; t - t')$ denote the Green's functions associated with the fracture and matrix BVPs, respectively. Their analytical expressions are given in Appendix A.1.

Our analytical models are first derived in the Fourier-Laplace (FL) space. For any suitable function $A(x, t)$, we define its Laplace and Fourier transformations as

$$\bar{A}(x, s) = \int_0^{\infty} A(x, t) e^{-st} dt, \quad (1.7a)$$

$$\tilde{A}(\xi, s) = \frac{1}{\sqrt{2\pi}} \int_{-\infty}^{\infty} \bar{A}(x, s) e^{-ix\xi} dx. \quad (1.7b)$$

1.3.1 General solution in Fourier-Laplace space

We show in Appendix A.2 that the FL transforms of the temperature in the fracture, $\tilde{T}^f(\xi, z, s)$, and matrix, $\tilde{T}^m(\xi, z, s)$, are given by

$$\tilde{T}^f = \sqrt{2\pi} \left[\frac{F_1(\xi, s) \Delta \mathcal{F}(b; \xi; s)}{F_2(\xi, s) + 1/\beta} - \Delta \mathcal{F}(z; \xi; s) \right] \quad (1.8)$$

and

$$\tilde{T}^m = -\frac{\sqrt{2\pi}}{\beta} \exp\left(-\frac{\psi|z-b|}{\sqrt{D_T^m}}\right) \frac{\Delta\mathcal{F}(b;\xi;s)}{F_2(\xi,s) + 1/\beta}. \quad (1.9)$$

Here $\Delta\mathcal{F}(z;\xi;s) = \tilde{\mathcal{F}}(z,0;\xi;s) - \tilde{\mathcal{F}}(z,b;\xi;s)$, $\tilde{\mathcal{F}}(z,z';\xi;s)$ is the antiderivative of $\tilde{f}\tilde{G}^f$ with respect to z' , $\psi = \sqrt{D_L^m\xi^2 + s}$, $\beta = \phi_m\sqrt{D_T^m}\psi$, and

$$F_1 = \frac{\tilde{G}_\xi^f(s)}{b} + \frac{2}{b} \sum_{n=1}^{\infty} (-1)^n \cos(\alpha_n z) \tilde{G}_\xi^f(s + \alpha_n^2 D_T^f) \quad (1.10a)$$

$$F_2 = \frac{\tilde{G}_\xi^f(s)}{b} + \frac{2}{b} \sum_{n=1}^{\infty} (-1)^{2n} \tilde{G}_\xi^f(s + \alpha_n^2 D_T^f) \quad (1.10b)$$

where $G_\xi^f(s)$ is given by (A.4) and $\alpha_n = n\pi/b$.

The FL transform of the temperature distribution in the fracture-matrix system, (1.8) and (1.9) is free of any simplifying assumptions. It captures full (two-way) coupling of the fracture-matrix exchange; and accounts for longitudinal and transverse dispersion and diffusion in the fracture and matrix, respectively. It also enables one to deal with arbitrary heat sources.

1.3.2 Explicit models of temperature in the fracture

In the case of complete transverse mixing ($D_T^f = \infty$) and negligible longitudinal dispersion ($D_L^f = 0$) in the fracture, the general FL solutions (1.8) and (1.9) can be inverted analytically, yielding a closed-form expression for the temperature distribution. These conditions are typical for fracture-matrix systems. Indeed, the impact of longitudinal dispersion is limited to low velocities ($\leq 10^{-7}$ m/s) [TFS81], and transverse dispersion is important only if $D_T^f < D_T^m$ [RdDT12].

Consider a continuous-in-time point source located at $x = 0$, such that $f = T_0 u \delta(x) \mathcal{H}(t)$, where T_0 is the temperature of the injected fluid (or the difference between the temperature of the injected fluid and its initial value T_i if the latter is not zero) and $\mathcal{H}(\cdot)$ is the Heaviside function.

In the limit of $D_T^f \rightarrow \infty$ and $D_L^f \rightarrow 0$, (1.8) reduces to

$$\tilde{T}^f = \frac{1}{\sqrt{2\pi s}} \frac{T_0 u}{\beta/b + s + u\xi i}. \quad (1.11)$$

Let us define dimensionless ratio R , coefficient K , and critical time t_{\min} as

$$R = \frac{\phi_m \sqrt{D_T^m D_L^m}}{ub}, \quad K = \frac{\phi_m}{2b} \sqrt{\frac{D_T^m}{D_L^m}}, \quad t_{\min} = \frac{10^4 b^2}{\phi_m^2 D_T^m}. \quad (1.12)$$

Note that since $\sqrt{D_T^m D_L^m}$ is the geometric mean of the heat diffusivity in the matrix and u/ϕ_m is a scaled advective velocity in the fracture, one can think of R as the inverse of a ‘‘fracture-matrix Péclet number’’ in that it represents a ratio of advection timescale in the fracture to diffusion timescale in the matrix. We show in Appendix A.3 that, for $R > 1$, $K > 1$ and $t > t_{\min}$, the inverse FL transformation of (1.11) yields

$$\begin{aligned} T^f(x, t) \sim & -\frac{T_0 R}{2\pi \mathcal{R}} \text{Ei} \left(-\frac{1}{4t_d^*} \right) + \frac{T_0}{2} \frac{1}{\mathcal{R}} \left\{ \text{sgn}(x) - \text{erf} \left[\frac{\text{sgn}(x)}{2\sqrt{t_d^*}} \frac{R}{\sqrt{\mathcal{R}}} \right] \right\} \\ & + \frac{T_0}{\pi} e^{-R^2/(4\mathcal{R}t_d^*)} \left\{ -\frac{\sqrt{\pi t_d^*} \text{sgn}(x)}{2t_a^* R \sqrt{\mathcal{R}}} + \frac{2t_a^* - 1}{2t_a^* \mathcal{R}^{3/2}} + \frac{2t_a^* - 3}{12t_a^* \mathcal{R}^{5/2}} \right. \\ & + \frac{1}{\mathcal{R}^{7/2}} \left[\frac{R^2(1 - 2t_a^*)}{24t_d^* t_a^*} + \frac{3}{40t_a^*} - \frac{3}{16t_a^{*2}} \right] \\ & \left. + \frac{R^2(5 - 6t_a^*)}{80t_d^* t_a^{*2} \mathcal{R}^{9/2}} + \frac{R^4(2t_a^* - 1)}{320t_d^* t_a^{*2} \mathcal{R}^{11/2}} \right\} \end{aligned} \quad (1.13)$$

where $\mathcal{R} = R^2 + 1$ and $t_a^* = tu/x$ and $t_d^* = tD_L^m/x^2$ are the dimensionless advection and (longitudinal) diffusion times, respectively.

The conditions $R > 1$, $K > 1$, and $t > t_{\min}$ are adequate for geothermal studies: Typical thermal diffusivity in rocks is $D^m = O(10^{-6} \text{m}^2/\text{s})$ [BK09] and typical prediction times are larger than hours. Therefore, (1.13) provides a robust explicit prediction of spatiotemporal evolution of temperature in an infinite fracture. It accounts for both longitudinal and transverse diffusion in the matrix.

In lieu of another example, we consider a pulse injection of duration t_p . This corresponds to the source term $f = T_0 u \delta(x) [\mathcal{H}(t) - \mathcal{H}(t - t_p)]$, and fracture temperature

$$T_p^f(x, t) = T^f(x, t) \mathcal{H}(t) - T^f(x, t - t_p) \mathcal{H}(t - t_p), \quad (1.14)$$

where $T^f(x, t)$ is given by (1.13).

1.3.3 Accuracy of analytical solutions

Our analytical solutions, e.g., (1.11), are exact in the Fourier-Laplace space. Their analytical inversion in Appendix A.3 is approximate since it is based on truncation of the Taylor series involved. We assess the accuracy of the resulting analytical solutions, e.g., (1.13), by comparing them with their counterparts computed with numerical inversion of the corresponding expressions in the Fourier-Laplace space, e.g., (1.11). The latter is accomplished by using the [dHKS82] algorithm and the MATLAB routine `ifft` to compute the inverse Laplace and Fourier transforms, respectively. In the simulations reported below we set $D_L^m = D_T^m = 9.16 \times 10^{-7} \text{ m}^2/\text{s}$, $\phi = 0.1$, $\rho_s = 2757 \text{ kg/m}^3$, $c_s = 1180 \text{ J/kgK}$, and $\phi_m = 0.78$.

Figures 1.2 and 2.3 exhibit distributions of the relative fracture temperature $T_r^f = T^f / T_0$ for two transport configurations. The first (Figs. 1.2) corresponds to flow with velocity $u = 1.4 \times 10^{-4} \text{ m/s}$ in a fracture whose aperture is $2b = 1.0 \times 10^{-3}$, 5.0×10^{-4} , and $2.0 \times 10^{-4} \text{ m}$ or $R = 10$, 20, and 50. The second (Figs. 2.3) corresponds to $u = 1.4 \times 10^{-3} \text{ m/s}$ and $2b = 1.0 \times 10^{-3}$, 5.0×10^{-4} , and $2.0 \times 10^{-4} \text{ m}$ or $R = 1$, 2, and 5. Both cases demonstrate the agreement between the analytical and numerical solutions for $t = 1 \text{ month}$ (Figs. 1.2a and 2.3a) and 1 year (Figs. 1.2b and 2.3b), which is to be expected since the conditions of validity of our solutions are fulfilled. Although not shown here, this agreement deteriorates for $R < 1$, a condition that is rarely (if ever) met in the field (see the discussion in the previous section).

1.4 Comparison with existing models

In this section we demonstrate that under certain conditions/assumptions our solutions reduce to the classical solutions of [TFS81] for semi-infinite fractures.

1.4.1 No dispersion in semi-infinite fracture

Setting $D_L^f = 0$, $D_L^m = 0$, and $D_T^f \rightarrow \infty$ (the complete mixing assumption) reduces our general solution (1.8) to

$$\tilde{T}^f = -\frac{\Delta\mathcal{F}(z; \xi; s)}{\alpha_s + u\xi i} \quad (1.15)$$

where $\alpha_s = \phi_m \sqrt{D_T^m s}/b + s$. For a point injection of fluid with temperature T_0 , i.e., for $f = T_0 u \delta(x) \mathcal{H}(t)$, this gives rise to the Laplace transform of temperature in the fracture,

$$\bar{T}^f = \frac{T_0}{s} \exp\left(-\frac{\alpha_s x}{u}\right), \quad x \geq 0. \quad (1.16)$$

This is identical to the analytical solution [TFS81] for heat transfer in a semi-infinite fracture with a fixed temperature T_0 at the fracture's inlet $x = 0$. This solution ignores longitudinal dispersion in the fracture and is referred to by [TFS81] as “transient solution with $D = 0$ ”.

1.4.2 Longitudinal dispersion in semi-infinite fracture

Setting $D_L^m = 0$ and $D_T^f \rightarrow \infty$ reduces our general solution (1.8) to

$$\tilde{T}^f = -\frac{\Delta\mathcal{F}(z; \xi; s)}{\alpha_s + D_L^f \xi^2 + u\xi i}. \quad (1.17)$$

The “general transient solution” of [TFS81] is recovered from (1.17) by choosing the source term to be

$$\bar{f} = \frac{T_0}{s} \sqrt{u^2 + 4D_L^f \alpha_s} \delta(x). \quad (1.18)$$

This choice accounts for the “lost” part of the injected flux due to the longitudinal diffusion in the negative half ($-\infty < x < 0$) of the infinite fracture. The resulting Laplace transform of temperature in the fracture is

$$\bar{T}^f = \frac{T_0}{s} \exp \left[- \left(\sqrt{\frac{u^2}{4} + D_L^f \alpha_s} - \frac{u}{2} \right) \frac{x}{D_L^f} \right], \quad x \geq 0. \quad (1.19)$$

1.5 Results and Discussion

The subsequent discussion serves to demonstrate the importance of accounting for two-dimensional heat conduction in rock matrix. In this discussion, we refer to (1.13) and (1.16) as “2-D solution” and “1-D solution”, respectively.

The results below correspond to continuous point injection ($x = 0$) of a fluid whose temperature T_0 is either warmer ($T_0 > 0$) or colder ($T_0 < 0$) than the host fluid (the initial temperature $T_i = 0$). Unless specified otherwise, a shale matrix has the following characteristics: $D_L^m = D_T^m = 9.16 \cdot 10^{-7}$ m²/s, $\phi = 0.1$, $\rho_s = 2757$ kg/m³, and $c_s = 1180$ J/kg K. Taking the fluid to be water ($\rho_f = 1070$ kg/m³ and $c_f = 4050$ J/kg K) yields $\phi_m = [\phi + (1 - \phi)\rho_s c_s / (\rho_f c_f)] = 0.78$.

The results are reported in terms of the relative fracture temperature

$$T_r^f(x, t) = T^f(x, t) / T_0, \quad (1.20)$$

which ranges from 0 (temperature is at its initial value T_i) to 1 (temperature at the local heat source).

1.5.1 Effects of heat conduction in matrix

Figure 1.4 depicts the temporal evolution of relative temperature T_r^f at the distance $x = 0.5$ m from the heat source. Flow velocity in the fracture is set to $u = 1.4 \times 10^{-4}$ m/s, and fracture aperture to $2b = 2 \times 10^{-4}$ m (Fig. 1.4a), 5×10^{-4} m (Fig. 1.4b), and 10^{-3} m (Fig. 1.4c). This choice of fracture apertures yields the values of the dimensionless ratio $R = 50$ (Fig. 1.4a), $R = 20$ (Fig. 1.4b), and $R = 10$ (Fig. 1.4c).

In the diffusion-dominated regime (Fig. 1.4a), the 1-D solution (no longitudinal heat conduction in the matrix) underestimates the relative temperature at short times and significantly overestimates it at later times. The longitudinal heat conduction in the matrix (the 2-D solution) causes the fracture temperature to rise at earlier times and shows that the local heat source impacts on the fracture temperature ($T_r^f > 0$) at much earlier times; after this initial time interval, the 1-D solution predicts a much larger rate of increase of the fracture temperature than the 2-D solutions do. This is because heat is transferred from the fracture into the matrix in the vicinity of the localized injection, diffuses longitudinally in the matrix, and then returns to the fracture at locations far from the injection. Our 2-D solution captures this heat transfer mechanism in the diffusion-dominated regime, while the classical 1-D solution does not. Figures 1.4b and 1.4c show that this mechanism does not occur in advection-dominated regimes.

In all heat transfer regimes (Figs. 1.4a–c), both temperature in the fracture and the time-to-equilibrium increase as the matrix diffusion coefficient D_L^m decreases. The smaller the value of R (i.e., the larger the fracture-matrix Péclet number), the more pronounced this effect becomes. Ignoring longitudinal diffusion in the matrix (the 1-D solution) significantly underestimates the fracture-matrix transfer and significantly overestimate both temperature in the fracture and the time-to-equilibrium.

Overestimation of the time-to-equilibrium has important practical implications, since determination of the time it takes a fracture-matrix system to reach thermal equilibrium (steady-state) is essential for estimation of the matrix penetration depth. The latter determines the

adequacy of conceptual representations of fracture-matrix systems, i.e., enables one to decide whether a single-fracture-in-infinite-matrix model is sufficient or more evolved fracture-network models are to be used instead. Our 2-D solution, which accounts for longitudinal heat conduction in the matrix, demonstrates that heat sources in a fracture affect much smaller regions of the adjacent matrix than would be predicted with the classical 1-D solution, which ignores longitudinal conduction. Consequently, a conceptualization of heat dissipation in fractured rocks as a system of isolated fractures in infinite matrix might be adequate for geothermal studies.

1.5.2 Performance of geothermal systems

Relative temperature drawdown, $P_f(x,t) = 1 - T_r^f(x,t)$, is an effective performance measure of geothermal systems. It quantifies the degree to which temperature at a point x is affected (changes from initial temperature T_i) by injection of a fluid with temperature T_0 at another point (say, $x = 0$). The value $P_f = 0$ corresponds to zero cooling/heating efficiency (the fluid extracted at point x has the same temperature as that of the fluid injected at $x = 0$), and $P_f = 1$ represents the maximum cooling/heating efficiency (extracted fluid is at its initial temperature). Its values provides a consistent measure of performance regardless of whether the injected fluid is cooler ($T_0 < 0$) or warmer ($T_0 > 0$) than the host fluid.

Figure C.3 exhibits $P_f(x,t)$ at $x = 10$ m for flow velocity $u = 1.4 \times 10^{-3}$ m/s and fracture aperture $2b = 10^{-3}$ m (Fig. C.3a), 5×10^{-4} m (Fig. C.3b), and 2×10^{-4} m (Fig. C.3c). These aperture values translate into the inverse fracture-matrix Péclet number $R = 1, 2,$ and $5,$ respectively. Isolines of $P_f(x,t)$ are plotted as a function of advection ($t_a^* = tu/x$) and diffusion ($t_d^* = tD_L^m/x^2$) times. This corresponds to physical time t ranging from 5×10^4 s to 10^9 s (from hours to 30 years).

Geothermal performance increases with R : it is lowest in the advection-dominated regime (Fig. C.3a) and highest in the diffusion-dominated regime (Fig. C.3c). In a given regime (as characterized by the value of R), the performance varies only slightly with t_a^* , i.e., it is relatively insensitive to convective properties of fractured rocks. This is to be expected from Fig. 1.4,

which shows that temperature in the fracture stabilizes quickly as the advection time t_a^* increases, so that subsequent increases in t_a^* have a limited impact on system performance.

When $R = O(1)$, the geothermal performance P_f depends strongly on the diffusion time t_d^* , with high performance occurring at small values of t_d^* . Therefore, the cooling/heating efficiency increases with the reservoir size (the distance x between fluid's injection and extraction) and decreases with exploitation time t . As R increases (from $R = 1$ in Fig. C.3a to $R = 5$ in Fig. C.3c), the dependence of the geothermal performance P_f on t_d^* diminishes, leading to stable and efficient configurations in the diffusion-dominated regime. For large values of t_d^* (the top of Figs. C.3a-c), the geothermal performance is slightly higher at small values of t_a^* . This implies that for rocks with large thermal diffusivity D_L^m (large values of t_d^*), the largest changes in fluid temperature in the fracture occur at early times t_a and the geothermal performance can be improved by decreasing flow velocity u .

Figure C.4 illustrates these points further. Extracted fluid remains at its initial temperature regardless of the temperature of injected fluid for $t_d^* < 10^{-2}$. The latter inequality holds for small values of D_L^m , short exploitation times t , and/or large distances (x) between the injection and extraction points. This nearly perfect geothermal performance ($P_f > 0.9$) is observed when $R > 7$. In other words, the diffusion-dominated regime is best suited for geothermal exploitation, since it limits the thermal impact of injected fluids on the host fluid in a fracture by maximizing heat dissipation into the matrix. In the advection-dominated regime with $R < 5$ (Fig. C.4b), the geothermal performance depends strongly on t_d^* , with small values of t_d^* (short exploitation times t or/and large injection-to-extraction distances x) improving P_f .

1.6 Conclusions

We developed analytical models for heat transfer in a single fracture surrounded by an infinite matrix. These models account for advection and hydrodynamic dispersion in the fracture, longitudinal and transverse conduction in the matrix, and a two-way coupling between heat

transfer in the fracture and matrix. They also handle any heat source configuration, such as distributed or localized heat sources of arbitrary duration.

In their most general form, these solutions are given by their Fourier and Laplace transforms and require numerical inversion. Under conditions that are typical of geothermal reservoirs, these solutions are inverted analytically, giving rise to an explicit closed-form model of heat transfer in fractured rocks. By accounting for two-dimensional heat conduction in rock matrix, this model represents a significant advance over the existing analytical solutions that restrict matrix conduction to the direction perpendicular to the fracture. Our analysis leads to the following major conclusions.

- Longitudinal thermal diffusivity in the matrix is a critical parameter that determines the impact of local heat sources on fluid temperature in the fracture.
- By neglecting longitudinal conduction in the matrix, the classical models significantly overestimate both fracture temperature and time-to-equilibrium.
- The inverse fracture-matrix Péclet number R and diffusion timescale t_d^* are two parameters that determine the efficiency of geothermal systems.
- The diffusion-dominated regime ($R > 7$) is ideal for geothermal exploitation, since it limits the thermal impact of injected fluids on the host fluid in a fracture by maximizing heat dissipation into the matrix.
- In the advection-dominated regime ($R < 5$), the geothermal performance depends strongly on t_d^* . It is highest at small values of t_d^* (short exploitation times and/or large injection-to-extraction distances).

Our analytical models provide an easy-to-use tool for parametric sensitivity analysis, benchmark studies, and validation of numerical simulations. They can be used for geothermal site evaluation and parameter identification. They will improve field-scale studies of

geothermal reservoirs, which rely on discrete-fracture-network approaches and consider only one-dimensional heat conduction in the rock. Our solutions obviate the need for this strong and limiting assumption, while retaining the analytic simplicity of the original approaches.

In the follow-up studies we will generalize these analytical models by incorporating the following phenomena.

- Fracture wall roughness. The numerical simulations of [NTS10] demonstrated the effects of fracture wall roughness on heat transfer in fractured rocks. Treating fracture walls as random fields, and combining our solutions with stochastic domain mappings [XT06, TX06, PIT12] and stochastic homogenization [TGR03], will enable us to investigate these effects in a computationally efficient semi-analytical manner. The latter step will rely on the Green's functions derived in this study.
- Heat transfer in fracture networks. Multiscale modeling approaches to flow and transport in fractured rocks [DM95, CPOS04, RLdD10, RdDT13] combine a discrete fracture network (DFN) representation at the field scale with analytical solutions at the fracture scale. We will embed our analytical solutions into particle-tracking DFN models to represent rock conduction effects at the field scale with optimized computational cost and representation accuracy.

1.7 Future Research

Recently, we have developed an analytical approximation for the temperature in the matrix. Calculating the inverse FL transform of the expression (1.9) and applying the same conditions of applicability that we imposed for the temperature in the fracture, we obtain the

following expression

$$\begin{aligned}
T^m(x, t) \sim & \frac{T_0}{\pi} \frac{1}{\mathcal{R}} \left\{ 2\pi \operatorname{sgn}(x) \operatorname{T} \left(\sqrt{2\lambda\mu} \operatorname{sgn}(x), \frac{|x|}{\mu} \right) - \frac{1}{2} R \operatorname{Ei} [-\lambda^2(x^2 + \mu^2)] \right\} \\
& - \frac{T_0}{\sqrt{4\pi v}} \frac{1}{\mu R} \operatorname{erfc}(\lambda\mu) \left(\frac{vR^2}{\mathcal{R}} - \frac{1}{4\lambda^2} \right) e^{-(x')^2/4v} \\
& - \frac{T_0}{2} \frac{1}{\mathcal{R}} \operatorname{erfc}(\lambda\mu) \operatorname{erf} \left(\frac{x'}{2\sqrt{v}} \right) \\
& + \frac{T_0}{\sqrt{4\pi v}} \frac{1}{\mathcal{R}} \frac{1}{\sqrt{\pi\lambda R}} e^{-\lambda^2\mu^2 - (x')^2/4v} \quad \text{for } z \in (-\infty, -b) \cup (b, \infty), \quad (1.21)
\end{aligned}$$

where

$$\lambda = \frac{1}{2\sqrt{D_L^m t}}, \quad \mu = |z - b| \sqrt{\frac{D_L^m}{D_T^m}}, \quad v = \frac{R^2 + 1}{R} \left(\frac{1}{4\lambda^2} + \frac{\mu D_L^m}{R u} \right), \quad x' = x + \frac{\mu}{R}, \quad (1.22)$$

and $\operatorname{T}(\sigma, \eta)$ is the Owen's T function defined as follows

$$\operatorname{T}(\sigma, \zeta) = \frac{1}{2\pi} \int_0^\zeta \frac{e^{-\frac{1}{2}\sigma^2(1+\zeta^2)}}{1+\zeta^2} d\zeta, \quad \text{for } -\infty < \sigma, \zeta < \infty. \quad (1.23)$$

Figures 1.7 and 1.8 represent distributions of the relative matrix temperature $T_r^m = T^m/T_0$ for two transport configurations. The first (Figs. 1.7) corresponds to a fracture whose aperture is $2b = 1.0 \times 10^{-3}$ m, $D_L^m = D_T^m = 9.16 \times 10^{-7}$ m²/s, $\phi_m = 0.78$, flow with velocity $u = 1.4 \times 10^{-3}$, 1.4×10^{-4} , and 1.4×10^{-5} m/s or $R = 1, 10$, and 100 , and distance from the center of the fracture $z = 5 \times 10^{-2}$ m. The second (Figs. 1.8) corresponds to a distance from the center of the fracture $z = 5$ m. Both cases demonstrate the agreement between the analytical and numerical solutions for $t = 1$ day, $t = 1$ month, and $t = 1$ year (Figs. 1.7), and $t = 5$ and 10 years (Figs. 1.8), which is to be expected since the conditions of validity of our solutions are fulfilled.

Since expression (1.21) provides with information of the temperature in the matrix at any distance from the fracture, we propose to use our solutions and the principle of superposition to develop simple analytical models for complex fracture networks. For instance, regardless of

the spatial distribution of fractures, expression (1.13) can tell us the temperature in a particular fracture due to a heat source and expression (1.21) can estimate the increment of temperature in such fracture due to the influence of distant fractures.

Chapter 1, in part, is a reprint of the material as it appears in Analytical models of heat conduction in fractured rocks 2014. Ruiz-Martínez, Á.; Roubinet, D.; and Tartakovsky, D.M., Journal of Geophysical Research, Solid Earth, 2014. The dissertation/thesis author was the primary investigator and author of this paper.

Chapter 1, last pages, are currently being prepared for submission for publication of the material. Ruiz-Martínez, Á. and Tartakovsky, D.M. The dissertation/thesis author was the primary investigator and author of this material.

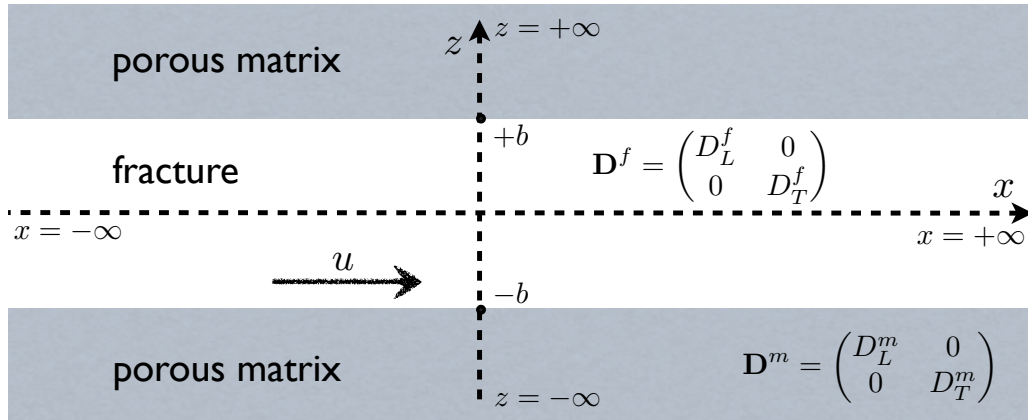


Figure 1.1. Single fracture embedded in an infinite matrix.

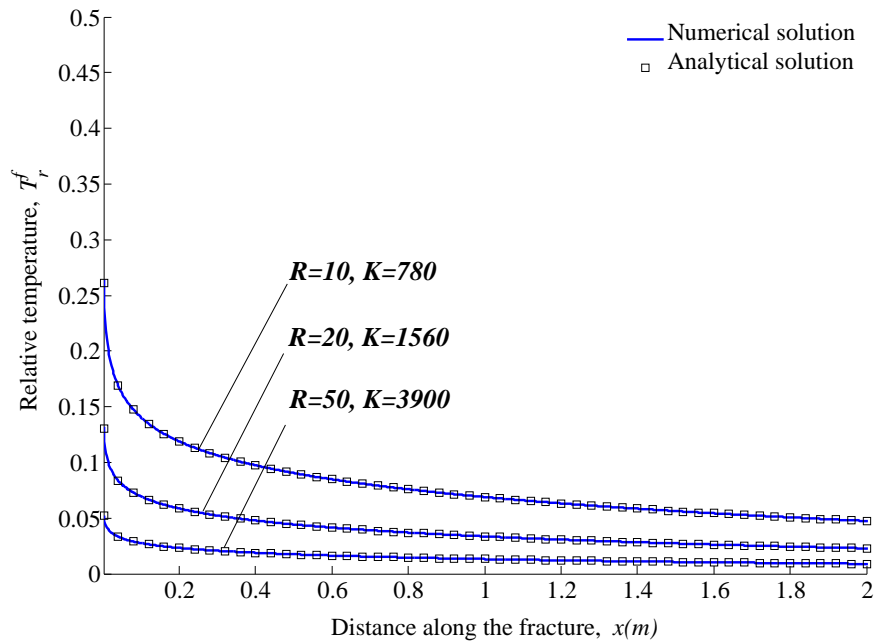
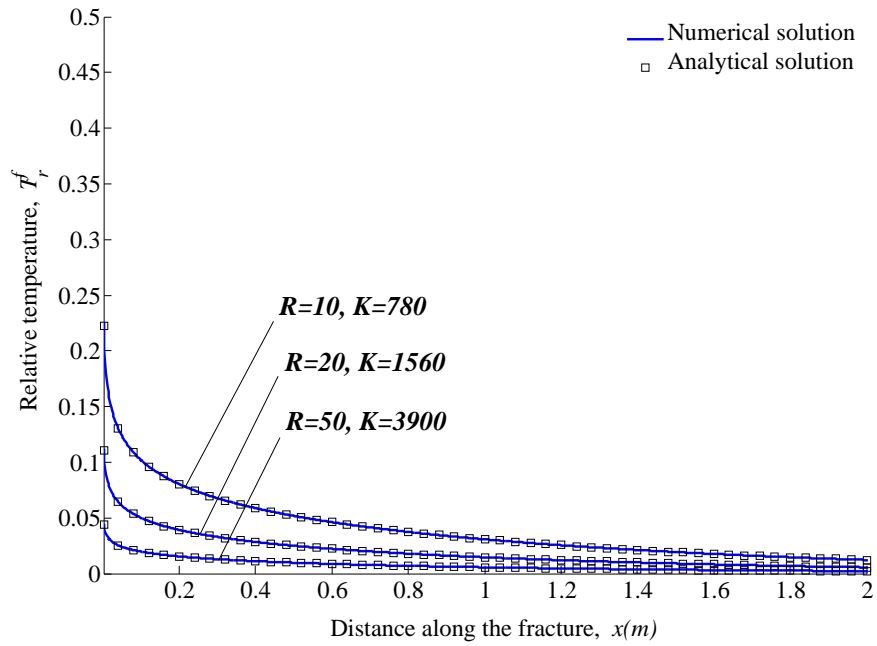


Figure 1.2. Distributions of the relative temperature along the fracture for flow velocity $u = 1.4 \times 10^{-4}$ m/s and different values of the dimensionless parameters R and K , computed with the analytical and numerical solutions. The liquid is injected at $x = 0$ during (a) $t = 1$ month and (b) $t = 1$ year.

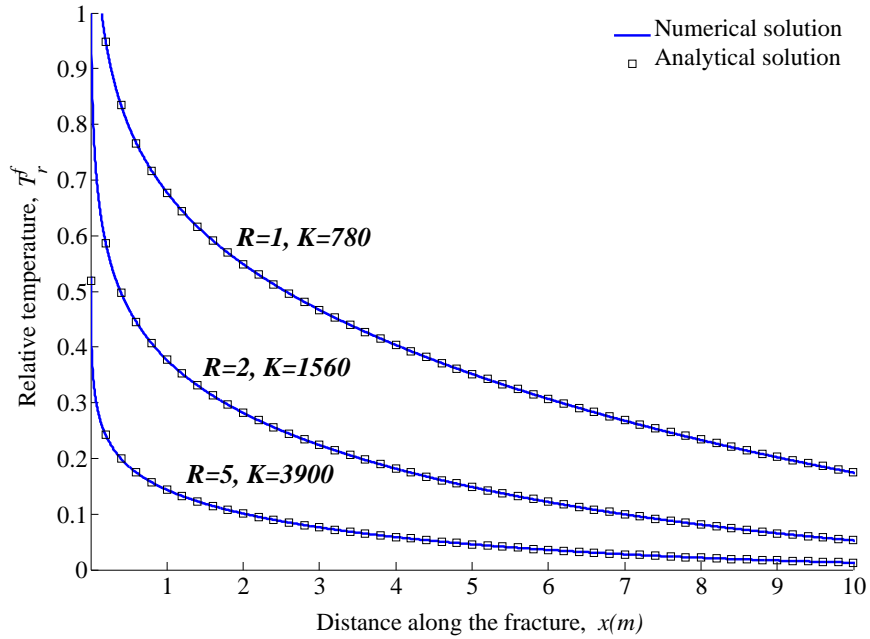
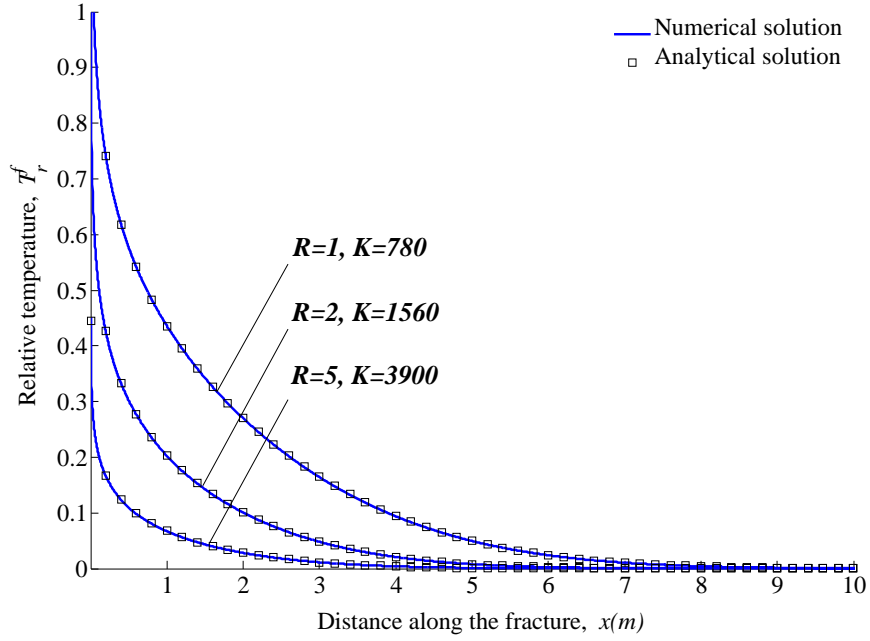


Figure 1.3. Distributions of the relative temperature along the fracture for flow velocity $u = 1.4 \times 10^{-3}$ m/s and different values of the dimensionless parameters R and K , computed with the analytical and numerical solutions. The liquid is injected at $x = 0$ during (a) $t = 1$ month and (b) $t = 1$ year.

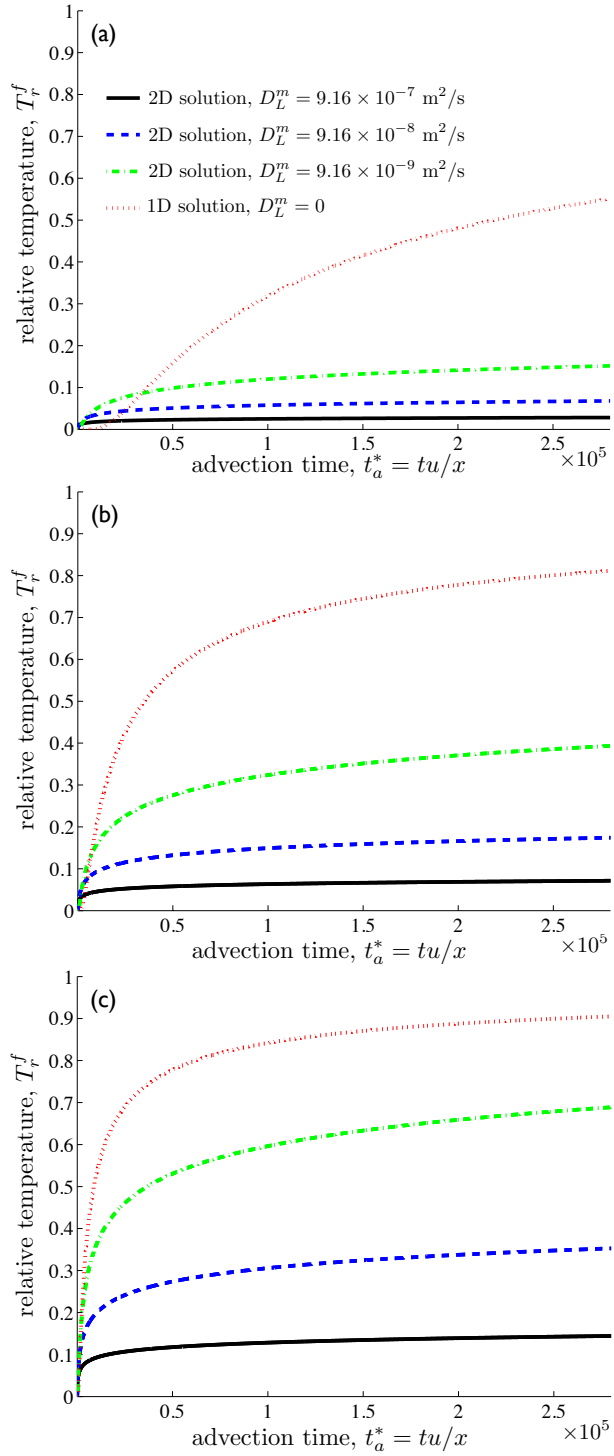


Figure 1.4. Relative temperature in the fracture T_r^f , as a function of advection time $t_a^* = tu/x$, computed with the 1-D solution (red dotted lines) and the 2-D solution for $D_L^m = 9.16 \times 10^9$ (green dash-dotted lines), 9.16×10^8 (blue dashed lines), and $9.16 \times 10^7 \text{ m}^2/\text{s}$ (black solid lines). Fracture aperture $2b$ is set to (a) $2 \times 10^4 \text{ m}$, (b) $5 \times 10^4 \text{ m}$, and (c) 10^3 m .

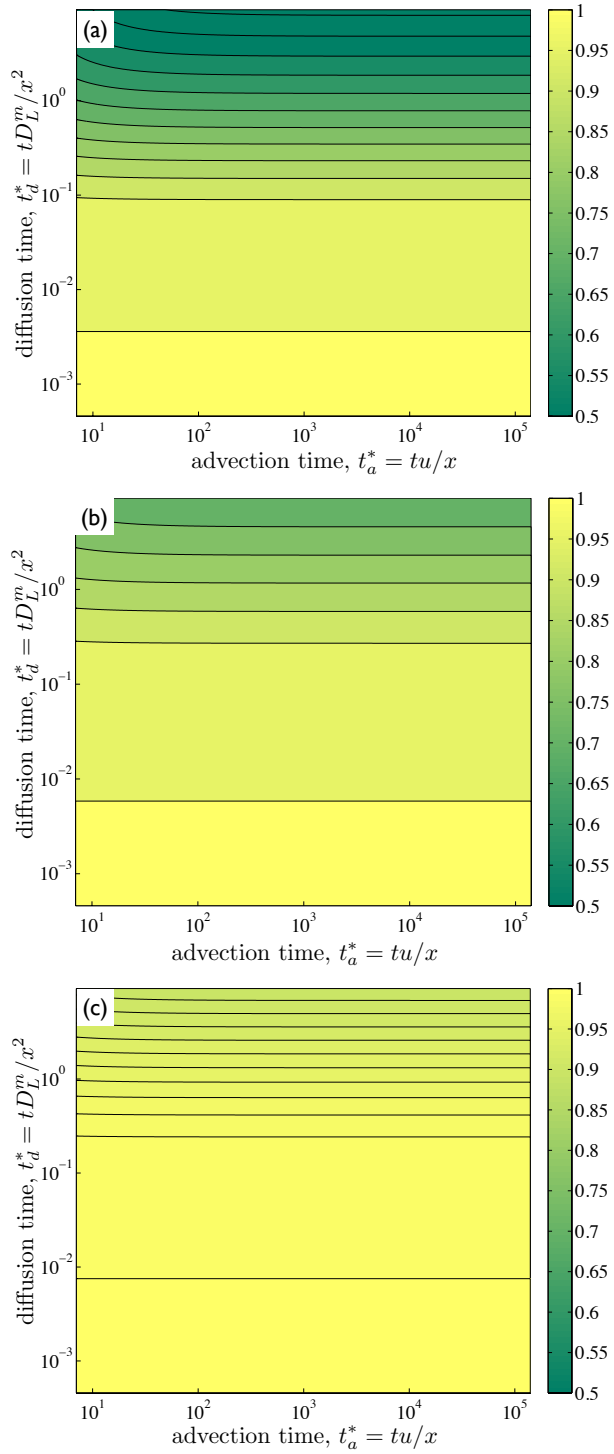


Figure 1.5. Isolines of the geothermal performance P_f in the space of advection (t_a^*) and diffusion (t_d^*) times, for (a) $R = 1$, (b) $R = 2$, and (c) $R = 5$.

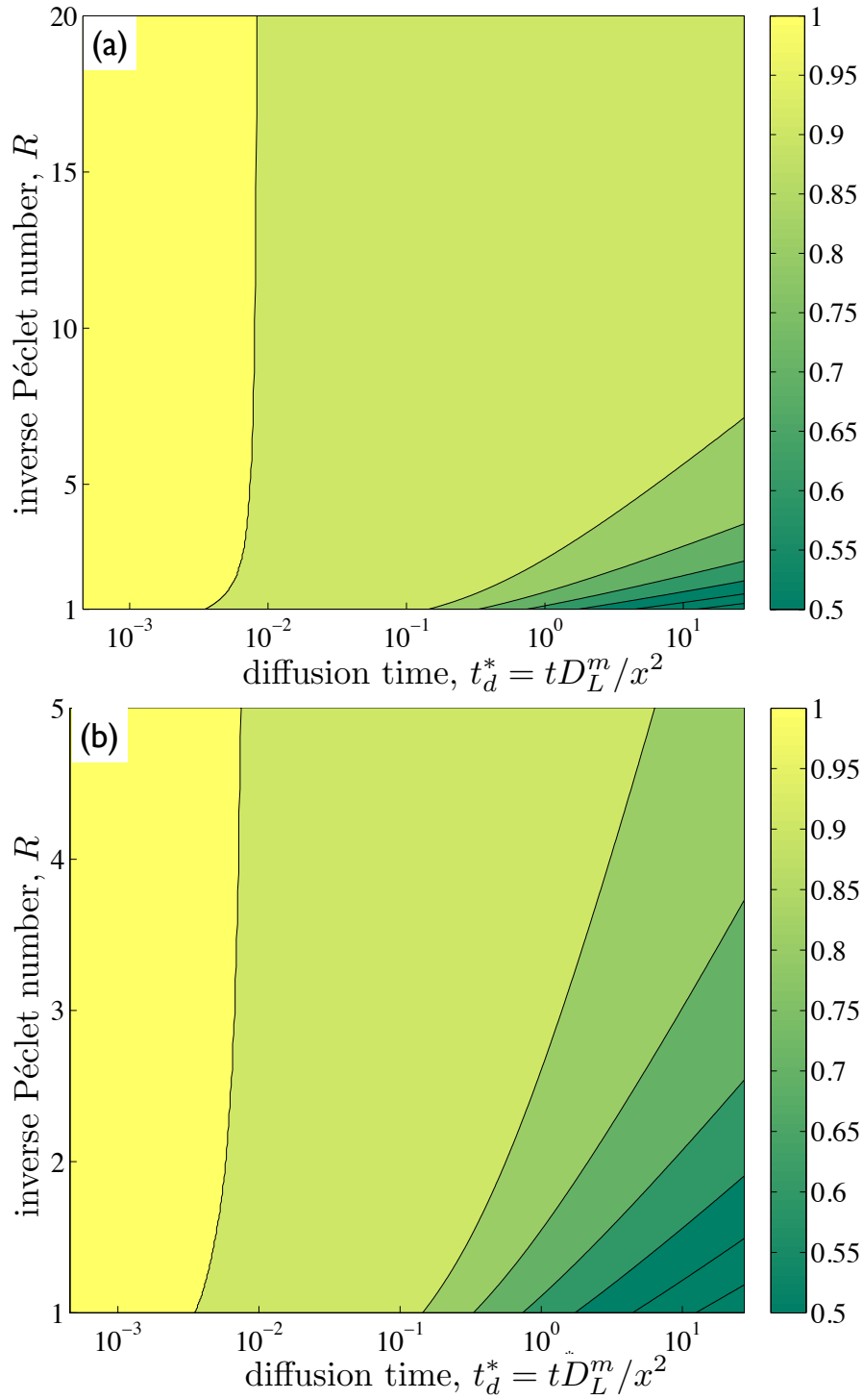


Figure 1.6. Isolines of the geothermal performance P_f in the space of diffusion time t_d^* and the inverse fracture-matrix Péclet number R , for (a) $1 \leq R \leq 20$ and (b) $1 \leq R \leq 5$.

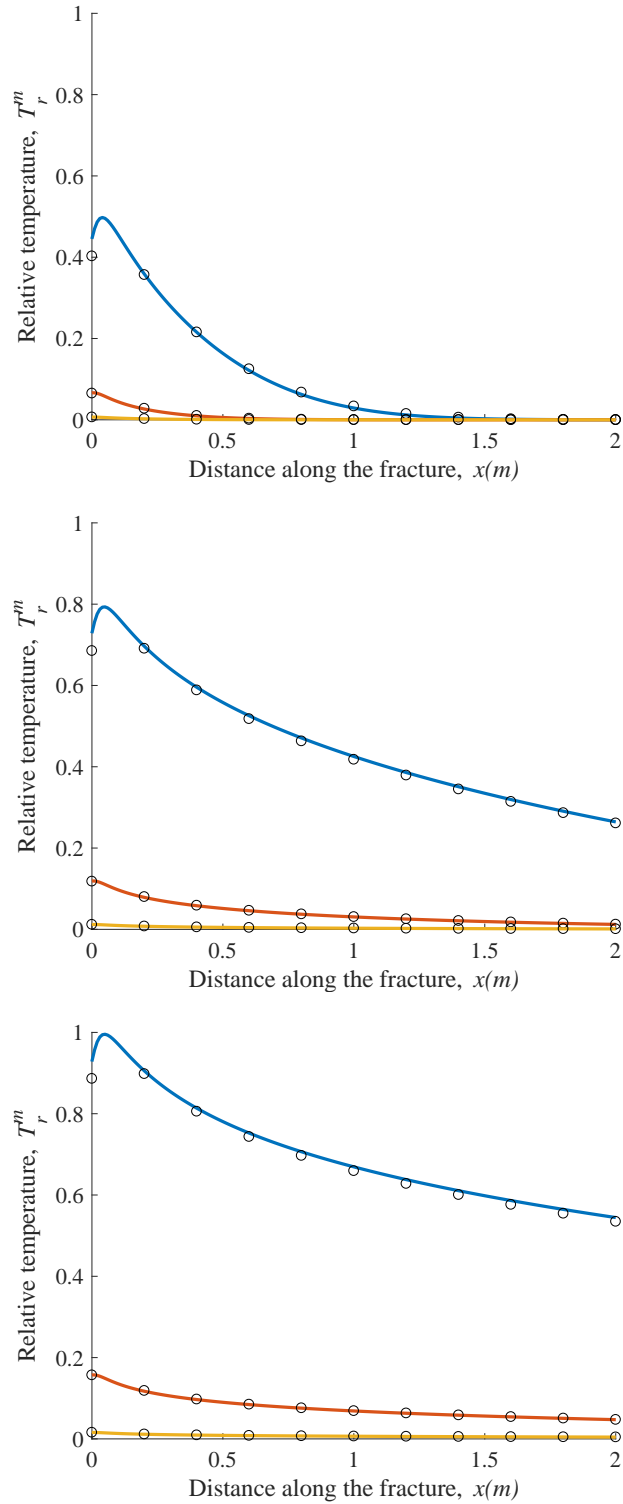


Figure 1.7. Distributions of the relative temperature in the porous matrix for fracture aperture $2b = 1 \times 10^{-3}$ m and distance from the center of the fracture $z = 5 \times 10^{-2}$ m computed with the analytical (circles) and numerical solutions for dimensionless parameter $R = 1, 10$ and 100 (blue, red and yellow lines, respectively). The liquid is injected at $x = 0$ during (a) $t = 1$ day, (b) $t = 1$ month and (c) $t = 1$ year.

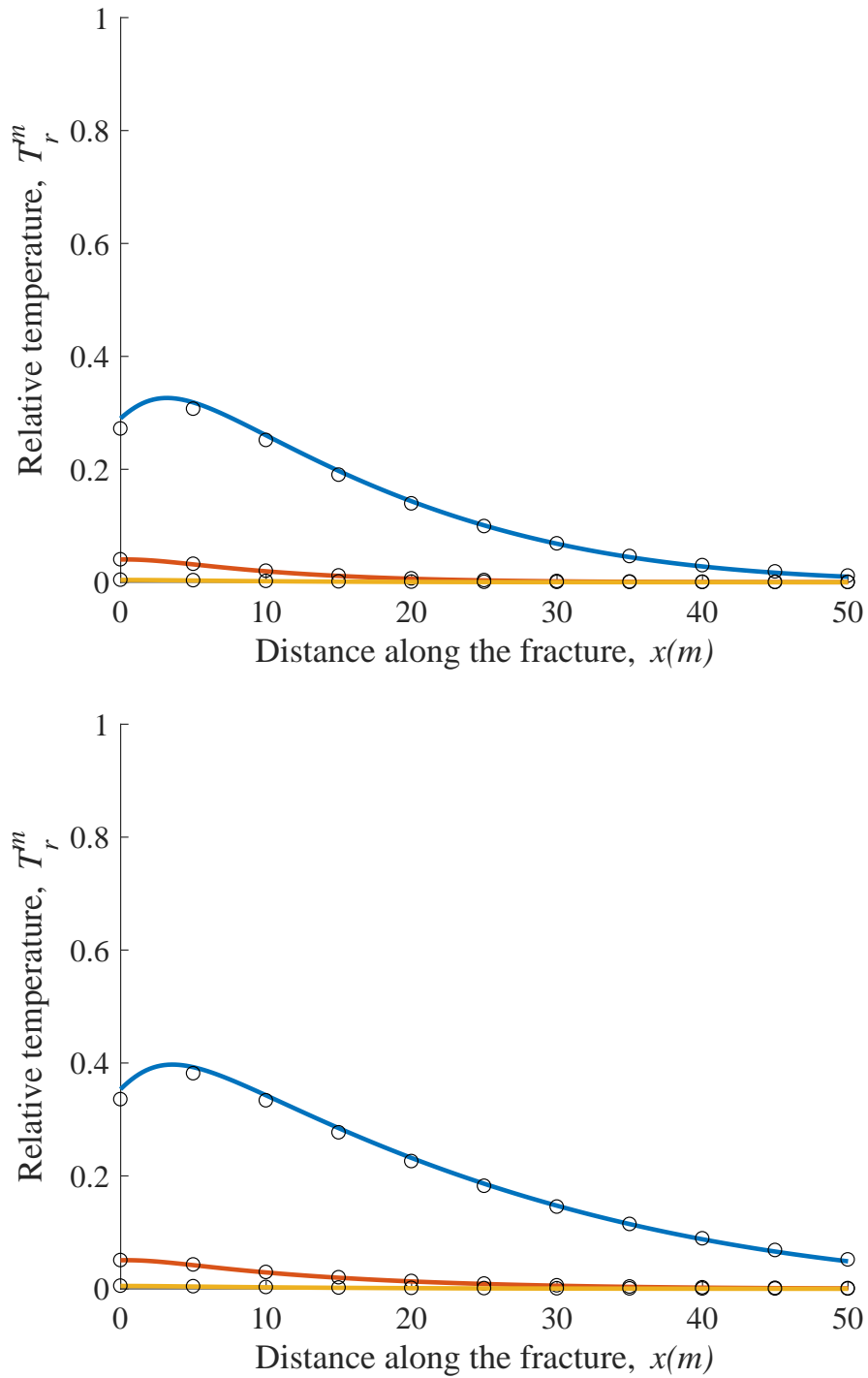


Figure 1.8. Distributions of the relative temperature in the porous matrix for fracture aperture $2b = 1 \times 10^{-3}$ m and distance from the center of the fracture $z = 5$ m computed with the analytical (circles) and numerical solutions for dimensionless parameter $R = 1, 10$ and 100 (blue, red and yellow lines, respectively). The liquid is injected at $x = 0$ during (a) $t = 5$ years and (b) $t = 10$ years.

Chapter 2

Efficient Multiscale Models of Polymerization Applied to *in vitro* FtsZ Assembly

2.1 Introduction

Shape and internal organization of cells is regulated by the cytoskeleton, a three-dimensional meshwork of filamentous proteins that also provides mechanical support for essential processes such as cell division, motility and intracellular transport [WG11, IMG12, XBZ12, YL12, FF15]. In a cell's cytoplasm, interacting monomers form long polymers called "filaments", which assemble and disassemble dynamically by elongation and annealing mechanisms. These filaments attach to the cell's membrane and constitute fundamental building elements of the cytoskeleton. Their arrangement into bundles contributes to the stability and strength of the network [BHC⁺08, LPD12]. In eukaryotic cells, both actin-based microfilaments and tubulin-based microtubules form bundles of different characteristics [DAR⁺08, EKC⁺14, WS10, SVM12]. For example, cell migration due to filopodia formation is regulated by the polymerization of long and tight filaments and by their subsequent bundling [DAR⁺08, ML08]. Another example is F-actin polymerization and bundling, both of which are critical processes in birth, growth and final form of mushroom-shaped dendritic spines as well as in the guidance and migration of neuronal growth cones [ML08, KH14, MBF06, PR12]. In prokaryotic cells, such as *Escherichia coli* or *Bacillus subtilis*, FtsZ and MreB proteins (homologs of eukaryotic tubulins and actins) are the most dominant components of their cytoskeletons. Whereas FtsZ is

responsible for division process, MreB controls the cell width. Different types of filaments and bundles of these proteins have been studied *in vitro* [SZL09, NM13, AGFE04] and *in vivo* [LTBJ07, FHB⁺10, SMMHB07]. In both eukaryotic and prokaryotic cells, continuous turnover of monomers between the cytosol and the network of polymers regulates the shape and size of filaments and bundles [KH14, MBF06, CE5b, CE09, RS11]. Assembly and disassembly of polymers are, therefore, permanent activities even in the steady state.

Cytoskeletal ring formation, of which FtsZ protein is the main agent, is a key part of prokaryotic cell division. In the cytosol of, e.g., *E. coli*, FtsZ monomers diffuse freely and form no structures as long as they remain bound to guanosine diphosphate (GDP). Interactions with guanosine triphosphate (GTP) initiate polymerization of FtsZ monomers. The resulting protofilaments then attach themselves to the cell membrane, a process facilitated by FtsA and ZipA proteins [HRRG⁺10, PL05, RM14, LM14]. In both the cytosol and membrane, these protofilaments elongate, anneal, bundle and form complex structures, such as entanglements and cross links. The *in vitro* experiments [MPV⁺09, BCH⁺13, DPLW10] suggest that proteins, such as ZapA or ZapB, reinforce the lateral bonds between filaments and bundles. Several positive and negative regulators of ring formation ensure that all of these processes take place in the center of the cell. A chain of several proteins (MatP, ZapA, and ZapB) in the replication terminus region (Ter macrodomain) promotes Z-ring formation at the midcell [MPS⁺08, BBW⁺14, MB15]. Both Min proteins, which oscillate between the two poles of a cell [HMW03, MdB01, KLSR06], and SlmA proteins, involved in nucleoid occlusion [CMDB11, TMC⁺13], inhibit polymerization everywhere except at the midcell [SL10, APS14, SL09, DL14]. Once the Z-ring structure forms in that location, it remains stable for several minutes [TRC⁺11], during which time there is still a continuous exchange of monomers between the cytoplasm and the FtsZ structure [CE5b, CE09]. This exchange increases the scaffold's robustness by modifying and repositioning the filaments. After that time, once the two new nucleoids are separated, contraction of the Z-ring is triggered, leading to the cell's division [DRRv13, Eri09, LWS07, TPD⁺12].

The *in vitro* experiments [CE5b, CE09, LM14, APS14, ACFE⁺12, CBRE5a] provide

further insight into the properties of FtsZ filaments. They established the existence of a critical concentration at which FtsZ monomers begin to polymerize; this critical concentration coincides with the concentration of FtsZ monomers observed in steady state. They showed that hydrolysis-induced turnover between FtsZ monomers in the pool and in the polymers/bundles network occurs at a constant rate in steady state; this phenomenon was also observed *in vivo* [SMSE02]. When the total concentration of FtsZ monomers in all forms (C_{tot}) is high enough to observe bundle formation, this turnover remains practically the same for higher C_{tot} [CE5b, RM04]. Finally, they showed that while filaments have different lengths at different concentrations [CE09, CBRE5a], the formation of bundles occurs only at high concentrations [CE5b, CE09, DLS⁺08, HLB⁺08, PIN⁺09].

The importance and ubiquity of polymer assembly provided an impetus for development of kinetics models of these processes. A number of these models [CE5b, DRRv13, CBRE5a, SML08, LDWS08] aim to describe the *in vivo* and *in vitro* observations of FtsZ assembly. Initial stages of FtsZ polymerization have been adequately captured with the eight-equation model [CBRE5a, CE5b]. The latter describes only the first seconds of polymerization for different FtsZ strains and buffer conditions, rather than the whole process of FtsZ assembly. The model's failure to handle later times and *in vivo* FtsZ concentrations stems from its inability to account for hydrolysis effects and transformations of filaments and bundles. Current models of full FtsZ assembly, e.g., [SML08, LDWS08, DRRv13], employ hundreds or even thousands of rate equations. Despite their complexity, most of them find it necessary to oversimplify the kinetics of hydrolysis and formation and dissociation of bundles, the processes that are known to be important at high concentrations of FtsZ protein found in living cells. Table 3.1 provides a comparison of these models in terms of their complexity, applicability range, and ability to predict the salient features of FtsZ assembly observed by Chen et al., [CE5b, CBRE5a].

We present a model of FtsZ assembly that ameliorates many of the shortcomings of its existing counterparts. It consists of only 17 equations, yet is capable of capturing the main characteristics of the *in vitro* experiment conducted by Chen and Erickson [CE5b] over a wide

range of FtsZ concentrations. The predictive accuracy of our model exceeds that of the more complex models (see Table 3.1). The significantly reduced complexity of our model stems from its reliance on an average length of filaments and bundles, rather than on a length distribution of different polymers. The initial stages of FtsZ assembly are described in our model with the eight rate equations introduced in [CBRE5a].

This chapter is organized as follows. In Section 2.2, we formulate a model of FtsZ assembly in terms of relevant unimolecular and bimolecular reactions and provide details on model parametrization, i.e., on selection of values of the reaction rates. In Section 4.4, we discuss the predictions and insights provided by our model, as well as its advantages over several other models. Major conclusions from our study are summarized in Section 2.4.

2.2 Model of FtsZ Assembly

We use coarse-graining to reduce all different sizes of polymers to a species called a filament whose average length is tracked in time during the entire process. The resulting coarse-grained model comprises 17 ordinary differential equations (ODEs).

2.2.1 Model formulation

The first critical concentration C_{cr}^1 is the minimum concentration of FtsZ proteins in the monomeric form at which polymerization begins, and it establishes two regimes of polymerization. The first regime, $C_{\text{tot}} \leq C_{\text{cr}}^1$, admits only monomers such that $[Z^{\text{na}}] + [Z] \approx C_{\text{tot}}$, where $[Z^{\text{na}}]$ and $[Z]$ denote concentrations of nonactivated (GDP-bound) and activated (GTP-bound) FtsZ monomers, respectively. The second regime, $C_{\text{tot}} > C_{\text{cr}}^1$, allows for FtsZ polymerization and bundling, with $C_{\text{cr}}^1 = 0.7 \mu\text{M}$, in accordance with the experimental evidence in [CE5b]. The analysis presented below is concerned with the second regime of polymerization.

Let Z^{na} and Z denote a nonactivated (GDP-bound) and activated (GTP-bound) monomer, respectively. The first five polymers obtained by combining the corresponding number of monomers are denoted by Z_i , where $i = 2, \dots, 6$. Longer polymers (i.e., filaments) are denoted by

F . Bundles of k filaments are denoted by B_k , where $k = 2, \dots, N$ and N is the maximum number of filaments in a bundle; it is allowed to increase with the total concentration of FtsZ monomers in all forms, C_{tot} . We show in Section B.1 of the Appendix B that $N = 10$ even in the physiologically extreme case of $C_{\text{tot}} = 10.0 \mu\text{M}$, i.e., our model relies on 17 species and equations to capture the process of FtsZ assembly. The basic structures (monomers, short polymers, filaments, and bundles) and their graphical representations are summarized in Figure 2.1.

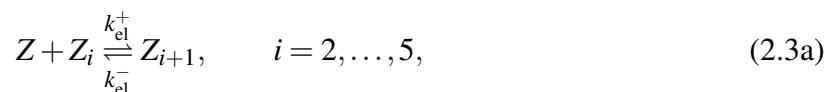
To avoid unphysical oversimplifications, we express the kinetics of the processes involved in FtsZ assembly, from its nonactivated monomeric form to long bundles of filaments, in terms of fundamental unimolecular and bimolecular reactions. The process of *activation* is described by a reaction



with forward and backward reaction rates k_{ac}^+ and k_{ac}^- , respectively. Activation and deactivation of monomers occurs due to their interactions with GTP and GDP nucleotides, respectively, even though GTP and GDP are not represented explicitly in our model. The process of *nucleation* is represented by a reaction



where k_{nu}^+ and k_{nu}^- are the forward and backward reaction rates, respectively. Formation of nucleus of two monomers (nucleation or dimerization) is a critical stage of initialization of the FtsZ assembly [CBRE5a]; it also determines the rate of assembly of the polymer network. The *elongation* process is modeled by a set of reactions





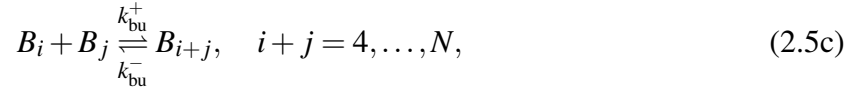
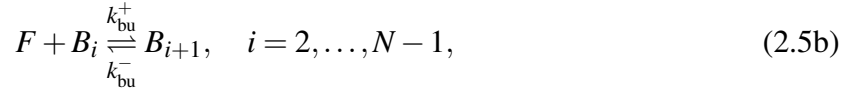
with forward and backward reaction rates k_{el}^+ and k_{el}^- , respectively.

The reactions defined above comprise the activation-nucleation-elongation model proposed by Chen and Erickson [CE5b], and used in [FG83, SXPM99, FLKG12] to describe the kinetics of actin polymerization. (These and other models, e.g., [CE5b, LDWS08], use the notation $Z + F \rightleftharpoons F$ in which a filament before and after elongation process is denoted by the same letter. To differentiate between reactant-filaments and product-filaments in a given reaction, we introduce subscripts that clarify the physical processes that these reactions represent. Thus, in Eq. 2.3c, F_{z^-} and F_{z^+} designate a filament F before and after the attachment of a monomer Z , respectively. The forward reaction implies a decrement of the concentration of activated monomers $[Z]$ with the rate $-k_{\text{el}}^+[Z][F_{z^-}]$. Similarly, the backward reaction represents the increment of the concentration of activated monomers with the rate $k_{\text{el}}^-[F_{z^+}]$. Like the aforementioned models, our model assumes that all filaments are present in the same concentration regardless of their length, such that $[F_{z^-}] = [F_{z^+}] = [F]$. Section B.1 of the Appendix B extends this assumption to other species and reactions in order to reduce the number of ODEs.) We posit that their model, including its values of the reaction rate constants, is sufficient to describe *short-time kinetics* and, hence, adopt it as a module in our model. This module is supplemented with models of filament annealing, bundling of both filaments and bundles, and hydrolysis/dissociation reactions to handle *long-time kinetics*, as described below. We assume that filaments and bundles have the same length when they connect laterally and that bundles grow laterally in structures of two dimensions. With these simplifications, the process of *filament annealing* is represented by a

reaction



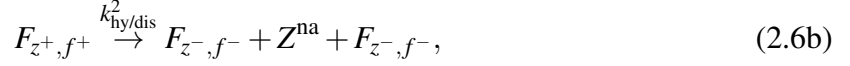
where k_{an}^+ and k_{an}^- are forward and backward reaction rates, respectively; and the subscripts f^- and f^+ designate a filament F before and after the attachment of another filament F . The process of *filament bundling* consists of reactions



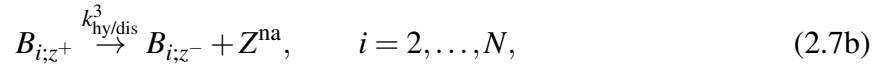
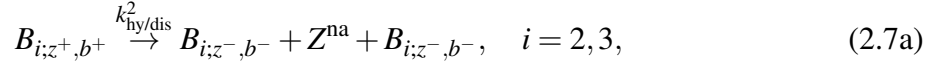
where k_{bu}^+ and k_{bu}^- are the forward and backward reaction rates. The latter rate varies with \bar{L}_{fb}^m , an average length of filaments of m monomers (or bundles made of filaments of m monomers), i.e., $k_{\text{bu}}^- = k_{\text{bu}}^-(\bar{L}_{\text{fb}}^m)$.

Two mechanisms contribute to the turnover of monomers between the solution and the network of filaments and bundles: hydrolysis of filaments and hydrolysis of bundles. The GTP-bound FtsZ monomers, which constitute the polymer network, exchange their nucleotides to GDP by hydrolysis. Subsequently, those monomers can detach from a filament or a bundle, restarting the polymerization process. In our model, *dissociation of monomers from filaments following GTP hydrolysis* involves two reactions





with reaction rates $k_{\text{hy/dis}}^1$ and $k_{\text{hy/dis}}^2$, and *dissociation of monomers from bundles following GTP hydrolysis* consists of two reactions,

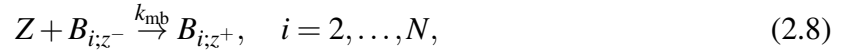


where $k_{\text{hy/dis}}^3$ is a reaction rate. It is worthwhile noting that the depolymerization process described by Eqs. 2.6a and 2.6b ignores depolymerization of the first oligomers Z_2, \dots, Z_6 . GTP hydrolysis does not affect either nucleation or first elongation phases because it occurs slowly, after the entry of a FtsZ subunit into a filament [CE5b, RM04]. For longer filaments, GTP hydrolysis precedes the loss of a nonactivated monomer from one of their ends, Eq. 2.6a, or even their middle, Eq. 2.6b, [LM14, MGPH⁺12]. Equation 2.7a represents the loss of a monomer that links both sides of a bundle; it implies a decrement of the bundle length (only applied to thin bundles of two or three filaments). Equation 2.7b represents bundles that lose nonactivated monomers from their middle or from their ends after GTP hydrolysis, without significantly changing their dimensions [APS14]. The subscripts z^\pm , f^\pm , and b^\pm indicate the loss or gain of monomers, filaments, and bundles, respectively, i.e., indicate variations in the concentrations of the corresponding species.

Our model does not provide explicit information about the binding sites where these species attach or detach. Figure 2.2 illustrates the actual process of shortening of a thin bundle after GTP hydrolysis and its simplified version implemented in our model. First, a bundle loses a GDP-bound FtsZ monomer somewhere in its middle after GTP hydrolysis (a process represented by Eq. 2.7b). Then, the same reaction can involve a monomer of the adjacent filament next to

the position of the departed monomer, yielding two separated and shorter bundles (a process described by Eq. 2.7a). An explicit description of these two processes would give information about the location of the monomers before they leave the bundle and the length of the new bundles. Our model lacks these details, providing information only about concentrations of both monomers and bundles (hence, the subscripts z^\pm and b^\pm in Eqs. 2.7a and 2.7b).

Finally, *attachment of monomers to bundles* is represented by a reaction



where k_{mb} is the attachment rate. This reaction accounts for interactions between activated monomers and the bundles and attachment of the former to the latter.

A graphical representation of reactions in Eqs. 2.1–2.8 is depicted in Figure 2.1. ODEs for each of the reactions in Eqs. 2.1–2.8 are provided in Section B.1 of the Appendix B.

Following other multifilament models, e.g., [LDWS08, FG83, SXPM99, FLKG12], we use the conservation of mass to estimate the average length of filaments and bundles, \bar{L}_{fb}^m . At any time, the total concentration of monomers, C_{tot} , is the sum of the concentration of nonactivated and activated monomers, $[Z^{na}]$ and $[Z]$, and the cumulative concentrations of monomers in different forms, e.g., twice the concentration of dimers, three times the concentration of trimers, etc. Because the length of filaments is a multiple of the monomers, this yields $C_{tot} = [Z^{na}] + [Z] + \sum_{i=2}^6 i[Z_i] + \bar{L}_{fb}^m([F] + \sum_{i=2}^N i[B_i])$ or

$$\bar{L}_{fb}^m = \frac{C_{tot} - [Z^{na}] - [Z] - \sum_{i=2}^6 i[Z_i]}{[F] + \sum_{i=2}^N i[B_i]}. \quad (2.9)$$

This quantity keeps track of the average number of monomers, hence the superscript m , longitudinally connected per filament/bundle during the entire assembly process. The smallest length of a filament is $\bar{L}_{fb}^m = 7$, i.e., a filament consist of seven monomers. This value is achieved instantaneously once $[F]$ becomes larger than zero. To avoid having to deal with this jump

discontinuity in time, we define an average total length, \bar{L}_{tot}^m , which includes the first oligomers (Z_2, \dots, Z_6),

$$\bar{L}_{\text{tot}}^m = \frac{\sum_{i=2}^6 i[Z_i] + \bar{L}_{\text{fb}}^m([F] + \sum_{i=2}^N i[B_i])}{\sum_{i=2}^6 [Z_i] + [F] + \sum_{i=2}^N i[B_i]}. \quad (2.10)$$

This parameter gives a complete description of the average length of filaments in all forms (short oligomers and longer filaments) and bundles. The average characteristics \bar{L}_{fb}^m and \bar{L}_{tot}^m play a crucial role in reducing the number of species and, therefore, the number of equations used to describe the protein assembly process. In Section C.1.1 of the Appendix B, we demonstrate that the definition of the average length in Eq. 3.4 enforces mass conservation. Energy is also conserved, but the principle of microscopic reversibility, or detailed balance, is violated (see Section C.1.1 for more detail).

Another important characteristic of the polymerization process is the average width of a bundle, \bar{W}_{tot}^f , or the average number of filaments per bundle. It is defined as

$$\bar{W}_{\text{tot}}^f = \frac{\sum_{i=2}^6 i[Z_i] + \bar{L}_{\text{fb}}^m([F] + \sum_{i=2}^N i[B_i])}{\sum_{i=2}^6 i[Z_i] + \bar{L}_{\text{fb}}^m([F] + \sum_{i=2}^N i[B_i])}. \quad (2.11)$$

where the species Z_2, \dots, Z_6 and F are treated as bundles of an average width 1.

Our model does not account for the “cozy corner association” [Eri09], which allows for simultaneous formation of longitudinal and lateral bonds and acts as a sliding mechanism between polymers. This omission is informed by the recent experimental study [APS14] that indicates that filaments in a bundle network do not slide but, rather, exhibit a treadmill-like behavior.

Models (2.1)–(3.4) consists of a system of 17 ODEs. This system was solved with an ODE45 Matlab function (The MathWorks, Natick, MA), which implements a combination of fourth- and fifth-order Runge-Kutta methods for nonstiff differential equations.

2.2.2 Model parametrization

We use the *in vitro* study [CE5b] of FtsZ-F268C polymerization in MMK buffer to parameterize our model, i.e., to determine values of the reaction rates in Eqs. 2.1–2.8. We focus on this strain because it is an innocuous mutation that shows identical assembly to the wild-type FtsZ [CE5b, CE09, APS14, ACF⁺12]. Unlike wild-type FtsZ, the mutant F268C has a single cysteine that provides a mechanism to attach the fluorescent labels and facilitates the assembly assay based on fluorescence resonance energy transfer. The experiments of Chen and Erickson [CE5b] cover a wide range of FtsZ concentrations, from the critical concentration to polymerize ($0.7 \mu\text{M}$ for this experiment) to the $5\text{--}10 \mu\text{M}$ representative of *in vivo* conditions [LDWS08, Lut07, ZML13], and their findings are in agreement with other investigations. These findings include the average filament length of $100\text{--}200 \text{ nm}$, also observed in [RSE01, DLS⁺08, PIN⁺09]; the average bundle width of $5\text{--}15 \text{ nm}$, as seen in [CE09, DLS⁺08, HLB⁺08, RSE01]; and the monomer turnover rate of 0.143 s^{-1} , which falls within the range of $0.112\text{--}0.233 \text{ s}^{-1}$ observed in *in vitro* experiments [APS14, RM04, RSBE05] and is close to *in vivo* values of $0.111\text{--}0.128 \text{ s}^{-1}$ [AGFE04].

Values of the reaction rates and other model parameters are summarized in Table 2.2. Most of them are taken from the literature, while the remaining four are estimated in Section C.2.1 of the Appendix B by calibrating our model to the low steady-state concentration data ($C_{\text{tot}} = 0.7\text{--}3.0 \mu\text{M}$) from [CE5b]. The low concentration data at short and long times are used in Section C.3 for model validation.

The values of the activation and nucleation reaction rates in Eqs. 2.1 and 2.2 are taken from the model in [CE5b]. Following [CE5b, FG83], we both assume the forward (k_{el}^+) and backward (k_{el}^-) reaction rates in Eq. 2.3 to be independent of a filament’s length (i.e., to be the same for all i) and set $k_{-7} = 0$. By treating the reaction in Eq. 2.3b as irreversible, the latter step allows one to avoid a buildup of Z_6 polymers as the concentration of filaments F increases, and ensures that the reaction rate values do not change when the number of elongation steps

increases beyond seven [CE5b].

While elongation and annealing in Eq. 2.4 are diffusion-limited reactions, we treat them as reaction-limited because of the small average size of the FtsZ polymers observed in the experiments. Previous models [LDWS08, SML08, DRRv13] assume that rates for elongation and annealing are equal and independent of the filament length, i.e., $k_{\text{el}}^+ = k_{\text{an}}^+ = \text{constant}$. Although the authors of [LDWS08] explicitly mention the diffusion-limited character of these reactions, they do not explain why the rates do not decrease as the filaments get longer; and the model in [Eri09] does the same for bundling reactions. We justify this choice by proposing an analogy between models of FtsZ filament growth and actin assembly. (For long filaments ($\bar{L}_{\text{actin}} \geq 100$ monomers), the annealing reaction rate of actin polymerization, $k_{\text{an, actin}}^+$, decreases with the average length [SXPM99, ABS⁺01, FPBM08]. For shorter filaments ($\bar{L}_{\text{actin}} = 65$ monomers), $k_{\text{an, actin}}^+$ is considered constant and smaller than the elongation rate $k_{\text{el, actin}}^+$ [KSEG93]. For small filaments ($\bar{L}_{\text{actin}} < 30$ monomers), the two rates are considered constant and similar, $k_{\text{an, actin}}^+ \approx k_{\text{el, actin}}^+ \approx 10 \mu\text{M}^{-1}\text{s}^{-1}$ [MGGP88].) Because the longest average length of FtsZ filaments in our model is $\bar{L}_{\text{tot}}^m \approx 30$ monomers, this analogy suggests $k_{\text{el}}^+ = k_{\text{an}}^+ = \text{constant}$.

For the concentrations reported in [CE5b], the bundling reaction rates in Eq. 2.5 are limited by the size of a filament bundling to either another filament or a bundle. Therefore, the bundling rate k_{bu}^+ should be close to the annealing rate k_{an}^+ , and its value must fall within the accepted range of protein-protein association rates, $2.0 - 7.5 \mu\text{M}^{-1}\text{s}^{-1}$ [CE5b, APS14, NE92]. The parameter identification procedure described in Section C.2.1 of the Appendix B honors this constraint.

The depolymerization reaction rates, k_{el}^- , k_{an}^- and k_{bu}^- , are determined from the respective internal energies of filaments and bundles. Specifically, the backward reaction rates for elongation and annealing are given by [LDWS08]

$$k_{\text{el}}^- = k_{\text{nu}}^- e^{-\Delta U_t} \quad \text{and} \quad k_{\text{an}}^- = k_{\text{nu}}^- e^{-\Delta U_m}, \quad (2.12)$$

where ΔU_t and ΔU_m are the increments in the energy of a monomer connected at the end and middle of a filament, respectively. The value of ΔU_t is calculated from the first expression in Eq. C.15, with the values for k_{nu}^- and k_{el}^- taken from [CE5b]. Conservation of energy suggests [LDWS08] that $\Delta U_m = 2\Delta U_t$. The lateral dissociation rate k_{bu}^- decreases exponentially with the average length of the connected filaments/bundles [LDWS08],

$$k_{\text{bu}}^- = k_{\text{bu}}^0 e^{-(\bar{L}_{\text{fb}}^m - 1)U_b}, \quad (2.13)$$

where U_b is the bond energy per lateral bond. Its value of $U_b = 0.175 k_B T$ represents both the average of the values reported in [DLS⁺08] for the same strain as in [CE5b] but a different buffer and the value used in [LDWS08] for a strain different from [CE5b] but for the same buffer. The reference dissociation rate k_{bu}^0 is one of the four parameters used for model calibration. In the absence of experimental evidence, we have explored a wide range of values ($0.0 - 500 \text{ s}^{-1}$) in the calibration procedure described in Section C.2.1.

Dissociation of monomers after GTP hydrolysis is essentially absent in the beginning of polymerization [CE5b, RM04]; it becomes more pronounced as the amount of polymers increases and they interact more frequently with GDP. This dependence of the hydrolysis/dissociation rates in Eqs. 2.6 and 2.7 on the amount of polymers is accounted for as

$$k_{\text{hy/dis}}^i = k_{\text{hss/dis}}^i \frac{C_{\text{tot}} - [Z^{\text{na}}] - [Z]}{C_{\text{tot}} - C_{\text{cr}}^1}, \quad i = 1, 2, 3, \quad (2.14)$$

where $C_{\text{cr}}^1 < C_{\text{tot}}$ in the second regime of polymerization. At the beginning of the assembly process, most FtsZ proteins are in the form of nonactivated (Z^{na}) and activated (Z) monomers, such that $[Z^{\text{na}}] + [Z] \approx C_{\text{tot}}$ and $k_{\text{hy/dis}}^i \rightarrow 0$. At steady-state, when the polymer network is formed and GDP deactivates monomers more often, these rates reach their maximum values, $k_{\text{hy/dis}}^i \approx k_{\text{hss/dis}}^i$ for $i = 1, 2, 3$. They represent the rate with which a GTP-bound monomer in a filament or a bundle changes its nucleotide and leaves the filament bounded to GDP, i.e., the

turnover rate predominantly associated with GTP hydrolysis.

The reaction rates controlling dissociation after GTP hydrolysis depend on the location of a deactivated monomer in the filament or bundle. In Table 2.2, $k_{\text{hss/dis}}^i$ ($i = 1, 2, 3$) denote values of the hydrolysis rates for filaments and bundles at steady state. Only the rate for detachment of monomers from filament ends, $k_{\text{hss/dis}}^1$, was calibrated. The rate for detachment of monomers from the middle of filaments and thin bundles, $k_{\text{hss/dis}}^2$, is set to the average value reported in [CE5b] for turnover of monomers at steady state (half-time of 7 s, i.e., 0.143 s^{-1}), because we assume that it is the depolymerization reaction that happens more often. This assumption is based on two facts: the predominant species observed in the experiment are filaments and thin bundles; and there are more monomers in the middle of filaments and bundles than in their ends. The value of $k_{\text{hss/dis}}^3$ is determined in [APS14] by observing the detachment of nonactivated monomers from thick bundles. These three rates satisfy the following order relations. It takes less energy to break a longitudinal bond at the filament end than two bonds at its middle, therefore, $k_{\text{hss/dis}}^1 > k_{\text{hss/dis}}^2$ [MGPH⁺12] (the condition imposed for calibration of $k_{\text{hss/dis}}^1$ in Section C.2.1 of the Appendix B). The values of $k_{\text{hss/dis}}^2$ for shortening of filaments and thin bundles are equal, because both reactions describe the loss of a monomer in the middle of a filament. The value of $k_{\text{hss/dis}}^3$ is the smallest of the three rates, because the monomers in a bundle can be doubly connected both longitudinally and laterally.

The rate at which activated monomers in the solution attach themselves to bundles, a process represented by Eq. 2.8, is quantified by the reaction rate constant k_{mb} . The latter serves as the final calibration parameter; its computed value (Table 2.2) is imposed to fall within the range of values of the protein-protein interaction rates of $2\text{--}7.5 \mu\text{M}^{-1}\text{s}^{-1}$. The condition $k_{\text{mb}} < k_{\text{el}}^+ = 6.6 \mu\text{M}^{-1}\text{s}^{-1}$ is also imposed (see Section C.2.1), because pure longitudinal attachments of monomers to filament ends are more favorable than combinations of both longitudinal and lateral attachments in a monomer-bundle interaction.

2.3 Results and Discussion

Results of model calibration and validation on the low concentration data from [CE5b], $C_{\text{tot}} = 0.7 - 3.0 \mu\text{M}$, are presented in Sections C.2.1 and C.3 of the Appendix B, respectively. In what follows, we present fit-free predictions for high concentrations of $C_{\text{tot}} = 3.0 - 10.0 \mu\text{M}$ (Section 2.3.1); discuss what are, to our knowledge, new insights provided by our model (Section 2.3.2); and compare its performance with that of its counterparts (Section 2.3.3). The steady-state data at high concentrations ($C_{\text{tot}} = 3 - 10 \mu\text{M}$) are taken from [CE5b] and used to validate our model.

2.3.1 Model predictions at high concentrations, $C_{\text{tot}} = 3.0 - 10.0 \mu\text{M}$

Average size of the filaments and bundles.

Under physiologically relevant conditions, $C_{\text{tot}} = 5.0 - 10.0 \mu\text{M}$, our model captures the observed tendency of the filaments to keep the same average length $\bar{L}_{\text{tot}}^m \approx 32 - 33$ subunits at steady state, regardless of the value of C_{tot} (Fig. 2.3). Tables 2.3 and C.5 (see the Appendix B) show that, for $C_{\text{tot}} = 2.0 - 10.0 \mu\text{M}$, the predicted average length is $\bar{L}_{\text{tot}}^m = 25 - 33$ subunits (125 - 165 nm), which is within the well-established range of 100 - 200 nm [Eri09, CBRE5a, DLS⁺08, HLB⁺08, PIN⁺09, RSE01].

Almost all filaments remain single-stranded when $C_{\text{tot}} < 2.0 \mu\text{M}$ (Table C.5 in the Appendix B). For larger concentrations up to $C_{\text{tot}} = 10.0 \mu\text{M}$, and for various buffers and FtsZ strains, filaments dominate and the majority of bundles consist of two filaments. All the computed values of the average bundle width \bar{W}_{tot}^f in Table 2.3 (and Fig. 2.3) are < 2 , which is in agreement not only with [CE5b] but also with other experiments [CE09, DLS⁺08, HLB⁺08, RSE01].

Concentration of monomers at steady state.

In the physiologically relevant range of $C_{\text{tot}} = 5.0 - 10.0 \mu\text{M}$, our model predicts the steady-state concentration of monomers to be $[Z^{\text{na}}]_{\text{ss}} + [Z]_{\text{ss}} \approx 0.7 \mu\text{M}$ (Table 2.3). This matches the observed monomer concentration [CE5b] and equals the first critical concentration, C_{cr}^1 . The

model presented in [CE5b] underestimates this observation, predicting a value of $[Z^{\text{na}}]_{\text{ss}} + [Z]_{\text{ss}} \approx 0.5 \mu\text{M}$.

2.3.2 Physiological insights

Second critical concentration.

An appreciable decrease in the fluorescence intensity at $C_{\text{tot}} = 3.0 \mu\text{M}$ (or, more generally, at $C_{\text{tot}} = 2.0 - 4.0 \mu\text{M}$, depending on the concentration of Mg^{2+} contained in the buffer) was observed, but not explained, by Chen and Erickson [CE5b]. A subsequent kinetics model in [LDWS08] utilized the experimental data from [CBRE5a] and [CE5b] to describe this phenomenon by identifying a critical concentration, C_{cr}^2 , at which the presence of bundles becomes pronounced. The model in [LDWS08] does not specify the value of C_{cr}^2 and, crucially, predicts formation of bundles comprising two or three filaments at low concentrations ($C_{\text{tot}} = 2.0 \mu\text{M}$), which is not supported by the observations. Our model correctly predicts the average length/width for filaments and bundles for a range of C_{tot} . This ratio reaches its maximum at $C_{\text{tot}} = 2.5 \mu\text{M}$, the critical concentration C_{cr}^2 after which the longitudinal growth (elongation and/or annealing) ceases to dominate the lateral growth (bundling) and bundles become an important factor in the overall kinetics (Fig. 2.4). Our predicted value of $C_{\text{cr}}^2 = 2.5 \mu\text{M}$ falls within the experimentally observed range of $2 - 4 \mu\text{M}$. We posit that the maximum average length/width corresponds to the transition between a network formed entirely by filaments and a thicker network made of both filaments and bundles.

Role of bundling in dissociation of monomers after hydrolysis.

Because the average length \bar{L}_{tot}^m remains nearly constant for $C_{\text{tot}} > 3.0 \mu\text{M}$ or 29-33 subunits (Table 2.3), this characteristic length is probably sufficient for formation of stable bundles. The bundling regulates turnover of monomers keeping GTP-hydrolysis/dissociation rate constant for concentrations $C_{\text{tot}} = 3.0-10.0 \mu\text{M}$, at which bundles become relevant [CE5b]. That regulation also helps to maintain the average length of the filaments constant and to keep the system at this equilibrium state regardless of the total concentration. Since this occurs at *in*

in vivo concentrations levels, $C_{\text{tot}} = 3.0\text{-}10.0 \mu\text{M}$, we posit that the interaction of bundle formation and GTP hydrolysis is a key part of the FtsZ ring formation and steady-state equilibrium until contraction.

Limitations of fluorescence resonance energy transfer assay for measurements related to bundling.

The existence of the second critical concentration related to bundling, C_{cr}^2 , highlights a potential limitation of the fluorescence resonance energy transfer assay used in [CE5b]. The authors reported the fluorescence intensities, which serve as proxy for the amount of FtsZ in filaments and bundles, to be lower than expected. Accounting for the exchange of monomers between solution and bundles (see Eqs. 2.7b and 2.8) provides an explanation for this phenomenon. These reactions cause the bundles to continuously lose and gain monomers even at steady state, which generates bundles partially connected longitudinally; this exchange can be described with a stochastic model [APS14]. This longitudinal elongation of the bundles distorts the measured fluorescence intensities, because the fluorescence resonance energy transfer assay signals are direct measurements of the longitudinal contacts of FtsZ species.

2.3.3 Comparison with alternative models

Borrowing from [CE09], our model accounts for the following aspects of FtsZ assembly: reversible exchange of monomers bounded to GTP at the end of filaments (Eq. 2.3c), irreversible annealing (forward reaction in Eq. 2.4), and the loss of monomers bounded to GDP at the ends (Eq. 2.6a) and middle of filaments (Eq. 2.6b) after GTP hydrolysis. Our model departs from [CE09] by introducing a reversible annealing (Eq. 2.4) because fragmentation of a filament in the middle can be due to the separation of two monomers bounded to GTP [RSE01]. Crucially, our model includes a description of the depolymerization process by including reactions for bundles (Eqs. 2.7a and 2.7b).

The predictive power of our model, which consists of 17 ODEs, compares favorably with that of its more complex alternatives, which comprise hundreds or thousands of ODEs (see

Table 3.1). Our model’s development was motivated by the three models of increasing complexity introduced by Lan et al. [LDWS08]. The simplest, single-filament model (denoted by M1 in Table 3.1) captures the kinetics of FtsZ assembly at low FtsZ concentrations, $C_{\text{tot}} \leq 2.0\text{-}3.0 \mu\text{M}$. Even though it employs 500 ODEs to determine the steady-state length distribution of filaments, it does not account for filament bundling and is discarded by the authors in favor of the more complex alternatives. By allowing formation of two-filament bundles, the second of these models (denoted by M2 in Table 3.1, and comprising 500 ODEs) improves the predictive accuracy of polymer length distribution at low concentrations ($C_{\text{tot}} = 2.0 \mu\text{M}$). Yet, model M2 significantly overestimates the length of bundles at high concentrations ($C_{\text{tot}} = 10.0 \mu\text{M}$).

The third model in [LDWS08] consists of 1254 ODEs and, similar to our model, computes an average length of filaments and bundles rather than a complete distribution of their lengths. It has been rejected by the authors because of its complexity and apparent inability to correctly predict the experimentally observed average length of filaments and bundles and the average width of bundles. Specifically, this model predicts the average length \bar{L}_{tot}^m to be 300 nm instead of the experimentally observed value of ~ 120 nm [CE5b]. Rather than attributing this overestimation to the deficiency of the modeling approach, i.e., the reliance on the average length, we believe it to stem both from an inappropriate choice of the value for reaction rate k_{nu}^- and from the oversimplified representation of dissociation of monomers after GTP hydrolysis. Likewise, their model overestimates the width of the bundles: it predicts an average of two or three filaments per bundle for $C_{\text{tot}} = 2.0 \mu\text{M}$, while the experiment [CE5b] found almost all filaments to be single-stranded. We attribute this discrepancy to an inappropriate selection of values of the reaction rates k_{bu}^+ and k_{bu}^0 , and to the overestimation of the average length ($\bar{L}_{\text{tot}}^m \approx 300$ nm). According to Eq. 2.13, the latter leads to an underestimation of the lateral dissociation rate of filaments/bundles k_{bu}^- .

The model of Surovtsev et al. [SML08] and its subsequent generalization [DRRv13] handle a distribution of polymer lengths (rather than their average) and explicitly account for hydrolysis reactions at both the ends and middle of a filament. While these models assume

that these two reactions have the same rate, our model assigns a higher rate for GDP-bound monomer dissociation from the end of a filament after hydrolysis than from the middle, as observed experimentally in [MGPH⁺12]. Consequently, our model makes better predictions for dissociation after hydrolysis than [SML08] (they estimated concentration of monomers at the steady-state 2-10 times lower than *in vitro* experimental values). Moreover, the models in [SML08, DRRv13] consist of ~ 300 ODEs and ignore filament bundling. The latter implies that they predict neither a bundle size nor the critical concentration at which bundles become pronounced. Finally, these models fail to identify the strong dependence between dissociation of monomers after GTP hydrolysis and bundle formation [APS14, RM04, RSE01].

2.4 Conclusions

We developed a computationally efficient model of protein polymerization, which relies on an average length of polymers (rather than on length distribution) to significantly reduce the number of reaction rate equations. Our model of FtsZ assembly in *E. coli*, a phenomenon used as an illustrative example, consists of 17 ODEs and equals or exceeds the predictive power of its alternatives [SML08, DRRv13, LDWS08], which comprise hundreds or thousands of ODEs. The simplicity and, hence, computability of our model are essential elements for its use as a component in simulations of an *E. coli* cell lifecycle, which in addition to FtsZ assembly also includes attachment/detachment to/from the cell membrane, polymerization inhibition by MinCD and SlmA proteins, formation of bundles and clusters by other proteins, etc.

It is often argued, e.g., by [LDWS08], that reducing the number of species (and, hence, ODEs) by defining an average concentration of filaments (and their average length) leads to significant model errors. We demonstrated that an improved kinetic description of the FtsZ assembly process yields more accurate and computationally efficient predictions than those obtained with the multifilament model [LDWS08].

Despite its relative simplicity, our model captures key aspects of depolymerization after

GTP hydrolysis and filament bundling in cytoskeletal structures in a way that its more complex counterparts do not. FtsZ filaments in *E. coli* bundle by lateral bonds or through the action of other proteins like ZapA or ZapB. Our model reproduces the experimental finding [DLS⁺08, LDWS08] that lateral interactions between FtsZ monomers or small filaments are weak. It also shows that, as filaments grow longitudinally, bundling becomes essential for the stability and robustness of the scaffold. In the physiologically relevant conditions of the total monomer concentration $C_{\text{tot}} = 5.0 - 10.0 \mu\text{M}$, once the filaments grow to the length of ~ 30 subunits, they start forming bundles. Our model reproduces, both qualitatively and quantitatively, this phenomenon as well as the FtsZ polymerization at low concentrations ($C_{\text{tot}} \leq 2.0 \mu\text{M}$) observed in [CE5b].

Because our model describes protein assembly in terms of elementary (and bimolecular) reactions only, it is readily amenable to stochastic simulations that replace continuum reaction rate ODEs with their discrete counterparts, e.g., [CMTS10]. Our model is directly applicable to homogeneous systems, such as *in vitro* experiments in which the entire process of protein assembly occurs in well-mixed solutions without spatial preferences to polymerize. It can be generalized to account for the presence of concentration gradients either by adding diffusion terms to the ODEs or by employing stochastic operator-splitting algorithms, e.g., [CMTS12].

Another approach to dealing with spatial heterogeneity ubiquitous in *in vivo* systems is to partition a cell into homogeneous compartments. In the context of bacterial cell division, such compartments are cell caps and a midcell region [DRRv13]. FtsZ filaments and bundles in the cell caps are shorter and thinner than in the midsection, because of the action of MinCD and SlmA proteins that continuously extract monomers from the FtsZ network [DL14, FFFG12, FFG11]. Deploying our model in each of the three homogeneous compartments and using Fick's law to compute fluxes of FtsZ species between any two adjacent components would yield spatially varying average length of filaments and bundles.

Our reduced-order representation of reactions, such as bundling or turnover of subunits as a consequence of hydrolysis, facilitates its adoption to other cytoskeletal biopolymers. Apart from elongation and annealing, the formation of bundles with and without intervention of other

proteins is a characteristic process in network assembly of actin filaments (by fimbrin or α -actinin), microtubules (by MAP2) and intermediate filaments in eukaryotes, or MreB (by YeeU) and ParM in prokaryotes [FLKG12, MTA⁺12, AJL⁺14]. Our FtsZ model can be modified to define the characteristic net cycle balance of other cytoskeletal filaments [Nee15, SW11, Weg76] in terms of simple reactions. Polymerization/depolymerization processes regulated by the action of nucleotides, such as ATP/ADP or GTP/GDP, are also common in cytoskeleton formation. Our model already includes reactions of this nature but it can be improved by defining nucleotides as new species and describing more explicitly their interactions with biopolymers. We leave these and other enhancements of our model for future studies.

Chapter 2, in full, is a reprint of the material as it appears in Efficient multiscale models of polymer assembly 2016. Ruiz-Martínez; Á., Bartol, T.M.; Sejnowski, T.J.; and Tartakovsky, D.M., Biophysical Journal, 2016. The dissertation/thesis author was the primary investigator and author of this paper.

Table 2.1. Comparison of the kinetic *in vitro* models in terms of their complexity, applicability range, and ability to predict the observed features of FtsZ assembly. M1, M2, and M3 designate the single-filament, two-filament-bundling, and multi-filament-bundling models introduced in [LDWS08], respectively; C_{tot} is the total concentration of FtsZ monomers in all forms; low and high C_{tot} refers to its values of 2 and 10 μM , respectively; $C_{\text{cr}}^1 = [Z^{\text{na}}]_{\text{ss}} + [Z]_{\text{ss}} \approx 0.7 \mu\text{M}$ is the critical concentration at which polymerization begins, which is computed as the sum of the steady-state concentrations of nonactivated (GDP-bound) and activated (GTP-bound) FtsZ monomers, respectively; and $C_{\text{cr}}^2 \approx 3.0 \mu\text{M}$ is the critical value of concentration C_{tot} at which bundling becomes pronounced. The superscripts (+) and (−) denote the overestimated and underestimated predictions, respectively.

	Refs. [CBRE5a, CE5b]	M1, Ref. [LDWS08]	M2, Ref. [LDWS08]	M3, Ref. [LDWS08]	Ref. [SML08]	Our model
Number of ODEs	8	500	500	1254	300	17
Short time	Yes	Yes	Yes	Yes	Yes	Yes
Long time	No	Yes	Yes	Yes	Yes	Yes
Low C_{tot}	Yes	Yes	Yes	Yes	Yes	Yes
High C_{tot}	No	No	No	No	Yes	Yes
Filament length	No	Distribution	Distribution	Average ⁺	Distribution	Average
Bundle width	No	No	Two filaments	Distribution ⁺	No	Distribution
C_{cr}^1	Yes [−]	Yes	Yes	Yes	Yes [−]	Yes
C_{cr}^2	No	No	No	No	No	Yes

Table 2.2. Reaction rates and bond energies. \ddagger The energy units are expressed in terms of the Boltzmann constant k_B and room temperature T . \dagger Simple bundling model.

Parameter	Units	Value	Reference
k_{ac}^+	s^{-1}	0.38	[CE5b]
k_{ac}^-	s^{-1}	0.01	[CE5b]
k_{nu}^+	$\mu M^{-1} s^{-1}$	0.79	[CE5b]
k_{nu}^-	s^{-1}	199.8	[CE5b]
k_{el}^+	$\mu M^{-1} s^{-1}$	6.6	[CE5b]
k_{an}^+	$\mu M^{-1} s^{-1}$	6.6	[CE5b]
k_{bu}^+	$\mu M^{-1} s^{-1}$	3.5981	Calibrated
k_{bu}^0	s^{-1}	199.8221	Calibrated
k_{mb}	$\mu M^{-1} s^{-1}$	2.7288	Calibrated
$k_{hss/dis}^1$	s^{-1}	0.6681	Calibrated
$k_{hss/dis}^2$	s^{-1}	0.143	[CE5b]
$k_{hss/dis}^3$	s^{-1}	0.112	[APS14]
ΔU_t	$k_B T^{\ddagger}$	4.05	[CE5b, LDWS08]
ΔU_m	$k_B T^{\ddagger}$	8.10	[LDWS08]
U_b	$k_B T^{\ddagger}$	0.175	[DLS ⁺ 08, LDWS08] [†]

Table 2.3. Steady-state monomer concentration, and average length and width, predicted with our model and observed in experiments [CE5b].

Concentration C_{tot} (μM)	Average length: \bar{L}_{tot}^m		Average width: \bar{W}_{tot}^f		Monomer concentration: $[Z^{\text{na}}]_{\text{ss}} + [Z]_{\text{ss}}$ (μM)		
	Predicted	Observed	Predicted	Observed	Predicted	Observed	Model [CE5b]
4.0	31.42	30	1.39	< 2	0.693	0.7	0.537
5.0	32.14	30	1.50	< 2	0.691	0.7	0.538
6.0	32.55	30	1.60	< 2	0.690	0.7	0.538
7.0	32.81	30	1.69	< 2	0.690	0.7	0.539
8.0	32.99	30	1.77	< 2	0.689	0.7	0.539
9.0	33.12	30	1.84	< 2	0.689	0.7	0.539
10.0	33.21	30	1.91	< 2	0.690	0.7	0.539

POLYMER STRUCTURE	GRAPHICAL REPRESENTATION
<i>Non-activated monomer, Z^{na}</i>	
<i>Activated monomer, Z</i>	
<i>First five polymers, Z_2, \dots, Z_6</i>	
<i>Filament, F</i>	
<i>Bundles, B_2, B_3, \dots</i>	

REACTION	GRAPHICAL REPRESENTATION
<i>Activation (Eq. 1)</i>	
<i>Nucleation (Eq. 2)</i>	
<i>Elongation (Eqs. 3)</i>	
<i>Filament annealing (Eq. 4)</i>	
<i>Filament bundling (Eqs. 5)</i>	
<i>Dissociation of monomers from filaments following GTP hydrolysis (Eqs. 6)</i>	
<i>Dissociation of monomers from bundles following GTP hydrolysis (Eqs. 7)</i>	
<i>Attachment of monomers to bundles (Eq. 8)</i>	

Figure 2.1. Basic polymer structures and reactions and their graphical representation.

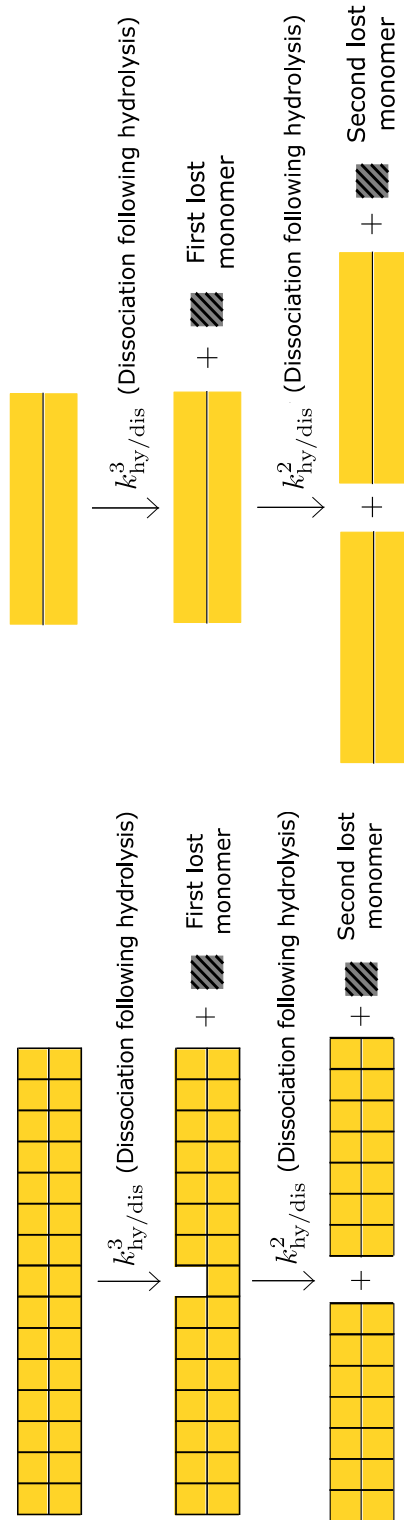


Figure 2.2. Shortening of a bundle of two filaments by hydrolysis (left) and its mathematical representation in our model (right).

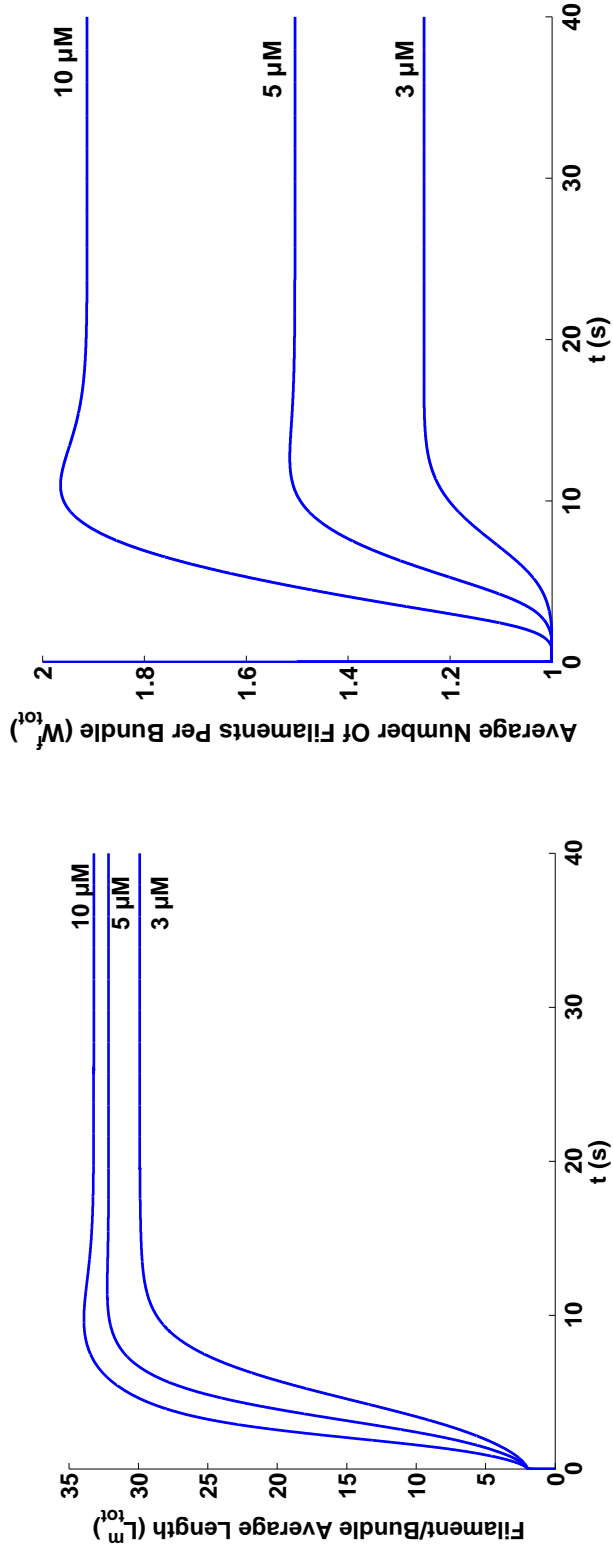


Figure 2.3. Temporal evolution of the average number of monomers connected longitudinally into filaments and bundles (left) and the average number of filaments per bundle (right), for $C_{tot} = 3.0, 5.0,$ and $10.0 \mu\text{M}$.

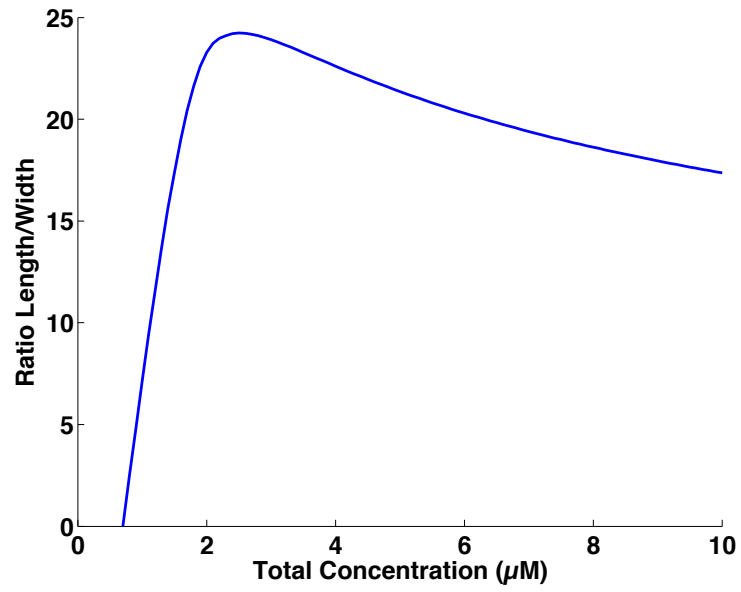


Figure 2.4. Length/width for the filaments and bundles at steady state, for a range of concentration C_{tot} .

Chapter 3

Efficient Multiscale Models of Polymerization Applied to *in vivo* FtsZ Ring Assembly in *Escherichia coli*

3.1 Introduction

In this chapter, we present a new modeling framework that is (many) orders of magnitude faster than the existing alternatives (e.g., those included in Table 3.1); this speed-up is achieved by replacing distributions of lengths and widths with their average counterparts and by introducing a hierarchical classification of species and reactions into sets. As in previous models, monomers, filaments and bundles are defined as interacting species; a system of coupled ordinary differential equations (ODEs) describes the temporal evolution of the species concentrations. Unlike those models, our approach involves a hierarchical classification of these species such that, for example, bundles are assembled from filaments which, in turn, are built from monomers. The resulting model comprises ODEs describing the dynamics of the concentrations of species classes and the exchange of elemental quantities (e.g., a monomer in filaments or a filament in bundles) between the classes.

While some kinetic models gain in computational efficiency by replacing filaments of different sizes with filaments of an average length [LDWS08, FLKG12, RMBST16], they all treat bundles differing by a single filament as distinct species. Hence, their computational cost

increases with total protein concentration, C_{tot} . That is because higher concentrations of C_{tot} result in larger polymers and bundles and, consequently, increase the variability of their sizes; the latter enlarges the number of species and ODEs describing their dynamics. At relatively high concentrations, some of the models comprise hundreds or thousands ODEs (Table 3.1). In contrast, the number of ODEs in our model (10 or 11, depending on the presence of a membrane) does not change with C_{tot} .

We use *in vitro* and *in vivo* FtsZ ring assembly in *E. coli* to demonstrate the veracity and computational efficiency of our model. This complex kinetics process involves a plethora of chemical reactions and species; large concentrations accompanying *in vivo* assembly of the FtsZ ring put this phenomenon out of reach of most current models. Our approach requires an addition of a single ODE to account for the influence of the membrane and FtsA, ZipA and ZapA proteins. The resulting 11-ODE model accurately predicts key observed features of the ring formation, such as time to reach the steady state, total concentration of FtsZ species in the ring, total concentration of monomers, and average dimensions of filaments and bundles. It also allows one to generate a hypothesis, for example, about the role of ZapA proteins in positioning and stability of the FtsZ-ring.

3.2 Average Feature Model of Polymerization

We reduce multiple sizes of polymers to species called a filament and a wide bundle whose average features are tracked in time. The resulting model comprises 10 ODEs. Our model does not provide information about the exact binding sites where species attach or detach. Instead, it estimates variations in concentration of monomers, filaments and/or bundles. Consequently, we refer to it as an Average Feature Model or AFM.

The first critical concentration C_{cr}^1 is the minimum concentration of FtsZ proteins in the monomeric form at which polymerization begins, and it establishes two regimes of polymerization. The first regime, $C_{\text{tot}} \leq C_{\text{cr}}^1$, admits only monomers such that $[Z^{\text{na}}] + [Z] \approx C_{\text{tot}}$, where

$[Z^{\text{na}}]$ and $[Z]$ denote concentrations of nonactivated (GDP-bound) and activated (GTP-bound) FtsZ monomers, respectively. The second regime, $C_{\text{tot}} > C_{\text{cr}}^1$, allows for FtsZ polymerization and bundling, with $C_{\text{cr}}^1 = 0.7 \mu\text{M}$ [CE5b].

3.2.1 Short-time kinetics

The first protofilaments obtained by combining the corresponding number of monomers are denoted by Z_i with $i = 2, 3$. Longer polymers (i.e., filaments) are denoted by F . The basic structures (monomers, protofilaments, filaments, thin bundles, and wide bundles) and their graphical representations are summarized in Figure C.1 of the Appendix C. We describe the early-time kinetics of polymerization with the reduced version [RMBST16] of the activation-nucleation-elongation model [CE5b]; the latter was used in [FG83, SXPM99, FLKG12] to describe the kinetics of actin polymerization. In so doing, we express the kinetics of all of the processes involved in FtsZ assembly, from its nonactivated monomeric form to long bundles of filaments, in terms of fundamental unimolecular and bimolecular reactions. These are summarized in Table 3.2 and represented graphically in Figure C.1.

The process of *activation* is described by reaction I in Table 3.2, with forward and backward reaction rates k_{ac}^+ and k_{ac}^- , respectively. Activation and deactivation of monomers occurs due to their interactions with GTP and GDP nucleotides, respectively, even though they are not represented explicitly in our model. The process of *nucleation* is represented by reaction II in Table 3.2, with forward and backward reaction rates k_{nu}^+ and k_{nu}^- , respectively. Formation of the nucleus of two monomers (nucleation or dimerization) is a critical stage of initialization of the FtsZ assembly [CBRE5a]; it also determines the rate of assembly of the polymer network. The *elongation* process is modeled by Reactions III–V in Table 3.2, with forward and backward reaction rates k_{el}^+ and k_{el}^- , respectively.

3.2.2 Long-time kinetics

The first bundles of k filaments are denoted by B_k with $k = 2, 3$. Bigger structures of laterally attached filaments are referred to as wide bundles and are denoted by B_w . We assume that filaments and bundles have the same length when they connect laterally and that bundles grow laterally into 3D structures. With these simplifications, the process of *filament annealing* is represented by reaction VI in Table 3.2, with forward and backward reaction rates k_{an}^+ and k_{an}^- , respectively. The process of *filament bundling* is modeled similarly to elongation/annealing of filaments; that is, bundles of up to three filaments are explicitly defined by reactions VII–XI in Table 3.2, with forward and backward reaction rates k_{bu}^+ and k_{bu}^- , respectively. The former rate depends on the number of filaments comprising both reactants; the latter rate varies with the number of filaments comprising the reactant and \bar{L}_{fb}^m , an average filament length (expressed as the number of monomers in a filament)—that is, $k_{\text{bu}}^- = k_{\text{bu}}^-(\bar{L}_{\text{fb}}^m)$.

Hydrolysis of both filaments and bundles contributes to the turnover of monomers between a network of filaments/bundles and the ambient solution.

Dissociation of monomers from filaments after GTP hydrolysis is modeled by irreversible reactions XII and XIII in Table 3.2, with rates $k_{\text{hy/dis}}^1$ and $k_{\text{hy/dis}}^2$, respectively. To model *dissociation of monomers from bundles* after GTP hydrolysis, we supplement the two reactions used in [RMBST16] with a third one for wide bundles (reactions XIV–XVI in Table 3.2). The first of these reactions has rate $k_{\text{hy/dis}}^2$, and the remaining two have rate $k_{\text{hy/dis}}^3$. Biochemical implications and limitations of our conceptualization of monomer turnover are discussed in [RMBST16].

Finally, *attachment of monomers to bundles* is represented by reactions XVII and XVIII in Table 3.2, with attachment rate k_{mb} . These reactions account for interactions between activated monomers and the bundles and attachment of the former to the latter.

3.2.3 Concentration of species sets

A key component of AFM is a classification of the FtsZ species into different sets (Table 3.3). Exchange of FtsZ structures between these sets is defined in terms of the elementary reactions collated in Table 3.2. A set containing all FtsZ species, \mathbb{S}_z , includes monomers (m), filaments (f) and bundles (b), and is endowed with average filament length (\bar{L}_{fb}^m) and bundle width (\bar{f}_{wb} , the number of filaments in a bundle). It comprises a subset of monomers and protofilaments, \mathbb{S}_{mp} , and a subset of filaments and bundles, \mathbb{S}_{fb} , such that $\mathbb{S}_z = \mathbb{S}_{mp} \cup \mathbb{S}_{fb}$. The total concentration (in \mathbb{S}_z) of FtsZ monomers in all forms, C_{tot} , is the sum $C_{tot} = C_{mp}^m + C_{fb}^m$ of the concentration (in \mathbb{S}_{mp}) of monomers in the monomer and protofilament forms and the concentration (in \mathbb{S}_{fb}) of monomers in the filament and bundle forms, with both concentrations defined in Table 3.3. Transfer of monomers from \mathbb{S}_{mp} to \mathbb{S}_{fb} is due to a reaction set $\mathbb{R}_{mp \rightarrow fb}^m$ (see Table 3.3). The number of monomers (in both monomer and protofilament forms) involved in reaction R_1 is $m_r^1 = 4$ for the reactants and $m_p^1 = 0$ for the reaction product; the same for reaction R_k ($k = 2, 3, 4$) is $m_r^k = 1$ and $m_p^k = 0$. Likewise, transfer of monomers from \mathbb{S}_{fb} to \mathbb{S}_{mp} is due to a reaction set $\mathbb{R}_{fb \rightarrow mp}^m$. For each reaction R_n ($n = 1, \dots, 6$), $m_r^n = 0$ and $m_p^n = 1$. Then,

$$\frac{dC_{fb}^m}{dt} = \sum_{\substack{k=1 \\ \mathbb{R}_{mp \rightarrow fb}^m}}^4 \kappa_k (m_r^k - m_p^k) - \sum_{\substack{n=1 \\ \mathbb{R}_{fb \rightarrow mp}^m}}^6 \kappa_n (m_p^n - m_r^n), \quad (3.1)$$

where κ_k ($k = 1, \dots, 10$) are the reaction rates for reactions R_k from the reaction sets $\mathbb{R}_{mp \rightarrow fb}^m$ and $\mathbb{R}_{fb \rightarrow mp}^m$. This formulation conserves mass and energy, although the principle of microscopic reversibility, or detailed balance, is violated (see Section C.1.1 of the SI).

The subset \mathbb{S}_{fb} is, in turn, subdivided into subsets of filaments and thin bundles, \mathbb{S}_{ftb} , and wide bundles, \mathbb{S}_{wb} (see Table 3.3). The total concentration (in \mathbb{S}_{fb}) of FtsZ filaments in filament and bundle forms, C_{fb}^f , is the sum $C_{fb}^f = C_{ftb}^f + C_{wb}^f$ of the concentration (in \mathbb{S}_{ftb}) of filaments in the filament and thin bundle forms, C_{ftb}^f , and the concentration (in \mathbb{S}_{wb}) of filaments in the wide bundle form, C_{wb}^f . (Both C_{ftb}^f and C_{wb}^f are defined in Table 3.3.) Transfer of filaments from \mathbb{S}_{ftb} to

S_{wb} is due to a reaction set $\mathbb{R}_{\text{fb} \rightarrow \text{wb}}^f$. The number of filaments (in both filament and thin bundle forms) involved in reaction R_1 is $f_r^1 = 4$ for the reactants and $f_p^1 = 0$ for the reaction product; for reaction R_2 these are $f_r^2 = 1$ and $f_p^2 = 0$. The transfer from S_{wb} to S_{fb} is due to reaction R_3 ; it results in $f_r^1 = 0$ and $f_p^1 = 1$. Then

$$\frac{dC_{\text{wb}}^f}{dt} = \sum_{\substack{k=1 \\ \mathbb{R}_{\text{fb} \rightarrow \text{wb}}^f}}^2 \kappa_k (f_r^k - f_p^k) - \sum_{\substack{n=1 \\ \mathbb{R}_{\text{wb} \rightarrow \text{fb}}^f}}^1 \kappa_n (f_p^n - f_r^n). \quad (3.2)$$

where κ_k are the reaction rates for reactions R_k from the reaction sets $\mathbb{R}_{\text{fb} \rightarrow \text{wb}}^f$ and $\mathbb{R}_{\text{wb} \rightarrow \text{fb}}^f$ (see Table 3.3).

The definitions of C_{fb}^m and C_{wb}^f relate to the average structural features to the concentrations

$$\bar{L}_{\text{fb}}^m = \frac{C_{\text{fb}}^m}{[F] + 2[B_2] + 3[B_3] + C_{\text{wb}}^f}, \quad \bar{f}_{\text{wb}} = \frac{C_{\text{wb}}^f}{[B_w]}. \quad (3.3)$$

A smallest filament consists of four monomers (i.e., has the length $\bar{L}_{\text{fb}}^m = 4$). The latter is achieved instantaneously once $[F]$ becomes larger than zero. To consider all species, we define an average total length, \bar{L}_{tot}^m , which includes the first oligomers (Z_2 and Z_3),

$$\bar{L}_{\text{tot}}^m = \frac{2[Z_2] + 3[Z_3] + C_{\text{fb}}^m}{[Z_2] + [Z_3] + C_{\text{fb}}^m / \bar{L}_{\text{fb}}^m}. \quad (3.4)$$

It represents the average length of filaments in all forms (short oligomers, longer filaments, and bundles). Similarly, a smallest wide bundle consists of four filaments (i.e., has the width $\bar{f}_{\text{wb}} = 4$). This value is achieved instantaneously once $[B_w]$ becomes larger than zero. To consider all species, we define an average total number of filaments per bundle, \bar{f}_{tot} , which includes the

first oligomers (Z_2 and Z_3), longer filaments (F), and the first thin bundles (B_2 and B_3):

$$\bar{f}_{\text{tot}} = \frac{2[Z_2] + 3[Z_3] + C_{\text{fb}}^m}{2[Z_2] + 3[Z_3] + \bar{L}_{\text{fb}}^m([F] + [B_2] + [B_3] + [B_w])}. \quad (3.5)$$

Average characteristics \bar{L}_{fb}^m , \bar{L}_{tot}^m , \bar{f}_{wb} , and \bar{f}_{tot} play a crucial role in reducing the number of species and, therefore, the number of equations used to describe the protein assembly process. Section C.1 of the Appendix C contains ODEs corresponding to the reactions involved in the short- and long-term kinetics processes described above.

3.2.4 Model's calibration, validation, and computational cost

The system of 10 ODEs is parametrized and calibrated on the steady-state, low-concentration ($C_{\text{tot}} = 0.7 - 3.0 \mu\text{M}$) data from [CE5b] (see Section C.2.1 of the Appendix C). The resulting model is validated by comparing its fit-free predictions with the transient, low-concentration data and the steady-state high-concentration ($C_{\text{tot}} = 3.0 - 10.0 \mu\text{M}$) data, both from [CE5b] (Section C.3). This comparison demonstrates AFM's ability to accurately predict time evolution of nonactivated and activated monomers, the first critical concentration C_{cr}^1 at which polymerization begins, an average size of filaments and bundles, and the second critical concentration C_{cr}^2 at which bundles appear.

This predictive power of AFM is achieved at a fraction of the cost of its nearest competitor [RMBST16], which, in turn, is orders of magnitude faster than the models consisting of hundreds of ODEs (see Table 3.1). The computational efficiency of AFM, vis-à-vis [RMBST16] and other models of this kind, is magnified when it is used to simulate *in vivo* polymerization phenomena, which are characterized by high total concentrations. For $C_{\text{tot}} = 200 \mu\text{M}$, AFM is about 2 orders of magnitude faster than [RMBST16] (see Section C.4 for details).

3.3 FtsZ-Ring Assembly in *E. coli*

We use AFM to describe the Z-ring formation in the middle of an *E. coli* cell, within a torus adjacent to the cell membrane (CM) of volume V_{CM} . A typical cell has a volume $V_{\text{CELL}} = 1.374 \mu\text{m}^3$ and contains 5000 – 15000 FtsZ molecules, which translates into a range of FtsZ concentrations in the cytosol, $C_{\text{tot,C};0} = 6 - 18 \mu\text{M}$ [HdB97, RVM03, EAO10]; at the midcell, close to the membrane, the concentration is one to two orders of magnitude higher than that. Only a few polymerization models can handle such concentrations, and even the most computationally efficient among them, [RMBST16], (Table 3.1) would require hundreds of ODEs to handle all bundle sizes. AFM accomplishes the same with 11 ODEs, adding only one equation for the total concentration of FtsZ species (in all forms) attached to the membrane, $C_{\text{tot,CM}}^{\text{a}}$.

CM contributes to significant physical, chemical and structural differences between *in vitro* and *in vivo* polymerization. The augmented AFM accounts for some of these differences by incorporating the FtsZ species' attachment to and detachment from a CM. The parameters relevant to this process as well as other parameters describing cell geometry and bundling/dissociation kinetics come from the literature, so that predictions reported below are made without any fitting parameters. (A detailed formulation of the augmented AFM is provided in Section C.5 of the Appendix C.)

3.3.1 Timing of FtsZ ring formation

We define four stages of the ring formation in terms of their characteristic times: time it takes the FtsZ protofilaments in the cytoplasm to attach to the mid-CM and occupy all binding sites, t_{att} ; time to reach a constant average length of all filaments and bundles in the ring, $t_{\bar{L}}$; time to reach a constant concentration of monomers at the midcell region ($C_{\text{m,CM}}^{\text{d}}$), t_{mon} ; time to reach a constant average number of filaments per bundle in the ring, $t_{\bar{f}}$.

Let P denote an FtsZ ring property and P^∞ its value at $t \rightarrow \infty$; P stands for $C_{\text{tot,CM}}^{\text{a}}$ at time

t_{att} , \bar{L}_{tot}^m at time $t_{\bar{L}}$, $C_{\text{m,CM}}^d$ at time t_{mon} , and \bar{f}_{tot} at time $t_{\bar{f}}$. We compute these times by inverting the condition $|P(t) - P^\infty|/P^\infty < 0.01$. The results, reported in Table 3.4, reveal that changes in the total concentration $C_{\text{tot,C};0}$ appreciably affect t_{att} (early-time kinetics), while having an almost negligible impact on the other three characteristic times (long-time kinetics). These results identify the timing for three distinct stages of the ring formation (time $t = 0$ corresponds to the moment at which the Ter region is already located at the center of the cell).

Short-time kinetics.

Attachment of FtsZ protofilaments to the binding sites at the midcell takes 8–19 s. Although there are no data about the first seconds of *in vivo* polymerization to verify this prediction, the values that our model estimates are quite similar to the turnover half-times of FtsA (12–16.3 s) [GSM07] and ZipA mutants [(7.81–9.01 s, or $0.111\text{--}0.128\text{ s}^{-1}$) [AGFE04], which is the range of FtsZ turnover rate values, since according to [SMSE02] both FtsZ and ZipA may undergo similar dynamic exchanges. It seems reasonable to think that the emergence of the first FtsZ oligomers at the membrane will depend strongly on the time that FtsA and ZipA, both responsible of the attachment of FtsZ to the membrane, remain themselves attach to the membrane].

Intermediate kinetics.

Elongation of the species up to their average length takes 40 to 50 s. This is in line with the observations [ACL97, SM98] that ring assembly takes ~ 1 min. This suggests correspondence between the complete longitudinal elongation of the species and the ring formation.

Long-time kinetics.

Continuous exchange of monomers between the ring and the cytosol accompanies the formation of large FtsZ structures, at 3.5–4 min. This is consistent with observed time interval, ~ 4 min, between the ring's central positioning and the onset of septation [TRC⁺11]. These findings imply that dissociation of monomers after GTP hydrolysis plays a fundamental role in rearrangement of filaments and bundles, while formation of wide bundles contributes to

regulation of the dissociation in live cells, just as it does in *in vitro* studies [RMBST16]. Finally, the timing predictions obtained with our model and the *in vivo* version of [RMBST16] are compared in Section C.4 of the Appendix C.

3.3.2 FtsZ ring features

Our model predicts FtsZ concentrations in the ring to be around 40 times larger than cytosolic concentrations (Table 3.5). Variations in the total concentration $C_{\text{tot},C;0}$ do not materially affect the average length of the species at steady state, $\bar{L}_{\text{tot}}^{m,\infty} = 24$ to 25 monomers. That value corresponds to the experimentally observed characteristic length of 120 to 125 nm (since the monomer’s diameter is 5 nm) [CE5b], and falls within the range, 100 – 200 nm, found in other *in vitro* experiments [RSE01, DLS⁺08, PIN⁺09].

The predicted steady-state concentration of attached monomers, $C_{\text{tot},\text{CM}}^{\text{a},\infty} = 0.9\text{--}1.25 \mu\text{M}$, is insensitive to the total concentration $C_{\text{tot},C;0}$ (Table 3.5), and falls within the range of values of the first critical concentration in wild-type cells, $C_{\text{cr},\text{wt}}^1$ [CBRE5a]. We postulate this feature to be representative of polymer assembly regulation, both in *in vitro* and in *in vivo*.

The total cytosolic concentration $C_{\text{tot},C;0}$ does affect the average number of filaments per bundle at steady state, $\bar{f}_{\text{tot}}^\infty$ (Table 3.5). To investigate the prevalence of this form of FtsZ proteins at steady state, we consider the percentage of FtsZ proteins in the form of wide bundles, $\mathcal{R}_{\text{wb}}^\% \equiv 100\% \times C_{\text{wb},\text{CM}}^{f,\text{a}} / ([F] + 2[B_2] + 3[B_w] + C_{\text{wb},\text{CM}}^{f,\text{a}})$. Table 3.6 reveals that, at steady state, $\mathcal{R}_{\text{wb}}^\% = 85\% \text{--} 94\%$, depending on $C_{\text{tot},C;0}$, that is, wide bundles are the dominant species.

Once $C_{\text{tot},\text{CM}}^{\text{a}} = C_{\text{tot},\text{CM}}^{\text{a,max}}$ —that is, all FtsZ protofilaments are attached to the mid-CM—bundles form cross-linked structures (CLSs) along the ring. We refer to these structures as “clusters”, which in our model are formed at time $t = t_{\text{att}}$ and consist of bundles with an average number of filaments $\bar{f}_{\text{clu}} = \bar{f}_{\text{tot}}(t_{\text{att}})$. The predicted values $\bar{f}_{\text{clu}} = 6.1 \text{--} 9.5$ (Table 3.6) imply the average width of FtsZ-ZapA sheets of 12.2 – 19. This is consistent with the experimentally observed maximal number of FtsZ-ZapA filaments perfectly aligned at the mid-CM, $\bar{f}_{\text{clu},\text{ZapA}} < \bar{f}_{\text{wb},\text{ZapA}}^{\text{max}} = 20$ (see Section C.7 for details). The predicted minimal value, $\bar{f}_{\text{clu},\text{ZapA}} = 12.2$,

indicates that the two-layered sheets have to occupy at least half of the axial width of the ring. When that occurs, bundle interactions in the tangential direction, which induce bundles to push and lift each other, dominate their axial interactions.

For $t > t_{\text{att}}$, \bar{f}_{clu} remains constant as clusters interact only along the ring-forming CLSs. Since wide bundles contain most of the FtsZ at steady state, we define an average CLS width as $\bar{f}_{\text{CLS}} = \bar{f}_{\text{wb}}(t \rightarrow \infty)$. A number of clusters per CLS is $\mathcal{N}_{\text{clu}}^{\text{CLS}} \equiv \bar{f}_{\text{CLS}}/\bar{f}_{\text{clu}}$ and a number of CLSs is $\mathcal{N}_{\text{CLS}} \equiv [B_w]V_{\text{CM}}N_A/10^{21}$, where N_A is Avogadro's number. A number of clusters in the entire ring is $\mathcal{N}_{\text{clu}} = \mathcal{N}_{\text{clu}}^{\text{CLS}}\mathcal{N}_{\text{CLS}}$. Our model predicts $\mathcal{N}_{\text{clu}} = 9.0 - 18.9$ (Table 3.6), which conforms to the observed range of 10 – 20 clusters [CBPX16].

To sum up, our model predicts FtsZ rings that are mostly composed of 3 to 4 large structures, which are partially attached to the membrane and comprise 3 to 5 cross-linked clusters each. These clusters contain 6 to 10 filaments made up of 24 monomers each. The entire network also includes ZapA tetramers, which reinforce the lateral bonds of the clusters and the cross links between clusters, as observed *in vitro* [DPLW10] and *in vivo* [BCH⁺13]. Section C.4 includes a comparison between the ring feature predictions of our model and the *in vivo* version of [RMBST16].

3.3.3 ZapA deficiency

A recent experimental study [BCH⁺13] investigated *in vivo* polymerization in the absence of ZapA proteins. Our model predicts the resulting FtsZ concentrations to be only 10 times larger than their *in vitro* counterparts (Table 3.7). The average length (\bar{L}_{tot}^m) and concentration ($C_{\text{m,CM}}^{\text{d}}$) of detached monomers are insensitive to the total cytosolic concentration $C_{\text{tot,C};0}$. The predicted monomer concentrations $C_{\text{m,CM}}^{\text{d}}$ fall within the experimentally observed range of critical concentrations, $C_{\text{tot,CM}}^{\text{a},\infty} = 0.9 - 1.25 \mu\text{M}$.

The model also predicts the predominant presence of non-cross-linked and dispersed thin clusters along the entire cell, as observed [BCH⁺13]. In the absence of ZapA, $t_{\text{att}} = 20 - 30$ s is twice as long as that in the case with ZapA, while $t_{\bar{L}} = 40 - 50$ s remains about the same. The

times for bundling and dissociation of monomers after GTP hydrolysis, $t_{\text{mon}} \sim t_{\bar{f}} = 100 - 120$ s, are half of their counterparts in the presence of ZapA. Since FtsZ structures are more dispersed and interactions happen less frequently, the equilibrium is reached faster.

3.4 Conclusions

We developed a computationally efficient model of protein polymerization, which relies on concentrations and average features of different species. Orders of magnitude speed-up is achieved by replacing distributions of lengths and widths with their average counterparts and by introducing a hierarchical classification of species and reactions into sets. The resulting model consists of 10 or 11 ODEs, regardless of the total concentration of proteins. This is in contrast to previous polymerization models, in which the number of ODEs increases with the total concentrations, reaching into the thousands. Consequently, our model can be used to predict polymerization kinetics at high concentrations characteristic of *in vivo* processes and, especially, their compartmentalized representations.

We have used this model to study *in vitro* and *in vivo* FtsZ ring assembly in *E. coli*, a complex kinetics process with a large number of chemical reactions and species involved. The model's computational performance is not affected by the large concentrations of proteins located at the midcell, near the membrane. The model's prediction of key features of the ring formation, such as time to reach the steady state, total concentration of FtsZ species in the ring, total concentration of monomers, and average dimensions of filaments and bundles, are all in agreement with the experimentally observed values. Besides validating our model against the *in vivo* observations, this study fills some knowledge gaps by proposing a specific structure of the ring, describing the influence of the total concentration in short and long kinetics processes, determining some characteristic mechanisms in polymer assembly regulation, and providing insights about the role of ZapA proteins, a critical component for both positioning and stability of the ring.

The orders of magnitude computational speed-up provided by our model comes at a cost. An explicit representation of bundle size distribution [RMBST16] would improve a description of the ring's structure (e.g., heterogeneity of the bundle network). It would avoid overestimation of robustness at the sides of the ring where proteins like MinC promote debundling and depolymerization [DLS⁺08]. The influence of bundling on the dissociation of monomers upon GTP-hydrolysis process is also related to the size of the bundles, which is captured by the model [RMBST16]. Nevertheless, our results demonstrate that the models based on average characteristics yield predictions at least as accurate as those computed with their distribution-based models counterparts.

Chapter 3, in full, is a reprint of the material as it appears in Efficient models of polymerization applied to FtsZ ring assembly in *Escherichia coli* 2018. Ruiz-Martínez; Á., Bartol, T.M.; Sejnowski, T.J.; and Tartakovsky, D.M., PNAS, 2018. The dissertation/thesis author was the primary investigator and author of this paper.

Table 3.1. Comparison of the kinetic *in vitro* models in terms of their complexity, applicability range, and ability to predict the observed features of FtsZ assembly. M1, M2, and M3 designate the single-filament, two-filament-bundling, and multi-filament-bundling models introduced in [LDWS08], respectively; AFM denotes our Average Feature Model; C_{tot} is the total concentration of FtsZ monomers in all forms; low and high C_{tot} refers to its values of $2 \mu\text{M}$ and $10 \mu\text{M}$, respectively; $C_{\text{cr}}^1 = [Z^{\text{na}}]_{\text{ss}} + [Z]_{\text{ss}} \approx 0.7 \mu\text{M}$ is the critical concentration at which polymerization begins, and it is computed as the sum of the steady-state concentrations of nonactivated (GDP-bound) and activated (GTP-bound) FtsZ monomers, respectively; $C_{\text{cr}}^2 \approx 3.0 \mu\text{M}$ is the critical value of concentration C_{tot} at which bundling becomes pronounced. The superscripts $+$ and $-$ denote the overestimated and underestimated predictions, respectively.

	[CBRE5a, CE5b]	M1 in [LDWS08]	M2 in [LDWS08]	M3 in [LDWS08]	[SML08]	[RMBST16]	AFM
Number of ODEs	8	500	500	1254	300	17	10
Short time	Yes	Yes	Yes	Yes	Yes	Yes	Yes
Long time	No	Yes	Yes	Yes	Yes	Yes	Yes
Low C_{tot}	Yes	Yes	Yes	Yes	Yes	Yes	Yes
High C_{tot}	No	No	No	No	Yes	Yes	Yes
Filament length	No	Distribution	Distribution	Average ⁺	Distribution	Average	Average
Bundle width	No	No	2 filaments	Distribution ⁺	No	Distribution	Average
C_{cr}^1	Yes ⁻	Yes	Yes	Yes	Yes ⁻	Yes	Yes
C_{cr}^2	No	No	No	No	No	Yes	Yes

Table 3.2. Eighteen reactions comprising our FtsZ kinetics model. The subscripts $z^-/f^-/b^-$ (and $z^+/f^+/b^+$) designate a monomer/filament/bundle lost (or gained) by a species.

Reactions	Chemical equations
Reaction I	$Z^{\text{na}} \rightleftharpoons Z$
Reaction II	$2Z \rightleftharpoons Z_2$
Reactions III–V	$Z + Z_2 \rightleftharpoons Z_3, Z + Z_3 \rightarrow F, Z + F_{z^-} \rightleftharpoons F_{z^+}$
Reaction VI	$2F_{f^-} \rightleftharpoons F_{f^+}$
Reactions VII–XI	$2F \rightleftharpoons B_2, F + B_2 \rightleftharpoons B_3, F + B_3 \rightarrow B_w,$ $F + B_{w;f^-} \rightleftharpoons B_{w;f^+}, 2B_{w;b^-} \rightleftharpoons B_{w;b^+}$
Reactions XII and XIII	$F_{z^+} \rightarrow F_{z^-} + Z^{\text{na}}, F_{z^+,f^+} \rightarrow 2F_{z^-,f^-} + Z^{\text{na}}$
Reactions XIV–XVI with $i = 2, 3$	$B_{i;z^+,b^+} \rightarrow 2B_{i;z^-,b^-} + Z^{\text{na}},$ $B_{i;z^+} \rightarrow B_{i;z^-} + Z^{\text{na}}, B_{w;z^+} \rightarrow B_{w;z^-} + Z^{\text{na}}$
Reactions XVII and XVIII with $i = 2, 3$	$Z + B_{i;z^-} \rightarrow B_{i;z^+}, Z + B_{w;z^-} \rightarrow B_{w;z^+}$

Table 3.3. Species, reaction and concentration of species sets. FW and BW designate forward and backward reactions, respectively.

Types of sets	Notation
Species sets	$S_z = S_{\text{mp}} \cup S_{\text{fb}} = \{Z^{\text{na}}, Z, Z_2, Z_3, F, B_2, B_3, B_w; m, f, b; \bar{L}_{\text{fb}}^m, \bar{f}_{\text{wb}}\},$ $S_{\text{mp}} = \{Z^{\text{na}}, Z, Z_2, Z_3; m\},$ $S_{\text{fb}} = S_{\text{fb}}^{\text{f}} \cup S_{\text{wb}} = \{F, B_2, B_3, B_w; m, f, b; \bar{L}_{\text{fb}}^m, \bar{f}_{\text{wb}}\},$ $S_{\text{fb}}^{\text{f}} = \{F, B_2, B_3; m, f; \bar{L}_{\text{fb}}^m\},$ $S_{\text{wb}} = \{B_w; m, f, b; \bar{L}_{\text{fb}}^m, \bar{f}_{\text{wb}}\}$
Reaction sets	$\mathbb{R}_{\text{mp} \rightarrow \text{fb}}^m \equiv \{R_1 : \text{IV}; R_2 : \text{V}_{\text{FW}}; R_3 : \text{XVII}; R_4 : \text{XVIII}\},$ $\mathbb{R}_{\text{fb} \rightarrow \text{mp}}^m \equiv \{R_1 : \text{V}_{\text{BW}}; R_2 : \text{XII}; R_3 : \text{XIII}; R_4 : \text{XIV}; R_5 : \text{XV}; R_6 : \text{XVI}\},$ $\mathbb{R}_{\text{fb} \rightarrow \text{wb}}^f \equiv \{R_1 : \text{IX}; R_2 : \text{X}_{\text{FW}}\},$ $\mathbb{R}_{\text{wb} \rightarrow \text{fb}}^f \equiv \{R_1 : \text{X}_{\text{BW}}\}$
Concentrations of species sets	$C_{\text{tot}} = C_{\text{mp}}^m + C_{\text{fb}}^m,$ $C_{\text{mp}}^m = [Z^{\text{na}}] + [Z] + 2[Z_2] + 3[Z_3],$ $C_{\text{fb}}^m = \bar{L}_{\text{fb}}^m ([F] + 2[B_2] + 3[B_3] + \bar{f}_{\text{wb}}[B_w]),$ $C_{\text{fb}}^f = C_{\text{fb}}^f + C_{\text{wb}}^f,$ $C_{\text{fb}}^f = [F] + 2[B_2] + 3[B_3],$ $C_{\text{wb}}^f = \bar{f}_{\text{wb}}[B_w]$

Table 3.4. Timing of FtsZ ring formation for a characteristic range of *in vivo* FtsZ concentrations, $C_{\text{tot,C};0} = 6 - 18 \mu\text{M}$.

$C_{\text{tot,C};0} (\mu\text{M})$	$t_{\text{att}} (\text{s})$	$t_{\bar{L}} (\text{s})$	$t_{\text{mon}} (\text{s})$	$t_{\bar{f}} (\text{s})$
6.0	19	49	220	244
12.0	10	53	217	240
18.0	8	40	210	233

Table 3.5. FtsZ ring features for a characteristic range of *in vivo* FtsZ concentrations, $C_{\text{tot,C};0} = 6 - 18 \mu\text{M}$, at steady state ($t \rightarrow \infty$).

$C_{\text{tot,C};0} (\mu\text{M})$	$C_{\text{tot,CM}}^{\text{a},\infty} (\mu\text{M})$	$\bar{L}_{\text{tot}}^{m,\infty}$	$C_{\text{m,CM}}^{\text{d},\infty} (\mu\text{M})$	$\bar{f}_{\text{tot}}^{\infty}$
6.0	237	24.43	1.13	9.4
12.0	474	24.47	1.20	16.4
18.0	711	24.49	1.25	22.7

Table 3.6. Large FtsZ structures for a range of *in vivo* FtsZ concentrations, $C_{\text{tot,C};0} = 6 - 18 \mu\text{M}$. The structures are characterized by the percentage of FtsZ proteins in the wide-bundles form, $\mathcal{R}_{\text{wb}}^{\%}$; the average number of filaments per bundle in a cluster, \bar{f}_{clu} ; average width of CLSs, \bar{f}_{CLS} ; number of clusters per CLS, $\mathcal{N}_{\text{clu}}^{\text{CLS}}$; number of CLSs, \mathcal{N}_{CLS} ; and number of clusters, \mathcal{N}_{clu} .

$C_{\text{tot,C};0} (\mu\text{M})$	$\mathcal{R}_{\text{wb}}^{\%}$	\bar{f}_{clu}	\bar{f}_{CLS}	$\mathcal{N}_{\text{clu}}^{\text{CLS}}$	\mathcal{N}_{CLS}	\mathcal{N}_{clu}
6.0	85.1	6.1	19.6	3.2	2.8	9.0
12.0	91.6	7.6	35.0	4.6	3.4	15.6
18.0	94.0	9.5	48.5	5.1	3.7	18.9

Table 3.7. FtsZ species features for a characteristic range of *in vivo* FtsZ concentrations, $C_{\text{tot,C};0} = 6 - 18 \mu\text{M}$, in the absence of ZapA at steady state.

$C_{\text{tot,C};0} (\mu\text{M})$	$C_{\text{tot,CM}}^{\text{a,max}} (\mu\text{M})$	\bar{L}_{tot}^m	$C_{\text{m,CM}}^{\text{d}} (\mu\text{M})$	\bar{f}_{tot}
6.0	48	35.43	0.92	1.92
12.0	104	35.84	0.95	3.49
18.0	160	35.86	1.00	4.76

Chapter 4

Stochastic self-tuning hybrid algorithm for reaction-diffusion systems

4.1 Introduction

We present a self-tuning operator-splitting hybrid approach for the analysis of stochastic reaction-diffusion systems by studying a simple bimolecular reaction $A + B \rightarrow C$ and improving Choi et al., model [CMTS12], which in turn, improved the Gillespie Multi-Particle method (GMP) proposed previously by [DRKB07, RKK⁺06]. GMP method employed an operator-splitting scheme in which the Gillespie algorithm [Gil77] and cellular automata handled reactions and diffusion, respectively. Choi et al., model improved it by using Brownian dynamics for diffusion of particles, reducing the computational cost, and including an adaptive selection of the time-step depending on the regime of the system. Taking the latter as a reference, here we propose a new, more efficient, and versatile approach.

Firstly, although the accuracy and speed of Choi et al., model and our model highly depend on the size and shape of the mesh compartments, only our model redefines such features every time-step. This is remarkably important because the level of accuracy does not necessarily increase as the compartment size decreases; the amount of particles that potentially react and their spatial distribution are essential factors to redefine the compartment mesh. Secondly, whereas Choi et al., model defines a time-step proportional to the diffusion time, our algorithm chooses a time-step proportional to the maximum reaction time. Since the reaction time is

proportional to the volume of the compartment, the time-step also changes proportionally to its size, what makes our model both spatially and temporally adaptive. Finally, unlike its counterpart, our model does not need to predefine parameters to determine if reaction or diffusion effects are predominant or multiplicative factors to estimate a proper time-step.

In summary, we propose a hybrid micro-mesoscopic algorithm for the study of biological systems that efficiently handles from diffusion- to reaction-controlled scenarios minimizing the computational cost. Our presented results for an elemental bimolecular reaction in a system with simple geometry demonstrate the importance of self-regulation in reaction-diffusion algorithms to avoid the propagation of substantial errors in more complex systems. Hence, our novel approach can be potentially developed for the study of multi-reaction systems ensuring both accuracy and efficiency.

4.2 Description of the model

Similarly to Choi et al., model [CMTS12], we use an operator-splitting method to study reaction-diffusion systems. Mainly, their approach consists of two steps: 1) diffusion of the species a specific time-step using Brownian dynamics, i.e., diffusion at a particle level, and 2) reactions via the Gillespie algorithm [Gil77] in compartments where molecules ended up after such time-step, i.e., reaction at a compartment-based level with propensities defined in terms of the number of molecules in the compartments after diffusion. Our model also consists of two steps, but it is slightly different: 1) diffusion of the species a specific time-step using Brownian dynamics in order to estimate particle locations with no reaction effects, and 2) diffusion using Brownian dynamics during a specific time calculated via the Gillespie algorithm with propensities defined in terms of the particle locations before and after diffusion. Thus, the first step (only diffusion) is an estimate that helps to make more accurate calculations in the second step (diffusion until reaction happens).

As a general description, our stochastic operator-splitting algorithm can be outlined as

follows:

- Lattice: The space is discretized into a lattice of compartments depending on the amount of particles and their spatial distribution.
- Time: Maximum and minimum reaction times and diffusion time are calculated. The optimal time-step is calculated; it is proportional to the maximum reaction time, therefore, proportional to the compartment volume.
- System state: The ratio minimum reaction time/diffusion time defines whether the system is at diffusion- or reaction-controlled state.
- Only diffusion process: Diffusion of species between compartments is modeled via Brownian dynamics in order to estimate the concentration of species in each compartment after the optimal time-step previously estimated.
- Combined diffusion-reaction process: Reactions within some compartments are simulated via the Gillespie algorithm. Propensities are defined in terms of the concentrations before and after the time-step from the only-diffusion scenario. The time estimated by the Gillespie algorithm for every particle is assumed to be the time such particle is diffusing until it reacts.
- Time is increased by the time-step size and the above steps are repeated until the final desired time.

Now, we can observe that three main properties define our model: the appropriate choice of the compartment size, the time-step proportional to the maximum reaction time and the modified propensities for the Gillespie algorithm. The combination of such characteristics make up a novel approach that stands out for its computational efficiency even in limit cases with very low diffusion effects or, on the contrary, when the process is mainly controlled by reaction. This work focuses on the study of a simple bimolecular reaction $A + B \rightarrow C$, so henceforth mathematical expressions are defined in terms of the reactives A and B and the product C .

4.2.1 Compartment size choice

Choi et al., asserted that the accuracy of their model increased as the size of the compartment decreased. Nevertheless, our present work proves that it is not necessarily true, the right choice for the compartment size is critical to make accurate predictions. Increasing or decreasing such size can lead to wrong calculations when we use their model. In extreme cases (such as systems highly controlled by diffusion), the shape of the compartment is also a relevant factor to take into account.

Here, we suggest to choose different compartment sizes every time-step based on the amount of particles present in the system and their spatial distribution. Assuming all compartments are similar, we observe that an initial good estimate for the volume of a compartment i in a time-step j in a 3D space is $V_{ij} = V_{syst} / \min\{n_j^A, n_j^B\}$, where V_{syst} is the volume of the system and n_j^A and n_j^B are the total amount of particles of species A and B , respectively, that exist during a particular time-step j in the whole domain. For the cases presented in this work, we define a regular compartment in 3D cartesian coordinates such that $V_{ij} = V_j = \Delta x_j \Delta y_j \Delta z_j$, where Δs_j is the length of the compartment in a particular direction $s = x, y, z$. Once an initial size for the compartment is estimated and a mesh is created, we calculate the product of the number of particles A and B that can react in each compartment i in a time-step j according to the k bimolecular reaction $A + B \rightarrow C$ with the expression $P_{ijk} = (n_{ij}^A n_{ij}^B)_k$. The criteria to decide when the compartment size is good enough to make accurate predictions is to make it small enough so the number of compartments where $P_{ijk} = 1$ is larger than the number of compartments where $P_{ijk} > 1$. Therefore, we establish the condition

$$S_{jk}^1 / (S_{jk}^1 + S_{jk}^2) \geq \alpha, \quad (4.1)$$

where

$$S_{jk}^1 \equiv \{\text{total sum of compartments where } P_{ijk} = 1\}, \quad (4.2)$$

$$S_{jk}^2 \equiv \{\text{total sum of compartments where } P_{ijk} > 1\}, \quad (4.3)$$

and α is a number in the interval $[0.5, 1]$ that sets the limits for a proper compartment size. Our study shows that choosing the minimum value, 0.5, we get a good balance between accuracy and computational efficiency.

4.2.2 Time-step choice

Choi et al., model defined a time-step proportional to the diffusion time. They also defined a macroscopic time constant, $T_{R_{ij}} = 1/a_{sum}^{ij}$, where a_{sum}^{ij} is the sum of all propensities at the compartment i at the time-step j . Then, they took the minimum value of the macroscopic time constants over all compartments, $T_{R_j}^{min}$, and defined a reaction time, $\tau_{R_j} = T_{R_j}^{min} \ln(1/r)$, where r is a random number distributed uniformly on the unit interval $[0, 1]$.

Here, we propose a different approach by introducing a time-step proportional to the reaction time. Also, we define a maximum reaction time, $T_{R_j}^{max}$, that corresponds to the situation in which the minimum amount of particles react in a compartment, i.e., $T_{R_j}^{max} = 1/a_{min}^{jk}$, where a_{min}^{jk} is the propensity at the time-step j when there is a pair of molecules A and B that react according to the reaction k . Thus, analogously to Choi et al., model [CMTS12], we redefine the reaction time as $\tau_{R_j} = T_{R_j}^{max} \ln(1/r)$. As they demonstrated, the cumulative probability of $\ln(1/r) \leq 1$ is 0.63, i.e., in our case, the probability of $\tau_{R_j} \leq T_{R_j}^{max}$ is 63%. If the reaction time is smaller than the maximum reaction time in about 63% of the cases, then we can define an average value for the time-step such that,

$$\Delta t_j = 0.63 \times T_{R_j}^{max} = 0.63 \times \frac{1}{a_{min}^{jk}}. \quad (4.4)$$

Defining a constant reaction rate k_r for the k bimolecular reaction $A + B \rightarrow C$, the minimum propensity takes the value $a_{min}^{jk} = k_r/V_j$ and, consequently, the time-step changes as long as the volume of the compartments change as follows

$$\Delta t_j = 0.63 \times \frac{V_j}{k_r}. \quad (4.5)$$

Choi et al., algorithm calculated diffusion times according to the expression $\tau_D = (\Delta x)^2 / (2d \times \max\{D_A, D_B\})$, where D_A and D_B are the diffusion coefficients of particles A and B, respectively, and d is a dimensionality factor (1, 2, and 3 for 1D, 2D, and 3D systems, respectively). Besides the fact that our diffusion time changes every time-step, we also introduce a modification in order to consider the effects of non-regular shaped compartments in the calculations such that

$$\tau_{D_j} = \frac{(\max\{\Delta s_{jj}\})^2}{2d \times \max\{D_A, D_B\}}, \quad \text{where } s = x, y, z. \quad (4.6)$$

Now, in order to determine the regime of the system every time-step j , we use the minimum macroscopic time proposed by Choi et al., $T_{R_j}^{min}$, and define the ratio $R_j = T_{R_j}^{min} / \tau_{D_j}$. We set $R_j < 10$ for systems controlled by diffusion and $R_j \geq 10$ for systems where diffusion is predominant.

4.2.3 Modified Gillespie algorithm

Once the proper compartment size, the time-step, and the system regime are defined, we count the number of particles per compartment before any diffusion or reaction process happens. Then, we diffuse the species a time-step Δt_j using Brownian dynamics and count the molecules at each compartment after that. With such information and knowing the volume of the compartments, our algorithm computes propensity functions along particle trajectories. In order to study when and where a particle l reacts during time step Δt_j , we take the expression of a continuous random value Δt_{jkl} , equivalent to the one defined by Gillespie algorithm [Gil77],

such that

$$\Delta t_{jkl} = \frac{1}{a^{jkl}} \ln \left(\frac{1}{r} \right) \quad \text{or} \quad r = e^{-a^{jkl} \Delta t_{jkl}}, \quad (4.7)$$

where a^{jkl} is the propensity at the time-step j that depends on the system state and the concentrations of the species involved in the reaction k at the locations of the particle l before and after Δt_j and r is a random number distributed uniformly on the unit interval $[0,1]$. For the k bimolecular reaction $A + B \rightarrow C$ that we are studying, we define the propensity a^{jkl} as

$$a^{jkl} = k_r [\chi c_{ij}^A + (1 - \chi) c_{i'j'}^A] [\chi c_{ij}^B + (1 - \chi) c_{i'j'}^B], \quad (4.8)$$

where the subscripts i and i' refer to the compartments where the molecule l is located before and after diffusing a time-step Δt_j , j and j' denote the times before and after the time-step Δt_j advances, c_{ij}^A , c_{ij}^B are the concentrations of molecules A and B in compartment i and time t , $c_{i'j'}^A$, $c_{i'j'}^B$ are the concentrations of molecules A and B in compartment i' and time $t + \Delta t_j$, and χ is a factor that quantifies the probability of reaction of the molecule l at the initial and final locations. The parameter χ takes the value 0.5 for reaction-controlled systems and 0.37 for diffusion-controlled systems. For the former, the value 0.5 is chosen because diffusion dominates and we can assume that the reaction of other particles do not have influence in the probability of this particle to react. The propensity a^{jkl} is, therefore, defined in terms of the average of the initial and final concentrations. For the latter, reaction dominates and, according to our definition of the time-step Δt_j (4.4), it is reasonable to assume that 63% of the particles at the initial location i react fast and that only 37% of them have influence in the particle l . Consequently, our balance gives us an estimate of 63% of molecules in compartment i' that have noticeable influence in the particle l .

Another factor that we need to consider is the fact that, as reaction effects become dominant, the probability of other molecules reacting along the trajectory of the particle l

increases. The bigger the value of Δt_{jkl} , the less accurate the estimate. Consequently, for diffusion-controlled systems, instead of expression (4.4), we use a Taylor approximation of first order ($\Delta t_{jkl} \rightarrow 0$) such that

$$\Delta t_{jkl} \sim \frac{r}{a_{jkl}} \quad \text{or} \quad r \sim a_{jkl} \Delta t_{jkl}. \quad (4.9)$$

In summary, we can define the following expressions to determine the value of Δt_{jkl} for every particle l ,

$$\Delta t_{jkl} = \frac{\ln(1/r)}{0.25k_r[c_{ij}^A + c_{i'j'}^A][c_{ij}^B + c_{i'j'}^B]} \quad (4.10)$$

if the system is reaction-controlled ($R_j \geq 10$), or

$$\Delta t_{jkl} = \frac{r}{k_r[0.37c_{ij}^A + 0.63c_{i'j'}^A][0.37c_{ij}^B + 0.63c_{i'j'}^B]} \quad (4.11)$$

if the system is diffusion-controlled ($R_j < 10$).

4.3 Algorithm

A detailed algorithm for the numerical implementation of the above steps of our stochastic operator-splitting method for a general bimolecular reaction $A + B \rightarrow C$ is provided below.

- (1) Initialize $t = 0$.
- (2) While $t \leq t_{final}$
 - (I) Set $\Delta t_j = 0$ and define initial compartment size.
 - (II) While $\Delta t_j = 0$
 - (A) For each compartment i
 - (i) calculate n_{ij}^A and n_{ij}^B ,

- (ii) calculate P_{ijk} ,
- end
- (B) Count compartments with $P_{ijk} = 1$ to obtain S_{jk}^1 .
- (C) Count compartments with $P_{ijk} > 1$ to obtain S_{jk}^2 .
- (D) If $S_{jk}^1 / (S_{jk}^1 + S_{jk}^2) < \alpha$,
 - reduce compartment size,
 - else,
 - $\Delta t_j = 0.63 \times V_j / k_r$,
 - end
- end
- (III) Calculate concentration in all compartments before advancing species.
- (IV) Use Brownian dynamics to advance species with time-step Δt_j and estimate their concentrations with no reaction effects.
- (V) Assign an initial time $t_i = t$ to all compartments i and reset $t_{old,i} = t_i$.
- (VI) Calculate $T_{R_j}^{min}$, τ_{D_j} and the ratio R_j .
- (VII) Set $A_i = 0$ and $B_i = 0$ for all cells.
- (VIII) For each particle l (randomly selected from all the existent particles of species A or B; let's suppose a particle of A is selected)
 - (A) If the system is reaction-controlled ($R_j \geq 10$),
 - use expression (4.10) to determine Δt_{jkl} ,
 - if the system is diffusion-controlled ($R_j < 10$),
 - use expression (4.11) to determine Δt_{jkl} ,
 - end
 - (B) If $\Delta t_{jkl} < \Delta t_j$,

use Brownian dynamics to advance particle l with time-step Δt_{jkl} ,

else,

assume that the particle is at the location previously calculated in step (IV)

(in other words, $\Delta t_{jkl} = \Delta t_j$),

end

(C) Determine in which cell i^* the particle l is located after Δt_{jkl} .

(D) If $t_{i^*} \leq \Delta t_j + t_{old,i^*}$,

(i) $A_{i^*} = A_{i^*} + 1$,

(ii) define the reaction time associated to the particle l at the cell i^* as $t_{i^*l}^A = \Delta t_{jkl}$,

(iii) if $A_{i^*} > 0$ and $B_{i^*} > 0$,

(a) a reaction is fired and $t^* = \min\{t_{i^*l}^A, t_{i^*l'}^B\}$ determines the reaction time of a pair of particles l and l' from A and B species, respectively, at cell i^* ,

(b) update t_{i^*} such that $t_{i^*} = t^* + t_{i^*}$,

(c) remove molecule l of species A and molecule l' of species B and generate a molecule of C in a location halfway between the positions where such pair of molecules were located,

(d) $A_{i^*} = A_{i^*} - 1$ and $B_{i^*} = B_{i^*} - 1$,

(e) if $n_{i^*j'}^A > 0$ and $n_{i^*j'}^B > 0$,

$n_{i^*j'}^A = n_{i^*j'}^A - 1$ and $n_{i^*j'}^B = n_{i^*j'}^B - 1$ and, consequently, update concentrations $c_{i^*j'}^A$ and $c_{i^*j'}^B$,

else,

do not update $n_{i^*j'}^A$, $n_{i^*j'}^B$, $c_{i^*j'}^A$, and $c_{i^*j'}^B$,

end

else,

do not update, no reaction is fired,

```

        end
    else,
        do not update, no reaction is fired,
    end
end
end
(3) Set  $t = t + \Delta t_j$ .
end

```

4.4 Results and discussion

4.4.1 Performance analysis

We compare our model with Choi et al., approach to show that the former reaches a higher balance of accuracy, speed and versatility. We use the Douglas Gunn alternating-direction-implicit numerical method (ADI) to calculate a deterministic solution that we treat as a yardstick for validation.

Assuming a cubic domain of volume $V = 10^{-18} \text{ m}^3$, i.e., a domain \mathcal{D} defined as $\mathcal{D} \equiv \{0 \leq x \leq L, 0 \leq y \leq L, 0 \leq z \leq L\}$, with $L = V^{1/3}$, we randomly position an initial number of molecules of species A, N_{A_0} , and species B, N_{B_0} , in the half-domain region $\mathcal{D}' \equiv \{0 \leq x \leq L/2, 0 \leq y \leq L, 0 \leq z \leq L\}$. Such molecules diffuse with the same diffusion coefficient D and bounce on the boundaries so they never leave the domain. They also react according to the chemical reaction $A + B \rightarrow C$ with the reaction rate k_r . Molecules of species C are also assumed to diffuse with the same diffusion coefficient D .

The first comparison between Choi et al., model and our approach aims to show the importance of choosing the appropriate compartment size to get accurate results. We study the variation of the concentration of the species C in time in the region \mathcal{D}' in three different scenarios: dominant diffusion effects (Figure 4.1), similar diffusion and reaction effects (Figure 4.2), and

dominant reaction effects (Figure 4.3). The initial number of molecules of both species A and B is 600, i.e., $N_{A_0} = N_{B_0} = 600$. Since the number of molecules of species A in the system will be always the same than species B, we define the initial size compartment estimate for any time-step j as follows

$$V_j = V_{syst} / \min\{n_j^A, n_j^B\} = L^3 / n_j^A. \quad (4.12)$$

The volume of a regular compartment can be expressed as

$$V_j = \Delta x_j \Delta y_j \Delta z_j = (\Delta x_j)^3. \quad (4.13)$$

Thus, from expressions (4.12) and (4.13), we can estimate a parameter κ_j as follows

$$\Delta x_j = L / (n_j^A)^{1/3} \rightarrow \kappa_j = L / \Delta x_j = (n_j^A)^{1/3} \rightarrow \kappa_j \approx \lfloor (n_j^A)^{1/3} \rfloor, \quad (4.14)$$

that we can modify before moving forward in time to meet the condition (4.1) so the next time-step can be defined properly. By observing the distribution of the molecules at $t = 0$, we find reasonable to assume that κ_j is never smaller than 2 to ensure accurate results. Also, in this particular study, we have imposed κ_j to be an even number that increases by 2; thus, $\Delta x_j = L / \kappa_j$ is continually modified in step (II) of our algorithm until the condition (4.1) is met. Once the most optimal compartment volume, V_j , is estimated, the most optimal time-step, Δt_j , gets defined.

Now, we define the relative error as the ratio of the integrated absolute difference between the deterministic solution and one of the methods to the integrated absolute value of the deterministic solution over the time-course,

$$\text{Relative error} = \frac{|\text{Deterministic solution area} - \text{Model estimated area}|}{|\text{Deterministic solution area}|}. \quad (4.15)$$

Table 4.1 shows the values of the areas over 3 seconds of the deterministic solution and the

solutions estimated by Choi et al., model and our model for three different cases: dominant diffusion effects ($D_1 = D = 10^{-12} \text{ m}^2/\text{s}$, $k_{r1} = 3 \times 10^3 \text{ mM}^{-1}\text{s}^{-1}$), similar diffusion and reaction effects ($D_2 = D = 10^{-13} \text{ m}^2/\text{s}$, $k_{r1} = 3 \times 10^3 \text{ mM}^{-1}\text{s}^{-1}$), and dominant reaction effects ($D_2 = D = 10^{-13} \text{ m}^2/\text{s}$, $k_{r2} = 3 \times 10^4 \text{ mM}^{-1}\text{s}^{-1}$). Similarly, relative errors for the studied cases are presented.

From the obtained results, we remark some observations:

- Choi et al., model requires to predefine parameters (k_1 and k'_1 , according to their notation) to determine if reaction or diffusion effects are predominant as well as multiplicative factors (k_2 and k'_2) to estimate a proper time-step [CMTS12]. On the contrary, the accuracy of our model does not depend on values estimated by previous analysis but on the inherent characteristics of the system such as the number of molecules, their spatial distribution, diffusion coefficients or reaction rates.
- Our results show that Choi et al., model cannot ensure accurate results even defining parameters, multiplicative factors and system properties for the cases presented in this work similar to the ones proposed in their study. Their model only becomes accurate if the appropriate compartment size is heuristically estimated. By contrast, our model self-tunes every time-step to guarantee accuracy along the entire process.
- Regardless of the chosen compartment size, just by looking at Figures 4.1-4.3 and Table 4.1, we can conclude that the higher the reaction effects, the bigger the error of Choi et al., model in comparison to ours.

Now, we select $\Delta x = \Delta y = \Delta z = L/6$ as a compartment size that maximizes Choi et al., model efficiency in order to compare it to ours as fairly as possible. Table 4.2 and Figure 4.4 present the relative errors and the computational times of both models with respect to the diffusion coefficient for cases with reaction rate constant $k_r = 3 \times 10^3 \text{ mM}^{-1}\text{s}^{-1}$ and an initial number of molecules for both species A and B of 600.

Both models define two elemental states: reaction-controlled (RC) and diffusion-controlled (DC), although Choi et al., model defines a third state in between called mixed-zone (MZ). Table 4.2 also shows the regimes that define the state of the system until it reaches the steady-state time, t_{ss} .

The results demonstrate that our model is always more accurate than Choi et al., model. The highest differences in accuracy are reached in the diffusion-controlled regime, where the relative error of our model is one order of magnitude smaller. Interestingly, the computational time required by our model does not depend on the regime of the system. Choi et al., model calculations, however, need longer times as the diffusion effects increase, reaching values 4-5-fold the computational time required by our model. Although for diffusion-controlled scenarios Choi et al., model is 2-3 times faster, its accuracy gets reduced by one order of magnitude.

4.4.2 Limit case scenarios

To see how our model performs in more extreme cases, we propose two scenarios with high variations of the concentrations of the species in space and/or time. Figure 4.5 shows a very fast variation of the concentration of the product species C; in less than 0.002 seconds almost all molecules of A and B react in the half-domain \mathcal{D}' before diffusion happens. It is, therefore, an almost completely diffusion-controlled scenario ($D = 10^{-13} \text{ m}^2/\text{s}$, $k_r = 3 \times 10^6 \text{ mM}^{-1}\text{s}^{-1}$) with an average ratio $\bar{R}_j \sim 10^{-2}$ for the first time-steps, i.e., three orders of magnitude smaller than the transition regime value $R_j = 10$.

Figure 4.5 also shows that, in scenarios with very low diffusion, Choi et al., model misses high variations of concentration due to chemical reactions. Although, we set the most optimal compartment size, the accuracy of the model in the first time steps of the process is quite low. Besides that, Choi et al., model does not provide with information about events that happen during a specific time-step, such as location and time of particle reactions.

Our model selects smaller time steps and makes better predictions. Despite that, it is noticeable that our model loses accuracy when reaction effects dominate. In order to improve

our model, we propose an additional approach. We suggest that, for low diffusion scenarios, it is critical to determine in which spatial directions the concentration of molecules is changing more drastically, i.e., we need to estimate or calculate the concentration gradient over time and modify the compartment shape according to it. In the particular case that we are presenting here, we can expect that the concentration gradient is going to be higher in the x -direction during the entire process. Figure 4.5 shows that, if we define compartments with variable Δx but constant step sizes in the other directions, $\Delta y = \Delta z = L$, our model increases its sensitivity to detect variations in the concentration due to low diffusion improving the level of accuracy remarkably. Although, this adjustment implies high computational costs, we can counteract such drawback by making (4.1) less restrictive. Setting the parameter α to a smaller value reduces the computational cost while keeping a high level of accuracy: $\alpha = 0.1$ makes our non-regular-mesh model only three times slower than our regular-mesh model, $\alpha = 0.01$ makes it only twice slower, and even for $\alpha = 0.001$ the accuracy remains high with a negligible increment in the computational cost.

Figure 4.6 depicts a fast variation of the concentration of the reactive species A; in less than 0.002 seconds almost half of the molecules of A diffuse from the half-domain \mathcal{D}' before reaction happens. It is, therefore, an almost completely reaction-controlled scenario ($D = 10^{-10} \text{ m}^2/\text{s}$, $k_r = 3 \times 10^3 \text{ mM}^{-1}\text{s}^{-1}$) with an average ratio $\bar{R}_j \sim 10^4$ for the first time-steps, i.e., three orders of magnitude larger than the transition regime value, $R_j = 10$.

Choi et al., model makes very accurate predictions for this limit case when the appropriate compartment size is estimated, as Figure 4.6 shows. Nevertheless, such accuracy comes at a very high computational cost. Their model defines time-steps proportional to the diffusion time, therefore, the larger the diffusion coefficient, the shorter the time-steps.

In Figure 4.6 we can see that our model does not need short time-steps to guarantee high accuracy as diffusion effects increase. Long time-steps still ensure high levels of accuracy and computational speeds. Also, in contrast to Choi et al., model, step (a) of our algorithm makes possible to know what happens during the first time-step. It determines when and where reactions are fired; in other words, $t^* = \min\{t_{i^*l}^A, t_{i^*l'}^B\}$ determines the reaction time of any pair of

particles l and l' from A and B species, respectively, at cell i^* , during any time-step Δt_j .

4.4.3 Effect of number of molecules

In this section we study the influence of the number of particles present in the system in the accuracy and computational speed of our model. Figures D.1–D.4 of Appendix D.1 show the evolution in time of the concentration of the species C in the region \mathcal{D}' for different initial number of molecules; we have set the diffusion coefficient equal to $D = 10^{-13} \text{ m}^2/\text{s}$ and the reaction rate constant equal to $k_r = 3 \times 10^4 \text{ mM}^{-1}\text{s}^{-1}$. As expected, as the number of particles increase, more interactions happen and the system becomes more controlled by diffusion. We have chosen sizes for the compartments in Choi et al., model that maximize its efficiency. The more particles react, the smaller the optimal compartment.

We now define a relative peak concentration, N_r , that indicates the amount of molecules of C present in the subdomain \mathcal{D}' when it reaches its maximum value divided by the initial number of molecules of A or B,

$$N_r = \frac{|\text{Maximum number of molecules of C present in } \mathcal{D}'|}{|\text{Initial number of molecules of A or B}|}. \quad (4.16)$$

Also, we define the parameter ϕ_r to determine the relative time gap between the deterministic solution and the model estimates,

$$\phi_r = \frac{|t_{ds} - t_{md}|}{t_{ds}}, \quad (4.17)$$

where t_{ds} is the required time to reach the maximum concentration predicted by the deterministic solution and t_{md} is the required time to reach the maximum concentration predicted by one of the models. Thus, Table 4.3 and Figure 4.7 show that our model predicts more accurate results than Choi et al., model for any initial concentration, although both get less accurate as the number of molecules increase.

Table 4.4 and Figure 4.7 show the computational times required by both models to reach the steady-state. The computational time required by Choi et al., model gets longer than the one

required by ours as the number of molecules in the system increases.

4.5 Conclusions

Based on previous works [CMTS12, DRKB07, RKK⁺06], we have developed a hybrid multiscale model that improves its counterparts by finding a better balance between accuracy and computational speed, by making it more versatile, and by increasing its range of applicability. In terms of accuracy and computational cost, it stands out remarkably in scenarios with predominant diffusion effects and high number of particles. In cases with predominant reaction effects and high number of particles, it also keeps a solid and optimal balance.

Combining our model with particle-based methods for reactions will undoubtedly improve estimates of steep variations of concentrations. It still misses the production of a small percentage of particles in extreme diffusion-controlled scenarios that particle-based methods would handle efficiently. Similarly, PDE-based methods would accelerate calculations for scenarios with large number of particles. Since our model is focused on a basic bimolecular reaction, $A + B \rightarrow C$, from a micro-mesoscopic scale, it would be ideal as a centerpiece in a future particle-based-PDE model where species A and B could be defined as deterministic and stochastic, respectively.

Moreover, its self-tuning nature and the fact that it covers a wide range of regimes make it appropriate for more complex scenarios with non-regular geometries and additional reactions. By guaranteeing a decent level of efficiency for a simple system, we ensure a smaller propagation of errors than its direct competitor [CMTS12].

Chapter 4, in part is currently being prepared for submission for publication of the material. Ruiz-Martínez; Á., Bartol, T.M.; Sejnowski, T.J.; and Tartakovsky, D.M., The dissertation/thesis author was the primary investigator and author of this material.

Table 4.1. Values of the areas over the 3 seconds time-course of the deterministic solution and the values of the areas and the correspondent relative errors of Choi et al., model and ours based on average of 1000 iterations. DS and CM refer to deterministic solution and Choi et al., model, respectively. s denotes the coordinates x , y , and z .

	DS		CM, $\Delta s = L/4$		CM, $\Delta s = L/8$		CM, $\Delta s = L/16$		Our model	
	Area	Relative error	Area	Relative error	Area	Relative error	Area	Relative error	Area	Relative error
D_1, k_{r1}	684.66	701.00	2.4×10^{-2}	685.49	1.2×10^{-3}	673.67	1.6×10^{-2}	684.77	1.6×10^{-4}	
D_2, k_{r1}	869.04	855.31	1.6×10^{-2}	861.64	8.5×10^{-3}	836.17	3.8×10^{-2}	872.27	3.7×10^{-3}	
D_2, k_{r2}	1079.60	1006.22	6.8×10^{-2}	1037.63	3.9×10^{-2}	1016.29	5.9×10^{-2}	1083.20	3.3×10^{-3}	

Table 4.2. Values of the relative errors of Choi et al., model and our model based on average of 100 iterations and computational times based on average of 10 iterations.

	Choi et al., model			Our model		
	Relative error	Computational time (s)	Regime	Relative error	Computational time (s)	Regime
$D = 10^{-11} m^2/s, t_{ss} = 15 s$	6.6×10^{-4}	2.24	RC	2.4×10^{-4}	0.49	RC
$D = 10^{-12} m^2/s, t_{ss} = 15 s$	1.1×10^{-3}	0.48	MZ-RC	3.1×10^{-4}	0.49	RC
$D = 10^{-13} m^2/s, t_{ss} = 15 s$	3.0×10^{-3}	0.28	DC-MZ-RC	1.8×10^{-4}	0.49	DC-RC
$D = 10^{-14} m^2/s, t_{ss} = 30 s$	3.8×10^{-2}	0.21	DC	2.5×10^{-3}	0.50	DC

Table 4.3. Values of relative peak concentration, N_r , and the relative time gap, ϕ_r , correspondent to Choi et al., model and our model for different initial concentrations of molecules, N_{A_0} and N_{B_0} , based on average of 1000 iterations.

N_{A_0} and N_{B_0}	Det. sol	Choi et al., model		Our model	
	N_r	N_r	ϕ_r	N_r	ϕ_r
60	0.53	0.48	0.31	0.55	0
600	0.77	0.70	0.53	0.76	0
6000	0.89	0.81	1.25	0.88	0.13
60000	0.95	0.86	2.75	0.93	0.44

Table 4.4. Values of the computational time until steady-state is reached correspondent to Choi et al., model and our model for different initial concentrations of molecules, N_{A_0} and N_{B_0} , based on average of 10 iterations.

N_{A_0} and N_{B_0}	Computational time (s)	
	Choi et al., model	Our model
60	0.18	0.37
600	0.29	0.52
6000	1.53	1.37
60000	30.48	9.63

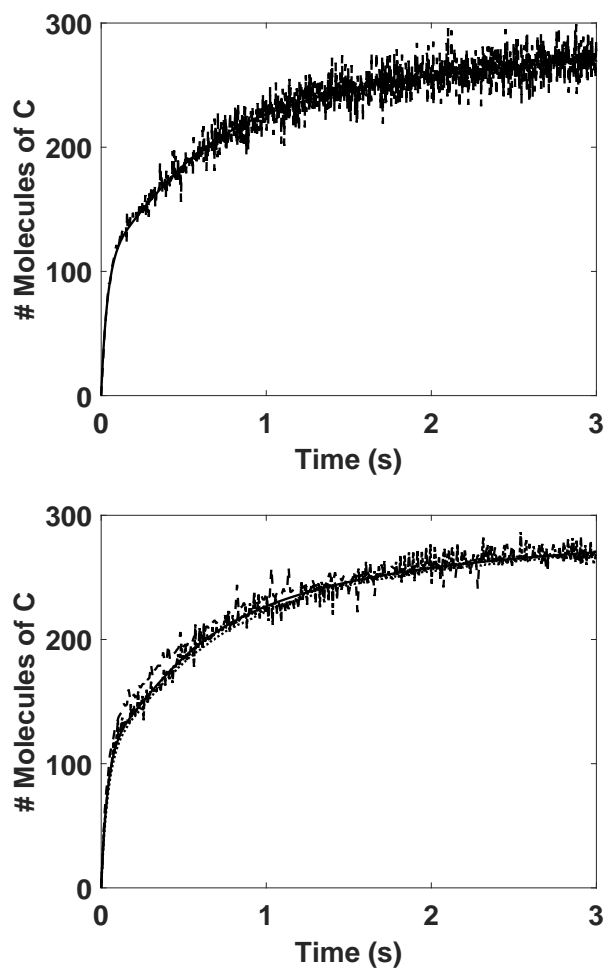


Figure 4.1. Temporal evolution of the concentration of the species C in the region \mathcal{D}' for a case with dominant diffusion effects ($D_1 = 10^{-12} \text{ m}^2/\text{s}$, $k_{r1} = 3 \times 10^3 \text{ mM}^{-1}\text{s}^{-1}$). Solid line is the deterministic solution in both graphics. Top: Dashed line is the solution obtained by our model based on average of 1000 iterations. Bottom: Dashed, dash-dot, and dotted lines are the solutions obtained by Choi et al., model setting $\Delta x = \Delta y = \Delta z = L/4, L/8,$ and $L/16,$ respectively. All results are based on average of 1000 iterations.

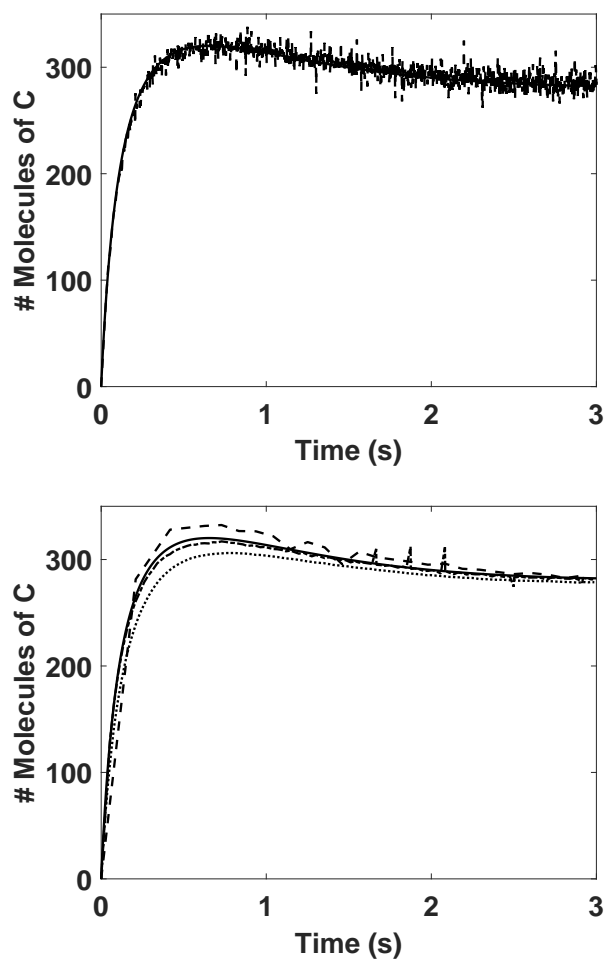


Figure 4.2. Temporal evolution of the concentration of the species C in the region \mathcal{D}' for a case with similar diffusion and reaction effects ($D_2 = 10^{-13} \text{ m}^2/\text{s}$, $k_{r1} = 3 \times 10^3 \text{ mM}^{-1}\text{s}^{-1}$). Solid line is the deterministic solution in both graphics. Top: Dashed line is the solution obtained by our model based on average of 1000 iterations. Bottom: Dashed, dash-dot, and dotted lines are the solutions obtained by Choi et al., model setting $\Delta x = \Delta y = \Delta z = L/4, L/8,$ and $L/16,$ respectively. All results are based on average of 1000 iterations.

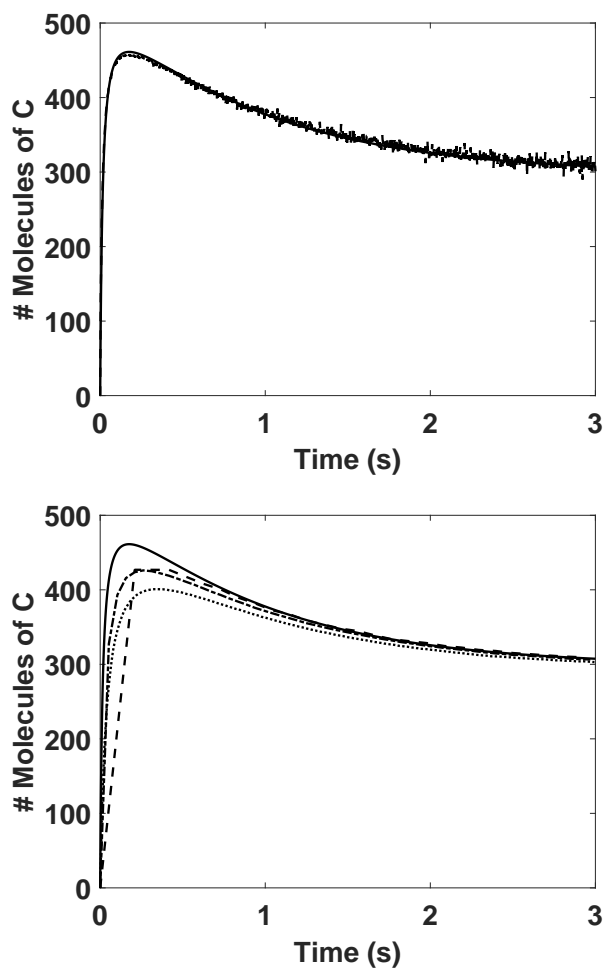


Figure 4.3. Temporal evolution of the concentration of the species C in the region \mathcal{D}' for a case with dominant reaction effects ($D_2 = 10^{-13} \text{ m}^2/\text{s}$, $k_{r2} = 3 \times 10^4 \text{ mM}^{-1}\text{s}^{-1}$). Solid line is the deterministic solution in both graphics. Top: Dashed line is the solution obtained by our model based on average of 1000 iterations. Bottom: Dashed, dash-dot, and dotted lines are the solutions obtained by Choi et al., model setting $\Delta x = \Delta y = \Delta z = L/4, L/8,$ and $L/16,$ respectively. All results are based on average of 1000 iterations.

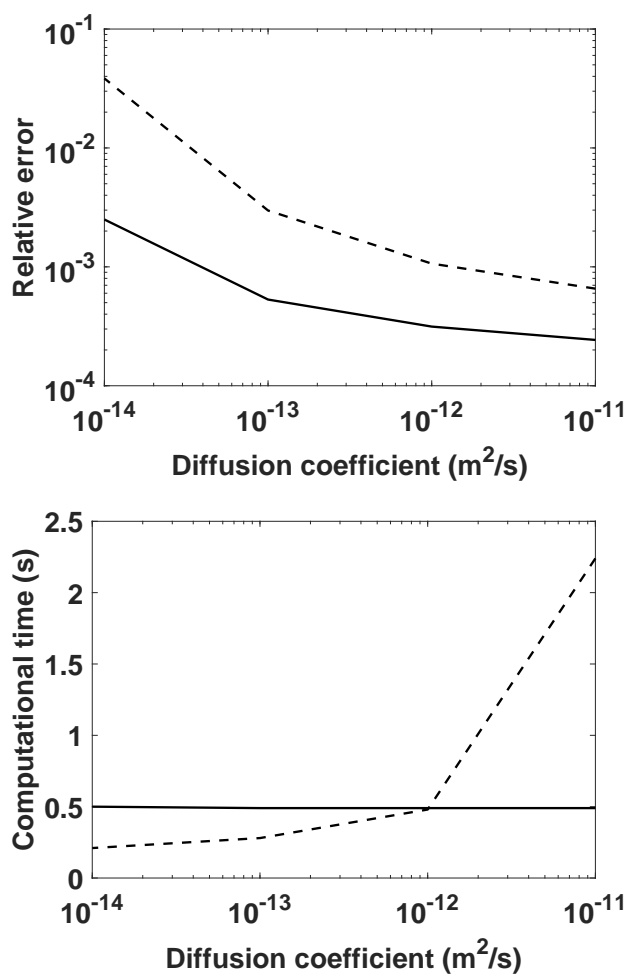


Figure 4.4. Top: Relative error for different regimes, from diffusion-controlled ($D = 10^{-14} m^2/s$) to reaction-controlled ($D = 10^{-11} m^2/s$). Solid and dashed lines represent the relative errors of our model and Choi et al., model with respect to the diffusion coefficient, respectively. Bottom: Computational time for different regimes. Solid and dashed lines represent the computational times of our model and Choi et al., model with respect to the diffusion coefficient, respectively.

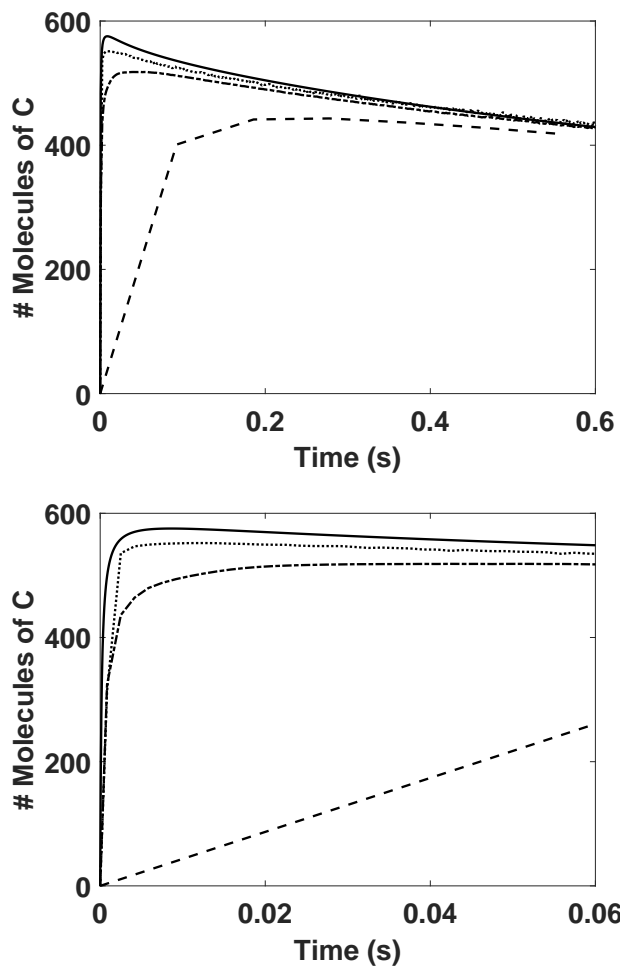


Figure 4.5. Temporal evolution of the concentration of the species C in the region \mathcal{D}' for a case with highly dominant reaction effects. Solid line is the deterministic solution in both graphics. Top: Dashed, dash-dot, and dotted lines are the solutions obtained by Choi et al., model setting $\Delta x = \Delta y = \Delta z = L/6$, our model with regular compartments, and our model with non-regular compartments and $\alpha = 0.1$, respectively, based on average of 1000 iterations. Bottom: Close-up of the first time-steps.

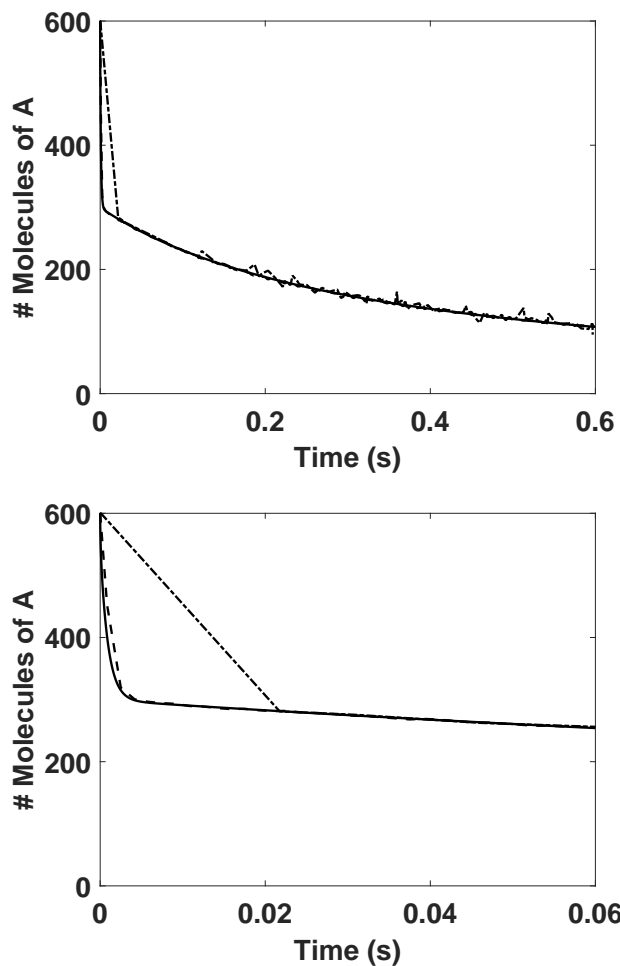


Figure 4.6. Temporal evolution of the concentration of the species A in the region \mathcal{D}' for a case with highly dominant diffusion effects. Solid line is the deterministic solution in both graphics. Top: Dashed and dash-dot lines are the solutions obtained by Choi et al., model setting $\Delta x = \Delta y = \Delta z = L/6$ based on average of 100 iterations and our model based on average of 1000 iterations, respectively. Bottom: Close-up of the first time-steps.

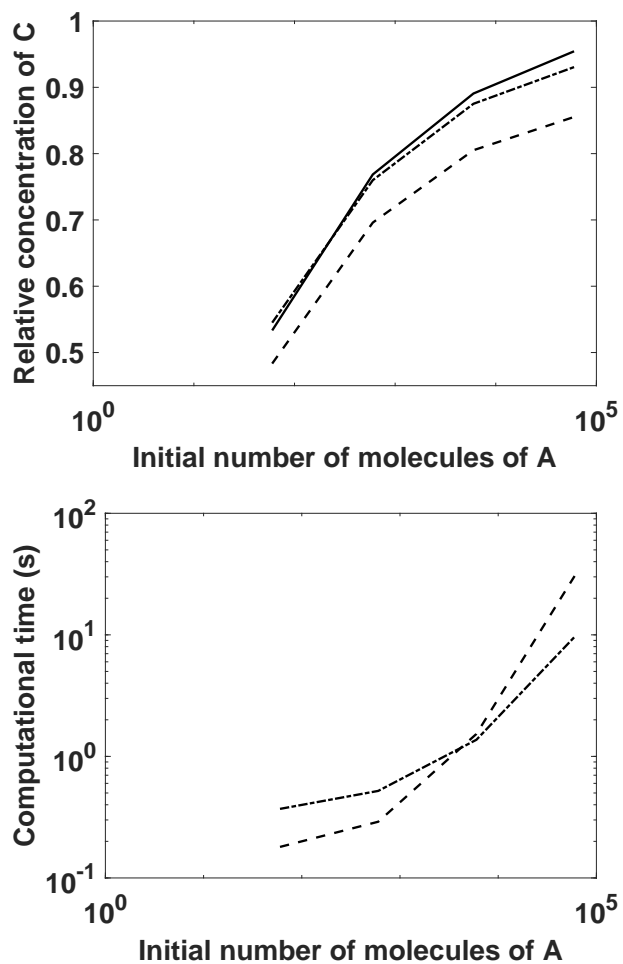


Figure 4.7. Top: Relative peak concentration, N_r , for different initial number of molecules of A. Solid, dashed, and dash-dot lines represent the values predicted by the deterministic solution, Choi et al., model, and our model, respectively. Bottom: Computational time required to reach the steady state for different initial number of molecules of A. Dashed and dash-dot lines represent the times required by Choi et al., model and our model, respectively.

Chapter 5

Conclusions

Based on our search for the optimal level of complexity, we have proposed approaches from different perspectives depending on the information we have aimed to capture from specific biophysical or geophysical processes: analytical solutions, coarse-grained models, and hybrid self-tuning algorithms. Thus, this dissertation can be summarized in the following major conclusions:

1. We have developed analytical models for advective and conductive heat transfer in a fracture surrounded by an infinite matrix. These models account for longitudinal and transverse diffusion in the matrix, a two-way coupling between heat transfer in the fracture and matrix, and an arbitrary configuration of heat sources. This is in contrast to the existing analytical solutions that restrict matrix conduction to the direction perpendicular to the fracture. We have demonstrated that longitudinal thermal diffusivity in the matrix is a critical parameter that determines the impact of local heat sources on fluid temperature in the fracture. By neglecting longitudinal conduction in the matrix, the classical models significantly overestimate both fracture temperature and time-to-equilibrium. We have also identified the fracture-matrix Péclet number, defined as the ratio of advection time scale in the fracture to diffusion time scale in the matrix, as a key parameter that determines the efficiency of geothermal systems. Our analytical models have provided an easy-to-use tool for parametric sensitivity analysis, benchmark studies, geothermal site evaluation, and parameter identification.

2. We have presented an effective kinetics model of filament formation, bundling and depolymerization following GTP-hydrolysis, which involves a relatively small number of species and reactions, and remains robust over a wide range of concentrations and time scales. We have applied this general model to study assembly of FtsZ protein, a basic element in the division process of prokaryotic cells such as *Escherichia coli*, *Bacillus subtilis* or *Caulobacter crescentus*. This analysis have demonstrated that our model outperforms its counterparts in terms of both accuracy and computational efficiency. Since our model comprises “only” seventeen ordinary differential equations (ODEs), its computational cost is orders of magnitude smaller than the current alternatives consisting of up to a thousand ODEs. It has also provided a new insight into the characteristics and functioning of FtsZ proteins at high concentrations. The simplicity and versatility of our model render it a powerful computational tool, which can be used either as a stand alone descriptor of other biopolymers’ assembly or as a component in more complete kinetic models.

3. We have presented a modeling approach, which achieves orders of magnitude speed-up by replacing distributions of lengths and widths with their average counterparts and by introducing a hierarchical classification of species and reactions into sets. We have used this model to study FtsZ ring assembly in *E. coli*. The model’s prediction of key features of the ring formation, such as time to reach the steady state, total concentration of FtsZ species in the ring, total concentration of monomers and average dimensions of filaments and bundles, have been all in agreement with the experimentally observed values. Besides validating our model against the *in vivo* observations, this study has filled some knowledge gaps by proposing a specific structure of the ring, describing the influence of the total concentration in short and long kinetics processes, determining some characteristic mechanisms in polymer assembly regulation and providing new insights about the role of ZapA proteins, critical component for both positioning and stability of the ring.

4. We have developed a hybrid self-tuning algorithm for the analysis of stochastic reaction-diffusion systems that remains efficient in wide range of regimes or under scenarios

with large variations of concentrations in time and/or space. By combining microscopic methods for diffusion (Brownian dynamics) with mesoscopic methods for reaction (Gillespie algorithm), refining the mesh, optimizing the time-step, and redefining propensities, we have achieved a more optimal balance between accuracy, robustness, and versatility than previous works based on similar approaches. We have studied a bimolecular reaction $A + B \rightarrow C$ in a simple domain to show the potential of our model at a large range of scenarios, from almost completely diffusion-controlled systems to cases where reactions rarely occur or take place very slowly. We have also demonstrated that the amount of particles present in the system do not affect the performance of our model with respect to its direct counterpart. The efficiency and versatility of our algorithm makes it a powerful approach to develop more complex multi-reaction models without propagating large calculation errors or increasing the computational time unnecessarily.

Appendix A

Analytical Models of Heat Conduction in Fractured Rocks

A.1 Green's functions

A.1.1 Green's function for fracture BVP

We represent the two-dimensional Green's function G^f as the product of two one-dimensional Green's functions, $G^f = G_x^f(x; x'; t - t')G_z^f(z; z'; t - t')$ [CJ59]

$$G_x^f = \frac{1}{2\sqrt{\pi D_L^f(t-t')}} \exp\left[\frac{-[x' - x + u(t-t')]^2}{4D_L^f(t-t')}\right] \quad (\text{A.1})$$

and

$$G_z^f = \frac{1}{b} + \frac{2}{b} \sum_{n=1}^{\infty} e^{-\alpha_n^2 D_T^f(t-t')} \cos(\alpha_n z) \cos(\alpha_n z') \quad (\text{A.2})$$

where $\alpha_n = n\pi/b$. The Fourier Laplace (FL) transform of G^f has the form

$$\tilde{G}^f = \frac{\tilde{G}_\xi^f(s)}{\sqrt{2\pi b}} + \sqrt{\frac{2}{\pi}} \sum_{n=1}^{\infty} \frac{\cos(\alpha_n z) \cos(\alpha_n z')}{b} \tilde{G}_\xi^f(s + \alpha_n^2 D_T^f) \quad (\text{A.3})$$

where

$$\tilde{G}_\xi^f(s) = \frac{1}{s + \xi^2 D_L^f + u\xi i}. \quad (\text{A.4})$$

A.1.2 Green's function for matrix BVP

The Green's function G^m is computed as the product of one-dimensional Green's functions, $G^m = G_x^m(x; x'; t - t') G_z^m(z; z'; t - t')$,

$$G_x^m = \frac{1}{2\sqrt{\pi D_L^m(t-t')}} \exp\left[\frac{-(x' - x)^2}{4D_L^m(t-t')}\right] \quad (\text{A.5})$$

and

$$G_z^m = \frac{e^{-(z'-z)^2/\omega} + e^{-(z'+z-2b)^2/\omega}}{2\sqrt{\pi D_T^m(t-t')}}. \quad (\text{A.6})$$

where $\omega = 4D_T^m(t-t')$. The FL transform of G^m is

$$\tilde{G}^m = \frac{e^{-\psi|z-z'|/\sqrt{D_T^m}} + e^{-\psi|z+z'-2b|/\sqrt{D_T^m}}}{2\sqrt{2\pi D_T^m}\psi} \quad (\text{A.7})$$

where $\psi = \sqrt{D_L^m \xi^2 + s}$.

A.2 Integral solutions of BVPs

Solutions of the fracture and matrix BVPs, expressed in terms of the Green's functions, are

$$\begin{aligned} T^f(x, z, t) = & \int_0^t \int_{-\infty}^{\infty} r(x', t') G^f(., x', b; .) dx' dt' \\ & + \int_0^t \int_0^b \int_{-\infty}^{\infty} f(x', z', t') G^f(., .; .) dx' dz' dt' \end{aligned} \quad (\text{A.8})$$

and

$$T^m(x, z, t) = -\frac{1}{\phi_m} \int_0^t \int_{-\infty}^{\infty} r(x', t') G^m(., x', b; .) dx' dt'. \quad (\text{A.9})$$

Their FL transforms are

$$\tilde{T}^f = \sqrt{2\pi} \left(\tilde{r}\tilde{G}^f|_{z'=b} + \int_0^b \tilde{f}\tilde{G}^f dz' \right) \quad (\text{A.10})$$

$$\tilde{T}^m = -\frac{\sqrt{2\pi}\tilde{r}\tilde{G}^m|_{z'=b}}{\phi_m}, \quad (\text{A.11})$$

where \tilde{G}^f and \tilde{G}^m are given by (A.3) and (A.7), respectively.

The FL transform of the fracture-matrix heat transfer, $\tilde{r}(\xi, s)$, is obtained from the continuity condition at the interface, $\tilde{T}^f(\xi, z = b, s) = \tilde{T}^m(\xi, z = b, s)$.

A.3 Fourier-Laplace inversions

Since $\tilde{T}^f(\xi, s) = \tilde{T}^*(-\xi, s)$ (where \tilde{T}^* denotes the conjugate of \tilde{T}^f , the inverse Fourier transform of \tilde{T}^f is

$$\bar{T}^f = \frac{1}{\sqrt{2\pi}} \int_0^{\infty} \left[\tilde{T}^f(\xi, s) e^{-ix\xi} + \tilde{T}^f(\xi, s) e^{ix\xi} \right] d\xi \quad (\text{A.12})$$

and its inverse Laplace transform is

$$T^f = \frac{1}{\sqrt{2\pi}} \int_0^{\infty} \left[L^{-1}[\tilde{T}^*] e^{-ix\xi} + L^{-1}[\tilde{T}^f] e^{ix\xi} \right] d\xi \quad (\text{A.13})$$

where $L^{-1}[\]$ represents the inverse Laplace operator.

A.3.1 Inverse Laplace transform of \tilde{T}^f

We decompose the FL transform \tilde{T}^f in (1.11) into simple fractions

$$\tilde{T}^f = A \sum_{i=1}^4 \frac{X_i}{\psi + b_i}, \quad A = \frac{T_0 u}{\sqrt{2\pi}} \quad (\text{A.14})$$

where $b_1 = B/2 + \sqrt{G - Di}$, $b_2 = B/2 - \sqrt{G - Di}$, $b_3 = -b_4 = \sqrt{C}$, $X_1 = 1/[(b_1 - b_2)(C - b_1^2)]$, $X_2 = -1/[(b_1 - b_2)(C - b_2^2)]$, $X_3 = -1/\{2\sqrt{C}[(C + b_1 b_2) - (b_1 + b_2)\sqrt{C}]\}$, $X_4 = 1/\{2\sqrt{C}[(C + b_1 b_2) + (b_1 + b_2)\sqrt{C}]\}$, and

$$B = \frac{\Phi_m \sqrt{D_T^m}}{b}, \quad C = D_L^m \xi^2, \quad D = u\xi, \quad G = \frac{B^2}{4} + C. \quad (\text{A.15})$$

Since only $\psi = \sqrt{C + s}$ depends on the Laplace variable s , and noticing that $\sum_{i=1}^4 X_i = 0$, the inverse Laplace of \tilde{T}^f is

$$\hat{T}^f = -A e^{-Ct} \sum_{i=1}^4 X_i b_i e^{b_i^2 t} \operatorname{erfc}(b_i \sqrt{t}) \quad (\text{A.16})$$

which can be recast in terms of the function $w(z) = e^{-z^2} \operatorname{erfc}(-iz)$ of a complex variable z [FT61] as

$$\begin{aligned} \hat{T}^f &= \frac{AB\sqrt{C}}{B^2C + D^2} [1 - \operatorname{erfc}(\sqrt{Ct})] \\ &\quad - \frac{ADi}{B^2C + D^2} [1 - e^{-Ct} w(ib_1 \sqrt{t})] \\ &\quad + AX_2 b_2 e^{-Ct} [w(ib_1 \sqrt{t}) - w(ib_2 \sqrt{t})], \end{aligned} \quad (\text{A.17})$$

A.3.2 Inverse Fourier transform of $\hat{T}f$

Recalling that b_1 and b_2 in (A.17) are given by

$$b_1 = \frac{B}{2} + \sqrt{\frac{\sqrt{G^2 + D^2} + G}{2}} - i\sqrt{\frac{\sqrt{G^2 + D^2} - G}{2}} \quad (\text{A.18})$$

$$b_2 = \frac{B}{2} - \sqrt{\frac{\sqrt{G^2 + D^2} + G}{2}} + i\sqrt{\frac{\sqrt{G^2 + D^2} - G}{2}}, \quad (\text{A.19})$$

expanding the square roots into Taylor series, and requiring $G \gg D$ leads to

$$b_1 \approx \frac{B}{2} + \sqrt{G + \frac{D^2}{4G}} - \frac{iD}{2\sqrt{G}}, \quad b_2 \approx \frac{B}{2} - \sqrt{G + \frac{D^2}{4G}} + \frac{iD}{2\sqrt{G}}. \quad (\text{A.20})$$

Requiring $B^2/4 \gg C$, and expanding the square roots into Taylor series, yields

$$b_1 \approx B - i\frac{D}{B}, \quad b_2 \approx -\frac{C}{B} - \frac{D^2}{B^3} + i\frac{D}{B}. \quad (\text{A.21})$$

Similarly, $X_2 b_2$ in (A.17) is approximated by

$$X_2 b_2 \approx \frac{1}{B^2} - \frac{iD}{B^2 C + D^2}. \quad (\text{A.22})$$

Finally, for small values of ξ , we approximate b_1 and b_2 in the arguments of $w(\cdot)$ with $b_1 \approx B$ and $b_2 \approx iD/B$, so that

$$\begin{aligned} w(ib_1\sqrt{t}) &\approx e^{B^2 t} \operatorname{erfc}(B\sqrt{t}) \\ w(ib_2\sqrt{t}) &\approx e^{-D^2 t/B^2} \operatorname{erfc}(iD\sqrt{t}/B). \end{aligned} \quad (\text{A.23})$$

For $t > 10^4/B^2$, expanding $\text{erfc}(iD\sqrt{t}/B)$ into a Taylor series yields

$$\begin{aligned} w(ib_1\sqrt{t}) &\approx 0 \\ w(ib_2\sqrt{t}) &\approx e^{-\varepsilon^2} \left[1 - \left(\frac{2}{\sqrt{\pi}}\varepsilon + \frac{2}{3\sqrt{\pi}}\varepsilon^3 + \frac{1}{5\sqrt{\pi}}\varepsilon^5 \right) i \right], \end{aligned} \quad (\text{A.24})$$

where $\varepsilon = D\sqrt{t}/B$. With these approximations, (A.17) is replaced with

$$\hat{T}^f \approx \frac{A\sqrt{C}}{B^2\kappa} \text{erf}(\sqrt{Ct}) - \frac{ADi}{B^2\kappa} - \frac{A(\kappa - Di)}{B^2\kappa} \left[1 - \left(\frac{2\varepsilon}{\sqrt{\pi}} + \frac{2\varepsilon^3}{3\sqrt{\pi}} + \frac{\varepsilon^5}{5\sqrt{\pi}} \right) i \right] e^{-\kappa t} \quad (\text{A.25})$$

where $\kappa = C + D^2/B^2$. Using (A.13) to compute the inverse Fourier transform leads to (1.13).

A.3.3 Limits of applicability of analytical model (1.13)

The Fourier transform of temperature in the fracture (A.25) and its exact analytical inversion (1.13) are derived under the following three conditions:

1. $B^2/4 + C \gg D$
2. $B^2/4 \gg C$
3. $t > 10^4/B^2$.

In what follows, we demonstrate the general applicability of these conditions.

Condition 1:

Solving the first condition $B^2/4 + C \gg D$ as an equation results in

$$\xi^2 = \frac{u^2}{2D_L^{m2}} - \frac{\phi_m^2 D_T^m}{4b^2 D_L^m} \pm \frac{u}{2D_L^{m2}} \sqrt{u^2 - \frac{\phi_m^2 D_L^m D_T^m}{b^2}}. \quad (\text{A.26})$$

Thus, ξ is real if

$$\frac{\phi_m \sqrt{D_L^m D_T^m}}{ub} > 1. \quad (\text{A.27})$$

Condition 2:

Recalling (A.15), this condition implies $\xi^2 \ll \phi_m^2 D_T^m / (4D_L^m b^2)$. When $\xi > 1$, this is equivalent to $\xi < \phi_m \sqrt{D_T^m / D_L^m} / (2b)$, which gives

$$\frac{\phi_m}{2b} \sqrt{\frac{D_T^m}{D_L^m}} > 1. \quad (\text{A.28})$$

Condition 3:

For $B^2 t = 10^4$, $e^{B^2 t} \text{erfc}(\sqrt{B^2 t}) \approx 0.0056$ and we treat it as 0. This yields a third constraint,

$$t > \frac{10^4 b^2}{\phi_m^2 D_T^m}. \quad (\text{A.29})$$

Appendix B

Efficient Multiscale Models of Polymerization Applied to *in vitro* FtsZ Assembly

B.1 Ordinary differential equations for concentrations

Polymerization and bundling processes are represented by the reactions listed in Section 2.2.1. Monomer and protofilament concentrations, $[Z^{\text{na}}]$, $[Z]$ and $[Z_i]$ with $i = 2, \dots, 6$, satisfy a system of ODEs,

$$\frac{d[Z^{\text{na}}]}{dt} = -k_{\text{ac}}^+[Z^{\text{na}}] + k_{\text{ac}}^-[Z] + k_{\text{hy/dis}}^1[F] + k_{\text{hy/dis}}^2[F] + k_{\text{hy/dis}}^2 \sum_{i=2}^3 [B_i] + k_{\text{hy/dis}}^3 \sum_{i=2}^N [B_i], \quad (\text{B.1})$$

$$\begin{aligned} \frac{d[Z]}{dt} = & k_{\text{ac}}^+[Z^{\text{na}}] - k_{\text{ac}}^-[Z] - 2k_{\text{nu}}^+[Z]^2 + 2k_{\text{ac}}^-[Z_2] - k_{\text{el}}^+[Z] \sum_{i=2}^6 [Z_i] - k_{\text{el}}^+[Z][F] \\ & + k_{\text{el}}^- \sum_{i=3}^6 [Z_i] + k_{\text{el}}^- [F] - k_{\text{mb}}[Z] \sum_{i=2}^N [B_i], \end{aligned} \quad (\text{B.2})$$

$$\frac{d[Z_2]}{dt} = k_{\text{nu}}^+[Z]^2 - k_{\text{nu}}^-[Z_2] - k_{\text{el}}^+[Z][Z_2] + k_{\text{el}}^-[Z_3], \quad (\text{B.3})$$

$$\frac{d[Z_i]}{dt} = k_{\text{el}}^+[Z]([Z_{i-1}] - [Z_i]) + k_{\text{el}}^-([Z_{i+1}] - [Z_i]), \quad i = 3, 4, 5, \quad (\text{B.4})$$

$$\frac{d[Z_6]}{dt} = k_{\text{el}}^+[Z]([Z_5] - [Z_6]) - k_{\text{el}}^-[Z_6], \quad (\text{B.5})$$

where N is the maximum number of filaments in a bundle. Filaments and bundles are assumed to be present in the same concentrations regardless of their length. Consequently, we set $[F] \equiv [F_{z^-}] = [F_{z^+}] = [F_{f^-}] = [F_{f^+}] = [F_{z^-,f^-}] = [F_{z^+,f^+}]$ and $[B_i] \equiv [B_{i;z^-}] = [B_{i;z^+}] = [B_{i;b^-}] =$

$[B_{i;b^+}] = [B_{i;z^-,b^-}] = [B_{i;z^+,b^+}]$ with $i = 2, \dots, N$. Thus, we only define ODEs for $[F]$ and $[B_i]$,

$$\begin{aligned} \frac{d[F]}{dt} &= k_{el}^+[Z][Z_6] - k_{an}^+[F]^2 + k_{an}^-[F] - k_{bu}^+[F] \left(2[F] + \sum_{i=2}^{N-1} [B_i] \right) + k_{bu}^- \left(2[B_2] + \sum_{i=3}^N [B_i] \right) \\ &\quad + k_{hy/dis}^2[F], \end{aligned} \quad (\text{B.6})$$

$$\begin{aligned} \frac{d[B_i]}{dt} &= -\frac{i}{2}k_{bu}^-[B_i] + k_{bu}^+ \left([B_{i/2}]^2 + \sum_{j=1}^{i-1} \frac{1 - \delta_{j,i-j}}{2} [B_j][B_{i-j}] \right) - k_{bu}^+[B_i] \sum_{j=1}^{N-i} ([B_j] + [B_i]\delta_{i,j}) \\ &\quad + k_{bu}^- \sum_{j=i+1}^N (1 + \delta_{2i,j})[B_j] + k_{hy/dis}^2[B_i]\delta_{i,2}, \quad \text{for } i = 2, 4, \dots, \begin{cases} N-2 & \text{even } N \\ N-1 & \text{odd } N \end{cases}, \end{aligned} \quad (\text{B.7})$$

$$\begin{aligned} \frac{d[B_i]}{dt} &= -\frac{i-1}{2}k_{bu}^-[B_i] + \frac{k_{bu}^+}{2} \sum_{j=1}^{i-1} [B_j][B_{i-j}] - k_{bu}^+[B_i] \sum_{j=1}^{N-i} ([B_j] + [B_i]\delta_{i,j}) \\ &\quad + k_{bu}^- \sum_{j=i+1}^N (1 + \delta_{2i,j})[B_j] + k_{hy/dis}^2[B_i]\delta_{i,3}, \quad \text{for } i = 3, 5, \dots, \begin{cases} N-1 & \text{even } N \\ N-2 & \text{odd } N \end{cases}, \end{aligned} \quad (\text{B.8})$$

$$\frac{d[B_N]}{dt} = -\frac{N}{2}k_{bu}^-[B_N] + k_{bu}^+ \left([B_{N/2}]^2 + \sum_{j=1}^{N-1} \frac{1 - \delta_{j,N-j}}{2} [B_j][B_{N-j}] \right) + k_{hy/dis}^2[B_N]\delta_{N,2}, \quad \text{even } N, \quad (\text{B.9})$$

$$\frac{d[B_N]}{dt} = -\frac{N-1}{2}k_{bu}^-[B_N] + \frac{1}{2}k_{bu}^+ \sum_{j=1}^{N-1} [B_j][B_{N-j}] + k_{hy/dis}^2[B_N]\delta_{N,3}, \quad \text{odd } N. \quad (\text{B.10})$$

In Eqs. B.7–B.10, $[B_1] = [F]$. Equations C.1–B.10 are subject to the following initial conditions: $[Z^{na}]_0 = C_{tot}$, $[Z]_0 = 0$, $[Z_i]_0 = 0$, $[F]_0 = 0$ and $[B_j]_0 = 0$, with $i = 2, \dots, 6$ and $j = 2, \dots, N$.

Figure B.1 demonstrates the fast converges of this system of ODEs with respect to N . For the extreme case of $C_{tot} = 10.0 \mu\text{M}$, one does not need to account for bundles of more than 9 or 10 filaments. This gives $N = 10$ and, therefore, results in the 17 ODEs.

B.2 Conservation of mass and energy

Conservation of mass.

For any $C_{\text{tot}} > C_{\text{cr}}^1$, the system of ODEs for FtsZ concentrations in all forms, Eqs. C.1–B.10, is solved numerically. Then, the average length, \bar{L}_{fb}^m , is defined as an unknown parameter in the conservation of mass law,

$$C_{\text{tot}} = \underbrace{[Z^{\text{na}}] + [Z]}_{\text{FtsZ in monomer form}} + \underbrace{\sum_{i=2}^6 i[Z_i] + \bar{L}_{\text{fb}}^m[F]}_{\text{FtsZ in filament form}} + \underbrace{\bar{L}_{\text{fb}}^m \sum_{i=2}^N i[B_i]}_{\text{FtsZ in bundle form}} . \quad (\text{B.11})$$

In other words, our way of calculating the average lengths of filaments and bundles automatically conserves mass at all times. Figure B.2 exhibits the temporal evolution of these three forms of FtsZ thus computed for $C_{\text{tot}} = 2.0$ and $10.0 \mu\text{M}$. As expected, the summation of FtsZ in all forms remains constant and equal to the total concentration C_{tot} for any C_{tot} at all times t .

Net cycle balance.

The detailed balance is violated because of the nature of the process that we are modeling. Cytoskeletal polymers, such as actin filaments and microtubules in eukaryotes and FtsZ, MreB, and ParM in prokaryotes, grow due to the accumulation of monomers bounded to ATP or GTP (nucleotide triphosphates). Those polymerized monomers can exchange their nucleotides with ADP or GDP (nucleotide diphosphates) and disassembly from the polymer structure. This turnover of monomers between the network and the solution is a nonequilibrium steady-state process (NESS), which violates the detailed balance; this is in contrast to equilibrium steady states (ESS), where the rate of all molecular processes is exactly balanced by the rate of the reverse processes [Nee15, SW11, Weg76, PCC01, Qia05, Qia07]. These cellular nonequilibrium systems or structures are referred to as “active matter”, and they are maintained by constant energy influx [Nee15]. In section 2.2.1, the reactions representing the assembly/disassembly of FtsZ monomers (Eqs. 2.1–2.3 and 2.6–2.8) constitute a NESS or net cycle balance. Eqs. 2.6–2.8 are irreversible reactions that imply consumption of energy and conformational changes that

destabilize the polymers [Nee15].

Regardless of the nonequilibrium steady state, it is important to note that Eq. 2.3b is an artificial irreversible reaction that previous models defined to limit the explicit description of the first steps of polymerization [FG83, SXPM99, CBRE5a, CE5b, FLKG12]. It can be viewed as a transition between a model for short-time kinetics, which describes how fast monomers assemble, and a model for long-time kinetics, which represent slow processes such as annealing, bundling or disassembly of monomers following GTP hydrolysis.

B.3 Parameter identification from steady-state, low concentration data ($C_{\text{tot}} = 0.7 - 3.0 \mu\text{M}$)

The steady-state experiments reported in [CE5b] reveal that

1. the amount of FtsZ in monomer form equals the first critical concentration, $C_{\text{cr}}^1 = 0.7 \mu\text{M}$, regardless of the value of C_{tot} in the range between $0.7 \mu\text{M}$ and $3.0 \mu\text{M}$;
2. the average length of filaments and bundles at $C_{\text{tot}} = 2.0 \mu\text{M}$ is $\bar{L}_{\text{tot}} = 120.0 \text{ nm}$. Since the diameter of FtsZ monomers is $4.0 - 5.0 \text{ nm}$ [CE5b, Eri09, FFFG12], this corresponds to $\bar{L}_{\text{tot}}^m = 24 - 30$, i.e., the average length of filaments comprising $24 - 30$ monomers;
3. the value of \bar{L}_{tot}^m remains practically unchanged for $C_{\text{tot}} = 3.0 \mu\text{M}$; and
4. the majority of filaments are single-stranded at all levels of C_{tot} in the range between $0.7 \mu\text{M}$ and $3.0 \mu\text{M}$. This suggests an average width of a bundle to be not larger than $\bar{W}_{\text{tot}}^f = 1.5$, where the superscript f designates the number of filaments per bundle.

These observations are used to calibrate our model. The calibration procedure employs `fmincon` Matlab optimization routine, which allows one to find minima of constrained nonlinear multi-variable functions. Calibration of our model consists in the following steps.

1. Define the coupled functionals to be minimized at steady state:

- (a) the derivatives of all concentrations in Eqs. C.1–B.10;
- (b) the difference between the first critical concentration and the sum of nonactivated and activated monomers, $[Z^{\text{na}}] + [Z] - C_{\text{cr}}^1$;
- (c) the difference between the total amount of FtsZ in the experiment, C_{tot} , and the sum of all forms in which FtsZ exists, $C_{\text{tot}} - \{[Z^{\text{na}}] + [Z] + \sum_{i=2}^6 i[Z_i] + \bar{L}_{\text{fb}}^m([F] + \sum_{i=2}^N i[B_i])\}$;
- (d) the difference between the average width of filaments and bundles, \bar{W}_{tot}^f , and the total FtsZ concentration in filament and bundle forms, normalized with the sum of the concentration of filaments and bundles weighted by their lengths, $\bar{W}_{\text{tot}}^f - \{[\sum_{i=2}^6 i[Z_i] + \bar{L}_{\text{fb}}^m([F] + \sum_{i=2}^N i[B_i])]\} / [\sum_{i=2}^6 i[Z_i] + \bar{L}_{\text{fb}}^m([F] + \sum_{i=2}^N i[B_i])]$.

2. Define a set of C_{tot} -dependent constraints (for $C_{\text{tot}} = 0.7, 0.8, 1.0, 1.5, 2.0, 2.5,$ and $3.0 \mu\text{M}$):

- (a) lower and upper bounds for the parameters to be calibrated (Table C.2);
- (b) lower and upper bounds for the monomer concentration, average length and average width (Table C.3);
- (c) order relations for the average length, $\bar{L}_{\text{fb}}^m(C_{\text{tot}})$, and width, $\bar{W}_{\text{tot}}^f(C_{\text{tot}})$: the higher the total concentration C_{tot} (in μM), the longer and wider the filaments and bundles are, i.e.,

$$\bar{L}_{\text{fb}}^m(0.7) < \bar{L}_{\text{fb}}^m(0.8) < \bar{L}_{\text{fb}}^m(1.0) < \bar{L}_{\text{fb}}^m(1.5) < \bar{L}_{\text{fb}}^m(2.0) < \bar{L}_{\text{fb}}^m(2.5) < \bar{L}_{\text{fb}}^m(3.0)$$

and

$$\bar{W}_{\text{tot}}^f(0.7) < \bar{W}_{\text{tot}}^f(0.8) < \bar{W}_{\text{tot}}^f(1.0) < \bar{W}_{\text{tot}}^f(1.5) < \bar{W}_{\text{tot}}^f(2.0) < \bar{W}_{\text{tot}}^f(2.5) < \bar{W}_{\text{tot}}^f(3.0)$$

3. Pick initial guesses for the optimization variables ($k_{\text{bu}}^+ = 3.0 \mu\text{M}^{-1}\text{s}^{-1}$, $k_{\text{bu}}^0 = 200.0 \text{s}^{-1}$, $k_{\text{mb}} = 2.0 \mu\text{M}^{-1}\text{s}^{-1}$ and $k_{\text{hss/dis}}^1 = 1.0 \text{s}^{-1}$) and functionals (see Table C.4).

4. Run the Matlab subroutine `fmincon` with a tolerance of 10^{-8} to estimate the parameters and use those estimates as new initial guesses. Repeat successively in a loop of 20 iterations. Rerun `fmincon` while using the last estimates as new initial guesses and decreasing the tolerance to 10^{-9} to get a second, more accurate calibration, iterating again 20 times.

This calibration procedure yields the values of k_{bu}^+ , k_{bu}^0 , k_{mb} and $k_{\text{hss/dis}}^1$ reported in Table 2.2 in section C.2.

B.4 Model validation

With the parameters either found in the literature or calibrated on the steady-state observations, we use our model to predict short- and long-time FtsZ polymerization dynamics. Comparison with the corresponding data serves to validate the model.

Short-time kinetics validation.

Annealing, bundling and GTP-hydrolysis/dissociation reactions are thought to be absent during the first seconds of polymerization. The Fluorescence Resonance Energy Transfer experiment [CE5b] yielded data, which provide information about the temporal evolution of FtsZ-F268C that assembles into filaments or bundles. Fluorescence is defined in terms of the concentrations of nonactivated (Z^{na}) and activated (Z) monomers as

$$\mathcal{F} = a_1([Z^{\text{na}}] + [Z]) + a_2(C_{\text{tot}} - [Z^{\text{na}}] - [Z]),$$

where the parameters a_1 and a_2 represent the fluorescence of monomers and proteins in polymer form, respectively. Figure C.2 exhibits the temporal evolution of \mathcal{F} for $C_{\text{tot}} = 1.22, 1.98$ and $3.12 \mu\text{M}$ observed in [CE5b] and predicted with our model. The agreement between the model and the observations indicates the model's validity at early times. The plateau of the intensity curves corresponds to the situation in which all FtsZ-F268C proteins are assembled, except for monomers with concentration similar to the first critical concentration, $C_{\text{cr}}^1 = 0.7 \mu\text{M}$. Although

C_{cr}^1 is the same regardless of C_{tot} , the fluorescence intensities for each plateau are different. That is because the fluorescence \mathcal{F} is proportional to the amount of polymerized FtsZ-F268C and the latter increases with C_{tot} .

Also shown in Figure C.2 are predictions of the Chen and Erickson (CE) model [CE5b] of the early stages of FtsZ polymerization. The agreement between the two models illustrates that annealing, bundling and GTP-hydrolysis/dissociation reactions (all of which are absent from the CE model) do not have a strong influence in the beginning of assembly process.

Long-time kinetics validation.

The predicted steady-state statistics of FtsZ assembly, i.e., \bar{L}_{tot}^m , \bar{W}_{tot}^f and $C_{\text{cr}}^1 = [Z^{\text{na}}]_{\text{ss}} + [Z]_{\text{ss}}$, are compared with their observed counterparts in Table C.5. Since the steady-state data were used for parameter identification, it is to be expected that the steady-state model predictions are in agreement with observations [CE5b]: the average length for $C_{\text{tot}} = 2.0 - 3.0 \mu\text{M}$ is between 24 and 30 monomers; the majority of the filaments are single-stranded for low concentrations, i.e., $\bar{W}_{\text{tot}}^f < 1.5$ for $C_{\text{tot}} < 3.0 \mu\text{M}$; and $[Z^{\text{na}}]_{\text{ss}} + [Z]_{\text{ss}} = 0.7 \mu\text{M}$, which coincides with the value reported in [CE5b] for C_{tot} in the range between $0.7 \mu\text{M}$ and $3.0 \mu\text{M}$. While such an agreement is not surprising, it is worthwhile pointing out that the CE model [CE5b], which was designed to reproduce these experiments, underestimates the first critical concentration, yielding $[Z^{\text{na}}]_{\text{ss}} + [Z]_{\text{ss}} \approx 0.5 \mu\text{M}$. This underestimation is due to both the dissociation of monomers from filaments following GTP hydrolysis and the effects of bundling on the turnover rate. These two processes are explicitly accounted for in our model, but are absent in the CE model.

The temporal evolution of both the average length of the first oligomers, polymers and bundles (\bar{L}_{tot}^m) and the average width of a bundle (\bar{W}_{tot}^f) is depicted in Figure B.4 for $C_{\text{tot}} = 1.0, 2.0, \text{ and } 3.0 \mu\text{M}$.

Table B.1. Lower and upper bounds for the kinetic parameters used in the model calibration procedure.

	k_{bu}^+ ($\mu\text{M}^{-1}\text{s}^{-1}$)	k_{bu}^0 (s^{-1})	k_{mb} ($\mu\text{M}^{-1}\text{s}^{-1}$)	$k_{\text{hss/dis}}^1$ (s^{-1})
Lower bound	2.0	0.0	2.0	0.143
Upper bound	7.5	500.0	6.6	∞

Table B.2. Lower and upper bounds for the concentrations (in μM , with $i = 2, \dots, 6$ and $j = 2, \dots, 10$), average length and average width, informed by the data in [CE5b].

	$[Z^{\text{na}}]$	$[Z]$	$[Z_i]$	$[F]$	$[B_j]$	\bar{L}_{fb}^m	\bar{W}_{tot}^f
Lower bound ($C_{\text{tot}} = 0.7 \mu\text{M}$)	0.0	0.0	0.0	0.0	0.0	1	1
Upper bound ($C_{\text{tot}} = 0.7 \mu\text{M}$)	0.7	0.7	∞	∞	∞	1	1
Lower bound ($C_{\text{tot}} = 0.8 \mu\text{M}$)	0.0	0.0	0.0	0.0	0.0	1	1
Upper bound ($C_{\text{tot}} = 0.8 \mu\text{M}$)	0.7	0.7	∞	∞	∞	27	1.5
Lower bound ($C_{\text{tot}} = 1.0 \mu\text{M}$)	0.0	0.0	0.0	0.0	0.0	1	1
Upper bound ($C_{\text{tot}} = 1.0 \mu\text{M}$)	0.7	0.7	∞	∞	∞	27	1.5
Lower bound ($C_{\text{tot}} = 1.5 \mu\text{M}$)	0.0	0.0	0.0	0.0	0.0	1	1
Upper bound ($C_{\text{tot}} = 1.5 \mu\text{M}$)	0.7	0.7	∞	∞	∞	27	1.5
Lower bound ($C_{\text{tot}} = 2.0 \mu\text{M}$)	0.0	0.0	0.0	0.0	0.0	24	1
Upper bound ($C_{\text{tot}} = 2.0 \mu\text{M}$)	0.7	0.7	∞	∞	∞	30	1.5
Lower bound ($C_{\text{tot}} = 2.5 \mu\text{M}$)	0.0	0.0	0.0	0.0	0.0	24	1
Upper bound ($C_{\text{tot}} = 2.5 \mu\text{M}$)	0.7	0.7	∞	∞	∞	30	1.5
Lower bound ($C_{\text{tot}} = 3.0 \mu\text{M}$)	0.0	0.0	0.0	0.0	0.0	24	1
Upper bound ($C_{\text{tot}} = 3.0 \mu\text{M}$)	0.7	0.7	∞	∞	∞	30	1.5

Table B.3. Initial guesses for the concentrations (in μM , with $i = 2, \dots, 6$ and $j = 2, \dots, 10$), average length and average width.

$C_{\text{tot}} (\mu\text{M})$	$[Z^{\text{na}}]$	$[Z]$	$[Z_i]$	$[F]$	$[B_j]$	\bar{L}_{fb}^m	\bar{W}_{tot}^f
0.7	0.01	0.01	0	0.01	0.01	1	1
0.8	0.01	0.01	0	0.01	0.01	5	1
1.0	0.01	0.01	0	0.01	0.01	10	1
1.5	0.01	0.01	0	0.01	0.01	20	1
2.0	0.01	0.01	0	0.01	0.01	24	1
2.5	0.01	0.01	0	0.01	0.01	30	1
3.0	0.01	0.01	0	0.01	0.01	30	1

Table B.4. Steady-state monomer concentration ($[Z^{\text{na}}]_{\text{ss}} + [Z]_{\text{ss}}$), and average length (\bar{L}_{tot}^m) and width (\bar{W}_{tot}^m), predicted with our model and observed in experiments [CE5b].

Concentration $C_{\text{tot}} (\mu\text{M})$	Average length (\bar{L}_{tot}^m)		Average width (\bar{W}_{tot}^f)		$[Z^{\text{na}}]_{\text{ss}} + [Z]_{\text{ss}} (\mu\text{M})$		
	Predicted	Observed	Predicted	Observed	Predicted	Observed	Model in [CE5b]
1.0	7	< 27	1.0	< 1.5	0.701	0.7	0.526
2.0	25	24 – 30	1.1	< 1.5	0.699	0.7	0.534
3.0	30	24 – 30	1.3	< 1.5	0.695	0.7	0.536

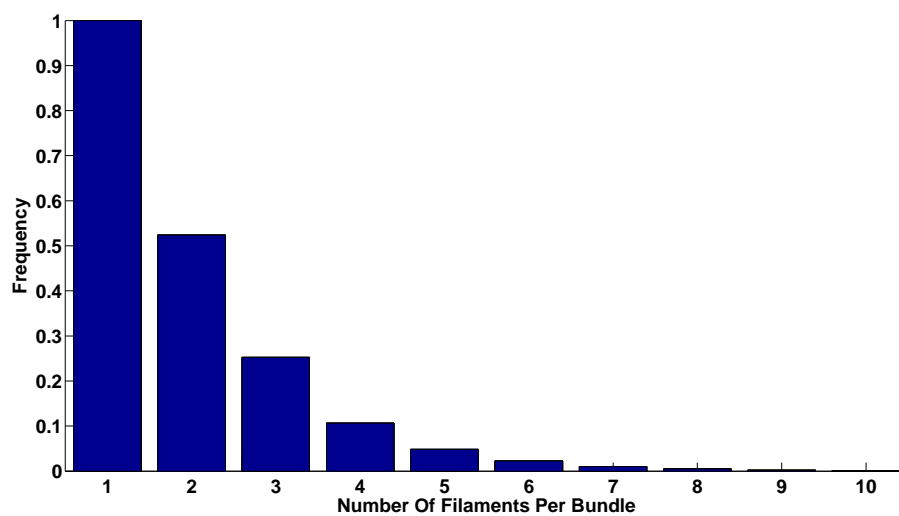


Figure B.1. Convergence of the system at the maximum concentration $C_{\text{tot}} = 10 \mu\text{M}$. Bundles with more than 10 filaments can be considered negligible.

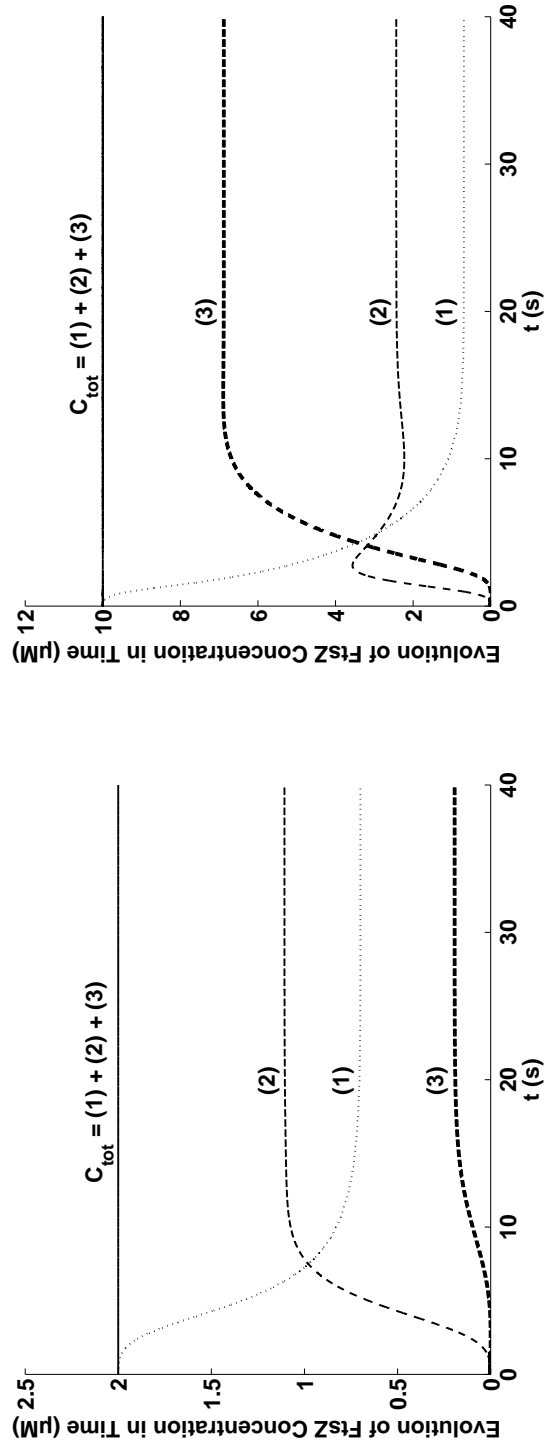


Figure B.2. Temporal evolution of FtsZ concentrations in the monomer, filament and bundle forms (dotted lines, thin dashed lines and thick dashed lines, respectively) for total concentration $C_{\text{tot}} = 2.0 \mu\text{M}$ (left) and $10.0 \mu\text{M}$ (right). The sum of these three concentrations remains constant and equal to C_{tot} at all times t (solid lines).

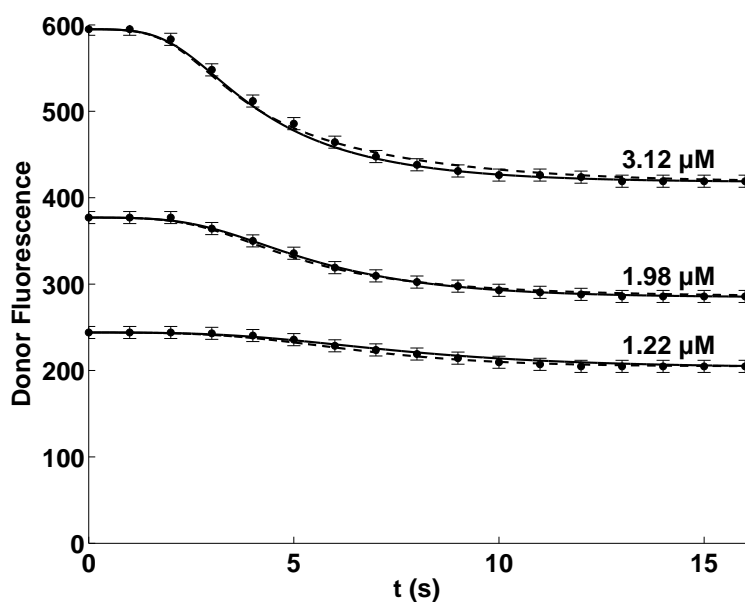


Figure B.3. Kinetics of the initial FtsZ-F268C assembly detected by the Fluorescence Resonance Energy Transfer experiment [CE5b], for three values of total concentration C_{tot} . The data points and solid lines represent the measurements and predictions of the Chen and Erickson (CE) model [CE5b], respectively. The agreement between this model and ours (dashed lines) is to be expected since annealing, bundling and GTP-hydrolysis/dissociation, all which are not accounted for in the CE model, do not become pronounced until the later stages of polymerization.

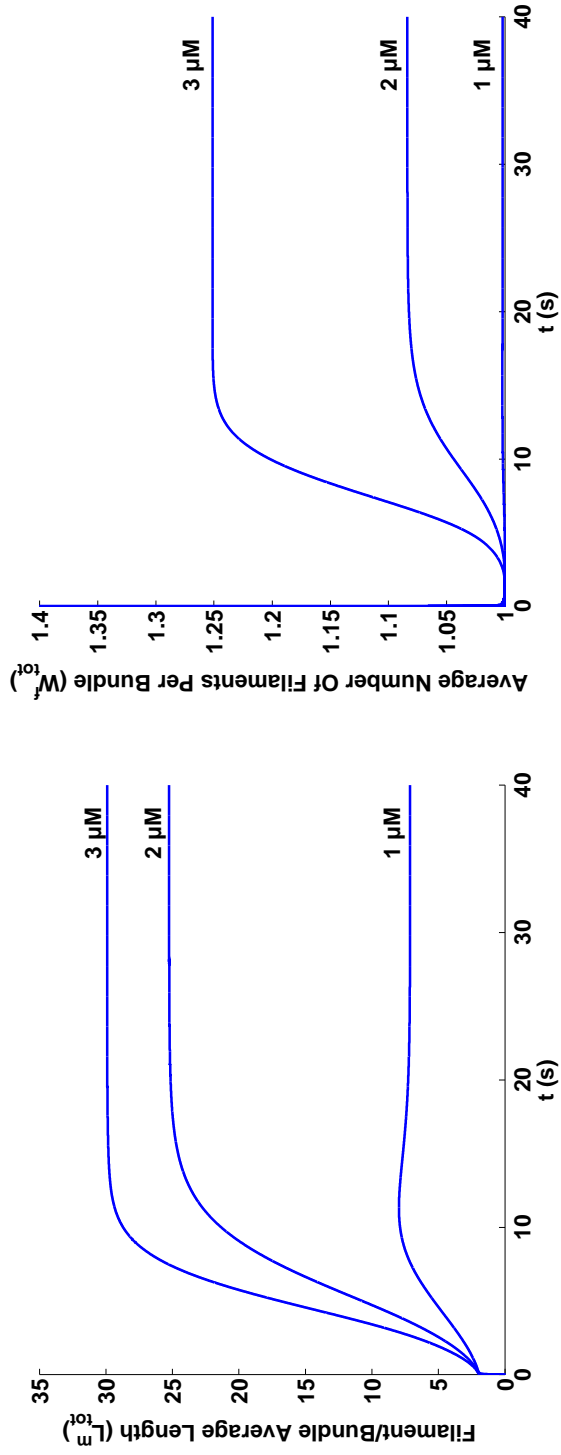


Figure B.4. Temporal evolution of the average number of monomers connected longitudinally into filaments and bundles (left) and the average number of filaments per bundle (right), for $C_{tot} = 1.0, 2.0,$ and $3.0 \mu\text{M}$.

Appendix C

Efficient Multiscale Models of Polymerization Applied to *in vivo* FtsZ Ring Assembly in *Escherichia coli*

C.1 ODEs for *in vitro* Systems

Basic structures (monomers, protofilaments, filaments, thin bundles and wide bundles) and their graphical representations are summarized in Figure C.1. The reactions involved in the short- and long-time kinetics of polymerization and bundling are described in the eponymous sections. The concentrations, $[\cdot]$, of nonactivated (Z^{na}) and activated (Z) monomers, dimers (Z_2) and trimers (Z_3) satisfy a system of ODEs,

$$\frac{d[Z^{\text{na}}]}{dt} = -k_{\text{ac}}^+[Z^{\text{na}}] + k_{\text{ac}}^-[Z] + k_{\text{hy/dis}}^1[F] + k_{\text{hy/dis}}^2([F] + [B_2] + [B_3]) + k_{\text{hy/dis}}^3\Sigma_B, \quad (\text{C.1})$$

$$\begin{aligned} \frac{d[Z]}{dt} = & k_{\text{ac}}^+[Z^{\text{na}}] - k_{\text{ac}}^-[Z] - 2k_{\text{nu}}^+[Z]^2 + 2k_{\text{nu}}^-[Z_2] - k_{\text{el}}^+[Z]([Z_2] + [Z_3] + [F]) \\ & + k_{\text{el}}^-([Z_3] + [F]) - k_{\text{mb}}[Z]\Sigma_B, \end{aligned} \quad (\text{C.2})$$

$$\frac{d[Z_2]}{dt} = k_{\text{nu}}^+[Z]^2 - k_{\text{nu}}^-[Z_2] - k_{\text{el}}^+[Z][Z_2] + k_{\text{el}}^-[Z_3], \quad (\text{C.3})$$

$$\frac{d[Z_3]}{dt} = k_{\text{el}}^+[Z]([Z_2] - [Z_3]) - k_{\text{el}}^-[Z_3]. \quad (\text{C.4})$$

where $\Sigma_B \equiv [B_2] + [B_3] + [B_w]$.

Filaments (F) and thin bundles (B_2 and B_3) are assumed to be present in the same concentrations regardless of their length. Consequently, we set $[F] \equiv [F_{z^-}] = [F_{z^+}] = [F_{f^-}] = [F_{f^+}] = [F_{z^-,f^-}] = [F_{z^+,f^+}]$, $[B_i] \equiv [B_{i;z^-}] = [B_{i;z^+}] = [B_{i;b^-}] = [B_{i;b^+}] = [B_{i;z^-,b^-}] = [B_{i;z^+,b^+}]$ with $i = 2, 3$. Likewise, wide bundles (B_w) are assumed to be present in the same concentrations regardless of their length and number of filaments, so that $[B_w] \equiv [B_{w;z^-}] = [B_{w;z^+}] = [B_{w;b^-}] = [B_{w;b^+}] = [B_{w;z^-,b^-}] = [B_{w;z^+,b^+}]$. Thus, we only define ODEs for $[F]$, $[B_2]$, $[B_3]$ and $[B_w]$,

$$\frac{d[F]}{dt} = k_{\text{el}}^+[Z][Z_3] - k_{\text{an}}^+[F]^2 + k_{\text{an}}^-[F] - k_{\text{bu}}^+[F](2[F] + \Sigma_B) + k_{\text{bu}}^-([B_2] + \Sigma_B) + k_{\text{hy/dis}}^2[F], \quad (\text{C.5})$$

$$\frac{d[B_2]}{dt} = k_{\text{bu}}^-([B_3] - [B_2]) + k_{\text{bu}}^+[F]([F] - [B_2]) + k_{\text{hy/dis}}^2[B_2], \quad (\text{C.6})$$

$$\frac{d[B_3]}{dt} = -k_{\text{bu}}^-[B_3] + k_{\text{bu}}^+[F]([B_2] - [B_3]) + k_{\text{hy/dis}}^2[B_3], \quad (\text{C.7})$$

$$\frac{d[B_w]}{dt} = k_{\text{bu}}^+[F][B_3] - k_{\text{bu}}^+[B_w]^2 + k_{\text{bu}}^-[B_w]. \quad (\text{C.8})$$

Finally, the concentration of monomers in long filaments and bundles (C_{fb}^m) and the concentration of filaments in wide bundles (C_{wb}^f) satisfy

$$\begin{aligned} \frac{dC_{\text{fb}}^m}{dt} &= 4k_{\text{el}}^+[Z][Z_3] + k_{\text{el}}^+[Z][F] - k_{\text{el}}^-[F] - k_{\text{hy/dis}}^1[F] - k_{\text{hy/dis}}^2([F] + [B_2] + [B_3]) \\ &\quad - k_{\text{hy/dis}}^3\Sigma_B + k_{\text{mb}}[Z]\Sigma_B, \end{aligned} \quad (\text{C.9})$$

$$\frac{dC_{wb}^f}{dt} = 4k_{bu}^+[F][B_3] - k_{bu}^-[B_w] + k_{bu}^+[F][B_w]. \quad (\text{C.10})$$

Eqs. C.1–C.10 are subject to initial conditions $[Z^{na}]_0 = C_{tot}$, $[Z]_0 = 0$, $[Z_i]_0 = 0$, $[F]_0 = 0$, $[B_i]_0 = 0$, $[B_w]_0 = 0$, $C_{fb;0}^m = 0$ and $C_{wb;0}^f = 0$, with $i = 2, 3$. These equations form a system of ten ODEs, which is solved with a combination of fourth- and fifth-order Runge-Kutta methods for non-stiff ODEs, implemented in ODE45 Matlab function.

C.1.1 Conservation of mass

Recall that the total concentration of FtsZ monomers in all forms, C_{tot} , is the sum $C_{tot} = C_{mp}^m + C_{fb}^m$ of the concentration of monomers in the monomer and protofilament forms, $C_{mp}^m = [Z^{na}] + [Z] + 2[Z_2] + 3[Z_3]$, and the concentration of monomers in the filament and bundle forms, $C_{fb}^m = \bar{L}_{fb}^m ([F] + 2[B_2] + 3[B_3] + \bar{f}_{wb}[B_w])$. It follows from this definition of C_{mp}^m and Eqs. C.1–C.4 that

$$\begin{aligned} \frac{dC_{mp}^m}{dt} = & -k_{el}^+[Z](4[Z_3] + [F]) + k_{el}^-[F] + k_{hy/dis}^1[F] + k_{hy/dis}^2([F] + [B_2] + [B_3]) \\ & + k_{hy/dis}^3\Sigma_B - k_{mb}[Z]\Sigma_B. \end{aligned} \quad (\text{C.11})$$

Combining Eqs. C.9 and C.11 with the definitions of C_{tot} and C_{fb}^m yields

$$\frac{dC_{tot}}{dt} = 0. \quad (\text{C.12})$$

This proves conservation of the total concentration of FtsZ monomers in all forms, C_{tot} .

C.1.2 Conservation of energy

In common with [RMBST16], our model does not satisfy the detailed (net cycle) balance. That is because the turnover of monomers between the polymer structure and the solution is a nonequilibrium steady-state process (NESS), which violates the detailed balance. While the

reactions we used to model the assembly/disassembly of FtsZ monomers constitute a NESS and satisfy the net cycle balance, the irreversible reactions describing the dissociation of monomers from filaments and bundles imply consumption of energy and conformational changes that destabilize the polymers [Nee15].

Regardless of the nonequilibrium steady state, artificial irreversible reactions $Z + Z_3 \rightarrow F$ and $F + B_3 \rightarrow B_w$ provide a coarsened representation of a transition between a model for short-time kinetics, which describes how fast monomers assemble, and a model for long-time kinetics, which represent slow processes such as annealing, bundling or disassembly of monomers following GTP hydrolysis. For a more detailed discussion, we refer the interested reader to [RMBST16] and the references therein.

C.2 Model Parametrization

We use the *in vitro* study [CE5b] of FtsZ-F268C polymerization to determine values of the reaction rates in ODEs C.1–C.10. The study covers a wide range of FtsZ concentrations, and its findings are in agreement with other investigations.

All but four parameter values are taken from the literature (Table C.1). The remaining four are estimated with a model calibration procedure described in the end of this section. The calibration is carried out on the steady-state, low-concentration ($C_{\text{tot}} = 0.7\text{--}3.0 \mu\text{M}$) data from [CE5b].

Following [CE5b, FG83, RMBST16] and reducing the number of elongation steps from 5 to 2, we assume the forward (k_{el}^+) and backward (k_{el}^-) reaction rates to be independent of a filament length (i.e., to be the same for all i). This is in contrast to the variable bundling rates $k_{\text{bu}}^\pm = k_{\text{bu}}^\pm(\bar{f}_{R_1}, \bar{f}_{R_2}; R_1, R_2, P)$ of a generic bundling reaction,



between two linear chain molecules R_i ($i = 1, 2$) with average number of filaments \bar{f}_{R_i} , which

diffuse and bind laterally to produce a species P . The bundling process, when it occurs, is mainly diffusion-limited [RMBST16]. We show in Section C.6 that, for any two reactants R_i from the set $\{F, B_2, B_3, B_w\}$, the forward bundling rate, $k_{\text{bu}}^+(\bar{f}_{R_1}, \bar{f}_{R_2}; R_1, R_2, P)$, is given by

$$k_{\text{bu}}^+ = \frac{1}{2} k_{\text{bu}}^{0+} F_F(\bar{f}_F) \sum_{i=1}^2 \frac{1}{\sqrt[3]{\bar{f}_{R_i} F_{R_i}(\bar{f}_{R_i})}}, \quad (\text{C.14a})$$

where

$$\bar{f}_{R_i} = \begin{cases} 1 & \text{if } R_i = F \\ 2 & \text{if } R_i = B_2 \\ 3 & \text{if } R_i = B_3 \\ \bar{f}_{\text{wb}} & \text{if } R_i = B_w \end{cases}, \quad i = 1, 2; \quad (\text{C.14b})$$

and

$$F_{R_i} = \sum_{k=0}^7 a_k x_{R_i}^k, \quad x_{R_i} = \frac{1}{2} \ln[3/(2\bar{f}_{R_i})], \quad (\text{C.14c})$$

with values of the constants a_k provided in Section C.6. The lateral association rate of two filaments, k_{bu}^{0+} , corresponds to a reaction involving $R_1 = F$ and $R_2 = F$, such that Eq. C.14 yields $k_{\text{bu}}^+ = k_{\text{bu}}^{0+}$. A value of k_{bu}^{0+} is uncertain but must fall within the accepted range of protein-protein association rates, $2.0 - 7.5 \mu\text{M}^{-1}\text{s}^{-1}$ [CE5b, APS14, NE92]. It is determined with our model calibration procedure. Rate expression C.14 is valid for polymers whose size satisfies the requirement $\bar{f}_{R_i} \in [1.5 \times 10^{-4}, 1.5 \times 10^4]$. This is not overly restrictive, since $\bar{f}_{R_i} < 1.5 \times 10^{-4}$ is equivalent to the absence of filaments and bundles (in which case $k_{\text{bu}}^+ \equiv 0$), and $\bar{f}_{R_i} > 1.5 \times 10^4$ is not observed in the experiments [CE5b].

Our model achieves an orders-of-magnitude computational speed-up by postulating that both elongation and bundling processes can be reduced to just a few steps (up to bundles of

three filaments, in the case of bundling). We demonstrate the accuracy of this approximation in Section C.3.

The depolymerization reaction rates, k_{el}^- , k_{an}^- and k_{bu}^- , are determined from the respective internal energies of filaments and bundles. Specifically, the backward reaction rates for elongation and annealing are given by [LDWS08]

$$k_{\text{el}}^- = k_{\text{nu}}^- e^{-\Delta U_t} \quad \text{and} \quad k_{\text{an}}^- = k_{\text{nu}}^- e^{-\Delta U_m}, \quad (\text{C.15})$$

where ΔU_t and ΔU_m are the increments in the energy of a monomer connected at the end and middle of a filament, respectively. The value of ΔU_t is calculated from the first expression in Eq. C.15, with the values for k_{nu}^- and k_{el}^- taken from [CE5b]. Conservation of energy suggests [LDWS08] that $\Delta U_m = 2\Delta U_t$.

The variable lateral dissociation rates k_{bu}^- in Eq. C.13 are computed as (Section C.6)

$$k_{\text{bu}}^- = k_{\text{bu}}^{0-} \begin{cases} 1 & \bar{L}_{\text{fb}}^m \leq 1 \\ e^{-(\bar{L}_{\text{fb}}^m - 1)U_b} & \bar{L}_{\text{fb}}^m > 1 \end{cases} \quad \text{for } P = B_2 \quad (\text{C.16})$$

and

$$k_{\text{bu}}^- = k_{\text{bu}}^{0-} e^{-\Delta U_b} \begin{cases} 1 & \bar{L}_{\text{fb}}^m \leq 1 \\ e^{-(\bar{L}_{\text{fb}}^m - 1)(U_b + \Delta U_b)} & \bar{L}_{\text{fb}}^m > 1 \end{cases} \quad \text{for } P = B_3. \quad (\text{C.17})$$

The backward reaction with $P \equiv B_w$, $R_1 = F$ and $R_2 = B_w$ in Eq. C.13 does not take place ($k_{\text{bu}}^- = 0$) until $\bar{f}_{\text{wb}} > 1.5 \times 10^{-4}$. After that, in the range of bundle sizes $\bar{f}_{\text{wb}} \in (1.5 \times 10^{-4}, 1.5 \times 10^4)$,

$$k_{\text{bu}}^- = k_{\text{bu}}^{0-} e^{-26(U_b + \Delta U_b) - \Delta U_b}. \quad (\text{C.18})$$

Finally, reaction Eq. C.13 with $P = B_w$, $R_1 = B_w$ and $R_2 = B_w$ is shown to be practically

irreversible within the given parameter range, i.e., its rate is $k_{\text{bu}}^- = 0$. The bond energy per lateral bond, U_b , is set to $U_b = 0.175 k_B T$, which represents both the average of the values reported in [DLS⁺08] for the same strain as in [CE5b] but a different buffer and the value used in [LDWS08] for a strain different from [CE5b] but for the same buffer. Experimental evidence [DLS⁺08, LDWS08] suggests that the bond energy per longitudinal bond is around 100 times larger than the bond energy per lateral bond. Assuming that increments of longitudinal and lateral energies keep the same proportion, we obtain $\Delta U_t / \Delta U_b \sim 100$, which gives $\Delta U_b = 0.0405 k_B T$. The reference dissociation rate k_{bu}^{0-} is one of the four parameters used for model calibration. In the absence of experimental evidence, we have explored a wide range of its values ($0.0 - 500 \text{ s}^{-1}$) during the model calibration.

The choice of the remaining parameters is identical to that in [RMBST16]. Dissociation of monomers following GTP hydrolysis is essentially absent in the beginning of polymerization [CE5b, RM04], and becomes more pronounced as the amount of polymers increases and they interact more frequently with GDP. This dependence of the hydrolysis/dissociation rates on the polymer concentrations is accounted for as

$$k_{\text{hy/dis}}^i = k_{\text{hss/dis}}^i \frac{C_{\text{tot}} - [Z^{\text{na}}] - [Z]}{C_{\text{tot}} - C_{\text{cr}}^1}, \quad i = 1, 2, 3, \quad (\text{C.19})$$

where $C_{\text{cr}}^1 < C_{\text{tot}}$ in the second regime of polymerization. At the beginning of the assembly process, most FtsZ proteins are in the form of nonactivated (Z^{na}) and activated (Z) monomers, such that $[Z^{\text{na}}] + [Z] \approx C_{\text{tot}}$ and $k_{\text{hy/dis}}^i \rightarrow 0$. At steady-state, when the polymer network is formed and GDP deactivates monomers more often, these rates reach their maximum values, $k_{\text{hy/dis}}^i \approx k_{\text{hss/dis}}^i$ for $i = 1, 2, 3$.

The reaction rates controlling dissociation after GTP hydrolysis depend on the location of a deactivated monomer in the filament or bundle. In Table C.1, $k_{\text{hss/dis}}^i$ ($i = 1, 2, 3$) denote values of the hydrolysis rates for filaments and bundles at steady-state. Only the rate for detachment of monomers from filament ends, $k_{\text{hss/dis}}^1$, was calibrated. The rate for detachment of monomers

from the middle of filaments and thin bundles, $k_{\text{hss/dis}}^2$, is set to the average value reported in [CE5b] for turnover of monomers at steady state (half-time of 7 s, i.e., 0.143 s^{-1}), because we assume that it is the depolymerization reaction that happens more often. This assumption is based on two facts: the predominant species observed in the experiment are filaments and thin bundles, and there are more monomers in the middle of filaments and bundles than in their ends. The value of $k_{\text{hss/dis}}^3$ is determined in [APS14] by observing the detachment of nonactivated monomers from thick bundles. These three rates satisfy the following order relations. It takes less energy to break a longitudinal bond at the filament end than two bonds at its middle, therefore, $k_{\text{hss/dis}}^1 > k_{\text{hss/dis}}^2$ [MGPH⁺12]. We use this condition for calibration of $k_{\text{hss/dis}}^1$. The values of $k_{\text{hss/dis}}^2$ for shortening of filaments and thin bundles are equal, because both reactions describe the loss of a monomer in the middle of a filament. The value of $k_{\text{hss/dis}}^3$ is the smallest of the three rates, since the monomers in a bundle can be doubly connected both longitudinally and laterally. In the absence of wide bundles, i.e., for $\bar{f}_{\text{wb}} \leq 1.5 \times 10^{-4}$, $k_{\text{hss/dis}}^3 = 0$.

The rate at which activated monomers in the solution attach themselves to bundles is quantified by the reaction rate constant k_{mb} . The latter serves as the final calibration parameter; its computed value (Table C.1) falls within the range of values of the protein-protein interaction rates of $2\text{--}7.5 \mu\text{M}^{-1}\text{s}^{-1}$. The condition $k_{\text{mb}} < k_{\text{el}}^+ = 6.6 \mu\text{M}^{-1}\text{s}^{-1}$ is also imposed during calibration, because pure longitudinal attachments of monomers to filament ends are more favorable than combinations of both longitudinal and lateral attachments in a monomer-bundle interaction. In the absence of wide bundles, i.e., for $\bar{f}_{\text{wb}} \leq 1.5 \times 10^{-4}$, k_{mb} is assumed to be zero.

C.2.1 Model calibration procedure

The steady-state experiments reported in [CE5b] reveal that

- the amount of FtsZ in monomer form equals the first critical concentration, $C_{\text{cr}}^1 = 0.7 \mu\text{M}$, regardless of the value of C_{tot} in the range between $0.7 \mu\text{M}$ and $3.0 \mu\text{M}$;
- the average length of filaments and bundles at $C_{\text{tot}} = 2.0 \mu\text{M}$ is $\bar{L}_{\text{tot}} = 120.0 \text{ nm}$. Since the

diameter of FtsZ monomers is 4.0 – 5.0 nm [CE5b, Eri09, FFFG12], this corresponds to $\bar{L}_{\text{tot}}^m = 24 - 30$, i.e., the average length of filaments comprising 24 – 30 monomers;

- the value of \bar{L}_{tot}^m remains practically unchanged for $C_{\text{tot}} = 3.0 \mu\text{M}$; and
- the majority of filaments are single-stranded at all levels of C_{tot} in the range between 0.7 μM and 3.0 μM . This suggests an average number of filaments per bundle to be no larger than $\bar{f}_{\text{tot}} = 1.5$.

These observations serve to constrain the model calibration. We employ the Matlab optimization routine `fmincon`, which enables one to find minima of constrained nonlinear multivariable functions. Our calibration procedure is similar to that in [CE5b] and consists of the following steps.

1. Define the coupled functionals to be minimized at steady state:

(a) Eqs. C.1–C.10 with the time derivatives set to 0;

(b) $([Z^{\text{na}}] + [Z]) - C_{\text{cr}}^1$;

(c) $C_{\text{fb}}^m - \bar{L}_{\text{fb}}^m([F] + 2[B_2] + 3[B_3] + C_{\text{wb}}^f)$;

(d) $\bar{f}_{\text{tot}} - \frac{\sum_{i=2}^3 i[Z_i] + \bar{L}_{\text{fb}}^m([F] + \sum_{i=2}^3 i[B_i] + \bar{f}_{\text{wb}}[B_w])}{\sum_{i=2}^3 i[Z_i] + \bar{L}_{\text{fb}}^m([F] + \sum_{i=2}^3 [B_i] + [B_w])}$.

2. Define a set of C_{tot} -dependent constraints (for $C_{\text{tot}} = 0.7, 0.8, 1.0, 1.5, 2.0, 2.5$, and 3.0 μM):

(a) lower and upper bounds for the parameters to be calibrated (Table C.2);

(b) lower and upper bounds for the monomer concentration, average length and average number of filaments per bundle (Table C.3);

(c) order relations for the average length, $\bar{L}_{\text{fb}}^m(C_{\text{tot}})$, and number of filaments per bundle, $\bar{f}_{\text{tot}}(C_{\text{tot}})$: the higher the total concentration C_{tot} (in μM), the longer and wider

the filaments and bundles are, i.e., $\bar{L}_{\text{fb}}^m(0.7) < \bar{L}_{\text{fb}}^m(0.8) < \bar{L}_{\text{fb}}^m(1.0) < \bar{L}_{\text{fb}}^m(1.5) < \bar{L}_{\text{fb}}^m(2.0) < \bar{L}_{\text{fb}}^m(2.5) < \bar{L}_{\text{fb}}^m(3.0)$ and $\bar{f}_{\text{tot}}(0.7) < \bar{f}_{\text{tot}}(0.8) < \bar{f}_{\text{tot}}(1.0) < \bar{f}_{\text{tot}}(1.5) < \bar{f}_{\text{tot}}(2.0) < \bar{f}_{\text{tot}}(2.5) < \bar{f}_{\text{tot}}(3.0)$.

3. Make initial guesses for the optimization variables (Table C.2) and functionals (see Table C.4).
4. Estimate the parameters by run `fmincon` with the Sequential Quadratic Programming algorithm, `sqp`, and tolerance 10^{-8} . Use the estimates as new initial guesses and repeat 20 times to get an accurate calibration.

This calibration procedure yields the values of k_{bu}^{0+} , k_{bu}^{0-} , k_{mb} and $k_{\text{hss/dis}}^1$ reported in Table C.1.

C.3 Model Validation

With the parameter values fixed in the previous section, we use our model (hereafter referred to as Average-Features Model or AFM) to obtain fit-free predictions of the FtsZ polymerization dynamics at low concentration ($C_{\text{tot}} = 0.7 - 3.0 \mu\text{M}$) and its steady-state limit at high concentrations ($C_{\text{tot}} = 3.0 - 10.0 \mu\text{M}$). Comparison with the corresponding data from the Fluorescence Resonance Energy Transfer experiment [CE5b] serves to validate the model.

C.3.1 Transient, low-concentration phenomena

Short-time kinetics.

Annealing, bundling and GTP-hydrolysis/dissociation reactions are thought to be absent during the first seconds of polymerization. The experiment [CE5b] yielded information about the temporal evolution of FtsZ-F268C that assembles into filaments or bundles. Fluorescence is defined in terms of the concentrations of nonactivated (Z^{na}) and activated (Z) monomers as $\mathcal{F} = \alpha_1([Z^{\text{na}}] + [Z]) + \alpha_2(C_{\text{tot}} - [Z^{\text{na}}] - [Z])$, where the parameters α_1 and α_2 represent the fluorescence of monomers and proteins in polymer form, respectively. Figure C.2 exhibits the temporal evolution of \mathcal{F} for $C_{\text{tot}} = 1.22, 1.98$ and $3.12 \mu\text{M}$ observed in [CE5b] and predicted

with AFM. The agreement between the two indicates the model's validity at early times. The plateau of the intensity curves corresponds to the situation in which all FtsZ-F268C proteins are assembled, except for monomers with concentration similar to the first critical concentration, $C_{\text{cr}}^1 = 0.7 \mu\text{M}$. Although C_{cr}^1 is the same regardless of C_{tot} , the fluorescence intensities for each plateau are different. That is because the fluorescence \mathcal{F} is proportional to the amount of polymerized FtsZ-F268C and the latter increases with C_{tot} . The agreement between the data and AFM confirms that the reduced version of elongation process (up to trimers) is sufficient to make accurate predictions.

Long-time kinetics.

The predicted steady-state statistics of FtsZ assembly, i.e., \bar{L}_{tot}^m , \bar{f}_{tot} and $C_{\text{cr}}^1 = [Z^{\text{na}}]_{\text{ss}} + [Z]_{\text{ss}}$, are compared with their observed counterparts in Table C.5. Since the steady-state data were used for parameter identification, it is to be expected that the steady-state model predictions are in agreement with observations [CE5b]: the average length for $C_{\text{tot}} = 2.0 - 3.0 \mu\text{M}$ is between 24 and 30 monomers; the majority of the filaments are single-stranded for low concentrations, i.e., $\bar{f}_{\text{tot}} < 1.5$ for $C_{\text{tot}} < 3.0 \mu\text{M}$; and $[Z^{\text{na}}]_{\text{ss}} + [Z]_{\text{ss}} = 0.7 \mu\text{M}$, which coincides with the value reported in [CE5b] for C_{tot} in the range between $0.7 \mu\text{M}$ and $3.0 \mu\text{M}$. While such an agreement is not surprising, it is worthwhile pointing out that the model in [CE5b], which was designed to reproduce these experiments, underestimates the first critical concentration, yielding $[Z^{\text{na}}]_{\text{ss}} + [Z]_{\text{ss}} \approx 0.5 \mu\text{M}$. This underestimation is due to both the dissociation of monomers from filaments following GTP hydrolysis and the effects of bundling on the turnover rate. These two processes are explicitly accounted for in our model, but are absent in the CE model. The agreement between the data and AFM confirms that the reduced version of bundling process (up to bundles of three filaments) is sufficient to make accurate predictions.

C.3.2 Steady-state, high-concentration phenomena

Average size of filaments and bundles.

Under physiologically relevant conditions, $C_{\text{tot}} = 5.0 - 10.0 \mu\text{M}$, AFM captures the observed tendency of filaments to keep fixed length, $\bar{L}_{\text{tot}}^m \approx 32 - 33$ subunits at steady-state, regardless of the value of C_{tot} . Tables C.5 and C.6 show that, for $C_{\text{tot}} = 2.0 - 10.0 \mu\text{M}$, the predicted average length is $\bar{L}_{\text{tot}}^m = 25 - 33$ subunits (125 – 165 nm), which is within the well established range of 100 – 200 nm [Eri09, CBRE5a, DLS⁺08, HLB⁺08, PIN⁺09, RSE01].

Almost all filaments remain single-stranded when $C_{\text{tot}} < 2.0 \mu\text{M}$ (Table C.5). For larger concentrations, up to $C_{\text{tot}} = 10.0 \mu\text{M}$, and for various buffers and FtsZ strains, filaments dominate and the majority of bundles consist of two filaments. All the computed values of \bar{f}_{tot} in Table C.6 are below 2, which is in agreement not only with [CE5b] but also with other experiments [CE09, DLS⁺08, HLB⁺08, RSE01].

Concentration of monomers at steady state.

In the physiologically relevant range of $C_{\text{tot}} = 5.0 - 10.0 \mu\text{M}$, AFM predicts the steady-state concentration of monomers to be $[Z^{\text{na}}]_{\text{ss}} + [Z]_{\text{ss}} \approx 0.7 \mu\text{M}$ (Table C.6). This matches the observed monomer concentration [CE5b] and equals the first critical concentration, C_{cr}^1 . The model presented in [CE5b] underestimates this observation, predicting a value of $[Z^{\text{na}}]_{\text{ss}} + [Z]_{\text{ss}} \approx 0.5 \mu\text{M}$.

Second critical concentration.

An appreciable decrease in the fluorescence intensity at $C_{\text{tot}} = 3.0 \mu\text{M}$ (or, more generally, at $C_{\text{tot}} = 2.0 - 4.0 \mu\text{M}$, depending on the concentration of Mg^{2+} contained in the buffer) was observed, but not explained, in [CE5b]. A subsequent kinetics model [LDWS08] utilized the experimental data from [CBRE5a] and [CE5b] to describe this phenomenon by identifying a critical concentration, C_{cr}^2 , at which the presence of bundles becomes pronounced. The model in [LDWS08] does not specify the value of C_{cr}^2 and, crucially, predicts formation of bundles comprised two or three filaments at low concentrations ($C_{\text{tot}} = 2.0 \mu\text{M}$), which is not supported

by the observations. Our model correctly predicts the ratio of an average number of monomers per filaments to an average number of filaments per bundle for a range of C_{tot} . This ratio reaches its maximum at $C_{\text{tot}} = 3.5 \mu\text{M}$, the critical concentration C_{cr}^2 after which the longitudinal growth (elongation and/or annealing) ceases to dominate the lateral growth (bundling) and bundles become an important factor in the overall kinetics (Fig. C.3). Our predicted value of $C_{\text{cr}}^2 = 3.5 \mu\text{M}$ falls within the experimentally observed range of $2 - 4 \mu\text{M}$.

C.4 Comparison of Computational Costs

The maximum number of filaments per bundle increases with the total concentration of FtsZ monomers in all forms, C_{tot} . The resulting growth in the number of bundle sizes requires more ODEs comprising the model [RMBST16], which raises the latter’s computational cost (Fig. C.4). The computational time required to reach steady-state with the model [RMBST16] increases linearly with the total concentration in both *in vitro* ($C_{\text{tot}} = 0.7 - 20 \mu\text{M}$, left column of Fig. C.4) and *in vivo* ($C_{\text{tot}} = 0.7 - 200 \mu\text{M}$, right column of Fig. C.4) regimes. Thus, the computational cost of the simulations of the first 40 s of *in vitro* polymerization increases six-fold as C_{tot} increases from $0.7 \mu\text{M}$ to $20 \mu\text{M}$. This degradation in the computational efficiency of the model [RMBST16] is due to the concomitant increase in both the number of species and in the number of ODEs needed to describe their dynamics (Fig. C.4). This is in contrast to AFM, which comprises 10 ODEs regardless of the value of total concentration C_{tot} . Consequently, its computational cost remains the same over the full range of C_{tot} ; it is more than half of the lowest computational cost of the model [RMBST16] with $C_{\text{tot}} = 0.7 \mu\text{M}$.

The computational efficiency of our model is magnified when it is used to simulate *in vivo* polymerization phenomena, which are characterized by high total concentrations. For $C_{\text{tot}} = 200 \mu\text{M}$, AFM is about two orders-of-magnitude faster than its competitor [RMBST16] (right column of Fig. C.4).

C.4.1 Comparison of *in vivo* predictions

From all previous works presented in Table 3.1, we see that [RMBST16] is able to make accurate predictions for the range of concentrations $C_{\text{tot}} = 3 - 10 \mu\text{M}$. By averaging the concentration and size of bundles, we have seen that AFM makes similar predictions at a lower computational cost. In Section C.5, we present variations associated to *in vivo* assembly to our *in vitro* AFM version such as the influence of the membrane or the presence of FtsA, ZipA and ZapA proteins. Introducing those modifications in the *in vitro* model from [RMBST16], we can compare both models and see that our current work improves the applicability range, the ability to predict ring features and the computational cost in a complex *in vivo* scenario.

All variations presented in C.5 are introduced in [RMBST16] except the ones related to the bundling rates that are inherent to AFM. We keep the constant values for forward bundling rates from [RMBST16] and modify the backward bundling rate to be able to introduce the influence of ZapA protein. Our study in [RMBST16] did not distinguish between the different backward bundling rates associated to the lateral dissociation of two filaments, a filament and a bundle or two bundles, therefore, we redefine k_{bu}^- as follows,

$$k_{\text{bu}}^- = k_{\text{bu}}^{0-} e^{-\Delta U_b^{\text{mod}}} \begin{cases} 1 & \bar{L}_{\text{fb}}^m \leq 1 \\ e^{-(\bar{L}_{\text{fb}}^m - 1)(U_b^{\text{mod}})} & \bar{L}_{\text{fb}}^m > 1 \end{cases} \quad (\text{C.20})$$

where U_b^{mod} and ΔU_b^{mod} are the modified bond energy per lateral bond and the modified increment of lateral energy, respectively. We define U_b^{mod} as the average of the bond energies per lateral bond correspondent to the three aforementioned types of dissociation, and ΔU_b^{mod} as the average increment of lateral energies associated to the last two dissociations in a similar way that are presented for AFM in C.7, i.e., $U_b^{\text{mod}} = [U_b + (U_b + \Delta U_{b,\text{ZapA}}) + (U_b + 2\Delta U_{b,\text{ZapA}})]/3$ and $\Delta U_b^{\text{mod}} = (\Delta U_{b,\text{ZapA}} + 2\Delta U_{b,\text{ZapA}})/2$.

Table C.7 shows the timing predicted by the *in vivo* version of [RMBST16] in comparison

to AFM predictions. Both intermediate and long kinetics predicted by [RMBST16] are not accurate; except for the attachment time of polymers to the membrane, t_{att} , the rest of the times are much shorter than the ones that have been observed experimentally.

Table C.8 shows correct predictions from both models for the amount of FtsZ attached to the membrane and the average length of the polymers at the steady state. The concentration of monomers at the steady state and the number of filaments per bundles, however, are overestimated and underestimated, respectively, by [RMBST16].

The computational time required by the *in vivo* version of [RMBST16] is 64.11 – 174.74 seconds (37-61 ODEs) for the range of concentrations $C_{\text{tot},C;0} = 6 - 18 \mu\text{M}$, whereas AFM only spends around 12 – 13 seconds (11 ODEs) regardless of the concentration, i.e., 6-14 times shorter. The average number of filaments per bundle predicted by [RMBST16] is 2-3 times lower than the number predicted by AFM and the ones estimated from the thick bundles/clusters observed experimentally. It means that the computational time would be even much larger for an improved *in vivo* version of [RMBST16] that predicted correct bundle sizes, since it would require even more ODEs.

Table C.9 includes the time required by our computer, Windows 10 Home, Intel(R) Core(TM) i7-6700HQ CPU 2.60 GHz, to execute six different MATLAB tasks: LU, perform LU decomposition of a full matrix; FFT, perform fast Fourier transform of a full vector; ODE, solve van der Pol equation with ODE45 subroutine; Sparse, solve a symmetric sparse linear system; 2-D, plot Lissajous curves; and 3-D, display colormapped peaks subroutine with clipping and transforms. We have used version R2016b of MATLAB and the subroutine bench, that measures the execution speed of six different MATLAB tasks and compares it to the speed of several other computers. Since the majority of the calculations performed by this study have required the use of the ODE45 subroutine, we highlight the correspondent computational times to that task. As we can see, our computer is one of the fastest.

Some of the MATLAB codes developed for this study are available for download in the github repository ‘AlvaroRuizMartinez/ecoliproject.github’.

C.5 AFM-based Description of Z-ring Formation

C.5.1 Physiological considerations

In *Escherichia coli* cells, the Ter linkage, a chain made of several proteins (MatP, ZapA, and ZapB), coordinates localization of both the Z-ring and the Ter macrodomain region of the chromosome at the center of a mother cell. Once a daughter cell is born, its correspondent linkage is localized at the nucleoid periphery close to one of its poles. Then, the Ter region moves to the center of the nucleoid and promotes Z-ring formation in the middle of a cell [MPS⁺08, BBW⁺14, MB15, EBD⁺12]. While this happens, FtsZ proteins in monomeric or protofilament forms diffuse in the cytoplasm. FtsA and ZipA proteins are responsible for the attachment of FtsZ to the membrane, while ZapA proteins increase the stiffness of FtsZ bundles.

Cell shape.

Since our model is designed for well-mixed systems, we focus on the concentration of FtsZ proteins in a region in the middle of the cell and close to the membrane (Fig. C.5). We conceptualize this region, CM, as a torus of elliptical cross-section with axial width w_a and radial width w_r , so that its volume is

$$V_{\text{CM}} = \underbrace{2\pi \left(R - \frac{w_r}{2} \right)}_{\text{ring's length}} \underbrace{\pi \frac{w_a}{2} \frac{w_r}{2}}_{\text{ring's cross-section}} \quad (\text{C.21})$$

where R is the cell's radius. The cell of length L is composed of two semi-spherical caps, CC, and a cylindrical middle, MID, whose volumes are V_{CC} and V_{MID} , respectively (Fig. C.5). Then, the cell's volume is

$$V_{\text{CELL}} = \underbrace{2 \frac{2}{3} \pi R^3}_{2 \times V_{\text{CC}}} + \underbrace{(L - 2R) \pi R^2}_{V_{\text{MID}}}. \quad (\text{C.22})$$

The cell birth-growth-division process takes 20 min, with the period between Z-ring positioning in the middle and the onset of septation occurring from 4.5 min to 8.5 min after the cell's birth [TRC⁺11]. We focus on the latter time interval, during which the cell length increases from $L \approx 2.8 \mu\text{m}$ to $\approx 3.2 \mu\text{m}$ [RHK⁺14]. For this reason, we keep both L and R constant. Their values, as well as values of the other parameters introduced in this section, are collated in Table C.10.

Interactions between FtsZ species and the membrane.

The process of monomers interacting in the cytosol to form protofilaments is not explicitly modeled in AFM. Instead, following [SML08], we assume that monomers and first protofilaments diffuse in the cytosol and, upon attaching to the membrane at the midcell, they anneal and bundle to form the ring.

Let $C_{\text{tot},C;0} = N_{\text{FtsZ}}^{\text{cell}}/V_{\text{CELL}}$ denote the total cytosolic concentration of FtsZ molecules (in all forms) in the beginning of the assembly process, defined as the ratio of the total number of molecules in a cell ($N_{\text{FtsZ}}^{\text{cell}}$) to the cell volume (V_{CELL}). Let $C_{\text{tot},\text{CM}}^{\text{a}}$ and $C_{\text{tot},\text{CM}}^{\text{d}}$ designate the concentrations of FtsZ species (in all forms) that are respectively attached to and detached from the membrane within the CM region of the cell (Fig. C.5). As FtsZ molecules attach to the membrane within the CM region, the total cytosolic concentration of detached FtsZ molecules in the cell ($C_{\text{tot},C}$) decreases,

$$C_{\text{tot},C} = C_{\text{tot},C;0} - C_{\text{tot},\text{CM}}^{\text{a}} \frac{V_{\text{CM}}}{V_{\text{CELL}}}. \quad (\text{C.23})$$

This relation assumes that during the ring assembly, which takes approximately 1 min [ACL97, SM98], the cell produces no appreciable amount of new FtsZ molecules. This is a reasonable assumption, given that this time interval is a small fraction of the 20-min life cycle during which the cell doubles the initial number of FtsZ proteins for its two descendants.

Detached FtsZ molecules in the CM region are assumed to be in the form of either monomers or protofilaments, so that their total concentration $C_{\text{tot},\text{CM}}^{\text{d}}$ is the sum of the two,

$C_{\text{tot,CM}}^{\text{d}} = C_{\text{m,CM}}^{\text{d}} + C_{\text{p,CM}}^{\text{d}}$, with $C_{\text{m,CM}}^{\text{d}}$ and $C_{\text{p,CM}}^{\text{d}}$ denoting the local (within CM) concentrations of monomers and protofilaments, respectively. Henceforth, we assume that $C_{\text{tot,CM}}^{\text{d}} = C_{\text{tot,C}}$ since CM region is a subvolume of the entire cell; also $C_{\text{m,CM}}^{\text{d}} = [Z^{\text{na}}] + [Z]$, therefore, the concentration of detached protofilaments in the CM region is defined as $C_{\text{p,CM}}^{\text{d}} = C_{\text{tot,CM}}^{\text{d}} - C_{\text{m,CM}}^{\text{d}} = C_{\text{tot,CM}} - [Z^{\text{na}}] - [Z]$. Experimental evidence [LM14] suggests that single monomers do not attach to the membrane, while larger structures do, i.e., $C_{\text{tot,CM}}^{\text{a}} \approx C_{\text{p,CM}}^{\text{a}}$. Among the latter, FtsZ dimers are shown to be too weak [CE5b], so that trimers are the smallest attached protofilaments in our model. The rate with which FtsZ trimers are attached to the membrane is given by

$$k_{\text{bind}}^+ \frac{C_{\text{p,CM}}^{\text{d}}}{3} (C_{\text{tot,CM}}^{\text{a,max}} - C_{\text{tot,CM}}^{\text{a}}), \quad (\text{C.24})$$

where k_{bind}^+ is a rate constant [DRRv13]; and a value of the maximal concentration of FtsZ (in all forms) attached to the membrane at the midcell, $C_{\text{tot,CM}}^{\text{a,max}}$, is estimated from the following considerations.

In vivo model in [DRRv13] defined a fix number of FtsA and ZipA molecules per cell. We, however, set constant FtsZ/FtsA and FtsZ/ZipA cytosolic concentration ratios from experimental data so the number of binding sites is proportional to the FtsZ concentration. The ratio of cytosolic concentrations of FtsA and FtsZ molecules is $[\text{FtsA}]_{\text{C}}/[\text{FtsZ}]_{\text{C}} = 1/5$ [RVM03]; and the number of ZipA and FtsZ molecules in a cell are, respectively, $N_{\text{ZipA}}^{\text{cell}} = 100 - 1000$ and $N_{\text{FtsZ}}^{\text{cell}} = 5000 - 15000$ [HdB97, RVM03, EAO10]. This gives a range $[\text{ZipA}]_{\text{C}}/[\text{FtsZ}]_{\text{C}} \in [100/15000, 1000/5000] = [0.007, 0.2]$, of which we take an intermediate value $[\text{ZipA}]_{\text{C}}/[\text{FtsZ}]_{\text{C}} = 0.1$. Approximately 30% of ZipA is incorporated into the ring [SMSE02]; the same percentage of FtsA is assumed in our model. Therefore, the number of binding sites in the CM region is

$$\begin{aligned} N_{\text{bs}} &= 0.3 ([\text{FtsA}]_{\text{C}} + [\text{ZipA}]_{\text{C}}) \frac{N_{\text{A}} V_{\text{CELL}}}{10^{21}} = 0.3 \left(\frac{1}{5} C_{\text{tot,C;0}} + \frac{1}{10} C_{\text{tot,C;0}} \right) \frac{N_{\text{A}} V_{\text{CELL}}}{10^{21}} \\ &= \frac{9}{100} \frac{C_{\text{tot,C;0}} N_{\text{A}} V_{\text{CELL}}}{10^{21}} = \frac{9}{100} N_{\text{FtsZ}}^{\text{cell}}, \end{aligned} \quad (\text{C.25})$$

where N_A is Avogadro's number and $C_{\text{tot},C;0}$ has been taken as a reference for the FtsZ/FtsA and FtsZ/ZipA ratios such that $[\text{FtsZ}]_C = C_{\text{tot},C;0}$.

We estimate a molecule of FtsA or ZipA to include 3 – 4 FtsZ monomers. (This is consistent with an average distance, $d_{\text{FtsA-ZipA}}$, between the FtsA and ZipA molecules homogeneously distributed at the membrane in the CM region. Indeed, for a midrange value $N_{\text{FtsZ}}^{\text{cell}} = 10000$,

$$d_{\text{FtsA-ZipA}} = \sqrt{\frac{\text{Midcell area}}{N_{\text{bs}}}} = \sqrt{\frac{2\pi R w_a}{N_{\text{bs}}}} = 16.7\text{nm}, \quad (\text{C.26})$$

which corresponds to the length of a FtsZ protofilament made of 3 – 4 monomers of 5 nm diameter per monomer.) Taking the midrange value of 3.5 FtsZ monomers per molecule of FtsA or ZipA, the maximal concentration of FtsZ (in all forms) attached to the membrane at the midcell is

$$C_{\text{tot,CM}}^{\text{a,max}} = 3.5 \frac{N_{\text{bs}}}{V_{\text{CM}}} \frac{10^{21}}{N_A} \approx 0.315 \frac{V_{\text{CELL}}}{V_{\text{CM}}} C_{\text{tot},C;0}. \quad (\text{C.27})$$

This estimate is in agreement with an estimate that 30 – 35% of total FtsZ is incorporated into the ring [SMSE02, AGFE04].

Finally, we allow the shortest and weakest protofilaments, i.e., dimers, to detach at the rate

$$k_{\text{bind}}^-[Z_2]. \quad (\text{C.28})$$

Bundling.

The FtsZ assembly process in wild-type cells remains unknown. However, there are numerous of *in vitro* and *in vivo* studies that show filaments forming bundles and more complex structures [GVJ⁺05, LRE00, DPLW10, HDHJ13, BCH⁺13, APS14]. Following a recent *in vivo* study [CBPX16], which suggests a heterogeneous and discontinuous three-dimensional ring structure made of FtsZ clusters, we propose a two-stages bundling process:

1. FtsZ filaments, F , and first bundles, B_2 and B_3 , associate laterally to form two-dimensional sheets upon attaching to the membrane, as observed *in vitro* [ETTB96, APS14] and *in vivo* [LTBJ07]. Wider bundles, B_w , grow in axial direction as long as the concentration of FtsZ proteins at the membrane, $C_{\text{tot,CM}}^a$, increases. They are also allowed to grow in radial direction by pushing and lifting each other from the membrane. That results in formation of bundles partially attached to the membrane with more degrees of freedom to rearrange into three-dimensional cross-linked clusters along the CM region.
2. In the second stage, all binding sites at the membrane are occupied by FtsZ proteins and there is not much space for wide bundles to grow in two dimensions. Wide bundles only form three-dimensional cross-linked clusters.

C.5.2 ODEs for *in vivo* systems

In vivo polymerization and bundling processes are represented by the following ODEs. Concentrations in the CM region, *in vivo* reaction rates, and parameters θ and χ are defined in this Section. Section C.7 includes information about *in vivo* bundling rates.

$$\frac{d[Z^{\text{na}}]}{dt} = -k_{\text{ac}}^+[Z^{\text{na}}] + k_{\text{ac}}^- [Z] + k_{\text{hy/dis}}^1 [F] + k_{\text{hy/dis}}^2 \left([F] + \sum_{i=2}^3 [B_i] \right) + k_{\text{hy/dis}}^3 \left(\sum_{i=2}^3 [B_i] + [B_w] \right), \quad (\text{C.29})$$

$$\begin{aligned} \frac{d[Z]}{dt} = & k_{\text{ac}}^+[Z^{\text{na}}] - k_{\text{ac}}^- [Z] - 2k_{\text{nu}}^+[Z]^2 + 2k_{\text{nu}}^- [Z_2] - k_{\text{el}}^+[Z] \sum_{i=2}^3 [Z_i] - k_{\text{el}}^+[Z][F] + k_{\text{el}}^- [Z_3] \\ & + k_{\text{el}}^- [F] - k_{\text{mb}}[Z] \left(\sum_{i=2}^3 [B_i] + [B_w] \right), \end{aligned} \quad (\text{C.30})$$

$$\frac{d[Z_2]}{dt} = k_{\text{nu}}^+[Z]^2 - k_{\text{nu}}^- [Z_2] - k_{\text{el}}^+[Z][Z_2] + k_{\text{el}}^- [Z_3] - k_{\text{bind}}^- [Z_2], \quad (\text{C.31})$$

$$\frac{d[Z_3]}{dt} = k_{\text{el}}^+[Z]([Z_2] - [Z_3]) - k_{\text{el}}^- [Z_3] + \frac{1}{3}k_{\text{bind}}^+ C_{\text{p,CM}}^{\text{d}} (C_{\text{tot,CM}}^{\text{a,max}} - C_{\text{tot,CM}}^{\text{a}}), \quad (\text{C.32})$$

$$\begin{aligned} \frac{d[F]}{dt} = & k_{\text{el}}^+[Z][Z_3] - k_{\text{an}}^+[F]^2 + k_{\text{an}}^- [F] - k_{\text{bu}}^+[F] \left(2\theta[F] + \theta \sum_{i=2}^3 [B_i] + \chi[B_w] \right) + \\ & k_{\text{bu}}^- (2[B_2] + [B_3] + [B_w]) + k_{\text{hy/dis}}^2 [F], \end{aligned} \quad (\text{C.33})$$

$$\frac{d[B_2]}{dt} = k_{\text{bu}}^- ([B_3] - [B_2]) + \theta k_{\text{bu}}^+[F]([F] - [B_2]) + k_{\text{hy/dis}}^2 [B_2], \quad (\text{C.34})$$

$$\frac{d[B_3]}{dt} = -k_{\text{bu}}^- [B_3] + \theta k_{\text{bu}}^+[F]([B_2] - [B_3]) + k_{\text{hy/dis}}^2 [B_3], \quad (\text{C.35})$$

$$\frac{d[B_w]}{dt} = \theta k_{\text{bu}}^+[F][B_3] - \chi k_{\text{bu}}^+[B_w]^2 + k_{\text{bu}}^- [B_w]. \quad (\text{C.36})$$

We also define ODEs for the concentration of monomers in long filaments and bundles attached to the membrane, $C_{\text{fb,CM}}^{m,\text{a}}$, and the concentration of filaments in wide bundles at the membrane, $C_{\text{wb,CM}}^{f,\text{a}}$,

$$\begin{aligned} \frac{dC_{\text{fb,CM}}^{m,\text{a}}}{dt} = & 4k_{\text{el}}^+[Z][Z_3] + k_{\text{el}}^+[Z][F] - k_{\text{el}}^- [F] - k_{\text{hy/dis}}^1 [F] - k_{\text{hy/dis}}^2 \left([F] + \sum_{i=2}^3 [B_i] \right) - \\ & k_{\text{hy/dis}}^3 \left(\sum_{i=2}^3 [B_i] + [B_w] \right) + k_{\text{mb}}[Z] \left(\sum_{i=2}^3 [B_i] + [B_w] \right), \end{aligned} \quad (\text{C.37})$$

$$\frac{dC_{wb,CM}^{f,a}}{dt} = 4\theta k_{bu}^+[F][B_3] - k_{bu}^-[B_w] + \chi k_{bu}^+[F][B_w]. \quad (C.38)$$

Finally, the ODE for the concentration of FtsZ in polymer form attached to the membrane is defined as follows,

$$\begin{aligned} \frac{dC_{tot,CM}^a}{dt} = & 2k_{nu}^+[Z]^2 - 2k_{nu}^-[Z_2] + k_{el}^+[Z] \left(\sum_{i=2}^3 [Z_i] + [F] \right) - k_{el}^-([Z_3] + [F]) - k_{hy/dis}^1[F] - \\ & k_{hy/dis}^2 \left([F] + \sum_{i=2}^3 [B_i] \right) - k_{hy/dis}^3 \left(\sum_{i=2}^3 [B_i] + [B_w] \right) + k_{mb}[Z] \left(\sum_{i=2}^3 [B_i] + [B_w] \right) + \\ & k_{bind}^+ C_{p,CM}^d (C_{tot,CM}^{a,max} - C_{tot,CM}^a) - 2k_{bind}^- [Z_2]. \end{aligned} \quad (C.39)$$

Eqs. C.29–C.39 are subject to initial conditions $[Z^{na}]_0 = C_{m,CM;0}^d$, $[Z]_0 = 0$, $[Z_i]_0 = 0$, $[F]_0 = 0$, $[B_i]_0 = 0$, $[B_w]_0 = 0$, $C_{fb,CM;0}^{m,a} = 0$, $C_{wb,CM;0}^{f,a} = 0$ and $C_{tot,CM;0}^a = 0$, with $i = 2, 3$.

The system of 11 ODEs is solved with `ODE15s` Matlab function for stiff problems. It is a variable-step, variable-order (VSVO) solver based on the numerical differentiation formulas (NDFs) of orders 1 to 5.

C.5.3 Model parametrization

First critical concentration.

An experimentally determined range of the first critical concentration for FtsZ mutants, $C_{cr,mut}^1 = 0.1 - 0.7 \mu\text{M}$ (the majority of mutants from [CBRE5a]) and the mutant from [CE5b]), is lower than the values observed in wild-type FtsZ proteins, $C_{cr,wt}^1 = 0.9 - 1.25 \mu\text{M}$ [GJV⁺03, CBRE5a]. In our model of *in vivo* wild-type FtsZ assembly, we take an intermediate value in the latter range, $C_{cr,wt}^1 = 1.1 \mu\text{M}$, instead of the value $C_{cr}^1 = 0.7 \mu\text{M}$ used in our model of the mutant FtsZ-F268C.

Bundling.

In both stages of the bundling process described above, ZapA tetramers contribute to increase the size and the rigidity of the two-dimensional sheets and the three-dimensional cross-linked clusters. Section C.7 shows the influence of these structural changes on the forward and backward bundling rates.

Crowding at the membrane increases reaction rates of a reaction-limited bundling, i.e., when proteins are small and crowding favors protein-protein association; on the other hand, crowding reduces reaction rates once the bundling reaction becomes diffusion-limited, i.e., when molecules are large [Eil01]. As in the case of *in vitro* polymerization, we treat bundling as a diffusion-limited reaction. Thus, the bundling reaction rate is reduced by a concentration-dependent factor θ that is defined as

$$\theta = 1 + (\chi - 1) \frac{C_{\text{tot,CM}}^a}{C_{\text{tot,CM}}^{a,\text{max}}}, \quad (\text{C.40})$$

where $\chi = D_{\text{CM}}^a/D_{\text{CM}}^d$ is the ratio of the diffusion of the species attached to crowded membranes to the diffusion of the ones that are not attached (see Table C.10). In the beginning of the assembly process, the concentration of polymers attached to the membrane is $C_{\text{tot,CM}}^a = 0$. The factor θ reaches its maximum value, $\theta = 1$, in the absence of crowding effects, i.e., FtsZ species bundle at the maximal rates. Once all binding sites are occupied by FtsZ species, the CM region becomes completely crowded such that $C_{\text{tot,CM}}^a = C_{\text{tot,CM}}^{a,\text{max}}$ and θ reaches its minimum value, $\theta = \chi$.

As in the *in vitro* case, wide bundles, B_w , are relevant at long times and high concentrations. Thus, we set $\theta = \chi$ for any forward bundling reaction with B_w as a reactant.

Hydrolysis/dissociation rates.

Dissociation upon hydrolysis rates are redefined for the CM region as

$$k_{\text{hy/dis}}^i = k_{\text{hss/dis}}^i \frac{C_{\text{tot,CM}}^{\text{a}} + C_{\text{tot,CM}}^{\text{d}} - [\text{Z}^{\text{na}}] - [\text{Z}]}{C_{\text{tot,CM}}^{\text{a}} + C_{\text{tot,CM}}^{\text{d}} - C_{\text{cr,wt}}^{\text{l}}} = k_{\text{hss/dis}}^i \frac{C_{\text{tot,CM}}^{\text{a}} + C_{\text{tot,C}} - [\text{Z}^{\text{na}}] - [\text{Z}]}{C_{\text{tot,CM}}^{\text{a}} + C_{\text{tot,C}} - C_{\text{cr,wt}}^{\text{l}}} \quad (\text{C.41})$$

for $i = 1, 2, 3$.

C.5.4 ZapA deficiency

Lack of ZapA proteins introduces five modifications in our model.

1. The absence of ZapA alters the chain of molecules that compose the terminal Ter, therefore, we assume that FtsZ attach to the whole membrane rather than its CM part. Consequently, we redefine the CM region as a thin volume of radial width $w_r = 20$ nm along the entire cell,

$$V_{\text{CM}} = 2\pi \left(R - \frac{w_r}{2} \right) (L - 2R) w_r + 4\pi \left(R - \frac{w_r}{2} \right)^2 w_r. \quad (\text{C.42})$$

2. The percentage of FtsA and ZipA at the membrane is assumed to be 100% instead of 30%.
3. The average number of filament per bundle is computed with Eq. C.14b.
4. The stiffness of FtsZ bundles is not altered by ZapA, so that $\Delta_{\text{ZapA}} = 1$.
5. An estimated average length for wide bundles is assumed to equal the maximum length predicted by our *in vitro* model at high concentrations. We base this assumption on the facts that concentrations at the membrane are higher than *in vitro* concentrations and also that there are no ZapA proteins to stabilize longitudinal bonds. Consequently, we set $\bar{L}_{\text{fb}}^m = 35$ in the backward bundling rate applied to wide bundles in Section C.7.

C.6 *In vitro* bundling reactions and their rates

C.6.1 Forward bundling rate

A general forward bundling reaction can be defined as



where R_1 and R_2 denote two linear chain molecules diffusing and binding laterally in order to produce the species P . If bundling is a diffusion-limited process, then Smoluchowski's formula,

$$k_{\text{bu}}^+ = 4\pi(D_{R_1} + D_{R_2})(r_{\text{h},R_1} + r_{\text{h},R_2}), \quad (\text{C.44})$$

enables one to express the bundling rate k_{bu}^+ in terms of the diffusion coefficients, D_{R_1} and D_{R_2} , and the hydraulic radii, r_{h,R_1} and r_{h,R_2} , of the reactants R_1 and R_2 .

To estimate values of D_{R_i} ($i = 1, 2$), we deploy the Rouse model that treats a short unentangled polymer as a linear series of n beads connected by springs with negligible hydrodynamic interactions [Ter02]. This description is applicable to polymers with a number of beads smaller than a characteristic entanglement length, $n_e \approx 35$ [KG90]. Treating each monomer as a ‘‘bead’’, the number of beads in a filament or bundle is given by the latter's average length, i.e., $n = \bar{L}_{\text{fb}}^m$. The Rouse model is applicable to the experiments [CE5b], since the observed average length of FtsZ species is $\bar{L}_{\text{fb}}^m < 30$. Thus, if reactants R_i ($i = 1, 2$) represent FtsZ filaments (F) and/or bundles (B_2 , B_3 and B_w), their diffusion coefficient is

$$D_{R_i} = \frac{k_B T}{\bar{L}_{\text{fb}}^m \zeta_{\text{bead},R_i}}, \quad i = 1, 2. \quad (\text{C.45})$$

Here k_B is the Boltzmann constant, T is room temperature, and ζ_{bead,R_i} is the friction coefficient

of a bead. For a non-spherical molecule (bead) in a solvent of viscosity η_s ,

$$\zeta_{\text{bead},R_i} = 6\pi\eta_s r_{\text{bead},R_i}^s F_{\text{bead},R_i}, \quad i = 1, 2, \quad (\text{C.46})$$

where r_{bead,R_i}^s is the radius of a sphere whose volume equals that of the bead, and F_{bead,R_i} is the Perrin factor (or translational shape factor) defined as the ratio of the friction coefficient of a non-spherical molecule to that of a spherical molecule of the same volume [Per36]. The volume of a spherical monomer of radius r_m is $V = 4\pi r_m^3/3$. The volume of a bead comprising a filament or bundle, R_i , with average number of filaments \bar{f}_{R_i} is

$$V_{\text{bead},R_i} = \bar{f}_{R_i} \frac{4\pi}{3} r_m^3. \quad (\text{C.47})$$

An equivalent spherical bead of the same volume, V_{bead,R_i} , has the radius

$$r_{\text{bead},R_i}^s = \sqrt[3]{\bar{f}_{R_i} r_m}. \quad (\text{C.48})$$

For filaments and bundles R_i with cylindrical shapes, the beads are disks of thickness $2r_m$ and volume $V_{\text{bead},R_i}^d = 2\pi r_m (r_{\text{bead},R_i}^d)^2$ (see Figure C.6 in which the bundle is composed of 9 filaments). This volume equals that in Eq. C.47 if the disk-shaped bead has a radius

$$r_{\text{bead},R_i}^d = \sqrt{\frac{2}{3} \bar{f}_{R_i} r_m}. \quad (\text{C.49})$$

The Perrin factor for a disk of thickness $2r_m$ and diameter $2r_{\text{bead},R_i}^d$ is [Han04]

$$F_{\text{bead},R_i} = \sum_{k=0}^7 a_k x_{R_i}^k, \quad x_{R_i} = \ln p_{R_i}, \quad p_{R_i} = \frac{r_m}{r_{\text{bead},R_i}^d}, \quad (\text{C.50})$$

where $a_0 = 1.0304$, $a_1 = 0.0193$, $a_2 = 0.06229$, $a_3 = 0.00476$, $a_4 = 0.00166$, $a_5 = a_6 = 0$, and $a_7 = 2.66 \times 10^{-6}$. This polynomial representation is valid on the range $p_{R_i} \in [0.01, 100]$.

Substituting Eq. C.49 into Eq. C.50 yields $p_{R_i}^2 = 3/(2\bar{f}_{R_i})$ and defines the applicability range for the Rouse model as $\bar{f}_{R_i} \in [1.5 \times 10^{-4}, 1.5 \times 10^4]$. This is not overly restrictive, since $\bar{f}_{R_i} < 1.5 \times 10^{-4}$ is equivalent to the absence of filaments and bundles, and $\bar{f}_{R_i} > 1.5 \times 10^4$ is not observed in the experiments [CE5b]. Substituting Eqs. C.46, C.48 and C.50 into Eq. C.45 gives the Rouse diffusion coefficient for reactant R_i ,

$$D_{R_i} = \frac{A}{\bar{L}_{\text{fb}}^m \sqrt[3]{\bar{f}_{R_i}} F_{\text{bead},R_i}(\bar{f}_{R_i})}. \quad (\text{C.51})$$

where A is a computable constant.

The hydrodynamic radius of a chain of n molecules of radius r_m is proportional to $r_m n^{\nu}$, where

$$\nu = \begin{cases} 3/(d+2) & d \leq 4 \\ 1/2 & d > 4 \end{cases} \quad (\text{C.52})$$

is referred to as the Flory exponent, a scaling factor for the average end-to-end distance of the polymer introduced to consider polymer self-avoidance effects, and d is a dimensionality factor. When $d \leq 1/2$, polymers are represented by a d -dimensional sphere (line, circle, sphere for $d = 1, 2, 3$) filled with n polymer segments with mutual repulsive interaction; $d > 4$ corresponds to a particular case in which “real polymer chains” behave as if they were ideal, i.e. excluded volume effects are negligible [vDW97, Ter02, BGM13]. We set $d = 1$, which corresponds to a one-dimensional self-avoiding walk, i.e. a straight line with length n [vDW97]. The following reasons justify this choice. First, FtsZ protofilaments and short filaments are usually straight when GTP nucleotides are dominant in the structure [LRE00]. Second, our filaments and bundles are relatively short, $\bar{L}_{\text{fb}}^m \leq 30$, and bundles get stiffer as they get wider [DLS⁺08]. The resulting FtsZ species are, approximately, straight three-dimensional cylindrical structures, as that shown in Figure C.6. Setting $d = 1$ and, hence, $\nu = 1$ translates into the hydrodynamic radius of reactant

R_i ,

$$r_{h,R_i} \propto r_m \bar{L}_{fb}^m. \quad (\text{C.53})$$

Combining Eqs. C.51, C.53 and C.44 leads to

$$k_{bu}^+ = M^+ \sum_{i=1}^2 \frac{1}{\sqrt[3]{\bar{f}_{R_i} F_{\text{bead},R_i}(\bar{f}_{R_i})}}, \quad (\text{C.54})$$

where $M^+ = k_{bu}^{0+} F_{\text{bead},F}(\bar{f}_F)/2$, and k_{bu}^{0+} is the lateral association rate of two filaments.

C.6.2 Backward bundling rate

In a generic backward bundling reaction,



a linear chain molecule P divides laterally into two thinner chain molecules R_1 and R_2 . Following [LDWS08], we pursue an approach based on the energetic balance of lateral fragmentation of bundles. Let k_{bu}^{0-} denote the rate of lateral detachment of two monomers, and U_b designate the lateral interaction energy of two laterally-bound monomers. In analogy to Eq. C.15 for the longitudinal detachment of filaments, the dissociation rates for the bonds at the lateral tip and in the middle of bundles of one monomer long are, respectively,

$$k_{bu}^{0-} e^{-\Delta U_b} \quad \text{and} \quad k_{bu}^{0-} e^{-2\Delta U_b}, \quad (\text{C.56})$$

where ΔU_b is the increment in the energy of a laterally connected monomer. In analogy to the backward rates for nucleation, elongation and annealing of bundles [LDWS08], we define the

bundling backward rates for filament-filament,

$$k_{\text{bu}}^{0-} e^{-(\bar{L}_{\text{fb}}^m - 1)U_b}, \quad (\text{C.57a})$$

filament-bundle,

$$k_{\text{bu}}^{0-} e^{-(\bar{L}_{\text{fb}}^m - 1)(U_b + \Delta U_b) - \Delta U_b}, \quad (\text{C.57b})$$

and bundle-bundle,

$$k_{\text{bu}}^{0-} e^{-\sqrt{2\bar{f}_P/3}[(\bar{L}_{\text{fb}}^m - 1)(U_b + 2\Delta U_b) + 2\Delta U_b]}. \quad (\text{C.57c})$$

Here \bar{f}_P is the average number of filaments in the product P ; and the factor $\sqrt{2\bar{f}_P/3}$ represents the ratio of the radii of the product P and the filament, as defined in Eq. C.49. For our kinetics model of bundling, we define bundling reaction backward rates as follows.

1. If a bundle of two filaments of average length \bar{L}_{fb}^m dissociates laterally to form two independent filaments, i.e., if $P = B_2$, then

$$k_{\text{bu}}^- = k_{\text{bu}}^{0-} \begin{cases} 1 & \bar{L}_{\text{fb}}^m \leq 1 \\ e^{-(\bar{L}_{\text{fb}}^m - 1)U_b} & \bar{L}_{\text{fb}}^m > 1. \end{cases} \quad (\text{C.58})$$

2. If a bundle of three filaments of average length \bar{L}_{fb}^m dissociates laterally to form a filament and a bundle, i.e., if $P = B_3$, then

$$k_{\text{bu}}^- = k_{\text{bu}}^{0-} e^{-\Delta U_b} \begin{cases} 1 & \bar{L}_{\text{fb}}^m \leq 1 \\ e^{-(\bar{L}_{\text{fb}}^m - 1)(U_b + \Delta U_b)} & \bar{L}_{\text{fb}}^m > 1. \end{cases} \quad (\text{C.59})$$

3. Wide bundles are mainly present at long times and high concentrations, wherein the

experimentally observed average length is in the range of 24 – 30 monomers [CE5b]. We pick an intermediate value of $\bar{L}_{fb}^m = 27$. Thus, if a wide bundle, with average number of filaments \bar{f}_{wb} and average length \bar{L}_{fb}^m , dissociates laterally to form a filament and another bundle, i.e., if $P = B_w$, $R_1 = F$ and $R_2 = B_w$, then

$$k_{bu}^- = k_{bu}^{0-} e^{-26(U_b + \Delta U_b) - \Delta U_b}. \quad (C.60)$$

Wide bundles exist, and hence this dissociation reaction takes place and Eq. C.60 is applicable, when $1.5 \times 10^{-4} \leq \bar{f}_{wb} \leq 1.5 \times 10^4$ (see the preceding section). If $\bar{f}_{wb} < 1.5 \times 10^{-4}$, then this reaction is absent so that its rate is $k_{bu}^- = 0$.

4. If a wide bundle, with average number of filaments \bar{f}_{wb} and average length $\bar{L}_{fb}^m = 27$, dissociates laterally to form two bundles, i.e., if $P = B_w$, $R_1 = B_w$ and $R_2 = B_w$, then

$$k_{bu}^- = k_{bu}^{0-} e^{-\sqrt{2\bar{f}_{wb}/3}[26(U_b + 2\Delta U_b) + 2\Delta U_b]}. \quad (C.61)$$

This expression holds for $1.5 \times 10^{-4} \leq \bar{f}_{wb} \leq 1.5 \times 10^4$; if $\bar{f}_{wb} < 1.5 \times 10^{-4}$, then $k_{bu}^- = 0$.

For the values of U_b and ΔU_b reported in Table C.1, and for $\bar{f}_{wb} = 4$ associated with case 4 above, Eq. C.61 gives an order-of-magnitude estimate

$$k_{bu}^- \sim O(10^{-5}) \quad \text{for reaction 4.} \quad (C.62)$$

Among the remaining three cases previously defined, case 3 is the least energetically favorable; even for that case, an order-of-magnitude analysis of Eq. C.60 results in

$$k_{bu}^- \sim O(10^{-3}) \quad \text{for reaction 3.} \quad (C.63)$$

Hence, the backward bundling rate for case 4 is negligible relative to any other cases, i.e., case 4,

or reaction $2B_{w;b-} \rightarrow B_{w;b+}$, is assumed to be irreversible.

C.7 *In vivo* bundling reactions and their rates

In regions adjacent to membranes, we redefine bundles as two-dimensional sheets of cylindrical beads. Overlapped bundles rearrange to form three-dimensional cross-linked clusters along the CM region, which we conceptualize as long, thick structures composed of big spherical beads.

Forward bundling rate.

The presence of ZapA proteins between FtsZ filaments changes a diffusion coefficient of bundles and, consequently, diffusion-limited reaction rates. Guided by the *in vitro* observations [MPV⁺09], we consider structures with a pair of FtsZ filaments connected by ZapA tetramers, and assume that both ZapA and FtsZ monomers have the same diameter, $\phi_m \approx 5$ nm. We allow these ZapA tetramers to diffuse like the pair of filaments. Table C.11 provides discrete values of the average number of filaments of a reactant R_i without (\bar{f}_{R_i}) and with ($\bar{f}_{R_i, \text{ZapA}}$) ZapA in between pairs of FtsZ filaments.

Geometric considerations give $\bar{f}_{R_i, \text{ZapA}} = 2\bar{f}_{R_i}$ for bundles of more than two filaments. Consequently, we redefine Eq. C.14b as

$$\bar{f}_{R_i, \text{ZapA}} = \begin{cases} 1 & \text{for } R_i = F \\ 2 & \text{for } R_i = B_2 \\ 6 & \text{for } R_i = B_3 \\ \bar{f}_{\text{wb}, \text{ZapA}} & \text{for } R_i = B_w, \end{cases} \quad (\text{C.64})$$

where $\bar{f}_{\text{wb}, \text{ZapA}} = 2\bar{f}_{\text{wb}}$. Now, we define a dimensionality factor \tilde{d} that corresponds to a subsequent bundling stage: $\tilde{d} = 2$ for bundling over the membrane, and $\tilde{d} = 3$ for bundling over and perpendicular to the membrane. For each \tilde{d} , we redefine the radius of the spherical beads and the

Perrin factor as follows.

For $\tilde{d} = 2$, bundles are distributed along a two dimensional membrane as sheets (Fig. C.7).

The radius of a spherical bead is defined as

$$r_{\text{bead},R_i}^{s(2)} = r_m \sqrt[3]{\bar{f}_{R_i,\text{ZapA}}} \quad (\text{C.65})$$

by equating volumes of a bead and its spherical counterpart,

$$V_{\text{bead},R_i} = \bar{f}_{R_i,\text{ZapA}} \frac{4\pi}{3} r_m^3, \quad V_{\text{bead},R_i}^s = \frac{4\pi}{3} [r_{\text{bead},R_i}^{s(2)}]^3. \quad (\text{C.66})$$

The Perrin factor $F_{\text{bead},R_i,\text{ZapA}}^{(2)}$ in Eq. C.50 is now computed for $p_{R_i} = l_{\text{bead},R_i}^c / \phi_{\text{bead},R_i}^c$, where l_{bead,R_i}^c and ϕ_{bead,R_i}^c are respectively the length and diameter of the bead. Since $l_{\text{bead},R_i}^c = \bar{f}_{R_i,\text{ZapA}} \phi_m$ and $\phi_{\text{bead},R_i}^c = \phi_m$, we have $p_{R_i} = \bar{f}_{R_i,\text{ZapA}}$. The Perrin factor expression for a cylinder [Han04], restricts values of $\bar{f}_{R_i,\text{ZapA}}$ to the interval [0.01,100]. This constraint is always satisfied for *in vivo* cases:

1. $\bar{f}_{R_i,\text{ZapA}}$ only changes in time for wide bundles, i.e., when $R_i = B_w$. Our *in vitro* model predicts $\bar{f}_{\text{wb}} > 0.01$ for $C_{\text{tot}} = 4 - 6 \mu\text{M}$, which are the lowest cytosolic concentrations observed experimentally (3000-5000 FtsZ molecules). Since concentrations are much higher at the membrane than in the cytosol, and ZapA proteins (absent in the *in vitro* experiment) promote bundling, $\bar{f}_{\text{wb},\text{ZapA}}^{\text{in vivo}} \gg \bar{f}_{\text{wb}}^{\text{in vitro}} > 0.01$ for $C_{\text{tot},C} > 4 \mu\text{M}$.
2. The maximal axial width of the CM region is $w_a = 100 \text{ nm}$ (Table C.10). For monomer diameter $\phi_m \approx 5 \text{ nm}$, the maximal number of FtsZ/ZapA filaments laterally associated and perfectly aligned is 20. Thus, $\bar{f}_{\text{wb},\text{ZapA}}^{\text{max}} = 20 < 100$ for any cytosolic concentration, $C_{\text{tot},C}$.

For $\tilde{d} = 3$, bundles are partially attached to the membrane and distributed along the midcell region as long cross-linked bundles with more complex beads. Figure C.8 shows an example of beads of three-dimensional wide bundles; the bead's length (three monomers long in

the longitudinal direction) is proportional to the number of cross-linked bundles. The radius of a spherical bead is

$$r_{\text{bead},R_i}^{s(3)} = r_m \sqrt[3]{\bar{f}_{R_i,\text{ZapA}}}, \quad (\text{C.67})$$

which is obtained by equating volumes of a bead and its spherical representation,

$$V_{\text{bead},R_i} = \bar{f}_{R_i,\text{ZapA}} \frac{4\pi}{3} r_m^3, \quad V_{\text{bead},R_i}^s = \frac{4\pi}{3} [r_{\text{bead},R_i}^{s(3)}]^3. \quad (\text{C.68})$$

The Rouse model's condition for the number of beads to be smaller than the entanglement length limit, $n < n_e$, is still fulfilled. The length of the beads is taken proportional to the number of cross-linked bundles connected longitudinally. Furthermore, for $\tilde{d} = 3$, the Perrin factor is defined for spheres, i.e., $F_{\text{bead},R_i,\text{ZapA}}^{(3)} = 1$,

The hydrodynamic radius r_{h,R_i} is computed with Eq. C.53. This yields an expression for the forward reaction rate,

$$k_{\text{bu}}^+ = \tilde{k}_{\text{bu}}^{0+} \sum_{i=1}^2 \sum_{\tilde{d}=2}^3 \frac{\gamma_{R_i}^{(\tilde{d})}}{\sqrt[3]{\bar{f}_{R_i,\text{ZapA}} F_{\text{bead},R_i,\text{ZapA}}^{(\tilde{d})} (\bar{f}_{R_i,\text{ZapA})}}}, \quad (\text{C.69})$$

where

$$\tilde{k}_{\text{bu}}^{0+} = \frac{1}{2} k_{\text{bu}}^{0+} F_{F,\text{ZapA}}^{(2)} (\bar{f}_{F,\text{ZapA}}), \quad (\text{C.70})$$

$$\gamma_{R_i}^{(\tilde{d})} = \begin{cases} 1 & \tilde{d} = 2 \\ 0 & \tilde{d} = 3 \end{cases} \quad \text{if } R_i = F, B_2, \text{ or } B_3 \quad (\text{C.71a})$$

and

$$\gamma_{R_i}^{(\tilde{d})} = \begin{cases} 1 - \frac{C_{\text{tot,CM}}^a}{C_{\text{tot,CM}}^{a,\text{max}}} & \tilde{d} = 2 \ (\bar{f}_{\text{wb,ZapA}} \leq 20) \\ \frac{C_{\text{tot,CM}}^a}{C_{\text{tot,CM}}^{a,\text{max}}} & \tilde{d} = 3 \ (\bar{f}_{\text{wb,ZapA}} > 20) \end{cases} \quad \text{if } R_i = B_w. \quad (\text{C.71b})$$

First species in the bundling process, F , B_2 and B_3 , are assumed to grow exclusively over the membrane. The amount of wide bundles growing over the membrane decreases as the total FtsZ concentration at the membrane, $C_{\text{tot,CM}}^a$, increases, i.e., as the membrane gets crowded and there is less space for bundles to diffuse and grow in two dimensions. On the other hand, the amount of wide bundles growing in all directions and forming cross-linked structures increases with the total FtsZ concentration at the membrane, i.e., when the membrane gets crowded and bundles push and lift each other to rearrange in three dimensions. When $C_{\text{tot,CM}}^a = C_{\text{tot,CM}}^{a,\text{max}}$, bundles grow exclusively in three dimensions.

Backward bundling rate.

Local concentration of ZapA interacting stoichiometrically with FtsZ at the division site may be sufficient to induce a tetrameric conformation [LML04, GG12]. Some studies [GFL02, LML04, MPV⁺09] suggest the stoichiometry of ZapA-FtsZ interaction to be 1:1, while others [DPLW10, PGCH⁺13] estimated stoichiometries up to 4:1 since ZapA concentration in the ring is four times higher than FtsZ concentration [DPLW10]. Nevertheless, *in vitro* and *in vivo* experiments show interactions between ZapA and ZapB [BCH⁺13, BCS⁺15] and sequestration of ZapA by ZapB [GG12] that can reduce the stoichiometry up to 1:2. We take the intermediate value 1:1 for ZapA-FtsZ interaction.

We estimate the influence of ZapA proteins on the lateral bounds of FtsZ species from the *in vitro* experiments [DPLW10] that studied different stiffness of FtsZ/H6-ZapA structures by measuring their elastic modulus. At medium and long times, i.e., when bundling becomes important, FtsZ bundles without the presence of H6-ZapA had an average elastic modulus of

$\sim 9 \text{ dyn/cm}^2$. However, for a molar ratio of 1:1, the average elastic modulus was around 30 dyn/cm^2 . Defining Δ_{ZapA} as the increment of the stiffness of FtsZ bundles by ZapA and taking as a reference the scenario without ZapA, we have a value of $\Delta_{\text{ZapA}} = 30/9 = 3.33$. Since ZapA molecules tend to connect pairs of FtsZ filaments instead of single filaments [MPV⁺09], we multiply this factor by the increment of lateral bond energy associated to bundling of bundles of two or more filaments, i.e., $\Delta U_{b,\text{ZapA}} = \Delta_{\text{ZapA}} \Delta U_b$. Thus, we redefine the backward reaction rates as follows.

1. If a bundle of two filaments of average length \bar{L}_{fb}^m detaches laterally to form two independent filaments, i.e., if $P = B_2$, then

$$k_{\text{bu}}^- = k_{\text{bu}}^{0-} \begin{cases} 1 & \bar{L}_{\text{fb}}^m \leq 1, \\ e^{-(\bar{L}_{\text{fb}}^m - 1)U_b} & \bar{L}_{\text{fb}}^m > 1. \end{cases} \quad (\text{C.72})$$

If a bundle of three filaments of average length \bar{L}_{fb}^m detaches laterally to form a filament and a bundle, i.e., if $P = B_3$, then

$$k_{\text{bu}}^- = k_{\text{bu}}^{0-} e^{-\Delta U_{b,\text{ZapA}}} \begin{cases} 1 & \bar{L}_{\text{fb}}^m \leq 1, \\ e^{-(\bar{L}_{\text{fb}}^m - 1)(U_b + \Delta U_{b,\text{ZapA}})} & \bar{L}_{\text{fb}}^m > 1. \end{cases} \quad (\text{C.73})$$

2. Wide bundles are mainly present at long times and high concentrations. The tendency of ZapA proteins to make stiff bundles and to stabilize longitudinal bonds between FtsZ monomers [DPLW10] suggests that the average length of the species remains practically constant once ZapA proteins get attached to them. Our *in vitro* study demonstrated that bundles of pairs of filaments start forming at $C_{\text{tot}} = 2 \mu\text{M}$. At that concentration the average length of filaments and bundles is estimated by our model to be $\bar{L}_{\text{fb}}^m = 25$. Moreover, ZapA intervenes in bundling process when bundles are made of at least 2 filaments [MPV⁺09]. Therefore, we set $\bar{L}_{\text{fb}}^m = 25$ as the expected length for wide bundles at steady state. Thus, if

a wide bundle of average number of filaments $\bar{f}_{\text{wb,ZapA}}$ and average length \bar{L}_{fb}^m detaches laterally to form a filament and another bundle, i.e., if $P = B_w$, $R_1 = F$ and $R_2 = B_w$, then

$$k_{\text{bu}}^- = k_{\text{bu}}^{0-} e^{-24(U_b + \Delta U_{b,\text{ZapA}}) - \Delta U_{b,\text{ZapA}}}, \quad (\text{C.74})$$

Here, we do not distinguish between two stages of bundling. We assume that filaments detach at the same rate from sheets ($\tilde{d} = 2$) and from long cross-linked clusters ($\tilde{d} = 3$), i.e., cross-links do not highly affect the detachment of thin filaments.

3. If a wide bundle of average number of filaments $\bar{f}_{\text{wb,ZapA}}$ and average length $\bar{L}_{\text{fb}}^m = 25$ detaches laterally to form two bundles, i.e., if $P = B_w$, $R_1 = B_w$ and $R_2 = B_w$, then

$$k_{\text{bu}}^- = k_{\text{bu}}^{0-} e^{-[24(U_b + 2\Delta U_{b,\text{ZapA}}) + 2\Delta U_{b,\text{ZapA}}]} \left(1 - \frac{C_{\text{tot,CM}}^a}{C_{\text{tot,CM}}^{a,\text{max}}} \right) \quad (\text{C.75})$$

where only the proportion of wide bundles in sheet form ($\tilde{d} = 2$, Eq. C.71) is allowed to disassociate. The proportion of long cross-linked clusters ($\tilde{d} = 3$, Eq. C.71) is not considered in Eq. C.75 since cross-links are very strong to allow cluster dissociation [FLKG12, JMW15].

Table C.1. Reaction rate constants and bond energies. The energy units are expressed in terms of the Boltzmann constant k_B and room temperature T.

Parameter	Units	Value	Reference
k_{ac}^+	s^{-1}	0.38	[CE5b]
k_{ac}^-	s^{-1}	0.01	[CE5b]
k_{nu}^+	$\mu M^{-1} s^{-1}$	0.79	[CE5b]
k_{nu}^-	s^{-1}	199.8	[CE5b]
k_{el}^+	$\mu M^{-1} s^{-1}$	6.6	[CE5b]
k_{an}^+	$\mu M^{-1} s^{-1}$	6.6	[CE5b]
k_{bu}^{0+}	$\mu M^{-1} s^{-1}$	4.0955	Calibrated
k_{bu}^{0-}	s^{-1}	199.9704	Calibrated
k_{mb}	$\mu M^{-1} s^{-1}$	2.1957	Calibrated
$k_{hss/dis}^1$	s^{-1}	0.6998	Calibrated
$k_{hss/dis}^2$	s^{-1}	0.143	[CE5b]
$k_{hss/dis}^3$	s^{-1}	0.112	[APS14]
ΔU_t	$k_B T$	4.05	[CE5b, LDWS08]
ΔU_m	$k_B T$	8.10	[LDWS08]
U_b	$k_B T$	0.175	[DLS ⁺ 08, LDWS08]
ΔU_b	$k_B T$	0.0405	[DLS ⁺ 08, LDWS08]

Table C.2. Lower and upper bounds, and initial guesses, for the kinetic parameters used in the model calibration procedure.

	k_{bu}^{0+} ($\mu\text{M}^{-1}\text{s}^{-1}$)	k_{bu}^{0-} (s^{-1})	k_{mb} ($\mu\text{M}^{-1}\text{s}^{-1}$)	$k_{hss/dis}^1$ (s^{-1})
Lower bound	2.0	0.0	2.0	0.143
Upper bound	7.5	500.0	6.6	∞
Initial guess	4.0	200.0	2.0	0.7

Table C.3. Lower and upper bounds for the concentrations (in μM , with $i = 2, 3$ and $j = 2, 3$), average length and average number of filaments per bundle, informed by the data in [CE5b].

	$[Z^{\text{na}}]$	$[Z]$	$[Z_i]$	$[F]$	$[B_j]$	$[B_w]$	C_{fb}^m	C_{wb}^f	\bar{L}_{fb}^m	\bar{f}_{tot}
Lower bound ($C_{\text{tot}} = 0.7 \mu\text{M}$)	0.0	0.0	0.0	0.0	0.0	0.0	0.0	0.0	1	1
Upper bound ($C_{\text{tot}} = 0.7 \mu\text{M}$)	∞	∞	∞	∞	∞	∞	0.0	∞	1	1
Lower bound ($C_{\text{tot}} = 0.8 \mu\text{M}$)	0.0	0.0	0.0	0.0	0.0	0.0	0.1	0.0	1	1
Upper bound ($C_{\text{tot}} = 0.8 \mu\text{M}$)	∞	∞	∞	∞	∞	∞	0.1	∞	27	1.5
Lower bound ($C_{\text{tot}} = 1.0 \mu\text{M}$)	0.0	0.0	0.0	0.0	0.0	0.0	0.3	0.0	1	1
Upper bound ($C_{\text{tot}} = 1.0 \mu\text{M}$)	∞	∞	∞	∞	∞	∞	0.3	∞	27	1.5
Lower bound ($C_{\text{tot}} = 1.5 \mu\text{M}$)	0.0	0.0	0.0	0.0	0.0	0.0	0.8	0.0	1	1
Upper bound ($C_{\text{tot}} = 1.5 \mu\text{M}$)	∞	∞	∞	∞	∞	∞	0.8	∞	27	1.5
Lower bound ($C_{\text{tot}} = 2.0 \mu\text{M}$)	0.0	0.0	0.0	0.0	0.0	0.0	1.3	0.0	24	1
Upper bound ($C_{\text{tot}} = 2.0 \mu\text{M}$)	∞	∞	∞	∞	∞	∞	1.3	∞	30	1.5
Lower bound ($C_{\text{tot}} = 2.5 \mu\text{M}$)	0.0	0.0	0.0	0.0	0.0	0.0	1.8	0.0	24	1
Upper bound ($C_{\text{tot}} = 2.5 \mu\text{M}$)	∞	∞	∞	∞	∞	∞	1.8	∞	30	1.5
Lower bound ($C_{\text{tot}} = 3.0 \mu\text{M}$)	0.0	0.0	0.0	0.0	0.0	0.0	2.3	0.0	24	1
Upper bound ($C_{\text{tot}} = 3.0 \mu\text{M}$)	∞	∞	∞	∞	∞	∞	2.3	∞	30	1.5

Table C.4. Initial guesses of the concentrations (in μM , with $i = 2, 3$), average length and average number of filaments per bundle.

$C_{\text{tot}} (\mu\text{M})$	$[Z^{\text{na}}]$	$[Z]$	$[Z_i]$	$[F]$	$[B_i]$	$[B_w]$	C_{fb}^m	C_{wb}^f	\bar{L}_{fb}^m	\bar{f}_{tot}
0.7	0.0	0.0	0.0	0.01	0.01	0.01	0.0	0.0	1	1
0.8	0.0	0.0	0.0	0.01	0.01	0.01	0.1	0.0	5	1
1.0	0.0	0.0	0.0	0.01	0.01	0.01	0.3	0.0	10	1
1.5	0.0	0.0	0.0	0.01	0.01	0.01	0.8	0.0	18	1.02
2.0	0.0	0.0	0.0	0.01	0.01	0.01	1.3	0.0	25	1.04
2.5	0.0	0.0	0.0	0.01	0.01	0.01	1.8	0.0	27	1.08
3.0	0.0	0.0	0.0	0.01	0.01	0.01	2.3	0.0	28	1.11

Table C.5. Steady-state average length (\bar{L}_{tot}^m), number of filaments per bundle (\bar{f}_{tot}) and monomer concentration ($[Z^{\text{na}}]_{\text{ss}} + [Z]_{\text{ss}}$), predicted by [RMBST16], [CE5b] and AFM, and observed in the low-concentration experiment [CE5b].

C_{tot} (μM)	\bar{L}_{tot}^m		\bar{f}_{tot}		$[Z^{\text{na}}]_{\text{ss}} + [Z]_{\text{ss}}$ (μM)					
	[RMBST16]	AFM	Observed	[RMBST16]	AFM	Observed	[CE5b]	[RMBST16]	AFM	Observed
1.0	7	7	< 27	1.0	1.0	< 1.5	0.526	0.701	0.710	0.7
2.0	25	24	24 – 30	1.1	1.0	< 1.5	0.534	0.699	0.712	0.7
3.0	30	29	24 – 30	1.3	1.1	< 1.5	0.536	0.695	0.701	0.7

Table C.6. Steady-state average length (\bar{L}_{tot}^m), number of filaments per bundle (\bar{f}_{tot}) and monomer concentration ($[Z^{\text{na}}]_{\text{ss}} + [Z]_{\text{ss}}$), predicted by [RMBST16], [CE5b] and AFM, and observed in the high-concentration experiment [CE5b].

$C_{\text{tot}} (\mu\text{M})$	\bar{L}_{tot}^m		\bar{f}_{tot}		$[Z^{\text{na}}]_{\text{ss}} + [Z]_{\text{ss}} (\mu\text{M})$		Observed			
	[RMBST16]	AFM	Observed	[RMBST16]	AFM	Observed		[CE5b]	[RMBST16]	AFM
4.0	31.42	30.42	30	1.39	1.18	< 2	0.537	0.693	0.694	0.7
5.0	32.14	31.13	30	1.50	1.26	< 2	0.538	0.691	0.690	0.7
6.0	32.55	31.51	30	1.60	1.37	< 2	0.538	0.690	0.689	0.7
7.0	32.81	31.76	30	1.69	1.49	< 2	0.539	0.690	0.688	0.7
8.0	32.99	31.93	30	1.77	1.62	< 2	0.539	0.689	0.687	0.7
9.0	33.12	32.05	30	1.84	1.75	< 2	0.539	0.689	0.687	0.7
10.0	33.21	32.15	30	1.91	1.89	< 2	0.539	0.690	0.687	0.7

Table C.7. Comparison of timing predictions of FtsZ ring formation for a characteristic range of *in vivo* FtsZ concentrations, $C_{\text{tot},C;0} = 6 - 18 \mu\text{M}$. * denotes that the model [RMBST16] has been slightly modified by introducing *in vivo* factors.

$C_{\text{tot},C;0} (\mu\text{M})$	$t_{\text{att}} (\text{s})$		$t_{\bar{L}} (\text{s})$		$t_{\text{mon}} (\text{s})$		$t_{\bar{f}} (\text{s})$	
	[RMBST16]*	AFM	[RMBST16]*	AFM	[RMBST16]*	AFM	[RMBST16]*	AFM
6.0	19	19	26	49	37	220	31	244
12.0	11	10	13	53	22	217	19	240
18.0	8	8	15	40	32	210	24	233

Table C.8. Comparison of FtsZ ring feature predictions for a characteristic range of *in vivo* FtsZ concentrations, $C_{\text{tot,C;0}} = 6 - 18 \mu\text{M}$, at steady state ($t \rightarrow \infty$). * denotes that the model [RMBST16] has been slightly modified by introducing *in vivo* factors.

$C_{\text{tot,C;0}} (\mu\text{M})$	$C_{\text{tot,CM}}^{\text{a},\infty}$ [RMBST16]*	$C_{\text{tot,CM}}^{\text{a},\infty}$ (μM)	AFM	$\bar{L}_{\text{tot}}^{m,\infty}$ [RMBST16]*	AFM	$C_{\text{m,CM}}^{\text{d},\infty}$ [RMBST16]*	$C_{\text{m,CM}}^{\text{d},\infty}$ (μM)	AFM	$\bar{f}_{\text{tot}}^{\infty}$ [RMBST16]*	AFM
6.0	237	237	237	23.04	24.43	1.90	1.90	1.13	3.98	9.4
12.0	474	474	474	23.51	24.47	2.29	2.29	1.20	5.38	16.4
18.0	711	711	711	23.86	24.49	2.52	2.52	1.25	6.57	22.7

Table C.9. MATLAB Benchmarking (times in seconds)

Computer time	LU	FFT	ODE	Sparse	2-D	3-D
Windows 7, Intel Xeon E5-1650 v3 3.50 GHz	0.1330	0.1280	0.0535	0.0968	0.2334	0.2309
iMac, OS X 10.10.5, Intel Core i7 3.4 GHz	0.1422	0.1432	0.0967	0.1120	0.3811	0.3203
Windows 10, Intel Xeon X5650 2.67 GHz	0.1422	0.1432	0.0967	0.1120	0.3811	0.3203
Linux, Intel Xeon CPU W3690 3.47 GHz	0.2027	0.1250	0.1420	0.1337	0.9327	0.7505
Windows 10 Home, Intel(R) Core(TM) i7-6700HQ CPU 2.60 GHz	0.1649	0.1363	0.0660	0.1219	1.4447	1.4613
Surface Pro 3, Windows 8.1, Intel Core i5-4300U 1.9 GHz	0.4426	0.2447	0.1256	0.2108	0.9683	0.8135
MacBook Pro, OS X 10.11.4, Intel Core i5 2.6GHz	0.2537	0.1922	0.0678	0.1212	2.2133	1.7815
Windows 8, AMD A8-6410 APU 2.00 GHz	0.9729	0.5021	0.2867	0.6188	1.5988	1.3353

Table C.10. Parameters of the *in vivo* model.

Parameter	Units	Value	Reference
L	μm	3	[RHK ⁺ 14]
R	μm	0.4	[RHK ⁺ 14]
w_a	μm	0.10	[FHB ⁺ 10, CBPX16]
w_r	μm	0.06	[CBPX16]
$C_{\text{cr, wt}}^1$	μM	1.1	[CBRE5a, CE5b]
k_{bind}^+	$\mu\text{M}^{-1}\text{s}^{-1}$	0.142	[DRRv13]
k_{bind}^-	s^{-1}	0.0284	[DRRv13]
$[\text{FtsZ}]_{\text{C}}/[\text{FtsA}]_{\text{C}}$	—	5	[RVM03]
$[\text{FtsZ}]_{\text{C}}/[\text{ZipA}]_{\text{C}}$	—	10	[HdB97]
D_{CM}^{d}	$\mu\text{m}^2\text{s}^{-1}$	2.5	[FFFG12, CJR02]
D_{CM}^{a}	$\mu\text{m}^2\text{s}^{-1}$	0.1	[NY08]
Δ_{ZapA}	—	3.33	[DLS ⁺ 08, DPLW10]

Table C.11. Average number of filaments in a reactant R_i without and with ZapA proteins.

\bar{f}_{R_i}	$\bar{f}_{R_i, \text{ZapA}}$	Scheme
2	4	$(\text{ZapA})_2 - (\text{FtsZ})_2 - (\text{ZapA})_2$
4	8	$(\text{FtsZ}) - (\text{ZapA})_2 - (\text{FtsZ})_2 - (\text{ZapA})_2 - (\text{FtsZ})$
6	12	$(\text{FtsZ}) - (\text{ZapA})_2 - (\text{FtsZ})_2 - (\text{ZapA})_2 - (\text{FtsZ})_2 - (\text{ZapA})_2 - (\text{FtsZ})$
..

POLYMER STRUCTURE	GRAPHICAL REPRESENTATION
<i>Non-activated monomer, Z^{na}</i>	
<i>Activated monomer, Z</i>	
<i>Protofilaments, Z_2, Z_3</i>	
<i>Long filaments, F</i>	
<i>Thin bundles, B_2, B_3</i>	
<i>Wide bundles, B_w</i>	

REACTION	GRAPHICAL REPRESENTATION
<i>Activation</i>	
<i>Nucleation</i>	2
<i>Elongation</i>	
	F_{z-} +
<i>Filament annealing</i>	2 F_{f-}
<i>Filament bundling</i>	2
	$B_{w;f-}$ +
<i>Dissociation of non-activated monomers from filaments following GTP hydrolysis</i>	F_{z+}
	$F_{z+,f+}$
	$B_{2;z+,b+}$
<i>Dissociation of non-activated monomers from bundles following GTP hydrolysis</i>	$B_{2;z+}$
	$B_{w;z+}$
	$B_{2;z-}$ +
<i>Attachment of monomers to bundles</i>	$B_{w;z-}$ +

Figure C.1. Graphical representation of basic polymer structures and reactions.

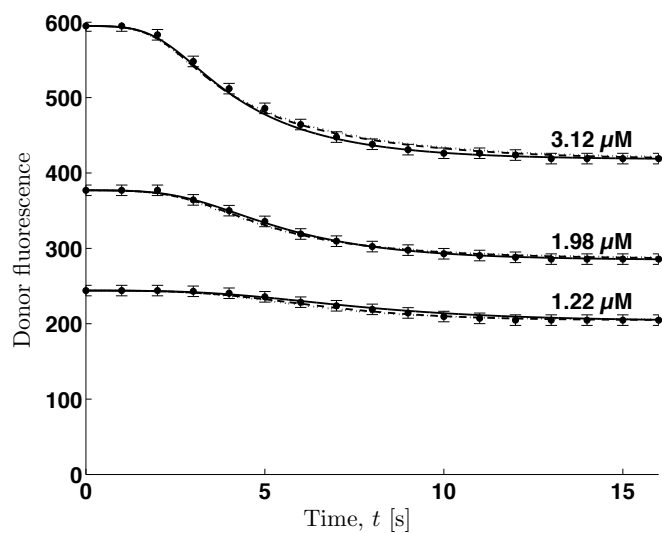


Figure C.2. Kinetics of the initial FtsZ-F268C assembly observed in [CE5b], for three values of total concentration C_{tot} . The data points and compared with predictions of the models in [CE5b] (solid lines) and [RMBST16] (dashed lines), as well as with those of AFM (dotted lines). The agreement between the three models is to be expected since annealing, bundling and GTP-hydrolysis/dissociation, all which are not accounted for in the model [CE5b], do not become pronounced until the later stages of polymerization.

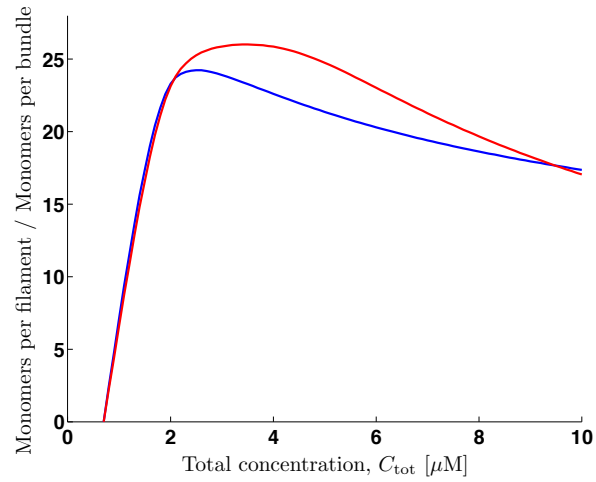


Figure C.3. Monomers per filament-to-Filaments per bundle ratio (or Monomers longitudinally connected per filament-to-Monomers laterally connected per bundle ratio) at steady state predicted by [RMBST16] (blue line) and AFM (red line), for a range of concentration C_{tot} .

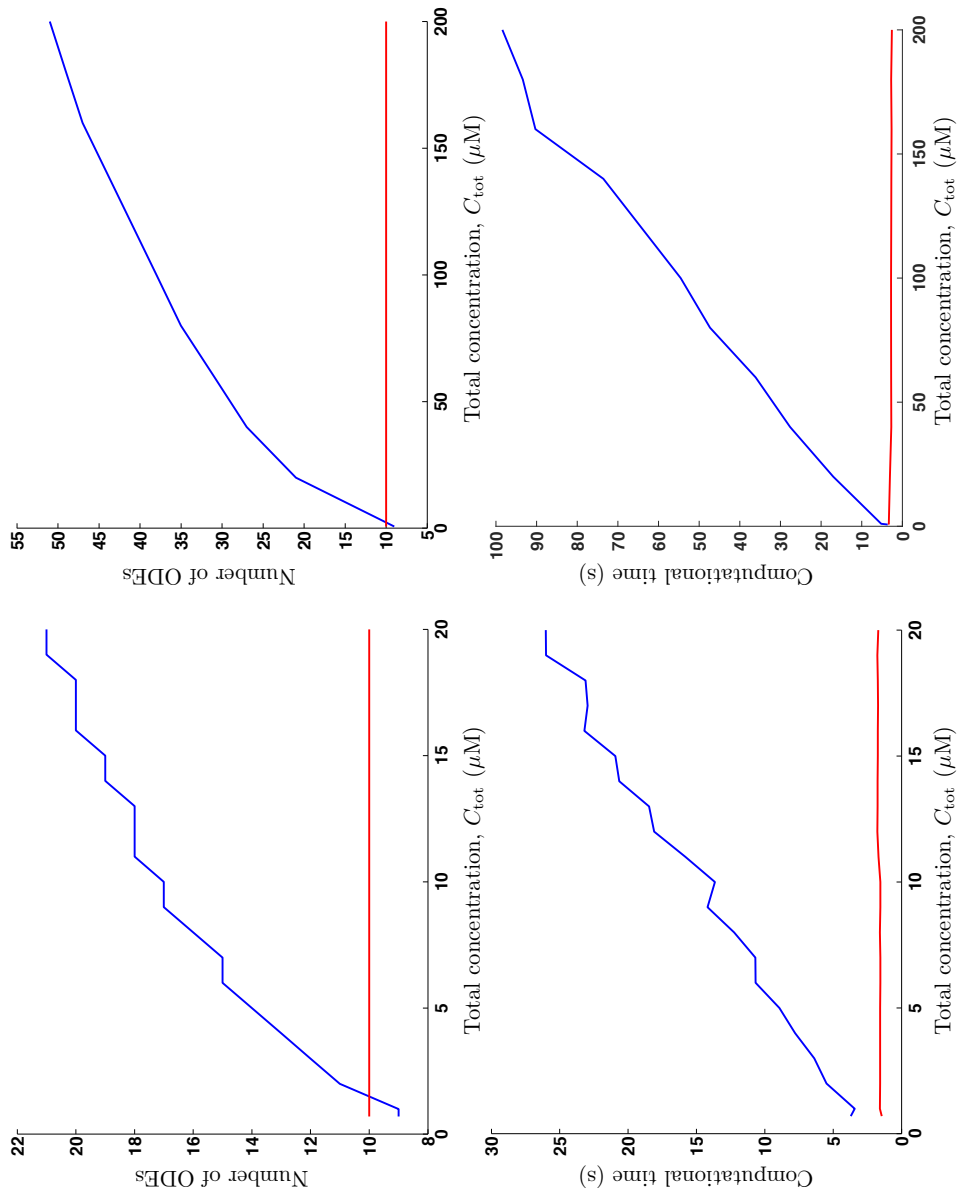


Figure C.4. The number of ODEs (top row) comprising the model [RBMST16] (blue lines) and AFM (red lines) and computational cost (bottom row) as a function of the *in vitro* (left column) and *in vivo* (right column) total concentration C_{tot} . The stopping criteria of convergence of [RBMST16] is set to $[B_N] < 10^{-4} \mu\text{M}$, where $[B_N]$ is the concentration of the largest bundle composed of N filaments.

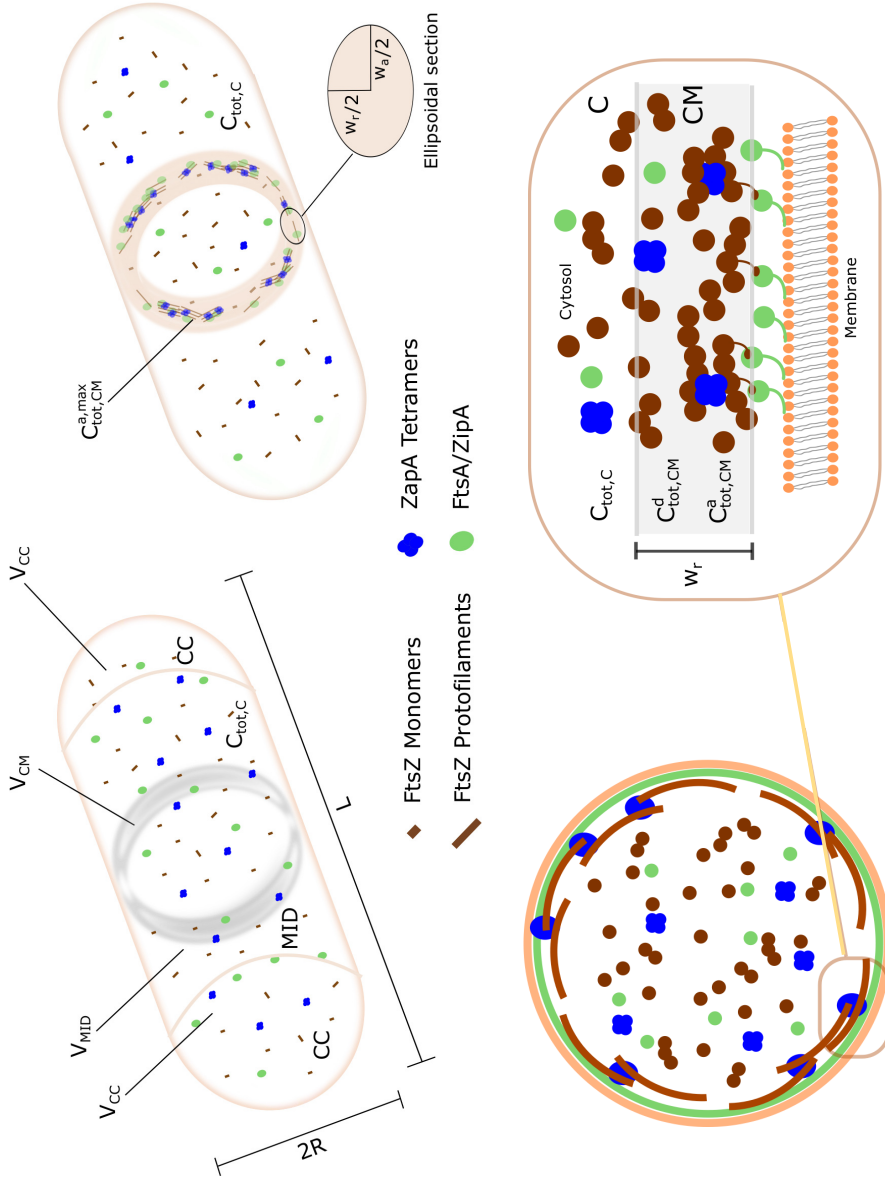


Figure C.5. Top row: *Escherichia coli* cell before (left) and after (right) ring formation. Bottom row: Cross-section of the cell (left) and a magnified region near the cell membrane (right).

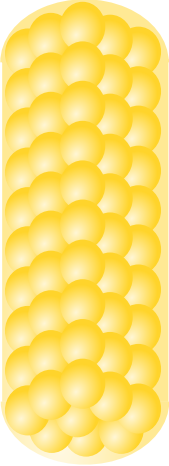
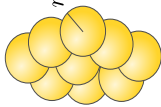
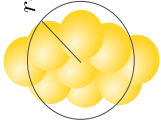
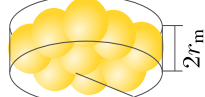
BUNDLE	Bead	Bead as a sphere	Bead as a disk
			
Bead dimensions	r_m	r_{bead, B_w}^s	$r_{\text{bead}, B_w}^d, 2r_m$
Bead volume	$V_{\text{bead}, B_w} = 9\frac{4}{3}\pi r_m^3$	$V_{\text{bead}, B_w}^s = \frac{4}{3}\pi (r_{\text{bead}, B_w}^s)^3$	$V_{\text{bead}, B_w}^d = 2r_m\pi (r_{\text{bead}, B_w}^d)^2$

Figure C.6. Alternative representations of a bead in a wide bundle of average width $\bar{f}_{\text{wb}} = 9$.

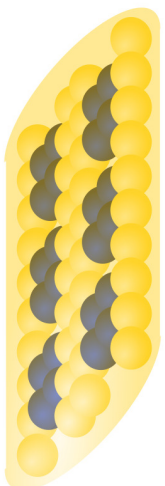
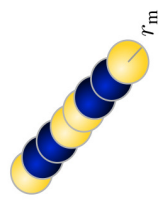
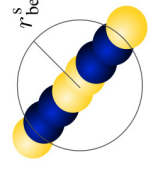
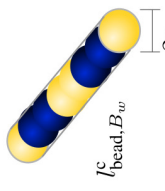
BUNDLE	Bead	Bead as a sphere	Bead as a cylinder
			
Bead dimensions	r_m	r_{bead, B_w}^S	$l_{\text{bead}, B_w}^C, 2r_m$
Bead volume	$V_{\text{bead}, B_w} = \bar{f}_{\text{wb}, \text{ZapA}} \frac{4}{3} \pi r_m^3$	$V_{\text{bead}, B_w}^S = \frac{4}{3} \pi (r_{\text{bead}, B_w}^S)^3$	$V_{\text{bead}, B_w}^C = l_{\text{bead}, B_w}^C \pi r_m^2$

Figure C.7. Graphical representations of a bead in a two-dimensional wide bundle of $\bar{f}_{\text{wb}, \text{ZapA}} = 8$.

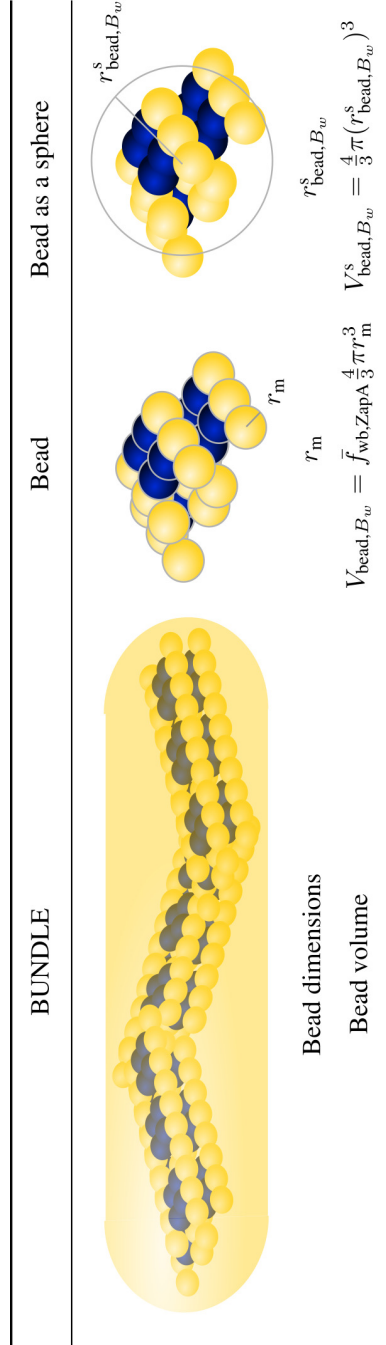


Figure C.8. Graphical representations of a bead in a three-dimensional structure made of cross-linked clusters of $\bar{f}_{\text{wb}, \text{ZapA}} = 36$.

Appendix D

Stochastic self-tuning hybrid algorithm for reaction-diffusion systems

D.1 Effect of number of molecules

Graphics of variations of the concentration of species C are presented in this Appendix. Regardless of the number of particles, our model makes more accurate predictions than its counterpart.

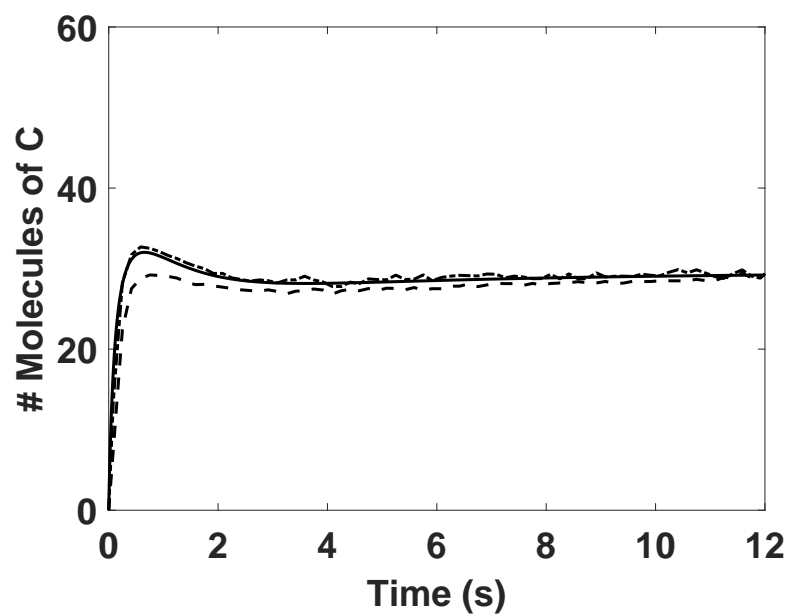


Figure D.1. Temporal evolution of the concentration of the species C for $N_{A_0} = N_{B_0} = 60$ particles. Solid, dashed, and dash-dot lines are the deterministic solution, the solution obtained by Choi et al., model setting $\Delta x = \Delta y = \Delta z = L/4$, and the solution obtained by our model, respectively. All results are based on average of 1000 iterations.

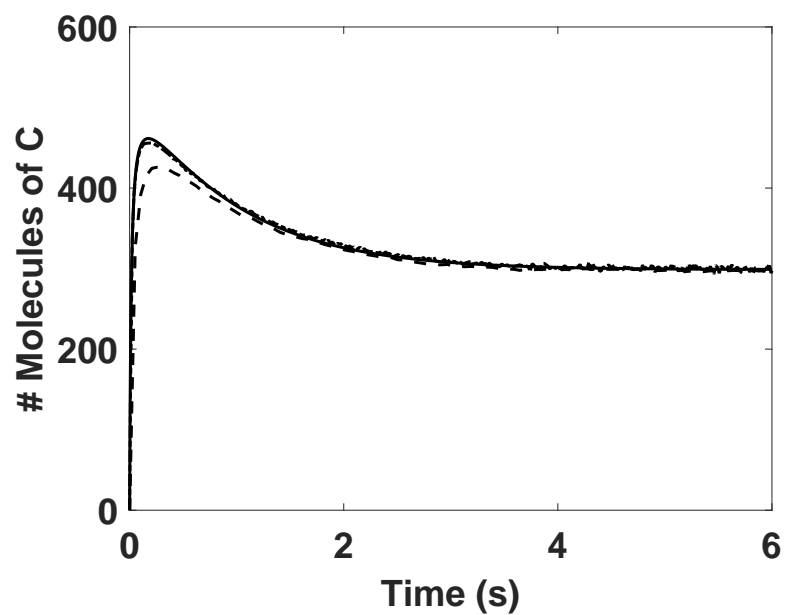


Figure D.2. Temporal evolution of the concentration of the species C for $N_{A_0} = N_{B_0} = 6 \times 10^2$ particles. Solid, dashed, and dash-dot lines are the deterministic solution, the solution obtained by Choi et al., model setting $\Delta x = \Delta y = \Delta z = L/8$, and the solution obtained by our model, respectively. All results are based on average of 1000 iterations.

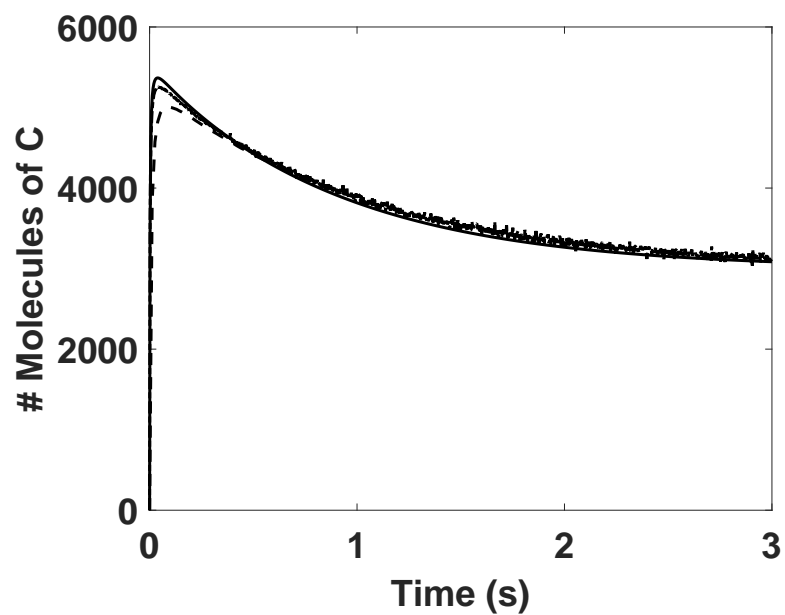


Figure D.3. Temporal evolution of the concentration of the species C for $N_{A_0} = N_{B_0} = 6 \times 10^3$ particles. Solid, dashed, and dash-dot lines are the deterministic solution, the solution obtained by Choi et al., model setting $\Delta x = \Delta y = \Delta z = L/16$, and the solution obtained by our model, respectively. All results are based on average of 1000 iterations.

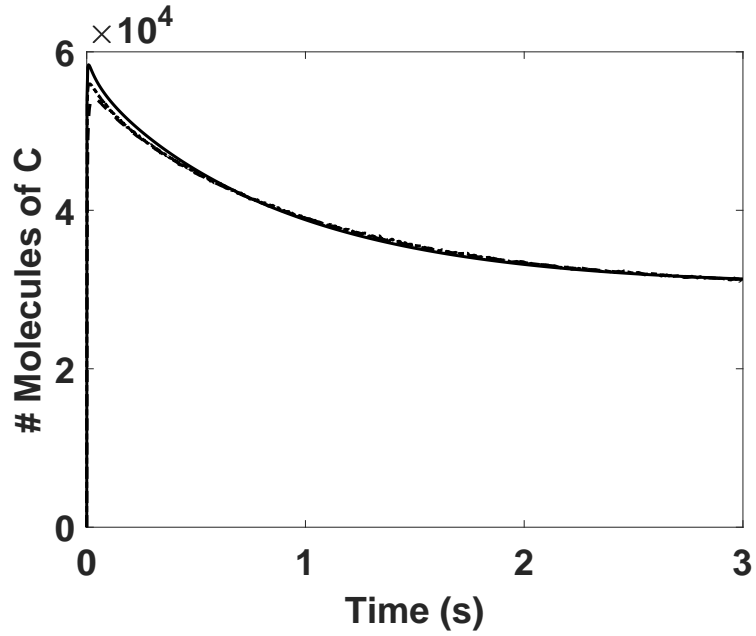


Figure D.4. Temporal evolution of the concentration of the species C for $N_{A_0} = N_{B_0} = 6 \times 10^4$ particles. Solid, dashed, and dash-dot lines are the deterministic solution, the solution obtained by Choi et al., model setting $\Delta x = \Delta y = \Delta z = L/32$, and the solution obtained by our model, respectively. All results are based on average of 1000 iterations.

Bibliography

- [ABS⁺01] E. Andrianantoandro, L. Blanchoin, D. Sept, J. A. McCammon, and T. D. Pollard. Kinetic mechanism of end-to-end annealing of actin filaments. *J. Mol. Biol.*, 312:721–730, 2001.
- [ACFF⁺12] S. Arumugam, G. Chwastek, E. Fischer-Friedrich, C. Ehrig, I. Mønch, and P. Schwille. Surface topology engineering of membranes of the mechanical investigation of the tubulin homologue FtsZ. *Angew. Chem. Int. Ed. Engl.*, 51(47):11858–11862, 2012.
- [ACL97] CS G. Addinall, C. Cao, and J. Lutkenhaus. Temperature shift experiments with an ftsZ84(Ts) strain reveal rapid dynamics of FtsZ localization and indicate that the Z ring is required throughout septation and cannot reoccupy division sites once constriction has initiated. *Journal of Bacteriology*, 179(13):4277–4284, 1997.
- [AGFE04] D. E. Anderson, F. J. Gueiros-Filho, and H. P. Erickson. Assembly dynamics of FtsZ rings in *Bacillus subtilis* and *Escherichia coli* and effects of FtsZ-regulating proteins. *J. Bacteriology*, 186(17):5775–5781, 2004.
- [AHB01] H. S. Al-Hadhrami and M. J. Blunt. Thermally induced wettability alteration to improve oil recovery in fractured reservoirs. *SPE Reservoir Evaluation & Engineering*, 4(3):179–186, Jun 2001.
- [AJL⁺14] B. Alberts, A. Johnson, J. Lewis, D. Morgan, M. Raff, K. Roberts, and P. Walter. *Molecular biology of the cell*. Garland Science, 6th edition, 2014.
- [APS14] S. Arumugam, Z. Petrásek, and P. Schwille. MinCDE exploits the dynamic nature of FtsZ filaments for its spatial regulation. *Proc. Natl. Acad. Sci. U.S.A.*, 111(13):1192–1200, 2014.
- [BBW⁺14] M. W. Bailey, P. Bisicchia, B. T. Warren, D. J. Sherratt, and J. Männik. Evidence for divisome localization mechanisms independent of the Min system and SlmA in *Escherichia coli*. *PLoS Genet.*, 10(8):e1004504, 2014.
- [BCH⁺13] J. Buss, C. Coltharp, T. Huang, C. Pohlmeier, S-C. Wang, C. Hatem, and J. Xiao. In vivo organization of the FtsZ-ring by ZapA and ZapB revealed by quantitative super-resolution microscopy. *Molecular Microbiol.*, 89(6):1099–1120, 2013.

- [BCS⁺15] J. Buss, C. Coltharp, G. Shtengel, X. Yang, H. Hess, and J. Xiao. A multi-layered protein network stabilizes the *Escherichia coli* FtsZ-ring and modulates constriction dynamics. *PLOS Genetics*, 11(4):795–802, 2015.
- [BGM13] S. M. Bhattacharjee, A. Giacometti, and A. Maritan. Flory theory for polymers. *J Phys Condens Matter*, 25(50), 2013.
- [BGRF06] A. Bataillé, P. Genthon, M. Rabinowicz, and B. Fritz. Modeling the coupling between free and forced convection in a vertical permeable slot: implications for the heat production of an enhanced geothermal system. *Geothermics*, 35(5-6):654–682, 2006.
- [BHC⁺08] M. Bathe, C. Heussinger, M. M. Claessens, A. R. Bausch, and E. Frey. Cytoskeletal bundle mechanics. *Biophys. J.*, 94:2955–2964, 2008.
- [BK09] D. P. Baston and B. H. Kueper. Thermal conductive heating in fractured bedrock: Screening calculations to assess the effect of groundwater influx. *Advances in Water Resources*, 32(2):231–238, Feb 2009.
- [BT82] G. S. Bodvarsson and C. F. Tsang. Injection and thermal breakthrough in fractured geothermal-reservoirs. *Journal of Geophysical Research*, 87(NB2):1031–1048, 1982.
- [CBPX16] C. Coltharp, J. Buss, T. M. Plumer, and J. Xiao. Defining the rate-limiting processes of bacterial cytokinesis. *PNAS*, 113(8):1044–1053, 2016.
- [CBRE5a] Y. Chen, K. Bjornson, S. D. Redick, and H. P. Erickson. A rapid fluorescence assay for FtsZ assembly indicates cooperative assembly with a dimer nucleus. *Biophys. J.*, 88:505–514, 2005a.
- [CE5b] Y. Chen and H. P. Erickson. Rapid in vitro assembly dynamics and subunit turnover of FtsZ demonstrated by Fluorescence Resonance Energy Transfer. *J. Biol. Chem.*, 280(23):22549–22554, 2005b.
- [CE09] Y. Chen and H. P. Erickson. FtsZ filament dynamics at steady state: subunit exchange with and without nucleotide hydrolysis. *Biochemistry*, 48(28):6664–6673, 2009.
- [CGD01] A. H. D Cheng, A. Ghassemi, and E. Detournay. Integral equation solution of heat extraction from a fracture in hot dry rocks. *International Journal for Numerical and Analytical Methods in Geomechanics*, 25(13):1327–1338, Nov 2001.
- [CJ59] H. S. Carslaw and J. C. Jaeger. *Conduction of Heat in Solids*. Oxford Univ. Press, New York, 1959.
- [CJR02] C. T. Culbertson, S. C. Jacobson, and J. M. Ramsey. Diffusion coefficient measurements in microfluidic devices. *Talanta*, 56:365–373, 2002.

- [CMDB11] H. Cho, H. R. McManus, S. L. Dove, and T. G. Bernhardt. Nucleoid occlusion factor SlmA is a DNA-activated FtsZ polymerization antagonist. *Proc. Natl. Acad. Sci. U.S.*, 108(9):3773–3778, 2011.
- [CMTS10] T.-J. Choi, M. R. Maurya, D. M. Tartakovsky, and S. Subramaniam. Stochastic hybrid modeling of intracellular calcium dynamics. *J. Chem. Phys.*, 133(16):165101, 2010.
- [CMTS12] T. J. Choi, M. R. Maurya, D. M. Tartakovsky, and S. Subramaniam. Stochastic operator-splitting method for reaction-diffusion systems. *J. Chem. Phys.*, 137(18):184102, 2012.
- [CPOS04] V. Cvetkovic, S. Painter, N. Outters, and J. O. Selroos. Stochastic simulation of radionuclide migration in discretely fractured rock near the Aspo Hard Rock Laboratory. *Water Resources Research*, 40(2), 2004.
- [CS11] X. Chen and P. M. Shearer. Comprehensive analysis of earthquake source spectra and swarms in the Salton Trough, California. *Journal of Geophysical Research-Solid Earth*, 118(3):1193–1194, Sep 2011.
- [DAR⁺08] R. D. Dixon, D. K. Arneman, A. S. Rachlin, N. R. Sundaresan, M. J. Costello, S. L. Campbell, and C. A. Otey. Palladin is an actin cross-linking protein that uses immunoglobulin-like domains to bind filamentous actin. *J. Biol. Chem.*, 283:6222–6231, 2008.
- [dHKS82] F. R. de Hoog, J. H. Knight, and A. N. Stokes. An improved method for numerical inversion of Laplace transforms. *SIAM Journal on Scientific and Statistical Computing*, 3(3):357–366, 1982.
- [DL14] S. Du and J. Lutkenhaus. SlmA antagonism of FtsZ assembly employs a two-pronged mechanism like MinCD. *PLoS Genet.*, 10(7):38–46, 2014.
- [DLS⁺08] A. Dajkovic, G. Lan, S. X. Sun, D. Wirtz, and J. Lutkenhaus. MinC spatially controls bacterial cytokinesis by antagonizing the scaffolding function of FtsZ. *Curr. Biol.*, 18:235–244, 2008.
- [DM95] W. Dershowitz and I. Miller. Dual-porosity fracture flow and transport. *Geophysical Research Letters*, 22(11):1441–1444, Jun 1995.
- [DPLW10] A. Dajkovic, S. Pichoff, J. Lutkenhaus, and D. Wirtz. Cross-linking FtsZ polymers into coherent Z rings. *Molec. Microbiol.*, 78(3):651–668, 2010.
- [DRKB07] M. Dobrzynski, J. V. Rodríguez, J. A. Kaandorp, and J. G. Blom. Computational methods for diffusion-influenced biochemical reactions. *Bioinformatics*, 23(15):1969–77, 2007.

- [DRRv13] C. E. Dow, A. Rodger, D. I. Roper, and H. A. van den Berg. A model of membrane contraction predicting initiation and completion of bacterial cell division. *Integr. Biol.*, 5:2778–795, 2013.
- [EAO10] H. P. Erickson, D. E. Anderson, and M. Osawa. FtsZ in bacterial cytokinesis: cytoskeleton and force generator all in one. *Microbiol. Mol. Biol. Rev.*, 74(4):504–528, 2010.
- [EBD⁺12] O. Espeli, R. Borne, P. Dupaigne, A. Thiel, E. Gigant, R. Mercier, and F. Boccard. A MatPdivisome interaction coordinates chromosome segregation with cell division in *E. coli*. *The EMBO Journal*, 31:3198–3211, 2012.
- [EKC⁺14] M. L. Erb, J. A. Kraemer, J. K. C. Coker, V. Chaikeeratisak, P. Nonejuie, D. A. Agard, and J. Pogliano. A bacteriophage tubulin harnesses dynamic instability to center DNA in infected cells. *eLife*, 3:6222–6231, 2014.
- [Ell01] R. J. Ellis. Macromolecular crowding: an important but neglected aspect of the intracellular environment. *Current Opinion in Structural Biology*, 11:114–119, 2001.
- [Eri09] H. P. Erickson. Modeling the physics of FtsZ assembly and force generation. *Proc. Natl. Acad. Sci. U.S.A.*, 106(23):9238–9243, 2009.
- [ETTB96] H. P. Erickson, D. W. Taylor, K. A. Taylor, and D. Bramhill. Bacterial cell division protein FtsZ assembles into protofilament sheets and minirings, structural homologs of tubulin polymers. *PNAS*, 93:519–523, 1996.
- [FF15] R. S. Fischer and V. M. Fowler. The state of the cytoskeleton in 2015. *J. Biol. Chem.*, 290(29), 2015.
- [FFFG12] E. Fischer-Friedrich, B. M. Friedrich, and N. S. Gov. FtsZ rings and helices: physical mechanisms for the dynamic alignment of biopolymers in rod-shaped bacteria. *Phys. Biol.*, 9(1), 2012.
- [FFG11] E. Fischer-Friedrich and N.S. Gov. Modeling FtsZ ring formation in the bacterial cell-anisotropic aggregation via mutual interactions of polymer rods. *Phys. Biol.*, 8:10, 2011.
- [FG83] C. Frieden and D.W. Goddette. Polymerization of actin and actin-like systems: evaluation of the time course of polymerization in relation to the mechanism. *Biochemistry*, 22:5836–5843, 1983.
- [FHB⁺10] G. Fu, T. Huang, J. Buss, C. Coltharp, Z. Hensel, and J. Xiao. In vivo structure of the *E. coli* FtsZ-ring revealed by photoactivated localization microscopy (PALM). *PLoS ONE*, 5(9):e12680, 2010.

- [FLKG12] T. T. Falzone, M. Lenz, D. R. Kovar, and M. L. Gardel. Assembly kinetics determine the architecture of α -actin in crosslinked F-actin networks. *Nature Comm.*, 3(861):266–272, 2012.
- [FPBM08] J. Fass, C. Pak, J. Bamberg, and A. Mogilner. Stochastic simulation of actin dynamics reveals the role of annealing and fragmentation. *J. Theor. Biol.*, 252:173–183, 2008.
- [FT61] V. N. Faddeeva and N. M. Terent’ev. *Tables of values of the function $w(z)$ for complex argument*. Pergamon press, New York, 1961.
- [GFJ03] R. C. Gunasekera, G. R. Foulger, and B. R. Julian. Reservoir depletion at The Geysers geothermal area, California, shown by four-dimensional seismic tomography. *Journal of Geophysical Research-Solid Earth*, 108(B3), Mar 2003.
- [GFL02] F. J. Gueiros-Filho and R. Losick. A widely conserved bacterial cell division protein that promotes assembly of the tubulin-like protein FtsZ. *Genes & Development*, 16(19):2544–2556, 2002.
- [GG12] E. Galli and K. Gerdes. FtsZ-ZapA-ZapB interactome of Escherichia coli. *Journal of Bacteriology*, 194(2):292–302, 2012.
- [Gil77] D. T. Gillespie. Exact stochastic simulation of coupled chemical reactions. *Journal of Physical Chemistry*, 81(25):2340–2361, 1977.
- [GJV⁺03] J. M. González, M. Jiménez, M. Vélez, J. Mingorance, J. M. Andreu, M. Vicente, and G. Rivas. Essential cell division protein FtsZ assembles into one monomer-thick ribbons under conditions resembling the crowded intracellular environment. *The Journal of Biological Chemistry*, 278(39):37664–37671, 2003.
- [GLK12] R. Gelet, B. Loret, and N. Khalili. A thermo-hydro-mechanical coupled model in local thermal non-equilibrium for fractured HDR reservoir with double porosity. *Journal of Geophysical Research-Solid Earth*, 117(B7), Jul 2012.
- [GSM07] B. Geissler, D. Shiomi, and W. Margolin. The ftsA* gain-of-function allele of escherichia coli and its effects on the stability and dynamics of the Z ring. *Microbiology*, 153(03):814–825, 2007.
- [GVJ⁺05] J. M. González, M. Vélez, M. Jiménez, C. Alfonso, P. Schick, J. Mingorance, M. Vicente, A. P. Minton, and G. Rivas. Cooperative behavior of escherichia coli cell-division protein ftsz assembly involves the preferential cyclization of long single-stranded fibrils. *Proc. Natl. Acad. Sci. U.S.A.*, 102(6):1895–1900, 2005.
- [GWO75] A. C. Gringarten, P. A. Witherspoon, and Y. Ohnishi. Theory of heat extraction from fractured hot dry rock. *Journal of Geophysical Research*, 80(8):1120–1124, 1975.

- [Han04] S. Hansen. Translational friction coefficients for cylinders of arbitrary axial ratios estimated by monte carlo simulation. *The Journal of Chemical Physics*, 121(18):9111–9115, 2004.
- [HdB97] C. A. Hale and A. J. de Boer. Direct binding of Ftsz to ZipA, an essential component of the septal ring structure that mediates cell division in *E. coli*. *Cell*, 88(2):175–185, 1997.
- [HDHJ13] K-H. Huang, J. Durand-Heredia, and A. Janakiraman. FtsZ ring stability: of bundles, tubules, crosslinks and curves. *Journal of Bacteriology*, 195(9):1859–1868, 2013.
- [HLB⁺08] S. Huecas, O. Llorca, J. Boskovic, J. Martín-Benito, J. M. Valpuesta, and J. M. Andreu. Energetics and geometry of FtsZ polymers: nucleated self-assembly of single protofilaments. *Biophys. J.*, 94:1796–1806, 2008.
- [HMW03] K. C. Huang, Y. Meir, and N. S. Wingreen. Dynamic structures in *Escherichia coli*: Spontaneous formation of MinE rings and MinD polar zones. *Proc. Natl. Acad. Sci. U.S.*, 100(22):12724–12728, OCT 2003.
- [HRRG⁺10] V. M. Hernández-Rocamora, B. Reija, C. García, P. Natale, C. Alfonso, A. P. Minton, S. Zorrilla, G. Rivas, and M. Vicente. Dynamic interaction of the *Escherichia coli* cell division ZipA and FtsZ proteins evidenced in nanodiscs. *Biochemistry*, 49:10780–10787, 2010.
- [IMG12] M. Ingerson-Mahar and Z. Gitai. A growing family: the expanding universe of the bacterial cytoskeleton. *FEMS Microbiol. Rev.*, 36:256–266, 2012.
- [JMW15] M. H. Jensen, E. J. Morris, and D. A. Weitz. Mechanics and dynamics of reconstituted cytoskeletal systems. *Biochimica et Biophysica Acta*, 1853(11):3038–3042, 2015.
- [KG90] K. Kremer and G. S. Grest. Dynamics of entangled linear polymer melts: A molecular-dynamics simulation. *The Journal of Chemical Physics*, 92(8):5057–5086, 1990.
- [KH14] M. Koskinen and P. Hotulainen. Measuring F-actin properties in dendritic spines. *Front. Neuroanatomy*, 8(74):1–14, 2014.
- [KLSR06] R. A. Kerr, H. Levine, T. J. Sejnowski, and W.-J. Rappel. Division accuracy in a stochastic model of Min oscillations in *Escherichia coli*. *Proc. Natl. Acad. Sci. U.S.*, 103(2):347–352, JAN 2006.
- [Kol95] O. Kolditz. Modeling flow and heat-transfer in fractured rocks - dimensional effect of matrix heat diffusion. *Geothermics*, 24(3):421–437, Jun 1995.

- [KSEG93] H. J. Kinosian, L. A. Selden, J. E. Estes, and L. C. Gershman. Actin filament annealing in the presence of ATP and Phalloidin. *Biochemistry*, 32:12353–12357, 1993.
- [LDWS08] G. Lan, A. Dajkovic, D. Wirtz, and S. X. Sun. Polymerization and bundling kinetics of FtsZ filaments. *Biophys. J.*, 95:4045–4056, 2008.
- [Lin02] W. Lin. Permanent strain of thermal expansion and thermally induced microcracking in Inada granite. *Journal of Geophysical Research*, 107(B10), Oct 2002.
- [LM14] M. Loose and T.J. Mitchinson. The bacterial cell division proteins FtsA and FtsZ self-organize into dynamic cytoskeletal patterns. *Nature Cell Biol.*, 16(1):38–46, 2014.
- [LML04] H. H. Low, M. C. Moncrieffe, and J. Lowe. The crystal structure of ZapA and its modulation of FtsZ polymerisation. *Journal of Molecular Biology*, 341:839–852, 2004.
- [LPD12] J. Lutkenhaus, S. Pichoff, and S. Du. Bacterial cytokinesis: from Z ring to divisome. *Cytoskeleton*, 69(10):778–790, 2012.
- [LRE00] C. Lu, M. Reedy, and H. P. Erickson. Straight and curved conformations of FtsZ are regulated by GTP hydrolysis. *Journal of Bacteriology*, 182(1):164–170, 2000.
- [LTBJ07] Z. Li, M. J. Trimble, Y. V. Brun, and G. J. Jensen. The structure of FtsZ filaments in vivo suggests a force-generating role in cell division. *EMBO J.*, 26:4694–4708, 2007.
- [Lut07] J. Lutkenhaus. Assembly dynamics of the bacterial MinCDE system and spatial regulation of the Z ring. *Annu. Rev. Biochem.*, 76:539–562, 2007.
- [LWS07] G. Lan, C. W. Wolgemuth, and S. X. Sun. Z-ring force and cell shape during division in rod-like bacteria. *Proc. Natl. Acad. Sci. U.S.*, 104(41):16110–16115, 2007.
- [MB15] J. Männik and M.W. Bailey. Spatial coordination between chromosomes and cell division proteins in Escherichia coli. *Front. Microbiol.*, 6(306), 2015.
- [MBF06] N. A. Medeiros, D.T. Burnette, and P. Forscher. Myosin II functions in actin-bundle turnover in neuronal growth cones. *Nature Cell Biol.*, 8:216–226, 2006.
- [MdB01] H. Meinhardt and P. A. J. de Boer. Pattern formation in Escherichia coli: A model for the pole-to-pole oscillations of Min proteins and the localization of the division site. *Proc. Natl. Acad. Sci. U.S.*, 98(25):14202–14207, DEC 2001.
- [Mey04] J. Meyer. Development of a heat transport analytical model for a single fracture in a porous matrix. *Report for Earth 661, University of Waterloo*, Apr 2004.

- [MGGP88] D. B. Murphy, R. O. Gray, W. A. Grasser, and T. D. Pollard. Direct demonstration of actin filament annealing in vitro. *J. Cell Biol.*, 106:1947–1954, 1988.
- [MGPH⁺12] P. Mateos-Gil, A. Paez, I. Hørger, G. Rivas, M. Vicente, P. Tarazona, and M. Vélez. Depolymerization dynamics of individual filaments of bacterial cytoskeletal protein FtsZ. *Proc. Natl. Acad. Sci. U.S.*, 109(21):8133–8138, 2012.
- [ML08] P. K. Mattila and P. Lappalainen. Filopodia: molecular architecture and cellular functions. *Nature Rev. Molecular Cell Biol.*, 9:446–454, 2008.
- [MPCP07] J. Molson, P. Pehme, J. Cherry, and B. Parker. Numerical analysis of heat transport within fractured sedimentary rock: implications for temperature probes. *NGWA/U.S.EPA Fractured Rock Conference: State of the Science and Measuring Success in Remediation, Portland, Maine, (5017):489–502, Sep 2007.*
- [MPS⁺08] R. Mercier, M-A Petit, S. Schbath, S. Robin, M. El Karoui, F. Bocard, and O. Espéli. The MatP/matS site-specific system organizes the terminus region of the E. coli chromosome into a macrodomain. *Cell*, 135:475–485, 2008.
- [MPV⁺09] T. Mohammadi, G. E. J. Ploeger, J. Verheul, A. D. Comvalius, A. Martos, C. Alfonso, J. van Marle, G. Rivas, and T. den Blaauwen. The GTPase activity of Escherichia coli FtsZ determines the magnitude of the FtsZ polymer bundling by ZapA in vitro. *Biochemistry*, 48:11056–11066, 2009.
- [MTA⁺12] H. Masuda, Q. Tan, N. Awano, K. P. Wu, and M. Inouye. YeeU enhances the bundling of cytoskeletal polymers of MreB and FtsZ, antagonizing the CbtA (YeeV) toxicity in Escherichia coli. *Mol. Microbiol.*, 84(5):979–989, 2012.
- [NE92] S. H. Northrup and H. P. Erickson. Kinetics of protein-protein association explained by Brownian dynamics computer simulation. *Proc. Natl. Acad. Sci. U.S.*, 89(8):3338–3342, 1992.
- [Nee15] D. Needleman. The material basis of life. *Trends in Cell Biology*, 25(12):713–716, 2015.
- [NM13] P. Nurse and K.J. Mariani. Purification and characterization of Escherichia coli MreB protein. *J. Biol. Chem.*, 288(5):34693475, 2013.
- [NTS10] A. Neuville, R. Toussaint, and J. Schmittbuhl. Hydrothermal coupling in a self-affine rough fracture. *Phys. Rev. E*, 82(036317), 2010.
- [NY08] L. Niu and J. Yu. Investigating intracellular dynamics of FtsZ cytoskeleton with photiactivation single-molecule tracking. *Biophysical Journal*, 95(4):2009–2016, 2008.
- [PCC01] D. Pantaloni, C. Le Clainche, and M-F. Carrier. Mechanism of actin-based motility. *Science*, 292:1502–1506, 2001.

- [Per36] F. Perrin. Mouvement brownien d'un ellipsoïde (ii). rotation libre et dpolarisation des fluorescences. translation et diffusion de molécules ellipsoïdales. *Journal de Physique et Le Radium*, 7(1):1–11, 1936.
- [PGCH⁺13] R. Pacheco-Gómez, X. Cheng, M. R. Hicks, C. J. I. Smith, D. I. Roper, S. Addinall, A. Rodger, and T. R. Dafforn. Tetramerization of ZapA is required for FtsZ bundling. *Biochemical Journal*, 449(13):795–802, 2013.
- [PGP07] P. E. Pehme, J. P. Greenhouse, and B. L. Parker. The Active Line Source temperature logging technique and its application in fractured rock hydrogeology. *Journal of Environmental and Engineering Geophysics*, 12(4):307–322, Dec 2007.
- [PIN⁺09] D. Popp, M. Iwasa, A. Narita, H. P. Erickson, and Y. Maéda. FtsZ condensates: an in vitro electron microscopy study. *Biopolymers*, 91(5):340–350, 2009.
- [PIT12] S.-W. Park, M. Intaglietta, and D. M. Tartakovsky. Impact of endothelium roughness on blood flow. *J. Theor. Biol.*, (300):152–160, 2012.
- [PL05] S. Pichoff and J. Lutkenhaus. Tethering the Z ring to the membrane through a conserved membrane targeting sequence in FtsA. *Molecular Microbiol.*, 55(6):1722–1734, 2005.
- [PPCG10] P. E. Pehme, B. L. Parker, J. A. Cherry, and J. P. Greenhouse. Improved resolution of ambient flow through fractured rock with temperature logs. *Ground Water*, 48(2):191–205, Mar-Apr 2010.
- [PR12] P. Penzes and I. Rafalovich. Regulation of the actin cytoskeleton in dendritic spines. *Adv. Exp. Med. Biol.*, 970:81–95, 2012.
- [Qia05] H. Qian. Cycle kinetics, steady state thermodynamics and motors - a paradigm for living matter physics. *J. Phys. Condens. Matter*, 17:3783–3793, 2005.
- [Qia07] H. Qian. Phosphorylation energy hypothesis: open chemical systems and their biological functions. *Annu. Rev. Phys. Chem.*, 58:113–142, 2007.
- [RdDT12] D. Roubinet, J. R de Dreuzy, and D. M. Tartakovsky. Semi-analytical solutions for solute transport and exchange in fractured porous media. *Water Resources Research*, 48:W01542, Jan 2012.
- [RdDT13] D. Roubinet, J. R de Dreuzy, and D. M. Tartakovsky. Particle-tracking simulations of anomalous transport in hierarchically fractured rocks. *Computers & Geosciences*, 50:52–58, Jan 2013.
- [RHK⁺14] L. Robert, M. Hoffmann, N. Krell, S. Aymerich, J. Robert, and M. Doumic. Division in *Escherichia coli* is triggered by a size-sensing rather than a timing mechanism. *Bmc Biology*, 12(17), 2014.

- [RKK⁺06] J. V. Rodríguez, J. A. Kaandorp, Jaap A Kaandorp, M. Dobrzynski, and J. G. Blom. Spatial stochastic modelling of the phosphoenolpyruvate-dependent phosphotransferase (PTS) pathway in *Escherichia coli*. *Bioinformatics*, 22(15):1895–1901, 2006.
- [RLdD10] D. Roubinet, H. H Liu, and J. R de Dreuzy. A new particle-tracking approach to simulating transport in heterogeneous fractured porous media. *Water Resources Research*, 46:W11507, Nov 2010.
- [RM04] L. Romberg and T. J. Mitchison. Rate-limiting guanosine 5'-triphosphate hydrolysis during nucleotide turnover by FtsZ, a prokaryotic tubulin homologue involved in bacterial cell division. *Biochemistry*, 43:282–288, 2004.
- [RM14] V. W. Rowlett and W. Margolin. 3D-SIM Super-resolution of FtsZ and its membrane tethers in *Escherichia coli* cells. *Biophys. J.*, 107:17–20, 2014.
- [RMBST16] A. Ruiz-Martinez, T. M. Bartol, T. J. Sejnowski, and D. M. Tartakovsky. Efficient multiscale models of polymer assembly. *Biophysical Journal*, 110(1):185–196, 2016.
- [RS11] K. Rottner and T. E. B. Stradal. Actin dynamics and turnover in cell motility. *Curr. Opinion Cell Biol.*, 23:569–578, 2011.
- [RSBE05] S. D. Redick, J. Stricker, G. Briscoe, and H. P. Erickson. Mutants of FtsZ targeting the protofilament interface: effects on cell division and GTPase activity. *J. Bacteriol.*, 187(8):2727–2736, 2005.
- [RSE01] L. Romberg, M. Simon, and H. P. Erickson. Polymerization of FtsZ, a bacterial homolog of tubulin: Is assembly cooperative? *J. Biol. Chem.*, 18(15):11743–11753, 2001.
- [RVM03] S. Rueda, M. Vicente, and J. Mingorance. Concentration and assembly of the division ring proteins FtsZ, FtsA, and ZipA during the *Escherichia coli* cell cycle. *Journal of Bacteriology*, 185(11):3344–3351, 2003.
- [SF82] E. A. Sudicky and E. O. Frind. Contaminant transport in fractured porous-media - analytical solutions for a system of parallel fractures. *Water Resources Research*, 18(6):1634–1642, 1982.
- [SL09] B. Shen and J. Lutkenhaus. The conserved C-terminal tail of FtsZ is required for the septal localization and division inhibitory activity of MinCC/MinD. *Molec. Microbiol.*, 72(2):410–424, 2009.
- [SL10] B. Shen and J. Lutkenhaus. Examination of the interaction between FtsZ and MinCN in *E. coli* suggests how MinC disrupts Z rings. *Molec. Microbiol.*, 75(5):1285–1298, 2010.

- [SM98] Q. Sun and W. Margolin. FtsZ dynamics during the division cycle of live *Escherichia coli* cells. *Journal of bacteriology*, 180(8):2050–2056, 1998.
- [SML08] I. V. Surovtsev, J. J. Morgan, and P. A. Lindhal. Kinetic modeling of the assembly, dynamic steady state and contraction of the FtsZ ring in prokaryotic cytokinesis. *PLoS Comput. Biol.*, 4(7), 2008.
- [SMMHB07] R. Srinivasan, M. Mishra, M. Murata-Hori, and M.K. Balasubramanian. Filament formation of the *Escherichia coli* actin-related protein, MreB, in fission yeast. *Curr. Biol.*, 17(3):266–272, 2007.
- [SMSE02] J. Stricker, P. Maddox, E. D. Salmon, and H. P. Erickson. Rapid assembly dynamics of the *Escherichia coli* FtsZ-ring demonstrated by fluorescence recovery after photobleaching. *Proc. Natl. Acad. Sci. U.S.*, 99(5):3171–3175, 2002.
- [SVM12] R. P. Stevenson, D. Veltman, and L. M. Machesky. Actin-bundling proteins in cancer progression at a glance. *J. Cell Sci.*, 125:1073–1079, 2012.
- [SW11] D. Swanson and N. S. Wingreen. Active biopolymers confer fast reorganization kinetics. *Phys. Rev. Lett.*, 107(21):218103, 2011.
- [SXPM99] D. Sept, J. Xu, T. D. Pollard, and J. A. McCammon. Annealing accounts for the length of actin filaments formed by spontaneous polymerization. *Biophys. J.*, 77:2911–1919, 1999.
- [SZL09] J. Salje, B. Zuber, and J. Lwe. Electron cryomicroscopy of *E. coli* reveals filament bundles involved in plasmid DNA segregation. *Science*, 323(509):509–512, 2009.
- [Ter02] I. Terakoa. *Polymer Solutions: An Introduction to Physical Properties*. John Wiley & Sons, Inc., 2002.
- [TFS81] D. H. Tang, E. O. Frind, and E. A. Sudicky. Contaminant transport in fractured porous-media - analytical solution for a single fracture. *Water Resources Research*, 17(3):555–564, 1981.
- [TGR03] D. M. Tartakovsky, A. Guadagnini, and M. Riva. Stochastic averaging of nonlinear flows in heterogeneous porous media. *J. Fluid Mech.*, 492:47–62, 2003.
- [TMC⁺13] N. K. Tonthat, S. L. Milam, N. Chinnam, T. Whitfill, W. Margolin, and M. A. Schumacher. SlmA forms a higher-order structure on DNA that inhibits cytokinetic Z-ring formation over the nucleoid. *Proc. Natl. Ac. Sci. U.S.*, 110(37):10586–10591, 2013.
- [TPD⁺12] D. J. Turner, I. Portman, T. R. Dafforn, A. Rodger, D. I. Roper, C. J. Smith, and M. S. Turner. The mechanics of FtsZ fibers. *Biophys. J.*, 102:731–738, 2012.
- [TRC⁺11] R. Tsukanov, G. Reshes, G. Carmon, E. Fischer-Friedrich, N. S. Gov, I. Fishov, and M. Feingold. Timing of Z-ring localization in *Escherichia coli*. *Phys. Biol.*, 8:13, 2011.

- [TX06] D. M. Tartakovsky and D. Xiu. Stochastic analysis of transport in tubes with rough walls. *J. Comput. Phys.*, 217(1):248–259, 2006.
- [vDW97] M. A. van Dijk and A. Wakker. *Concepts in Polymer Thermodynamics, Volume 2*. Technomic Publishing Company, Inc., 1997.
- [WBC⁺89] H. F. Wang, B. P. Bonner, S. R. Carlson, B. J. Kowallis, and H. C. Heard. Thermal-stress cracking in granite. *Journal of Geophysical Research-Solid Earth and Planets*, 94(B2):1745–1758, Feb 1989.
- [Weg76] A. Wegner. Head to tail polymerization of actin. *J. Mol. Biol.*, 108:139–150, 1976.
- [WG11] B. Wickstead and K. Gull. The evolution of the cytoskeleton. *J. Cell Biol.*, 194(4):513–525, 2011.
- [WRWT96] J. Willis-Richards, K. Watanabe, and H. Takahashi. Progress toward a stochastic rock mechanics model of engineered geothermal systems. *Journal of Geophysical Research-Solid Earth*, 101(B8):17481–17496, Aug 1996.
- [WS10] C. E. Walczak and S. L. Shaw. A MAP for bundling microtubules. *Cell*, 142(3):433–443, 2010.
- [WTCW81] J. S. Y. Wang, C. F. Tsang, N. G. W. Cook, and P. A. Witherspoon. A study of regional temperature and thermohydrologic effects of an underground repository for nuclear wastes in hard rock. *Journal of Geophysical Research*, 86(NB5), 1981.
- [XBZ12] K. Xu, H. P. Babcock, and X. Zhuang. Dual-objective STORM reveals three-dimensional filament organization in the actin cytoskeleton. *Nature Meth.*, 9(2):185–188, 2012.
- [XP01] T. F. Xu and K. Pruess. On fluid flow and mineral alteration in fractured caprock of magmatic hydrothermal systems. *Journal of Geophysical Research-Solid Earth*, 106(B2), Feb 2001.
- [XT06] D. Xiu and D. M. Tartakovsky. Numerical methods for differential equations in random domains. 28(3):1167–1185, 2006.
- [XZ12] Y. Xiang and Y. Zhang. Two-dimensional integral equation solution of advective-conductive heat transfer in sparsely fractured water-saturated rocks with heat source. *International Journal of Geomechanics*, 12(2):168–175, Mar-Apr 2012.
- [YL12] K. Yi and R. Li. Actin cytoskeleton in cell polarity and asymmetric division during mouse oocyte maturation. *Cytoskeleton*, 69(10):727–737, 2012.
- [YY09] S. Y. Yang and H. D. Yeh. Modeling heat extraction from hot dry rock in a multi-well system. *Applied Thermal Engineering*, 29(8-9):1676–1681, Jun 2009.

- [ZLM⁺07] Q. Zhou, H. H. Liu, F. J. Molz, Y. Zhang, and G. S. Bodvarsson. Field-scale effective matrix diffusion coefficient for fractured rock: Results from literature survey. *Journal of contaminant hydrology*, 93(1-4):161–187, Aug 2007.
- [ZML13] Z. Zhang, J. J. Morgan, and P. A. Lindhal. Mathematical model for positioning the FtsZ contractile ring in *Escherichia coli*. *J. Math. Biol.*, pages 911–930, 2013.